UNIVERSITAT POLITÈCNICA DE VALÈNCIA

Upscaling and Inverse Modeling of Groundwater Flow and Mass Transport in Heterogeneous Aquifers

PhD Thesis submitted by

Liangping Li

Advisor:

J. Jaime Gómez-Hernández

Valencia 2011

Upscaling and Inverse Modeling of Groundwater Flow and Mass Transport in Heterogeneous Aquifers

PhD Thesis submitted by
Liangping Li

Advisor:
J. Jaime Gómez-Hernández

Department:
Ingeniería Hidráulica y Medio Ambiente
Universitat Politècnica de València

September 2011

To Haiyan

Abstract

The need to reduce the computational cost of stochastic groundwater flow and mass transport predictions calls for efficient upscaling techniques which can transfer the heterogeneity across scales while preserving similar flow and transport behaviors. In addition, due to the scarcity of measurement data, inverse modeling is commonly used to calibrate the parameters by conditioning on direct and indirect data and hence reduce the uncertainty of flow and transport predictions. In this work, an upscaling technique is developed and applied both in a synthetic example and a real case; then upscaling and the Ensemble Kalman Filter (EnKF, a method for inverse modeling) are coupled to handle a high-resolution inverse model; and finally, the EnKF and its variant, the normal-score EnKF, is applied in the context of multiGaussian and non-multiGaussian media. The work included in this PhD can be grouped in three blocks.

First, simple averaging, simple-Laplacian, Laplacian-with-skin, and non-uniform coarsening upscaling techniques are reviewed and assessed in a three-dimensional hydraulic conductivity upscaling exercise. The reference is a fine scale conditional realization of the hydraulic conductivities at the MAcro-Dispersion Experiment site on Columbus Air Force Base in Mississippi (USA). This realization was generated using a hole-effect variogram model and it was shown that flow and transport modeling in this realization (at the fine scale) can reproduce the observed non-Fickian spreading of the tritium plume. The purpose of this work is twofold, first to compare the effectiveness of different upscaling techniques in yielding upscaled models able to reproduce the observed transport behavior, and second to demonstrate and analyze the conditions under which flow upscaling can provide a coarse model in which the standard advection-dispersion equation can be used to model transport in seemingly non-Fickian scenarios. Specifically, the use of the Laplacian-based upscaling technique coupled with a non-uniform coarsening scheme yields the best results both in terms of flow and transport reproduction, for this case study in which the coarse blocks are smaller than the correlation ranges of the fine scale conductivities. However, in some cases, we also observe the impossibility of reproducing transport at the coarse scale solely on the basis of a flow upscaling. For this reason, a methodology for transport upscaling is developed

for three-dimensional highly heterogeneous formations. The overall approach requires a prior hydraulic conductivity upscaling using an interblock-centered full-tensor Laplacian-with-skin method followed by transport upscaling. The coarse scale transport equation includes a multi-rate mass transfer term to compensate for the loss of heterogeneity inherent to all upscaling processes. The upscaling procedures for flow and transport are described in detail and then applied to a three-dimensional highly heterogeneous synthetic example. The proposed approach not only reproduces flow and transport at the coarse scale, but it also reproduces the uncertainty associated with the predictions as measured by the ensemble variability of the breakthrough curves.

Second, the ensemble Kalman filter is coupled with upscaling to build an aquifer model at a coarser scale than the scale at which the conditioning data (conductivity and piezometric head) had been taken for the purpose of inverse modeling. Building an aquifer model at such scale is most often impractical, since this would imply numerical models with millions of cells. If, in addition, an uncertainty analysis is required involving some kind of Monte-Carlo approach, the task becomes impossible. For this reason, a methodology has been developed that will use the conductivity data, at the scale at which they were collected, to build a model at a (much) coarser scale suitable for the inverse modeling of groundwater flow and mass transport. It proceeds as follows: (i) generate an ensemble of realizations of conductivities conditioned to the conductivity data at the same scale at which conductivities were collected, (ii) upscale each realization onto a coarse discretization; on these coarse realizations, conductivities will become tensorial in nature with arbitrary orientations of their principal directions, (iii) apply the EnKF to the ensemble of coarse conductivity upscaled realizations in order to condition the realizations to the measured piezometric head data. The proposed approach addresses the problem of how to deal with tensorial parameters, at a coarse scale, in ensemble Kalman filtering, while maintaining the conditioning to the fine scale hydraulic conductivity measurements. The approach is demonstrated in the framework of a synthetic worth-of-data exercise, in which the relevance of conditioning to conductivities, piezometric heads or both is analyzed.

Finally, the ensemble Kalman filter is applied to jointly update the flow and transport parameters (hydraulic conductivity and porosity) and state variables (piezometric head and concentration) of a groundwater flow and contaminant transport problem in a multi-Gaussian porous media. A synthetic experiment is used to demonstrate the capability of the EnKF to estimate the hydraulic conductivity and porosity by assimilating dynamic head and multiple concentration data in a transient flow and transport model. In this work the worth of hydraulic conductivity, porosity, head and concentration data is analyzed in the context of aquifer characterization. The results indicate that the characterization of the hydraulic conductivity and porosity fields is continuously

improved as more data is assimilated. Also the groundwater flow and mass transport predictions are improved if more and different types of data are assimilated. The beneficial impact of accounting for multiple concentration data is patent, particularly for the identification of the porosity field. Moreover, the normal score Ensemble Kalman Filter (NS-EnKF) method, which was recently developed to deal with the non-Gaussianity of parameters and state vectors in the EnKF, is used to assess the impact of prior conceptual model uncertainty on the characterization of conductivity and on the prediction of flow in a synthetic bimodal aquifer. In addition, the effect of distance-dependent localization functions and different set-ups of the boundary conditions in the aquifer are also examined. The results are evaluated in terms of ensemble means, variances and connectivities of the conditional realizations of conductivity and also looking at the uncertainty of predicted heads after solving the flow equation in the conditional conductivity realizations. For the cases analyzed it is found that (i) the patterns of simulated conductivity and flow prediction can be reproduced close to the reference for both the correct and wrong prior model using either the NS-EnKF or localized NS-EnKF as long as a sufficient number of piezometric head data are used for conditioning, (ii) coupling NS-EnKF with the localization function improves the conductivity identification, (iii) the performance of the NS-EnKF is not affected by the types of boundary conditions used.

Resumen

La necesidad de reducir el coste computacional de los modelos estocásticos de flujo de agua subterránea y de transporte de masa en acuíferos requieren técnicas de escalado eficaces que puedan transferir la heterogeneidad de una escala fina a otra gruesa, mientras que al mismo tiempo preserven el comportamiento en cuanto a flujo y transporte. Además, debido a la escasez de datos, comúnmente se utiliza la modelación inversa para calibrar los parámetros para el condicionamiento de los modelos tanto a medidas directas como a medidas indirectas, siempre con el objetivo de reducir la incertidumbre de las predicciones de flujo y transporte. En este trabajo, se ha desarrollado una técnica de escalado que se ha aplicado a un ejemplo de sintético y a un caso real, después, se ha acoplado el escalado con el filtro de Kalman de conjuntos (EnKF, un método de modelación inversa) para resolver un problema inverso en un acuífero del que se dispone de datos a una escala muy pequeña y, por último, el EnKF y su variante el EnKF con transformación gausiana, se usa para el análisis de medios multigausianos y no multigausianos. El trabajo desarrollado en esta tesis puede agruparse en tres bloques.

En el primer bloque, se han revisado las técnicas de escalado que utilizan una media simple, el método laplaciano simple, el laplaciano con piel y el escalado con mallado no uniforme y se han evaluado en un ejercicio tridimensional de escalado de la conductividad hidráulica. El campo usado como referencia es una realización condicional a escala fina de la conductividad hidráulica del experimento de macrodispersión realizado en la base de la fuerza aérea estadounidense de Columbus en Misuri (MADE en su acrónimo inglés). Esta realización se había generado mediante un variograma con efecto agujero y se había demostrado que el flujo y el transporte, a la escala fina, pueden reproducir el comportamiento no fickiano de la difusión del penacho contaminante de tritio. El objetivo de esta sección es doble, primero, comparar la efectividad de diferentes técnicas de escalado para producir modelos capaces de reproducir el comportamiento observado del movimiento del penacho de tritio, y segundo, demostrar y analizar las condiciones bajo las cuales el escalado puede proporcionar un modelo a una escala gruesa en el que el flujo y el transporte puedan predecirse con al ecuación de advección-dispersión en condiciones aparentemente no fickianas. En concreto, el uso de la técnica de escalado basada en

el laplaciano con piel junto con un mallado no uniforme produce los mejores resultados tanto en términos de flujo como de transporte, para este caso concreto en el que los bloques gruesos tienen un tamaño inferior a los rangos de correlación de las conductividades a escala fina. En otros casos, se observa que la discrepancia en la predicción del transporte entre las dos escalas persiste, y la ecuación de advección-dispersión no es suficiente para explicar el transporte en la escala gruesa. Por esta razón, se ha desarrollado una metodología para el escalado del transporte en formaciones muy heterogéneas en tres dimensiones. El método propuesto se basa en un escalado de la conductividad hidráulica por el método laplaciano con piel y centrado en los interbloques, seguido de un escalado de los parámetros de transporte que requiere la inclusión de un proceso de transporte con transferencia de masa multitasa para compensar la pérdida de heterogeneidad inherente al cambio de escala. Los procedimientos de escalado del flujo y del transporte se describen en detalle y se aplican a un ejemplo sintético en tres dimensiones con gran heterogeneidad. El método propuesto no sólo reproduce el flujo y el transporte en la escala gruesa, sino que reproduce también la incertidumbre asociada con las predicciones según puede observarse analizando la variabilidad del conjunto de curvas de llegada.

En el segundo bloque, el filtro de Kalman de conjuntos se acopla con el escalado para construir un modelo del acuífero a una escala mayor que la escala en la que los datos condicionantes (conductividad y la altura piezométrica) han sido tomados con el objetivo de realizar una modelación inversa. La construcción de un modelo de acuífero a la escala en la que se tomaron las medidas es, en general, poco práctico, ya que esto implicaría modelos numéricos con millones de celdas. Si, además, se requiere un análisis de incertidumbre que se base en un análisis de Monte-Carlo, la tarea se convierte en imposible. Por esta razón, se ha desarrollado una metodología que usa los datos de conductividad, a la escala a los que fueron recogidos, para construir un modelo a escala gruesa adecuado para la modelación inversa del flujo de aguas subterráneas y transporte en masa. El método procede de la siguiente manera: (i) generación de un conjunto de realizaciones de conductividades condicionadas a los datos de conductividad a la misma escala a la que se recogieron, (ii) escalado de cada realización a una discretización gruesa; en estas realizaciones a escala gruesa, las conductividades se convertirán en parámetros tensoriales con orientaciones arbitrarias de sus direcciones principales, y (iii) aplicar el EnKF al conjunto de relizaciones de conductividad a la escala gruesa para condicionarlas a las medidas de altura piezométrica. El método propuesto aborda el problema de cómo hacer frente a parámetros tensoriales, en una escala gruesa, usando el filtro de Kalman de conjuntos, mientras se mantiene el condicionamiento a las escalas de conductividad fina. Se demuestra en el marco de un análisis sintético del valor de la información en el que se analiza la importancia de condicionar en conductividades hidráulicas, alturas piezométricas o en ambos.

Por último, en el tercer bloque, el filtro de Kalman de conjuntos (EnKF) se aplica para condicionar de forma conjunta los parámetros que controlan el flujo y el transporte (conductividad hidráulica y porosidad) a las variables de estado (altura piezométrica y concentración). Se utiliza un experimento sintético para demostrar la capacidad del EnKF para estimar la conductividad hidráulica y la porosidad, por asimilación de alturas piezométricas y concentraciones. Se estudia el valor que tienen los datos de conductividad hidráulica, de porosidad, de altura piezométrica y de concentración en el contexto de la caracterización de acuíferos y de la reducción de la incertidumbre en parámetros y variables de estado. Los resultados indican que la caracterización de la conductividad hidráulica y de la porosidad es mejor cuantos más tipos de datos se consideren. Las predicciones de flujo y transporte también mejoran cuanto más datos se usen. Es importante resaltar el impacto que tiene el condicionamiento a los datos de concentración, especialmente en la caracterización de las porosidades. Por otra parte, el filtro de Kalman de conjuntos con transformación normal (NS-EnKF), recientemente desarrollado para hacer frente a la no gausianidad de parámetros y variables de estado, se ha usado para evaluar el impacto que tiene la incertidumbre del modelo conceptual en la modelación inversa. También se ha analizado el impacto de las condiciones de contorno y del uso de técnicas de localización de la covarianza en el EnKF. Los resultados de este último análisis se han evaluado en términos de valores medios y varianzas del conjunto de realizaciones, de las conectividades de las realizaciones, y de la incertidumbre en las predicciones de las alturas piezométricas después del condicionamiento. De los distintos escenarios evaluados se puede deducir que (i) la reproducción de los patrones de variabilidad de la conductividad como las predicciones de flujo son buenas utilizando el NS-EnKF tanto cuando se usa un modelo a priori correcto como aproximado, siempre y cuando el número de datos de piezometría condicionantes sea importante, (ii) el uso de técnicas de localización de la covarianza en el NS-EnKF mejora la identificación de la conductividad hidráulica y (iii) las condiciones de contorno no afectan a la bondad de los resultados obtenidos por NS-EnKF.

Resum

La necessitat de reduir el cost computacional dels models estocàstics de flux d'aigua subterrània i de transport de massa requereixen una tècnica d'escalat eficaç que puga transferir l'heterogeneïtat d'una escala fina a una altra gruixuda, mentre que al mateix temps es preserve el comportament quant a flux i transport. A més, a causa de l'escassetat de dades, comunament s'utilitza la modelització inversa per a calibrar els paràmetres per al condicionament dels models tant a mesures directes com a mesures indirectes, sempre amb l'objectiu de reduir la incertesa de les prediccions de flux i transport. En aquest treball, s'ha desenvolupat una tècnica d'escalat que s'ha aplicat a un exemple sintètic i a un cas real, després, s'ha acoblat l'escalat amb el filtre de Kalman de conjunts (EnKF, un mètode de modelització inversa) per a resoldre un problema invers en un aqüífer del que es disposa de dades a una escala molt xicoteta i, finalment, l'EnKF i la seua variant l'EnKF amb transformació gaussiana, s'usa per a l'anàlisi de mitjans multigaussians i no multigaussians. El treball desenvolupat en aquesta tesi pot agrupar-se en tres blocs.

En el primer bloc, s'han revisat les tècniques d'escalat que utilitzen una mitjana simple, el mètode laplacià simple, el laplacià amb pell i l'escalat amb discretització no uniform i s'han avaluat en un exercici tridimensional d'escalat de la conductivitat hidràulica. El camp de referència és una realització condicional a escala fina de la conductivitat hidràulica en l'experiment de macrodispersió realitzat en la base de la força aèria nord-americana a Columbus, Missouri (MADE en el seu acrònim anglès). Aquesta realització s'ha generat mitjançant un variogram amb efecte forat on s'havia demostrat que el flux i el transport, a l'escala fina, pot reproduir el comportament no fickià de la difusió del plomall contaminant de triti. L'objectiu d'aquesta secció és doble, primer comparar l'efectivitat de diferents tècniques d'escalat per a produir models capaços de reproduir el comportament observat del moviment del plomall de triti, i segon, per a demostrar i analitzar les condicions sota les quals l'escalat pot proporcionar un model a una escala gruixuda en el qual el flux i el transport puguen predir-se amb l'equació d'advecció-dispersió en condicions aparentment no fickianes. En concret, l'ús de la tècnica d'escalat basada en el laplacià amb pell juntament amb una discretització no uniforme produeix els millors resultats tant en termes de flux com de transport en aquest cas

concret en el qual els blocs gruixuts tenen una grandària inferior als rangs de correlació de les conductivitats a escala fina. En altres casos, s'observa que la discrepància en la predicció del transport entre les dues escales persisteix, i l'equació d'advecció-dispersió no és suficient per a explicar el transport en l'escala gruixuda. Per aquesta raó, s'ha desenvolupat una metodologia per a l'escalat del transport en formacions molt heterogènies en tres dimensions. El mètode proposat es basa en un escalat de la conductivitat hidràulica pel mètode laplacià amb pell i centrat en els interblocs, seguit d'un escalat dels paràmetres de transport que requereix la inclusió d'un procés de transport amb transferència de massa multitaxa per a compensar la pèrdua d'heterogeneïtat inherent al canvi d'escala. Els procediments d'escalat del flux i del transport es descriuen detalladament i s'apliquen a un exemple sintètic en tres dimensions amb gran heterogeneïtat. El mètode proposat no solament reprodueix el flux i el transport en l'escala gruixuda, sinó que reprodueix també la incertesa associada amb les prediccions segons pot observar-se analitzant la variabilitat del conjunt de corbes d'arribada.

En el segon bloc, el filtre de Kalman de conjunts s'acobla amb l'escalat per a construir un model de l'aqüífer a una escala major que l'escala en la qual les dades condicionants (conductivitat i altura piezomètrica) han sigut mesurats amb l'objectiu de realitzar una modelització inversa. La construcció d'un model d'aqüífer a l'escala en la qual es van prendre les mesures és, en general, poc pràctic, ja que açò implicaria models numèrics amb milions de cel·les. Si, a més, es requereix una anàlisi d'incertesa que es base en una anàlisi de Monte-Carlo, la tasca es converteix en impossible. Per aquesta raó, s'ha desenvolupat una metodologia que usa les dades de conductivitat, a l'escala als quals van ser arreplegats, per a construir un model a escala gruixuda adequat per a la modelització inversa del flux d'aigües subterrànies i transport en massa. El mètode procedeix de la següent manera: (i) generació d'un conjunt de realitzacions de conductivitats condicionades a les dades de conductivitat a la mateixa escala a la qual es van arreplegar, (ii) escalat de cada realització a una discretització gruixuda; en aquestes realitzacions a escala gruixuda, les conductivitats es convertiran en paràmetres tensorials amb orientacions arbitràries de les seues direccions principals, (iii) aplicar l'EnKF al conjunt de realitzacions de conductivitat a l'escala gruixuda per a condicionar-les a les mesures d'altura piezomètrica. La proposta aborda el problema de com fer front a paràmetres tensorials, en una escala gruixuda, usant EnKF, mentre es manté el condicionament a les escales de conductivitat fina. El mètode proposat es demostra en el marc d'una anàlisi sintètica del valor de la informació en el qual s'analitza la importància de condicionar en conductivitats hidràuliques, altures piezomètriques o en tots dos.

Finalment, en el tercer bloc, el filtre de Kalman de conjunts (EnKF) s'aplica per a condicionar de forma conjunta els paràmetres que controlen el

flux i el transport (conductivitat hidràulica i porositat) a les variables d'estat (altura piezomètrica i concentració). S'utilitza un experiment sintètic per a demostrar la capacitat de l'EnKF per a estimar la conductivitat hidràulica i la porositat, per assimilació d'altures piezomètriques i concentracions. S'estudia el valor que tenen les dades de conductivitat hidràulica, de porositat, d'altura piezomètrica i de concentració en el context de la caracterització d'aqüífers i de la reducció de la incertesa en paràmetres i variables d'estat. Els resultats indiquen que la caracterització de la conductivitat hidràulica i de la porositat és millor quants més quantitat i més tipus de dades es consideren. Les prediccions de flux i transport també milloren com més dades s'usen. És important ressaltar l'impacte que té el condicionament a les dades de concentració, especialment en la caracterització de les porositats. D'altra banda, el filtre de Kalman de conjunts amb transformació normal (NS-EnKF), recentment desenvolupat per a fer front a la no gaussianitat de paràmetres i variables d'estat, s'ha usat per a avaluar l'impacte que té la incertesa en el model conceptual en la modelització inversa. També s'ha analitzat l'impacte de les condicions de contorn i de l'ús de tècniques de localització de la covariança en l'EnKF. Els resultats d'aquesta última anàlisi s'han avaluat en termes de valors mitjans i variàncies del conjunt de realitzacions, de les connectivitats de les realitzacions, i de la incertesa en les prediccions de les altures piezomètriques després del condicionament. Dels diferents escenaris avaluats es pot deduir que (i) la reproducció dels patrons de variabilitat de la conductivitat com les prediccions de flux són bones utilitzant el NS-EnKF tant quan s'usa un model a priori correcte com a aproximat, sempre que el nombre de dades de piezometria condicionants siga important, (ii) l'ús de tècniques de localització de la covariança en el NS-EnKF millora la identificació de la conductivitat hidràulica i (iii) les condicions de contorn no afecten a la bondat dels resultats obtinguts pel NS-EnKF

Acknowledgements

I want to thank my advisor J. Jaime Gómez-Hernández for providing me the opportunity to carry out this study. I thank him for his academical instruction and encouragement in these four-year PhD study. I deeply appreciate his patience, his kindness and the time he spent with me.

This research was supported by European Union (Project PAMINA) and ENRESA, Empresa Nacional de Residuos Radiactivos S.A. An extra travel grant to the author from Ministry of Education is also gratefully acknowledged.

I would like to express my gratitude to Prof. Harrie-Jan Hendricks Franssen. I am grateful to him for his continuous suggestions since I visited his group in Forschungszentrum Jülich, Germany, in 2010. The developments of Chapter 4-6 benefit from his valuable comments and suggestions. Thanks also to Dr. Xian-Huan Wen for his help and support and to Dr. Jianlin Fu for his help in academia and life when I arrived at Valencia. Dr. Gerónimo Llerar-Meza provided me technical support for the Chapter 3 and is much appreciated. Thanks to Eduardo Cassiraga, who helped me prepare some documents. I always appreciate Prof. Li Wan and Prof. Fusheng Hu from China University of Geosciences (Beijing), who helped me so much since I started the Master study in China.

My special thanks to Haiyan for her interesting discussion and understanding, which would make our stay abroad so meaningful, colorful and fruitful, and it will be in my heart forever.

Many thanks to the colleagues in the group of hydrogeology: Andrés, Eduardo, Javier, Haiyan, Jianlin, Gero, Peter, Oscar, Amanda, Julio, Teng. I am very happy for my time in Valencia.

Finally I would like to thank Haiyan and our families. Without your support, nothing would be possible for me.

Contents

Abstract **v**

Resumen **ix**

Resum **xiii**

Acknowledgements **xvii**

1 Introduction **1**
1.1 Motivation and Objectives 1
1.2 Thesis Organization 2

2 A Comparative Study of Three-Dimensional Hydraulic Conductivity Upscaling at the MAcro-Dispersion Experiment (MADE) site, Columbus Air Force Base, Mississippi (USA) *(published in Journal of Hydrology)* **5**
2.1 Introduction 6
2.2 Modeling transport at the MADE site 8
2.3 Hydraulic conductivity upscaling 13
2.3.1 Simple averaging 13
2.3.2 Simple-Laplacian 14
2.3.3 Laplacian-with-skin 16
2.3.4 Non-uniform coarsening 19
2.4 Coarse model and simulation results 19
2.4.1 Coarse Flow and Transport Equations 19
2.4.2 Upscaling design and error measure 21
2.4.3 Results and Comparisons 23
2.5 Discussion 32
2.6 Summary and Conclusions 34
Bibliography 37

3 Transport Upscaling Using Multi-Rate Mass Transfer in Three-Dimensional Highly Heterogeneous Media *(published in Advances in Water Resources)* **43**
3.1 Introduction . . . 44
3.2 Methodology . . . 46
3.2.1 Background . . . 46
3.2.2 Hydraulic conductivity upscaling using the Laplacian-with-skin method . . . 49
3.2.3 Transport upscaling using mass transfer . . . 51
3.3 Numerical Evaluation . . . 53
3.3.1 Model Configuration . . . 53
3.3.2 Flow upscaling results . . . 56
3.3.3 Transport upscaling results . . . 58
3.3.4 Propagation of Uncertainty . . . 62
3.4 Discussion . . . 64
3.5 Summary and Conclusions . . . 67
Bibliography . . . 69

4 Modeling Transient Groundwater Flow by Coupling Ensemble Kalman Filtering and Upscaling *(submitted to Water Resources Research)* **75**
4.1 Introduction . . . 76
4.2 Methodology . . . 78
4.2.1 Generation of the Ensemble of Fine Scale Conductivities 78
4.2.2 Upscaling . . . 78
4.2.3 The EnKF with Hydraulic Conductivity Tensors . . . 80
4.3 Application Example . . . 83
4.3.1 Reference Field . . . 83
4.3.2 Hydraulic Conductivity Upscaling . . . 84
4.3.3 Case Studies . . . 86
4.3.4 Performance Measurements . . . 88
4.4 Discussion . . . 89
4.4.1 The EnKF Coupled with Upscaling . . . 90
4.4.2 Worth of Data . . . 96
4.4.3 Other Issues . . . 99
4.5 Conclusion . . . 100
Bibliography . . . 101

5 Jointly Mapping Hydraulic Conductivity and Porosity by Assimilating Concentration Data via Ensemble Kalman Filter *(submitted to Journal of Hydrology)* **105**
5.1 Introduction . . . 106

5.2 Data Assimilation with the EnKF . . . 109
5.2.1 Flow and Transport Equations . . . 109
5.2.2 Ensemble Kalman Filter . . . 109
5.3 Synthetic Example . . . 112
5.3.1 Experiment Setup . . . 112
5.3.2 Assessment Measures . . . 117
5.3.3 Data Assimilation Results . . . 118
5.3.4 Reactive Transport Prediction Analysis . . . 130
5.4 Conclusion . . . 131
Bibliography . . . 135

6 Groundwater Flow Inverse Modeling in non-multiGaussian Media: Performance Assessment of the Normal-Score Ensemble Kalman Filter *(submitted to Hydrol. Earth Syst. Sci.)* **141**
6.1 Introduction . . . 142
6.2 Mathematic Framework . . . 145
6.2.1 Flow equation . . . 145
6.2.2 The Normal-Score Ensemble Kalman Filter with Localization . . . 145
6.3 Synthetic Example . . . 147
6.3.1 Reference . . . 147
6.3.2 Scenarios . . . 150
6.3.3 Evaluation Criteria . . . 154
6.4 Results and discussion . . . 155
6.4.1 Effect of prior random function model . . . 155
6.4.2 Effect of localization . . . 163
6.4.3 Effect of boundary conditions . . . 164
6.4.4 Effect of number of conditioning piezometers . . . 165
6.4.5 Discussion . . . 166
6.5 Conclusion . . . 167
Bibliography . . . 167

7 Conclusions 175
7.1 Summary . . . 175
7.2 Recommendations for Future Research . . . 177

Appendix 179

A FLOWXYZ3D - A Three-Dimensional Finite-Difference Simulator with Full Conductivity Tensors 179

List of Figures

2.1 Plan view of model domain. Open circles denote multilevel sampler wells. Triangles indicate the tracer injection wells. Solid circles correspond to flowmeter well locations. 9

2.2 Horizontal and vertical experimental variograms, and fitted model, for the $\ln K$ flowmeter data. The rotation angle of the directional variograms is measured in degrees clockwise from the positive y-axis. 10

2.3 Longitudinal mass distribution profiles of the observed tritium plume at MADE, and predictions on several realizations of hydraulic conductivity. Each realization was generated (on natural-log space) over a grid of $110 \times 280 \times 70$ cells by sequential Gaussian simulation using the variogram model in Equation 2.1. 11

2.4 Realization #26 of $\ln K$ from Salamon et al. (2007). This realization exhibits a strong solute tailing and it is used as the reference in the upscaling exercise. (The scale of the z-axis is exaggerated seven times for clarity.) 12

2.5 Boundary conditions that would be used in 2D for the local flow model when performing the simple-Laplacian upscaling in order to determine the x-component of the hydraulic conductivity tensor. In the simple-Laplacian approach, it is always assumed that the principal directions of the conductivity tensor are parallel to the reference axes. 15

2.6 An example of four boundary condition sets that could be used in 2D for the local flow models when performing the Laplacian-with-skin upscaling. The white area is the block being upscaled, and the gray area is the skin region; the arrows indicate the (negative) mean head gradient induced by the prescribed head boundary conditions, and the shapes on the sides of the block indicate the magnitude of the prescribed heads given by tilting planes with gradients opposite to the arrows. 18

2.7 Flow comparison at the fine and coarse scales using simple averaging upscaling approaches. All circles within the dashed lines correspond to coarse scale values that deviate less than 10% from the reference ones; similarly, all circles within the outer solid lines correspond to coarse scale values that deviate less than 40%. The average relative bias, as defined in Equation 2.10, is reported in the lower right corner of each box. 25

2.8 Longitudinal mass distribution profiles of the tritium plume from the fine scale reference realization, and predictions by some simple averaging upscaling approaches at the coarse scale for $t = 328$ days. 26

2.9 Flow comparison at the fine and coarse scales using Laplacian-based upscaling approaches. All circles within the dashed lines correspond to coarse scale values that deviate less than 10% from the reference ones; similarly, all circles within the outer solid lines correspond to coarse scale values that deviate less than 40%. The average relative bias, as defined in Equation 2.10, is reported in the lower right corner of each box. 27

2.10 Longitudinal mass distribution profiles of the tritium plume from the fine scale reference realization, and predictions on uniform and non-uniform coarse scale grids, for $t = 328$ days. . . 28

2.11 Longitudinal mass distribution profiles of the tritium plume from the fine scale reference realization, and predictions by some Laplacian-based upscaling approaches at the coarse scale, for $t = 328$ days. 29

2.12 Transport in the fine scale reference realization for $t = 328$ days. (A) Depth-integrated normalized concentration distribution. (B) Laterally-integrated normalized concentration distribution. 30

2.13 Transport at the coarse scale after upscaling the reference realization on a uniform grid using a block-centered simple-Laplacian approach for $t = 328$ days. (A) Depth-integrated normalized concentration distribution. (B) Laterally-integrated normalized concentration distribution. 30

2.14 Transport at the coarse scale after upscaling the reference realization on a uniform grid using an interblock-centered simple-Laplacian approach for $t = 328$ days. (A) Depth-integrated normalized concentration distribution. (B) Laterally-integrated normalized concentration distribution. 31

2.15 Transport at the coarse scale after upscaling the reference realization on a non-uniform grid using an interblock-centered Laplacian-with-skin approach for t = 328 days. (A) Depth-integrated normalized concentration distribution. (B) Laterally-integrated normalized concentration distribution. 31

3.1 A realization of reference lnK field (σ^2_{lnK}=4.0) overlaid with the discretization of the numerical model at the coarse scale. . . . 55
3.2 Sketch of transport simulations. The shaded rectangle located in the upstream zone delineates the initial particle injection zone. Control planes are also shown for measuring the mass fluxes. 55
3.3 Flow comparisons at the fine and coarse scales on a single realization. (A) the block-centered simple-Laplacian method; (B) the interblock-centered simple-Laplacian method; (C) the interblock-centered full-tensor Laplacian-with-skin (skin size 3 m); (D) the interblock Laplacian-with-skin (skin size: 10 m along rows, 10 m along columns and 5 m along layers); (E) Landau-Lifshitz-Matheron conjecture for 3D isotropic media. . 57
3.4 Comparison of fine scale cumulative breakthrough curves with those obtained by the upscaled transport models at six different control planes. 60
3.5 Ensemble travel times (early, median, and late travel times) as a function of travel distance, and comparison of the fine scale simulations to the upscaled simulations. 61
3.6 Evolution of uncertainty as a function of travel distance for the early, median, and late travel times, as measured by the width of the 95% confidence interval derived from an ensemble of 30 realizations. Calculations were performed at the fine scale, and at the coarse scale for two different upscaling approaches. . . . 63

4.1 (A) Reference ln$K$ field overlaid with the discretization of the numerical model at the coarse scale. (B) Conditioning ln$K$ data. 84
4.2 Sketch of the flow problem with boundary conditions, observation and prediction wells. Empty squares correspond to the piezometric head observation wells (W1-W9); filled squares correspond to the control wells (W10-W13). 85
4.3 Upscaled values for the interblock tensor components: ln($Kmax$), ln($Kmin$) and rotation angle for the maximum component measured from the x-axis θ (in degrees), for both the interblocks between columns and the interblocks between rows. Upscaling method used: Laplacian with a skin of 10 m 87

4.4 Reference piezometric head at the 60th time step. Left, as obtained at the fine scale; right, as obtained at the coarse scale . 88
4.5 Piezometric head time series in the reference field and simulated ones for all cases at wells W1 (left column) and W9 (right column). The piezometric heads measured at these wells during the first 67.7 days were used as conditioning data for cases B and D. 91
4.6 Piezometric head time series in the reference field and simulated ones for all cases at control wells W10 (left column) and W13 (right column). These wells were not used as conditioning data for any case. 92
4.7 Ensemble average and variance of piezometric heads for the different cases. 94
4.8 Ensemble average absolute bias of piezometric heads for the different cases. 95
4.9 Ensemble average and variance of $\ln(Kmax)$ for the different cases. 97
4.10 Ensemble average absolute bias of $\ln(Kmax)$ for the different cases. 98

5.1 (A) Reference $\ln K$ field, (B) Conditioning $\ln K$ data, (C) Reference porosity(ϕ) field, (D) Conditioning porosity(ϕ) data. . . 113
5.2 Sketch of the flow and transport simulation with boundary conditions and observation and prediction wells. Filled circles correspond to the pressure head observation wells (#1-#9); Open circles denote the control wells (#10-#11). Empty squares indicate the wells where concentration is sampled. 114
5.3 Reference concentration fields at time 300(A), 400(C) and 500(E) days. Conditioning concentration data at time 300 (B), 400 (D), and 500 (F) days. 116
5.4 Ensemble average logconductivity fields for the different scenarios. 119
5.5 Ensemble logconductivity variance fields for the different scenarios 120
5.6 Ensemble average porosity fields for the different scenarios. . . 121
5.7 Ensemble porosity variance fields for the different scenarios. . . 122
5.8 Piezometric head time series for the reference field (black) and simulated ones (gray lines) for the S1,S2,S3 and S6 scenarios at the conditioning well W2 (left column) and verification well W10 (right column). 124
5.9 Ensemble average concentration fields at $t = 300$ day for the different scenarios. 126
5.10 Ensemble variance of concentration fields at $t = 300$ day for the different scenarios. 127

5.11 Ensemble average concentration fields at $t = 500$ day for the different scenarios. 128
5.12 Ensemble variance of concentration fields at $t = 500$ day for the different scenarios. 129
5.13 The reference concentration field at $t = 500$ days for the reactive transport prediction experiment. 131
5.14 Ensemble mean and variance of concentration fields at $t = 500$ day for the S2,S3 and S6. 132

6.1 Training image used to generate the facies distribution. 148
6.2 Reference lnK data 149
6.3 Spatial distribution of sampled head data and flow configurations: (A) boundary conditions A (B) boundary conditions B (the unit of flow in wells: m^3/d). 151
6.4 A-C show the spatial distribution of lnK, histogram and variogram of the 1st realization from the correct prior model; D-F show the same characteristics of the 1st realization from wrong prior model. In C and F, solid line and dotted line correspond to the experimental facies variogram in X and Y direction, respectively. 152
6.5 Ensemble average logconductivity fields at time step $nT = 60$ for the different scenarios. 156
6.6 Ensemble variance logconductivity fields at time step $nT = 60$ for the different scenarios. 157
6.7 $RMSE$ and ES of lnK for the different cases. 158
6.8 Connectivity function of logconductivity fields at time step $nT = 60$ for the different scenarios. Gray curves correspond to individual realizations, their mean is given by the triangles and the circles correspond to the reference. 160
6.9 $RMSE$ and ES of simulated heads for the different scenarios. . 161
6.10 (A) flow configuration and spatial distribution of sampled head data. (B) the ensemble mean of logconductivity with correct prior model. (C) the ensemble variance of logconductivity with correct prior model.(D) the ensemble mean of logconductivity with wrong prior model. (E) the ensemble variance of logconductivity with wrong prior model. 162

A.1 Schematic illustration of the 3D finite-difference spatial discretization 180

List of Tables

2.1 Variogram parameters for the model fit in Figure 2.2 10

4.1 Definition of Cases depending on the the different sets of conditioning data. 86
4.2 Bias and spread of predicted heads at time steps 30, 60 and 90 and of updated loghydraulic conductivity $\ln K^{b,r}_{max}$ at time step 60. 99

5.1 Parameters of the random functions for modeling the spatial distributions of $\ln K$ and porosity 112
5.2 Definition of scenarios based on the different sets of conditioning data. 117
5.3 Bias and spread of lnK and porosity for the different scenarios. 123
5.4 Bias and spread of predicted piezometric heads at time $t = 67.7$ days for the different scenarios. 125
5.5 Bias and spread of predicted concentrations at time $t = 300$, $t = 400$, $t = 500$ days for the different scenarios. 130

6.1 Parameters of the random functions describing the sand and shale 148
6.2 Definition of scenarios 150

1 Introduction

1.1 Motivation and Objectives

In the last several decades, groundwater flow and transport modeling is routinely utilized to assess groundwater resources, understand the evolution of contaminant plumes, and further provide the corresponding remediation strategies to the decision-maker.

In the past, deterministic numerical models were commonly considered with zoned hydrological parameters (e.g., porosity, conductivity, dispersivity), which were inversely determined by optimizing the fit between the observed aquifer response and the simulated values (e.g., piezometric heads, concentrations, temperatures and others). Trial-and-error at the beginning, and more advanced automatic matching techniques, later, were used for the inverse modeling. The main shortcoming of this approach is the loss of small scale variability of conductivity, which is usually very significant for transport predictions. Furthermore, if an assessment of the uncertainty is needed, a stochastic approach is needed instead of this type of deterministic model.

With the advance of geostatistics, stochastic hydrological modeling increasingly becomes the research focus in the last decennia. Unlike traditional zoned parameter values, equally-likely high-resolution parameter images are first generated by means of geostatistical techniques such as sequential Gaussian simulation or multiple point geostatistics. Then, inverse techniques such as the self-calibration and the ensemble Kalman filter can be used to calibrate

the parameters by conditioning on the aquifer response and hence reduce the uncertainty on groundwater flow and mass transport predictions.

In the framework of stochastic hydrogeology, two issues have gained prominence: upscaling and conditioning. The need of upscaling can be explained by the fact that the scale of measurements is usually smaller than the computational scale of the numerical models, which makes upscaling necessary to transfer the information across scale, while maintaining flow and transport predictions as accurate as possible. After upscaling, the predictions from the upscaled numerical model will not match the observed aquifer responses, calling for conditioning using some type of inverse model.

Since the need for upscaling was recognized in petroleum engineering and hydrogeology, different upscaling approaches have been developed to improve flow and transport predictions at the computational scale. To preserve the flows at the fine scale, flow upscaling techniques include the simple average, simple Laplacian, Laplacian with skin, local-global method and others have been proposed. To preserve the transport behavior at the fine scale, such as the early, median and late times in the breakthrough curves, transport upscaling techniques have been proposed such as the enhanced macrodispersion approach or the multi-rate mass transfer-based approach.

The problem of conditioning was first solved in a geostatistical framework and regarding the direct measurements of the parameters of interest. Conditioning to indirect data, such as aquifer responses to a set of parameters requires inverse modeling. The latest advances in inverse modeling aim at the generation of multiple conditional realizations of non multiGaussian parameters.

This thesis will elaborate on these two issues. More specifically, the objectives of this thesis are to compare the different upscaling approaches applied to the MADE site, to develop a three-dimensional multi-rate mass transfer transport upscaling technique, to couple the upscaling with ensemble Kalman filter to simulate the transient flow, to jointly calibrate the conductivity and porosity by conditioning on the multiple concentration data and to assess the normal-score ensemble Kalman filter applying in the bimodal aquifer with the uncertainty of prior model.

1.2 Thesis Organization

The document is organized as follows. This chapter presents the introduction and the motivation and objectives of this dissertation. Each of the following five chapters is comprised of a separate, self-contained paper which is published or is currently submitted for publication in a refereed international journal.

Chapter 2 provides an extensive review of flow upscaling techniques, outlines the benefits and limitations of the various methods, and applies them at the MADE site to overcome the problem of computational cost.

Chapter 3 presents a three-dimensional transport upscaling approach in highly heterogeneous media. Basically, it couples a prior flow upscaling, sophisticated Laplacian-with-skin method, and a transport upscaling, multi-rate mass transfer model-based. The methodology is demonstrated in a three-dimensional synthetic example.

In chapter 4, the ensemble Kalman filter is coupled with upscaling to solve a transient groundwater flow problem. This approach can deal with inverse conditioning for a high-resolution model, something that is impossible to do at the measurement scale. A two-dimensional synthetic example is used to demonstrate the effectiveness of the proposed method.

In chapter 5, the EnKF is applied to jointly calibrate conductivities and porosities by assimilating piezometric head and concentration data at different times. When the concentration data is used for conditioning, the characterization of aquifer heterogeneity and the predictions of flow and transport are both improved. This application is demonstrated in a two-dimensional synthetic example.

Chapter 6 uses the normal-score EnKF in a bimodal aquifer to assess the impact of prior model choice on flow and transport predictions in inverse modeling. The results show that even when the wrong prior model is considered, the localized normal-score EnKF has a capacity to identify the channels in the reference field as long as sufficient piezometric head data is used. This is demonstrated for two cases with different boundary conditions.

Finally, Chapter 7 summarizes the main conclusions of this thesis and points out possible topics for future research.

Appendix A briefly presents the algorithm of a nineteen-point finite-difference method to solve the groundwater flow equation with full conductivity tensors.

Journal of Hydrology, 404, 278-293. doi:10.1016/j.jhydrol.2011.05.001

2

A Comparative Study of Three-Dimensional Hydraulic Conductivity Upscaling at the MAcro-Dispersion Experiment (MADE) site, Columbus Air Force Base, Mississippi (USA)

Abstract

Simple averaging, simple-Laplacian, Laplacian-with-skin, and non-uniform coarsening are the techniques investigated in this comparative study of three-dimensional hydraulic conductivity upscaling. The reference is a fine scale conditional realization of the hydraulic conductivities at the MAcro-Dispersion Experiment site on Columbus Air Force Base in Mississippi (USA). This realization was generated using a hole-effect variogram model and it was shown that flow and transport modeling in this realization (at this scale) can reproduce the observed non-Fickian spreading of the tritium plume. The purpose

of this work is twofold, first to compare the effectiveness of different upscaling techniques in yielding upscaled models able to reproduce the observed transport behavior, and second to demonstrate and analyze the conditions under which flow upscaling can provide a coarse model in which the standard advection-dispersion equation can be used to model transport in seemingly non-Fickian scenarios. Specifically, the use of the Laplacian-based upscaling technique coupled with a non-uniform coarsening scheme yields the best results both in terms of flow and transport reproduction, for this case study in which the coarse blocks are smaller than the correlation ranges of the fine scale conductivities.

2.1 Introduction

In the last decades, two large-scale natural-gradient tracer tests were conducted to enhance the understanding of solute transport in highly heterogenous aquifers. These experiments were conducted at the Columbus Air Force Base in Mississippi, where the hydraulic conductivity variability is very high, with $\sigma^2_{lnK} \approx 4.5$ (Rehfeldt et al., 1992). The site and the experiments performed are commonly referred to as MADE (MAcro-Dispersion Experiment). The present analysis focuses on the second experiment, which was performed between June 1990 and September 1991 using tritium as a non-reactive tracer. The aim of the experiment was to develop an extensive field database for validating the type of geochemical models used to predict the transport and fate of groundwater contaminants (Boggs et al., 1993). The observed tritium plume exhibits a strongly non-Fickian, highly asymmetric spreading (at the formation scale) with high concentrations maintained near the source injection area and extensive low concentrations downstream.

Although there exists abundant literature on the modeling of the (so termed) anomalous spreading at the MADE site, only a few works related with this paper will be referred to in this introduction. These works can be classified into two groups according to the approach used for transport modeling.

In a first group, a number of authors have employed the classical advection-dispersion equation (ADE) to describe the strongly non-Fickian transport behavior (e.g., Adams and Gelhar, 1992; Eggleston and Rojstaczer, 1998; Barlebo et al., 2004; Salamon et al., 2007). Of these works, Salamon et al. (2007) showed that, with proper modeling of the fine-scale variability, it is possible to generate realizations of the hydraulic conductivity capable to reproduce the observed tracer movement, simply using the ADE. They used a hole-effect variogram model to characterize the flowmeter-derived conductivities. The final realizations displayed the apparent periodicity of the observed conductivities,

which was enough to induce the type of spreading observed in the experiment. However, in practice, it is difficult to work with this type of high-resolution models, involving millions of nodes, particularly if multiple realizations are to be analyzed. This difficulty is what motivates our paper.

In a second group, researchers have used models that go beyond the advection-dispersion model (e.g., Berkowitz and Scher, 1998; Feehley et al., 2000; Harvey and Gorelick, 2000; Benson et al., 2001; Baeumer et al., 2001; Schumer et al., 2003; Guan et al., 2008; Liu et al., 2008; Llopis-Albert and Capilla, 2009). These authors use dual-domain mass transfer models, continuous time random walk or other alternative models capable of accounting for the strongly delayed solute transport as an alternative to the classical ADE. However, these approaches are able to provide a good match to the observed field data only *a posteriori*; that is, they need to calibrate their model parameters once the concentration data are collected, and then, they can reproduce, almost perfectly, any departure from Fickian transport. These works prove that there are alternative transport models able to explain the MADE data; however, at this point, they lack predictive capabilities since their parameters can only be determined after the experiment is done.

All of these studies had varying degrees of success in reproducing the spreading of the tracer plume. For instance, Barlebo et al. (2004) obtained a good reproduction of the irregular plume using the ADE after calibrating the concentration measurements and head data. However, calibrated hydraulic conductivities resulted a factor of five larger than the flowmeter-derived measurements. The authors attributed this discrepancy to a systematical measurement error. The accuracy of the flowmeter-derived conductivities and of the measured concentrations have raised further discussions (see Molz et al., 2006; Hill et al., 2006).

Our work builds on the study by Salamon et al. (2007) with the purpose to show that the observed transport spreading at the MADE site can also be reproduced on a coarse model by the ADE. A high-resolution hydraulic conductivity realization is selected from the study by Salamon et al. (2007) and it is upscaled onto a coarser model with several orders of magnitude less elements. This upscaling approach, if successful, would permit multiple realization analyses since it would reduce significantly the computational effort needed to obtain the solute evolution at the site. Unlike previous studies of upscaling focusing on two-dimensional examples or synthetic experiments (e.g., Warren and Price, 1961; Gómez-Hernández, 1991; Durlofsky et al., 1997; Chen et al., 2003), we analyze, with real data, a variety of three-dimensional (3D) hydraulic conductivity upscaling techniques ranging from simple averaging over a uniform grid to sophisticated Laplacian-based upscaling approaches on non-uniform grids. To the best of our knowledge, this is the first time that an analysis of this type has been performed in a real 3D case. Since we will be

testing the use of a full tensor representation of conductivities in the upscaled model, our group had to develop a computer code (Li et al., 2010), which has been placed on the public domain, specifically designed to solve the finite-difference approximation of the groundwater flow equation without assuming that the principal directions of the hydraulic conductivity tensors are aligned to the reference axes.

The remaining of this paper is organized as follows. First, in section 2.2, we summarize the findings by Salamon et al. (2007) who used a hole-effect variogram model to describe the spatial variability of $\ln K$ and, thus, were able to reproduce the non-Fickian solute spreading observed in the field. Out of the several realizations analyzed by Salamon et al. (2007), we select the one with the best reproduction of the solute spreading. This realization will be used as the reference to test different upscaling approaches. Second, in section 2.3, simple average, simple-Laplacian, Laplacian-with-skin and non-uniform coarsening upscaling methods are revisited from the perspective of their numerical implementation. Third, in section 2.4, the flow and transport numerical models are discussed, and the benefits/limitations of using different upscaling methods at the MADE site are quantified and evaluated. Next, in section 2.5, there is a general discussion. Finally, in section 2.6, we summarize the main results and conclusions of this paper.

2.2 Modeling transport at the MADE site

In this work, we focus on the tritium data collected in the second MADE experiment. An extensive discussion of the main geological features and hydrogeological characterization of the site has been given by Boggs et al. (1992), Adams and Gelhar (1992), Rehfeldt et al. (1992), and Boggs and Adams (1992). Salamon et al. (2007) found that the non-Fickian solute spreading observed in the field could be reproduced using the standard advection-dispersion model as long as the spatial variability of hydraulic conductivity is properly characterized at the fine scale. For the sake of completeness, next we briefly comment the results by Salamon et al. (2007).

The geostatistical analysis of the 2 495 flowmeter-derived hydraulic conductivity measurements obtained at 62 boreholes (see Figure 2.1) indicates that the spatial variability of $\ln K$ shows a pseudo-periodic behavior in the direction of flow (Figure 2.2). This behavior is modeled using a hole-effect variogram, which is nested with a nugget effect and a spherical variogram as given by:

$$\gamma(\mathbf{h}) = c_0 + c_1 \cdot \mathrm{Sph}\big(\|\frac{h_x}{a_{x_1}}, \frac{h_y}{a_{y_1}}, \frac{h_z}{a_{z_1}}\|\big) + c_2 \cdot \left[1 - cos\big(\|\frac{h_x}{a_{x_2}}, \frac{h_y}{a_{y_2}}, \frac{h_z}{a_{z_2}}\|\pi\big)\right] \quad (2.1)$$

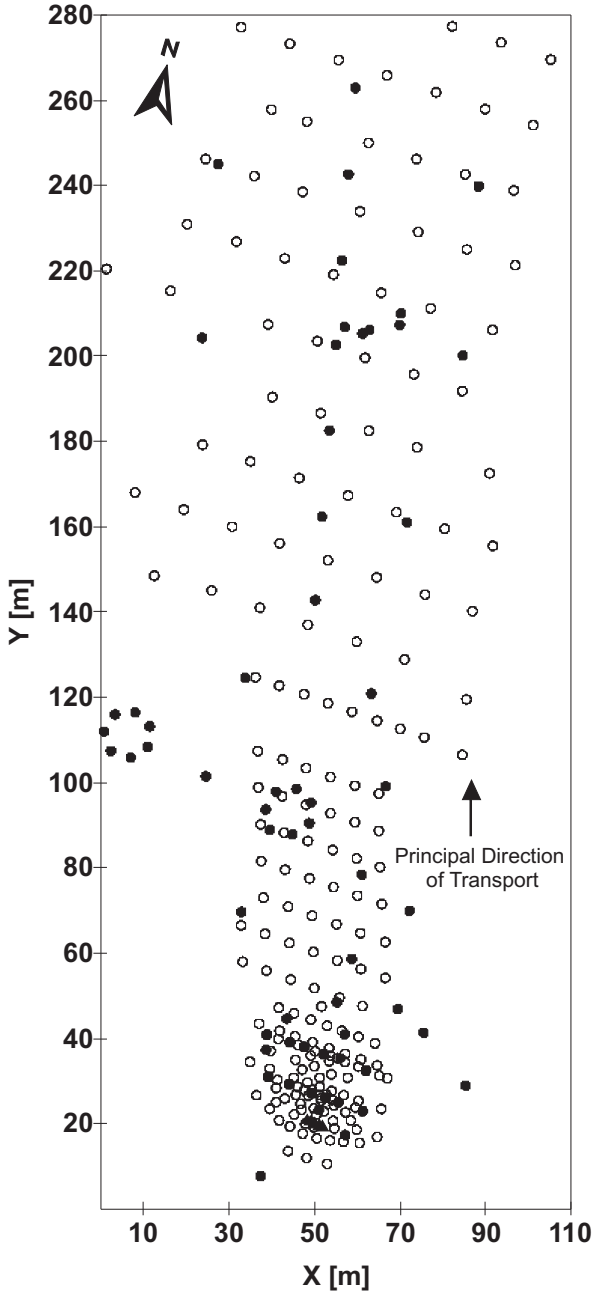

Figure 2.1: Plan view of model domain. Open circles denote multilevel sampler wells. Triangles indicate the tracer injection wells. Solid circles correspond to flowmeter well locations.

Table 2.1: Variogram parameters for the model fit in Figure 2.2

Model Type	Sill	Range [m]		
	c	a_x	a_y	a_z
Nugget	0.424			
Spherical	3.820	32	80	4.1
Hole effect	0.891	∞	80	∞

where $\mathbf{h} = (h_x, h_y, h_z)$ is the separation vector, $a_{x_1}, a_{y_1}, a_{z_1}$ are the ranges of the spherical variogram, $a_{x_2}, a_{y_2}, a_{z_2}$ are the ranges of the hole-effect variogram, $\|\cdot\|$ denotes vector modulus, c_0 is the nugget, c_1 is the sill of the spherical model, c_2 is the sill of the hole-effect model, with the y-axis oriented parallel to the flow direction, the x-axis is orthogonal to it on the horizontal plane, and the z-axis is parallel to the vertical direction. The parameter values used to fit the experimental variogram are given in Table 2.1. Notice that a_{y_2}, and a_{z_2} are equal to infinity, meaning that the hole-effect is only present along the flow direction. The fitted model is also shown in Figure 2.2.

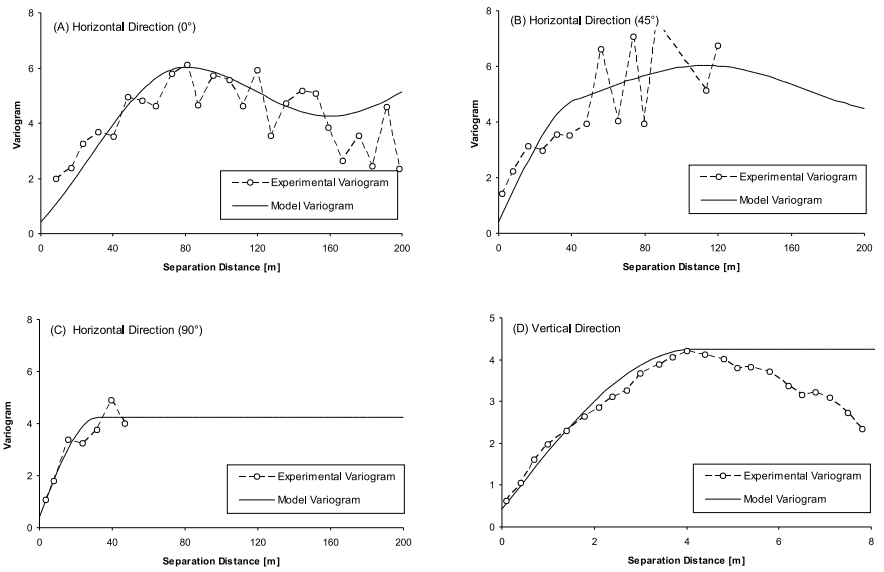

Figure 2.2: Horizontal and vertical experimental variograms, and fitted model, for the ln$K$ flowmeter data. The rotation angle of the directional variograms is measured in degrees clockwise from the positive y-axis.

The computational domain is a parallelepiped with dimensions of $x = 110$ m, $y = 280$ m, $z = 10.5$ m and it is discretized in 2 156 000 cells of size $\Delta x = \Delta y = 1.0$ m, and $\Delta z = 0.15$ m (see Figure 2.1). Cell size, according to Salamon et al. (2007), is similar in magnitude with the support scale of the flowmeter measurements. The aquifer is modeled as confined with impermeable boundaries on the faces parallel to flow, and constant head boundaries on the faces orthogonal to it. The values prescribed at the constant head boundaries are obtained by kriging the head averages over one-year observed in the nearby piezometers.

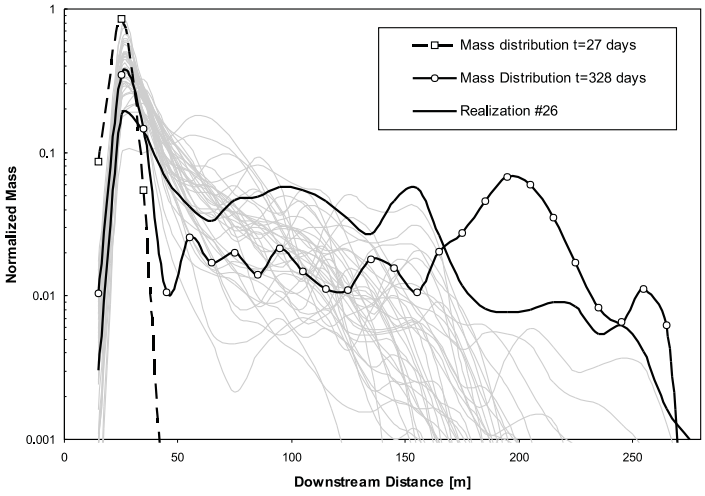

Figure 2.3: Longitudinal mass distribution profiles of the observed tritium plume at MADE, and predictions on several realizations of hydraulic conductivity. Each realization was generated (on natural-log space) over a grid of $110 \times 280 \times 70$ cells by sequential Gaussian simulation using the variogram model in Equation 2.1.

Salamon et al. (2007) used the random walk particle tracking code RW3D (Fernàndez-Garcia et al., 2005) to simulate solute transport. The local-scale longitudinal dispersivity was set as 0.1 m, which corresponds approximately to the value calculated by Harvey and Gorelick (2000). Transverse horizontal and vertical local-scale dispersivity values were chosen to be one order of magnitude smaller than the longitudinal dispersivity, i.e., 0.01 m. Apparent diffusion for tritium was set to 1.0 cm^2/d (Gillham et al., 1984). An average total porosity of 0.32 as determined from the soil cores by Boggs et al. (1992) was assigned uniformly to the entire model area. The observed mass distribution on the 27^{th} day was employed to establish the initial concentration

distribution. A simple interpolation of the initial concentrations was used to establish the concentrations in the model cells, and then 50 000 particles were distributed accordingly. The observed mass distribution on the 328^{th} day was used to obtain reference mass profile distributions to which the model is compared. These longitudinal profiles were obtained by integrating the mass from 28 equally-spaced vertical slices, each of 10 m width and parallel to flow. All results are displayed after normalizing the mass by the total mass injected. Figure 2.3 shows the longitudinal mass distribution profiles obtained by Salamon et al. (2007) after transport simulation on 40 realizations generated by sequential Gaussian simulation. These realizations were generated using the code GCOSIM3D, (Gómez-Hernández and Journel, 1993) with the variogram model given by equation (2.1) and the parameter values from Table 2.1. Out of these 40 realizations, solute transport on realization number 26 shows a spatial spread similar to the one observed in the field. For this reason, this conductivity realization is chosen as the reference field to test the different upscaling methods. Figure 2.4 shows the hydraulic conductivity field of realization number 26.

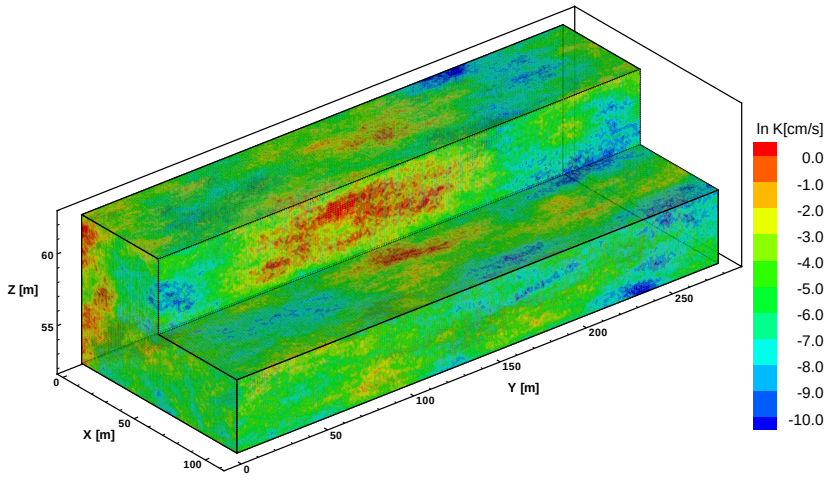

Figure 2.4: Realization #26 of $\ln K$ from Salamon et al. (2007). This realization exhibits a strong solute tailing and it is used as the reference in the upscaling exercise. (The scale of the z-axis is exaggerated seven times for clarity.)

Up to here, we have limited ourselves to briefly describe the specific results from Salamon et al. (2007) that this work uses as starting point. We are not trying to re-analyze MADE, but rather to demonstrate that careful hydraulic conductivity upscaling can be used to model flow and transport in highly heterogeneous fields exhibiting, at the formation scale, a non-Fickian behavior. To evaluate the upscaling procedure we will compare flow and transport in realization #26 before and after upscaling, aiming at obtaining the same results. Obviously, the departure of transport results computed on realization #26 from the experimental data will remain after upscaling. Trying to get the best reproduction of the experimental data will require a further calibration exercise that is not the objective of this paper.

2.3 Hydraulic conductivity upscaling

Although hydraulic conductivity upscaling has been disregarded by some researchers on the basis that the increase of computer capabilities will make it unnecessary, there will always be a discrepancy between the scale at which we can characterize the medium, and the scale at which we can run the numerical codes. This discrepancy makes upscaling necessary to transfer the information collected at the measurement scale into a coarser scale suitable for numerical modeling. The need for upscaling is even more justified when performing uncertainty analysis in a Monte Carlo framework requiring the evaluation of multiple realizations. Excellent reviews on upscaling geology and hydraulic conductivity are given by Wen and Gómez-Hernández (1996b), Renard and Marsily (1997) and Sánchez-Vila et al. (2006). In this section, we briefly revisit the most commonly used upscaling techniques with an emphasis on their numerical implementation procedures.

2.3.1 Simple averaging

It is well known that, for one-dimensional flow in a heterogeneous aquifer, the equivalent hydraulic conductivity (K^b) that, for a given hydraulic head gradient, preserves the flows crossing the aquifer is given by the harmonic mean of the hydraulic conductivities (Freeze and Cherry, 1979). In two-dimensional flow for media with isotropic spatial correlation and a lognormal probability distribution, the geometric mean provides good block conductivities (Matheron, 1967); Gómez-Hernández and Wen (1994) and Sánchez-Vila et al. (1996) used synthetic experiments to corroborate this conclusion.

Some heuristic rules have been proposed for three-dimensional upscaling. Cardwell and Parsons (1945) had already shown that the block conductivity should lie between the arithmetic mean and the harmonic mean when Journel et al. (1986) proposed the use of power averages (also referred to as ω-norms)

to estimate block conductivities. The power average is given by:

$$K^b = \left\{ \frac{1}{V(\mathbf{x})} \int_{V(\mathbf{x})} (K_x)^\omega dV \right\}^{1/\omega} \tag{2.2}$$

where $V(\mathbf{x})$ indicates the volume of the block; K^b is the block conductivity, and K_x represents the cell conductivities within the block, the power ω may vary from -1, yielding the harmonic mean, to $+1$, yielding the arithmetic mean, with $\omega = 0$ corresponding to the geometric mean. Although Desbarats (1992) demonstrated that ω equals 1/3 in 3D for statistically isotropic and mildly heterogeneous formations, the power coefficient (ω) has to be obtained by resorting to numerical flow experiments in arbitrary flow fields. The main advantages of this method are its mathematic conciseness and the easiness of implementation. However, there are several limitations to this power-average approach: first, the exponent ω is site-specific and cannot be predicted in a general anisotropic heterogeneous medium except after numerical calibration experiments; second, the shape and size of the blocks are not considered.

2.3.2 Simple-Laplacian

This approach is based on the local solution, for each block being upscaled, of a variant of the Laplace equation (steady-state, groundwater flow with neither sources nor sinks). In this approach, the block conductivity is assumed to be a tensor with principal directions parallel to the coordinate axes; and therefore, diagonal for this reference system.

To determine each component of the tensor, a local problem is solved inducing flow in the component direction. For instance, in 2D, the tensor will have two components, K^b_{xx}, and K^b_{yy}; to determine the component corresponding to the x direction, K^b_{xx}, the procedure would be as follows: (1) extract the block being upscaled and solve the groundwater flow equation just within the block, at the fine scale with no flow boundaries on the sides parallel to flow and prescribed heads on the sides perpendicular to flow as shown in Figure 2.5; (2) evaluate the total flow Q through any cross-section parallel to the y-axis from the solution of the flow equation, and (3) compute the block conductivity tensor component in the x-direction as:

$$K^b_{xx} = -\left(\frac{Q}{y_1 - y_0}\right) \Big/ \left(\frac{h_1 - h_0}{x_1 - x_0}\right) \tag{2.3}$$

where $y_1 - y_0$ is the block width; $h_1 - h_0$ is the difference between the prescribed heads on the opposite sides of the block (see Figure 2.5), and $x_1 - x_0$ is the block length. K^b_{yy} would be obtained similarly after solving a similar local flow problem with the boundary conditions in Figure 2.5 rotated 90°.

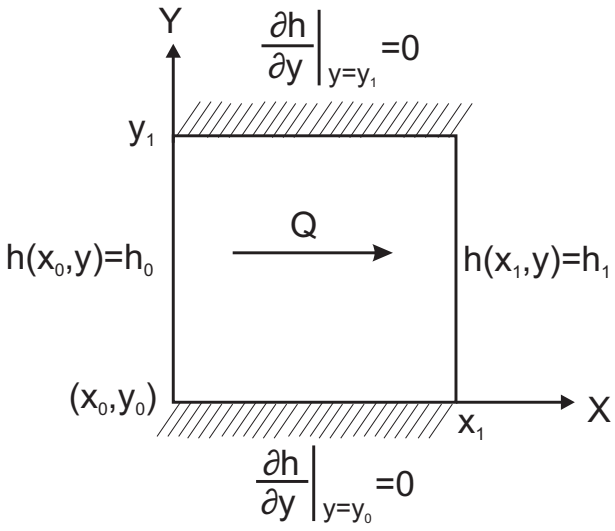

Figure 2.5: Boundary conditions that would be used in 2D for the local flow model when performing the simple-Laplacian upscaling in order to determine the x-component of the hydraulic conductivity tensor. In the simple-Laplacian approach, it is always assumed that the principal directions of the conductivity tensor are parallel to the reference axes.

The main shortcoming of this approach is that the assumption of a diagonal tensor is not well-founded for a heterogeneous aquifer. In other words, the heterogeneity within the block may induce an overall flux that is not parallel to the macroscopic head gradient, a behavior that cannot be captured with a diagonal tensor.

This method has been widely used to calculate block conductivities in petroleum engineering and hydrogeology (e.g., Warren and Price, 1961; Bouwer, 1969; Journel et al., 1986; Desbarats, 1987, 1988; Deutsch, 1989; Begg et al., 1989; Bachu and Cuthiell, 1990). More recently Sánchez-Vila et al. (1996) utilized this approach to study the scale effects in transmissivity; Jourde et al. (2002) used it to calculate block equivalent conductivities for fault zones; and Flodin et al. (2004) used this method to illustrate the impact of boundary conditions on upscaling. It has also been employed by Fernàndez-Garcia and Gómez-Hernández (2007) and Fernàndez-Garcia et al. (2009) to evaluate the impact of hydraulic conductivity upscaling on solute transport. Some reasons favoring this approach are that it is not empirical but phenomenological, i.e., it is based on the solution of the groundwater flow equation, and it yields a tensor representation of the block conductivity, which would be exact for the case of perfectly layered media, with the layers parallel to the coordinate axes.

2.3.3 Laplacian-with-skin

To overcome the shortcomings of the simple-Laplacian approach, the Laplacian-with-skin approach was presented by Gómez-Hernández (1991). In this approach, the block conductivity is represented by a generic tensor (not necessarily diagonal) and the local flow problem is solved over an area that includes the block plus a skin surrounding it (see Figure 2.6). The skin is designed to reduce the impact of the arbitrary boundary conditions used in the solution of the local flow problems letting the conductivity values surrounding the block to take some control on the flow patterns within the block.

For a 3D block, the overall algorithm is summarized as follows: (1) the block to upscale plus the skin is extracted from the domain; (2) flow is solved at the fine scale within the block-plus-skin region for a series of boundary conditions; (3) for each boundary condition the spatially-averaged specific discharge ($\mathbf{q}$) and gradient ($\mathbf{J}$) are calculated as,

$$\langle q_i \rangle = \frac{1}{V(\mathbf{x})} \int_{V(\mathbf{x})} q_i(\mathbf{x}) d\mathbf{x} \tag{2.4}$$

$$\langle J_i \rangle = \frac{1}{V(\mathbf{x})} \int_{V(\mathbf{x})} \frac{\partial h(\mathbf{x})}{\partial x_i} d\mathbf{x} \tag{2.5}$$

where i refers to the three components of the vectors (i.e., q_x, q_y and q_z; J_x,J_y and J_z); and (4) the tensor components of $\mathbf{K}^b$ are determined by solving

the following overdetermined system of linear equations by a standard least squares procedure (Press et al., 1988).

$$\begin{bmatrix} \langle J_x\rangle_1 & \langle J_y\rangle_1 & \langle J_z\rangle_1 & 0 & 0 & 0 \\ 0 & \langle J_x\rangle_1 & 0 & \langle J_y\rangle_1 & \langle J_z\rangle_1 & 0 \\ 0 & 0 & \langle J_x\rangle_1 & 0 & \langle J_y\rangle_1 & \langle J_z\rangle_1 \\ \langle J_x\rangle_2 & \langle J_y\rangle_2 & \langle J_z\rangle_2 & 0 & 0 & 0 \\ 0 & \langle J_x\rangle_2 & 0 & \langle J_y\rangle_2 & \langle J_z\rangle_2 & 0 \\ 0 & 0 & \langle J_x\rangle_2 & 0 & \langle J_y\rangle_2 & \langle J_z\rangle_2 \\ \cdots & \cdots & \cdots & \cdots & \cdots & \cdots \\ \langle J_x\rangle_n & \langle J_y\rangle_n & \langle J_z\rangle_n & 0 & 0 & 0 \\ 0 & \langle J_x\rangle_n & 0 & \langle J_y\rangle_n & \langle J_z\rangle_n & 0 \\ 0 & 0 & \langle J_x\rangle_n & 0 & \langle J_y\rangle_n & \langle J_z\rangle_n \end{bmatrix} \cdot \begin{bmatrix} K^b_{xx} \\ K^b_{xy} \\ K^b_{xz} \\ K^b_{yy} \\ K^b_{yz} \\ K^b_{zz} \end{bmatrix} = - \begin{bmatrix} \langle q_x\rangle_1 \\ \langle q_y\rangle_1 \\ \langle q_z\rangle_1 \\ \langle q_x\rangle_2 \\ \langle q_y\rangle_2 \\ \langle q_z\rangle_2 \\ \cdots \\ \langle q_x\rangle_n \\ \langle q_y\rangle_n \\ \langle q_z\rangle_n \end{bmatrix} \tag{2.6}$$

where $1, \ldots, n$ refers to the different boundary conditions; $K^b_{xx} \cdots K^b_{zz}$ are the components of the upscaled equivalent conductivity tensor $\mathbf{K}^b$. In principle, in 3D, two sets of boundary conditions are sufficient to determine $\mathbf{K}^b$. However, from a practical point of view, the number of boundary conditions should be greater than two ($n > 2$) to better approximate all possible flow scenarios.

Every three rows in Equation (2.6) are the result of enforcing Darcy's law on the average values in equations (2.4) and (2.5) for a given boundary condition:

$$\langle \mathbf{q} \rangle = -\mathbf{K}^b \langle \mathbf{J} \rangle \tag{2.7}$$

The block conductivity tensor must be symmetric and positive definite. Symmetry is easily enforced by making $K^b_{xy} = K^b_{yx}$, $K^b_{xz} = K^b_{zx}$ and $K^b_{yz} = K^b_{zy}$. Positive definiteness is checked a *posteriori*. In case the resulting tensor is non-positive definite, the calculation is repeated either with more boundary conditions or with a larger skin size (Wen et al., 2003; Li et al., 2011).

We note that the critical point in this approach is the selection of the set of n alternative boundary conditions. In general, this set of boundary conditions is chosen so as to induce flow in several directions (for instance, the prescribed head boundary conditions in Figure 2.6 induce flow at 0°, 45°, 90° and 135° angles with respect to the x-direction). For the boundary conditions, we have chosen to prescribe linearly varying heads along the sides of the blocks, other authors (Durlofsky, 1991) have proposed the use of periodic boundary conditions. Flodin et al. (2004) showed that the resulting block conductivities do not depend significantly on whether the boundary conditions are linearly varying or periodic.

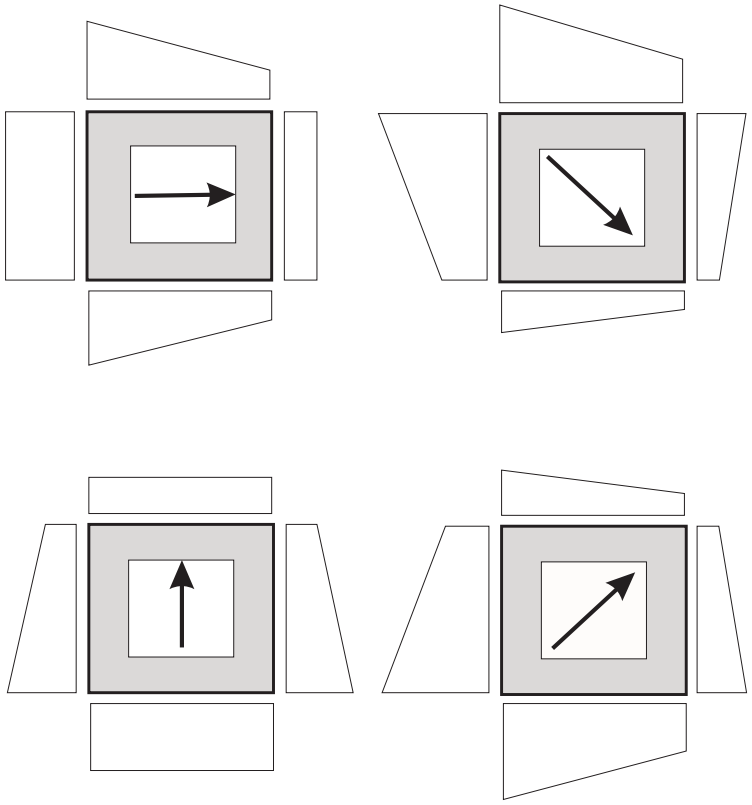

Figure 2.6: An example of four boundary condition sets that could be used in 2D for the local flow models when performing the Laplacian-with-skin upscaling. The white area is the block being upscaled, and the gray area is the skin region; the arrows indicate the (negative) mean head gradient induced by the prescribed head boundary conditions, and the shapes on the sides of the block indicate the magnitude of the prescribed heads given by tilting planes with gradients opposite to the arrows.

2.3.4 Non-uniform coarsening

Prior to upscaling, the fine-scale realization has to be overlain with the coarse-scale discretization that will be used in the numerical model. Each block in the coarse discretization must be assigned an upscaled conductivity value on the basis of the conductivity values in the fine-scale realization. Initially, all studies on hydraulic conductivity upscaling assumed that the coarse scale discretization was uniform, that is, all coarse blocks were of the same shape and size, until Durlofsky et al. (1997) introduced the concept of non-uniform coarsening. The rationale was simple, if upscaling induces smoothing, and the petroleum engineer is most interested in the water cut (the early breakthrough at the production wells when petroleum is being displaced by injected water) it is important to smooth the least the areas of high displacement velocities, whereas the smoothing in the areas of low velocities is less relevant. For this purpose, Durlofsky et al. (1997) suggest the following steps: (1) identify the underlying high velocity regions using a fine-scale single-phase flow simulation; (2) on the basis of this simulation define a discretization with small blocks in high-velocity areas and large ones elsewhere; and (3) apply the Laplacian-with-skin upscaling technique to calculate the block conductivity tensors of the coarse (non-uniform) blocks.

In a hydrogeological context, we can also use a non-uniform coarsening aimed to preserve small blocks in: (1) high flow velocity zones; (2) regions where hydraulic gradients change substantially over short distances, such as near pumping or injection wells (Wen and Gómez-Hernández, 1998); (3) areas near contaminant spills within a regional aquifer where accurate simulation of plume movement is of interest; and (4) in zones requiring a detailed representation of heterogeneity, for instance to capture channels or fractures (Durlofsky et al., 1997; Wen et al., 2003; Flodin et al., 2004).

2.4 Coarse model and simulation results

In this section, we first present the governing equation and the solution procedures for the flow and transport models, and then we discuss the results obtained applying the different upscaling techniques described in the previous section. All of these techniques are applied to realization #26 of the MADE aquifer in Salamon et al. (2007).

2.4.1 Coarse Flow and Transport Equations

Under steady-state flow conditions and in the absence of sinks and sources, the flow equation of an incompressible or slightly compressible fluid in saturated porous media can be expressed by combining Darcy's Law and the continuity

equation, which in Cartesian coordinates is (Bear, 1972; Freeze and Cherry, 1979):

$$\nabla\cdot\big(\mathbf{K}(\mathbf{x})\nabla h(\mathbf{x})\big) = 0 \tag{2.8}$$

where h is the piezometric head, and $\mathbf{K}$ is a second-order symmetric hydraulic conductivity tensor.

Most frequently, the hydraulic conductivity tensor is assumed isotropic and therefore can be represented by a scalar. In this case, a standard seven-point block-centered finite-difference stencil is typically employed to solve the partial differential equation in three dimensions. This approach is also valid if, for all blocks, the conductivity is modeled as a tensor with the principal directions aligned with the block sides (Harbaugh et al., 2000). However, when modeling geologically complex environments at a coarse scale, the assumption of isotropic block conductivity or even tensor conductivity with principal components parallel to the block sides is not warranted. It is more appropriate to use a full hydraulic conductivity tensor to capture properly the average flow patterns within the blocks (Bourgeat, 1984; Gómez-Hernández, 1991; Wen et al., 2003; Zhou et al., 2010). Recently, the commonly used groundwater model software MODFLOW implemented a new module that allows the use of a full tensorial representation for hydraulic conductivity within model layers (Anderman et al., 2002) which has been successfully applied in 2D examples such as in Fernàndez-Garcia and Gómez-Hernández (2007).

Modeling three-dimensional flow in a highly heterogeneous environment at a coarse scale, requires accounting for a tensorial representation of hydraulic conductivity. We cannot assume, *a priori* that specific discharge and hydraulic head gradient will be parallel, nor that the principal directions of the hydraulic conductivity tensors are the same in all blocks. For this reason, and given that MODFLOW can only account for 3D tensors if one of its principal directions is aligned with the vertical direction, Li et al. (2010) developed a three-dimensional groundwater flow simulation with tensor conductivities of arbitrary orientation of their principal directions. This code is based on an nineteen-point finite-difference approximation of the groundwater flow equation, so that the flow crossing any block interface will depend not only on the head gradient orthogonal to the face, but also on the head gradient parallel to it.

Finite-difference modeling approximates the specific discharges across the interface between any two blocks i and j as a function of the hydraulic conductivity tensor in between block centers. This tensor is neither the one of block i nor of the one of block j. For this reason, finite-difference numerical models need to approximate the interblock conductivity; the most commonly used approximation is taking the harmonic mean of adjacent block values.

When block conductivities are represented by a tensor, the concept of how to average the block tensors in adjacent blocks is not clear. To overcome this difficulty, the code developed by Li et al. (2010) takes directly, as input, interblock conductivity tensors, removing the need of any internal averaging of tensors defined at block centers. Within the context of upscaling, deriving the interblock conductivity tensors simply amounts to isolate the parallelepiped centered at the interface between adjacent blocks, instead of isolating the block itself, and then apply the upscaling techniques described in the previous section. In other contexts, the user must supply the interblock conductivity tensors directly. Several authors (Appel, 1976; Gómez-Hernández, 1991; Romeu and Noetinger, 1995; Li et al., 2010) have recommended to work directly with interblock conductivities for more accurate groundwater flow simulations.

Mass transport is simulated using the advection-dispersion equation: (Bear, 1972; Freeze and Cherry, 1979):

$$\phi\frac{\partial C(\mathbf{x},t)}{\partial t} = -\nabla\cdot\big(\mathbf{q}(\mathbf{x})C(\mathbf{x},t)\big) + \nabla\cdot\big(\phi\mathbf{D}\nabla C(\mathbf{x},t)\big) \tag{2.9}$$

where C is the dissolved concentration of solute in the liquid phase; ϕ is the porosity; $\mathbf{D}$ is the local hydrodynamic dispersion coefficient tensor, and $\mathbf{q}$ is the Darcy velocity given by $\mathbf{q}(\mathbf{x}) = -\mathbf{K}(\mathbf{x})\nabla h(x)$.

As in the works of Salamon et al. (2007) and Llopis-Albert and Capilla (2009) at the MADE site, the random walk particle tracking code RW3D (Fernàndez-Garcia et al., 2005; Salamon et al., 2006) is used to solve the transport equation (2.9). In this approach, the displacement of each particle in a time step includes a deterministic component, which depends only on the local velocity field, and a Brownian motion component responsible for dispersion. A hybrid scheme is utilized for the velocity interpolation which provides local as well as global divergence-free velocity fields within the solution domain. Meanwhile, a continuous dispersion-tensor field provides a good mass balance at grid interfaces of adjacent cells with contrasting hydraulic conductivities (LaBolle et al., 1996; Salamon et al., 2006). Furthermore, in contrast to the constant time scheme, a constant displacement scheme (Wen and Gómez-Hernández, 1996a), which modifies automatically the time step size for each particle according to the local velocity, is employed in order to reduce computational effort.

2.4.2 Upscaling design and error measure

In this work, we have performed both uniform and non-uniform upscaling. In the case of uniform upscaling, the original hydraulic conductivity realization discretized into $110 \times 280 \times 70$ cells of 1 m by 1 m by 0.15 m is upscaled onto a model with $11 \times 28 \times 14$ blocks of 10 m by 10 m by 0.75 m. This upscaling

represents going from 2 156 000 cells down to 4 312 blocks, i.e., a reduction by a factor of 500. The reduction in model size, undoubtedly, reduces the computational cost for flow and transport modeling. As will be shown, the flow and transport results can be improved using a non-uniform discretization of the coarse model. For the non-uniform upscaling, the discretization continues to be a rectangular grid, with the following coarse block dimensions: along the x-axis (orthogonal to flow), block dimension is 10 m, except between $x = 40$ m and $x = 90$ m where it is 5 m; along the y-axis (parallel to flow), block dimension is 10 m, except between $y = 20$ m and $y = 130$ m where it is 5 m; and along the z-axis, block dimension is 1.5 m between $z = 0$ m and $z = 3$ m and 0.75 m elsewhere. The final model has $16 \times 39 \times 12$ (7 488) blocks, with smaller blocks close to the source and along the area through which it is most likely that the solute plume will travel. The reduction factor in size, with respect to the initial discretization is close to 300.

The first set of upscaling runs use simple averaging rules to obtain the block conductivity values. The second set of runs use the Laplacian-based approaches. Within this second set of runs we carry out a first comparison using tensor conductivity values computed at block centers versus tensor conductivities computed at the interfaces; the former requires a further averaging of adjacent block values to approximate the interblock conductivities needed by the numerical solver, whereas the latter does not. Then, after showing that interface-centered conductivity upscaling is more appropriate, the following upscaling runs are always performed with interblock conductivities.

In the application of any of the Laplacian approaches for upscaling, the local flow model that must be run for each block was solved by finite differences using the preconditioned conjugate gradient method implemented in MODFLOW (Hill, 1990) since we found it to be the fastest algorithm for the same convergence criteria.

In the Laplacian-with-skin approach, the size of the skin was taken equal to half the block size in each direction. A prior sensitivity analysis revealed that this skin size was enough to capture accurately the average flow crossing each of the upscaled blocks. Zhou et al. (2010) also found that half the block size is a good choice for the skin size in most situations. The overdetermined system of equations from which the components of the block tensor are described is built after solving nine local flow problems. In each of the local problems the prescribed heads applied to the boundaries of the block vary linearly as a function of x, y and z so that they impose overall head gradients parallel to the directions given by the following nine vectors $(1,0,0)$,$(0,1,0)$,$(0,0,1)$,$(1,1,0)$,$(1,0,1)$,$(0,1,1)$,$(1,1,0)$, $(-1,0,1)$,$(0,-1,1)$.

To evaluate the performance of the different upscaling techniques we focus on the reproduction of the interblock fluxes and on the reproduction of the solute transport. For the fluxes, we compare the interblock specific discharges

obtained after solving the flow equation at the coarse scale with the corresponding values derived after solving the flow equation in the reference field at the fine scale. We focus on fluxes instead of piezometric heads because fluxes have a larger spatial variability and have a dominant role in solute transport. The metric we use to evaluate each technique is the average relative bias (RB) given by:

$$RB = \frac{1}{N}\sum_{i=1}^{N}\left|\frac{q_{f,i} - q_{c,i}}{q_{f,i}}\right| \cdot 100 \tag{2.10}$$

where N is the number of block interfaces; $q_{f,i}$ is the specific discharge through the block interface i computed from the fine scale solution, and $q_{c,i}$ is the specific discharge through the block interface i resulting from the coarse scale simulation.

Mass transport reproduction is evaluated qualitatively by comparing the longitudinal mass distribution profiles at the 328^{th} day obtained from the fine scale model with the one obtained from the coarse scale model.

Notice that the same transport parameters used for the fine scale simulation described in section 2.2 are also used for the coarse scale simulation.

2.4.3 Results and Comparisons

Next, we will discuss the flow and transport performance of the different upscaling approaches. The flow upscaling analysis excludes the interfaces of the blocks which are adjacent to the boundaries; the reason for the exclusion is that the boundary conditions have an impact on the results of upscaling in the nearby blocks (Vermeulen et al., 2006). Excluding these blocks, the discrepancies in flow reproduction between the coarse and fine scale simulations will be due to the upscaling method and not to the presence of the boundaries. This consideration is not necessary when analyzing the transport upscaling since the plume travels far enough from the boundaries. Also, since, for transport purposes, the flows along the y-axis are the most relevant (and of the highest magnitude), the graphs only shows the specific discharges across the interfaces orthogonal to the y-axis, similar results are obtained when analyzing the interfaces orthogonal to the x- and z-axis.

Figure 2.7 shows the scatterplots of reference versus upscaled fluxes through the block interfaces using simple averaging methods. All circles within the dotted lines have a relative bias smaller than 10% of the reference values, whereas the circles within the solid lines have a relative bias smaller than 40%. It is clear that, out of the different averages, the power average with a power of 0.5 gives the best results. The use of the harmonic mean (Figure 2.7A) (power average with $\omega = -1$) tends to severely underestimate the reference fluxes,

while the arithmetic mean (Figure 2.7C) (power average with $\omega = +1$) tends to overestimate them. The geometric mean (power average with $\omega = 0$) does a better work but stills tends to underestimate the fluxes (Figure 2.7B). The best average, as already pointed out by Cardwell and Parsons (1945) should be somewhere between the harmonic and the arithmetic averages. In this specific case, we found that the smallest bias occurs when $\omega = 0.5$ (Figure 2.7D), resulting in a relative bias, RB, of 11%. As mentioned earlier, for isotropic, mildly heterogeneous media, Desbarats (1992) found $\omega = 1/3$ to be the best power average for upscaling purposes. In the MADE case, the field is neither isotropic, nor mildly varying ($\ln K$ variance is close to 5), thus it is not surprising that the optimal power value does not coincide with the value reported by Desbarats (1992).

Figure 2.8 shows the longitudinal mass distribution profile (integrated along the direction orthogonal to flow, and normalized by the total mass) of the tritium plume using different simple averaging upscaling techniques at 328 days. The solid line represents the fine scale result. For reference, the initial conditions at 27 days are also shown by the bold dashed curve. The remaining of the curves are the upscaled results for the different averages. Both the upscaled models using the arithmetic mean and the 0.5 power average are capable of reproducing the long downstream spreading of the contaminant plume, with the power mean resulting in a better representation of the distribution close to the source. Yet, none of the methods exhibits a satisfactory accuracy.

Figure 2.9 shows the scatterplots of reference versus upscaled fluxes using different Laplacian approaches. Figures 2.9A and 2.9B display upscaling approaches using a simple-Laplacian (i.e., without skin, and assuming diagonal tensors) for block-centered and interblock-centered upscaling, respectively. It is clear that it is better to upscale directly the interblock conductivity than upscaling the block values and then let the numerical model estimate internally the interblock conductivity. This is consistent with earlier studies (Li et al., 2010).

Figures 2.9B and 2.9C display two different Laplacian approaches without skin. The simple-Laplacian in Figure 2.9B assumes a diagonal representation of the tensor in the reference axes, whereas the Laplacian-with-skin but with a skin set to zero in Figure 2.9C allows for the tensor representation to be non-diagonal. Allowing the tensor principal components not to be aligned with the reference axes results in a better representation of the fluxes, since it is unlikely that all interblocks would have conductivities with principal directions parallel to the reference axes.

Moreover, if the skin is allowed to increase up to half the block size, the results improve even further, as can be checked by comparing Figures 2.9C and 2.9D. This improvement can be related to the reduction of the influence

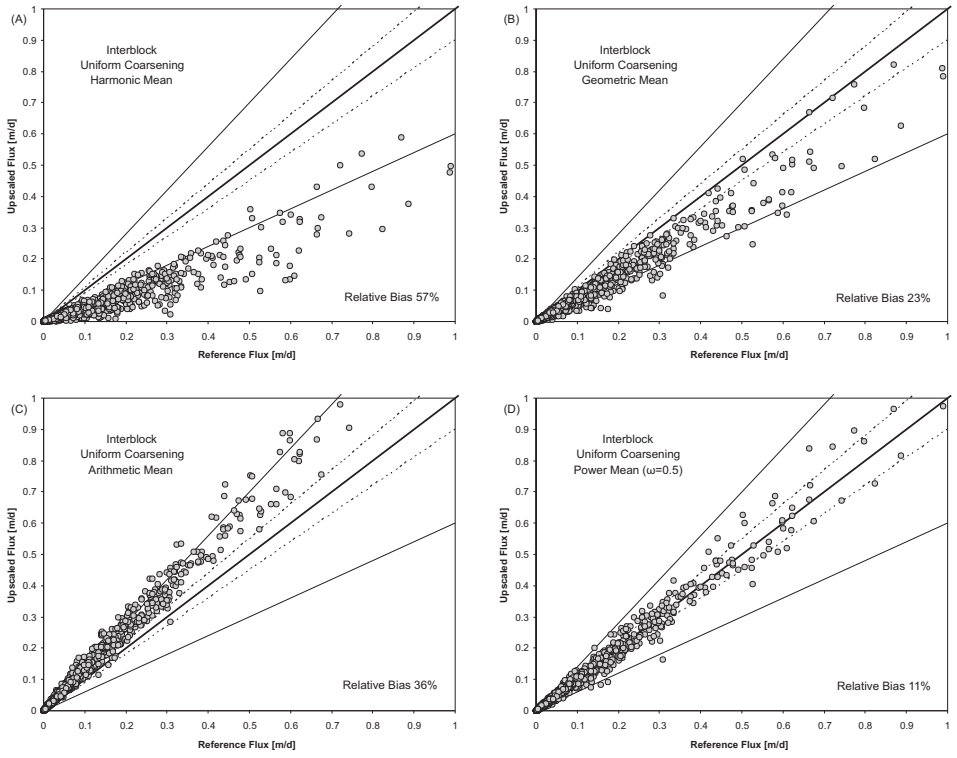

Figure 2.7: Flow comparison at the fine and coarse scales using simple averaging upscaling approaches. All circles within the dashed lines correspond to coarse scale values that deviate less than 10% from the reference ones; similarly, all circles within the outer solid lines correspond to coarse scale values that deviate less than 40%. The average relative bias, as defined in Equation 2.10, is reported in the lower right corner of each box.

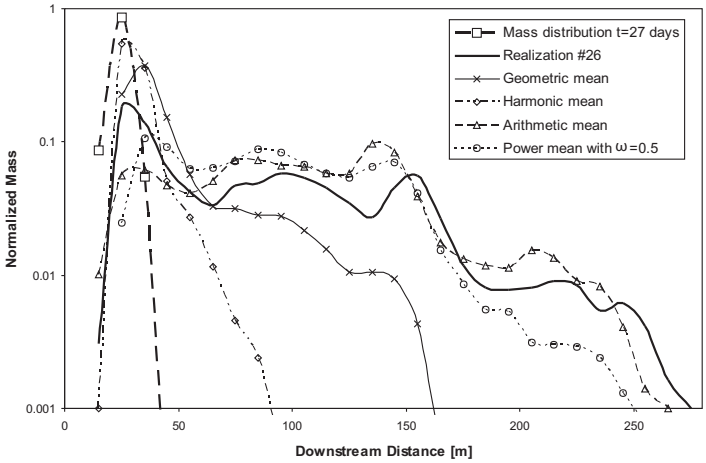

Figure 2.8: Longitudinal mass distribution profiles of the tritium plume from the fine scale reference realization, and predictions by some simple averaging upscaling approaches at the coarse scale for $t = 328$ days.

in the flow patterns within the block of the boundary conditions used in the local flow models in favor of the influence of the nearby conductivities from the reference aquifer.

Since most of the commonly available groundwater flow simulators only accept diagonal tensors as input parameter values, a test was made by solving the flow and transport in the coarse scale ignoring the off-diagonal components of the tensors used in Figure 2.9D. The results are shown in Figure 2.9E and they are qualitatively similar to those in Figure 2.9D. In this specific case, in which the reference axes of the numerical model are aligned with the main directions of the statistical anisotropy of hydraulic conductivity it could be expected that the off-diagonal components of the upscaled block conductivity tensors were small, and therefore, flow predictions neglecting them go almost unaffected. In a general setting with complex geology, cross-beddings, or non-uniform anisotropies, the use of a full tensor block conductivity would be necessary for a good reproduction of the aquifer response (Bierkens and Weerts, 1994).

Finally, Figure 2.9F shows that the best results are achieved when the upscaling is performed on a non-uniform coarse grid, which has been refined in the areas of highest velocities (see grid in Figure 2.15), using an interface-centered Laplacian-with-skin upscaling. While this result is expected, since the number of model blocks is larger in the non-uniform grid, the improvement is

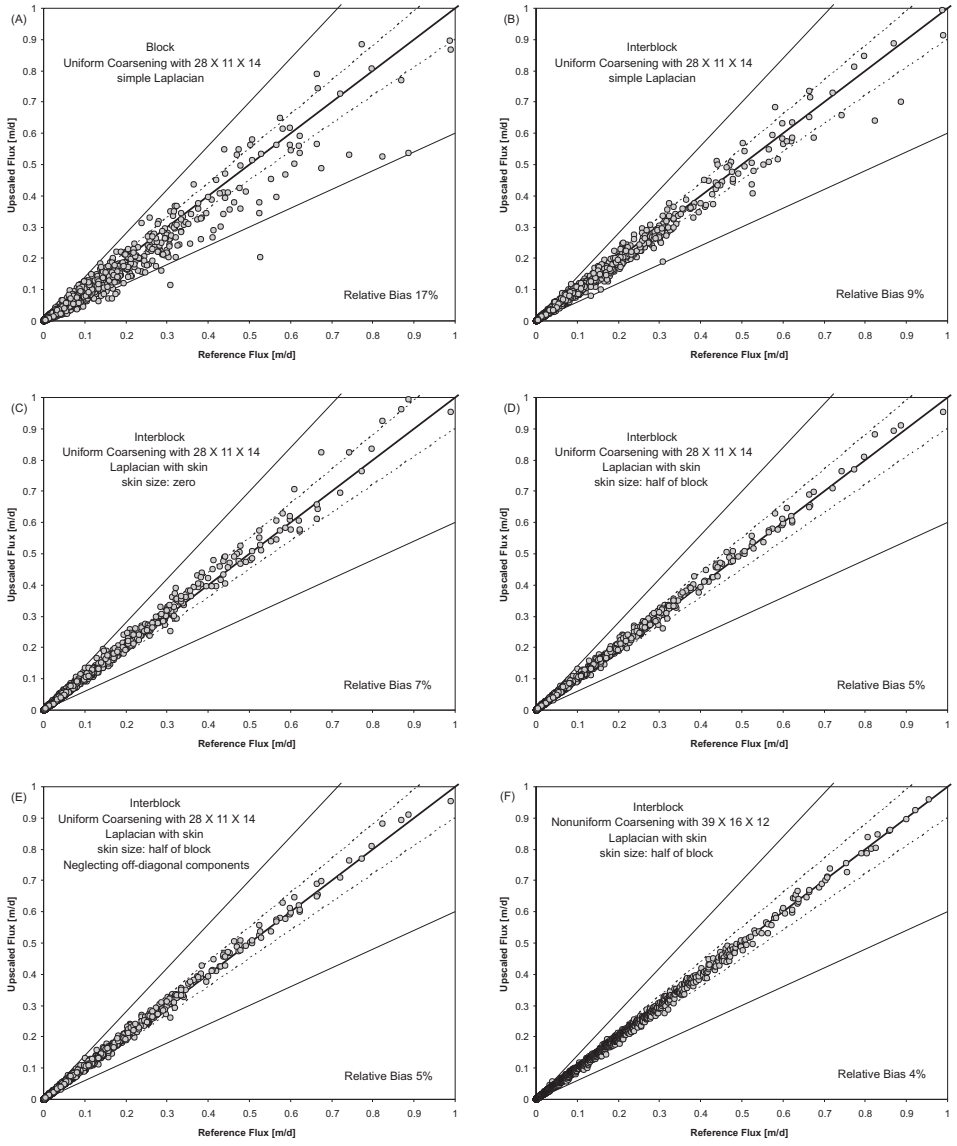

Figure 2.9: Flow comparison at the fine and coarse scales using Laplacian-based upscaling approaches. All circles within the dashed lines correspond to coarse scale values that deviate less than 10% from the reference ones; similarly, all circles within the outer solid lines correspond to coarse scale values that deviate less than 40%. The average relative bias, as defined in Equation 2.10, is reported in the lower right corner of each box.

not due just to having almost twice as many blocks, but to the fact, that these many more blocks are located in the zones where the variability of velocity is the highest. The message to take away is that it is advantageous to use a non-uniform coarse grid and that the definition of this grid is very important to achieve the best upscaling results. Other authors have investigated along these lines and have proposed the use of flexible grids which maintain a given topology (basically keeping constant the number of rows, columns and layers) but which are deformed so as to reduce the variability of the specific discharge vector within each coarse block (i.e, Garcia et al., 1992; Wen and Gómez-Hernández, 1998).

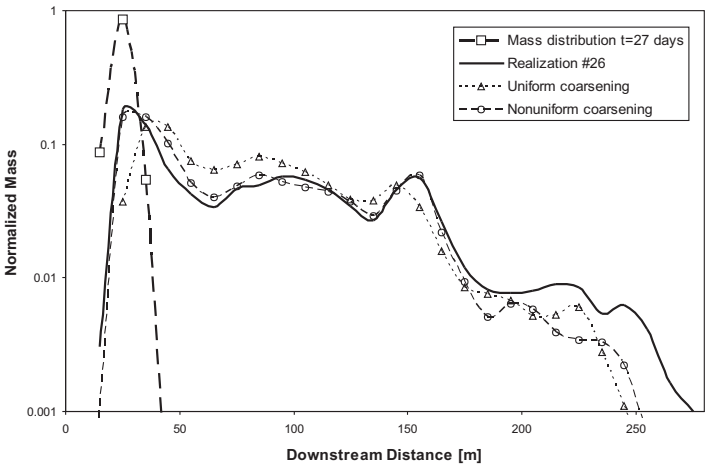

Figure 2.10: Longitudinal mass distribution profiles of the tritium plume from the fine scale reference realization, and predictions on uniform and non-uniform coarse scale grids, for $t = 328$ days.

Figure 2.11 compares the mass longitudinal profile of the upscaling approaches in Figures 2.9A (uniform grid, simple-Laplacian, block-centered), 2.9B (uniform grid, simple-Laplacian, interblock-centered) and 2.9D (uniform grid, Laplacian-with-skin, interblock-centered) with the reference profile at day 328. The improvement in the reproduction of the reference values by the difference upscaling techniques shows a similar progression as the improvement seen in the reproduction of the fluxes in Figure 2.9. Comparing these curves to any of the curves in Figure 2.8, which were obtained with simple averaging upscaling rules, it is clear that any upscaling approach based on a local solution of the flow equation provides a better representation of the hydraulic conductivity distribution and yields better transport predictions. The

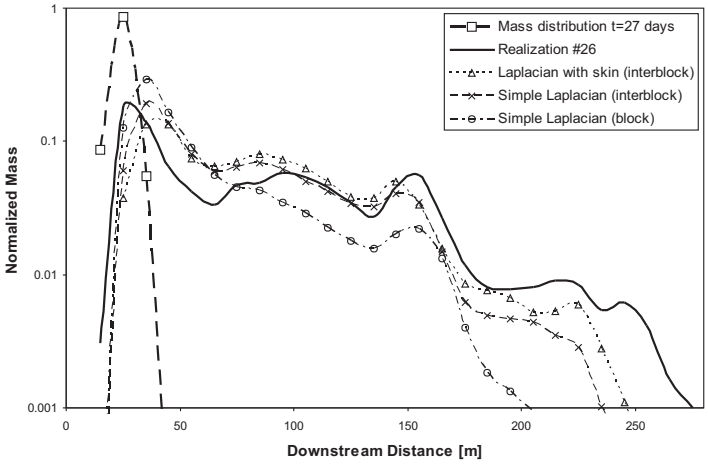

Figure 2.11: Longitudinal mass distribution profiles of the tritium plume from the fine scale reference realization, and predictions by some Laplacian-based upscaling approaches at the coarse scale, for $t = 328$ days.

two interblock-aimed upscaling approaches are able to capture both the peak concentration near the source and the downstream spreading.

Figure 2.10 shows the mass longitudinal profile of the upscaling approaches in Figures 2.9D (uniform grid, Laplacian-with-skin, interblock-centered) and 2.9F (non-uniform grid, Laplacian-with-skin, interblock-centered). It is evident that the non-uniform coarsening gives again the best results: up to a downstream distance of 200 m, the reproduction is almost perfect, and the very low concentrations for distances farther than 200 m are adequately reproduced.

A final comparison of the different approaches can be performed by analyzing the spatial distribution of the contaminant plume, both in plan view (depth integrated) and lateral view (integrated along the x-axis). Figure 2.12 shows the contaminant plume in the reference fine-scale conductivity realization. Figures 2.13, 2.14, and 2.15 show the corresponding distributions for the mass transport simulation in the upscaled fields using a block-centered, simple-Laplacian upscaling approach, an interblock-centered, Laplacian-with-skin approach, and the non-uniform coarsening, interblock-centered, Laplacian-with-skin approach, respectively. It is evident that the block-centered approach is not capable to produce a field in which the solute travels as far downstream as in the reference field, while the most elaborated upscaling approach of Figure 2.15 gives results which quite closely resemble the reference values.

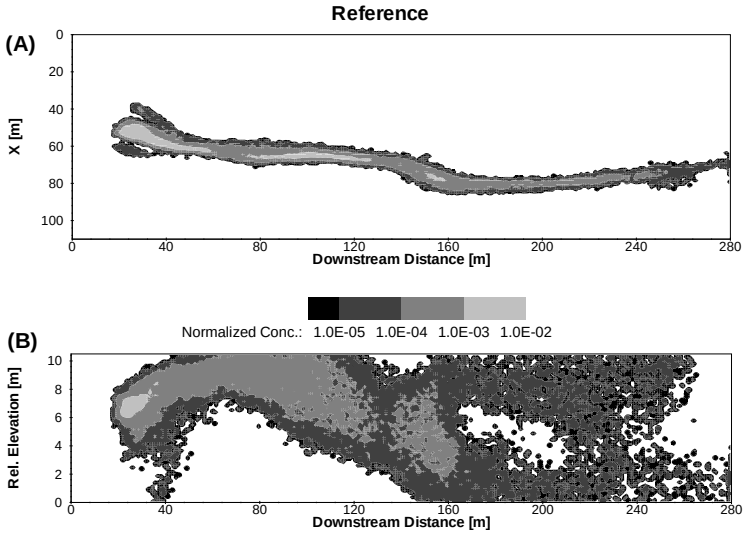

Figure 2.12: Transport in the fine scale reference realization for $t = 328$ days. (A) Depth-integrated normalized concentration distribution. (B) Laterally-integrated normalized concentration distribution.

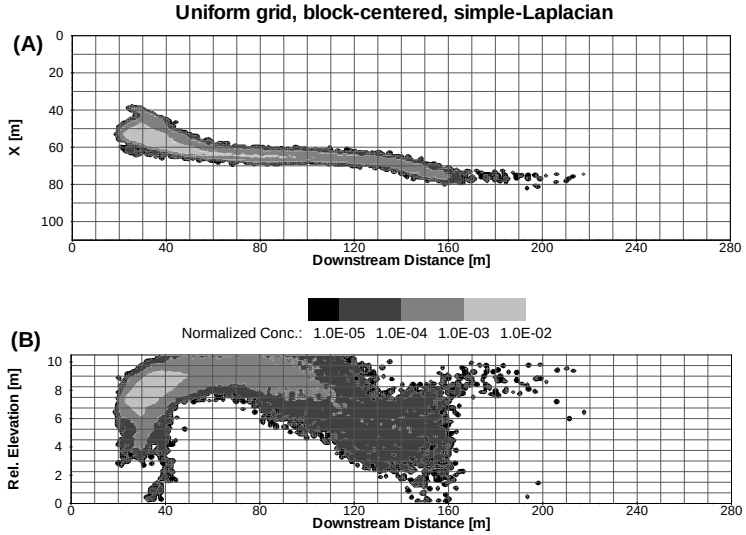

Figure 2.13: Transport at the coarse scale after upscaling the reference realization on a uniform grid using a block-centered simple-Laplacian approach for $t = 328$ days. (A) Depth-integrated normalized concentration distribution. (B) Laterally-integrated normalized concentration distribution.

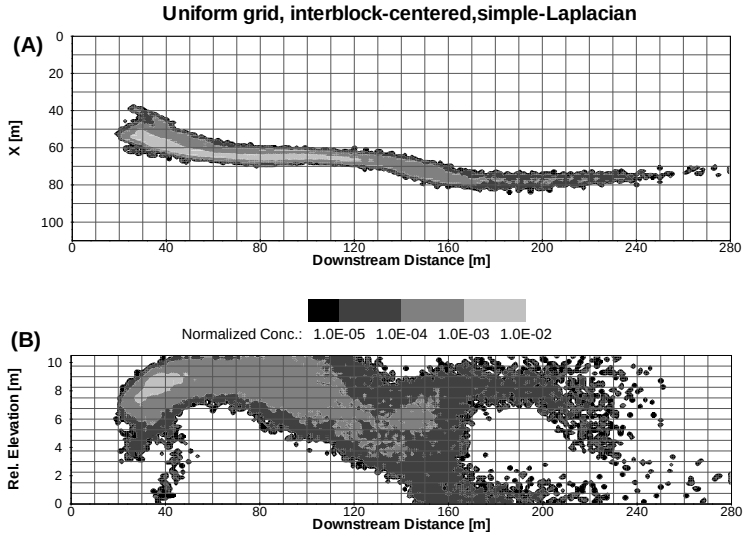

Figure 2.14: Transport at the coarse scale after upscaling the reference realization on a uniform grid using an interblock-centered simple-Laplacian approach for $t = 328$ days. (A) Depth-integrated normalized concentration distribution. (B) Laterally-integrated normalized concentration distribution.

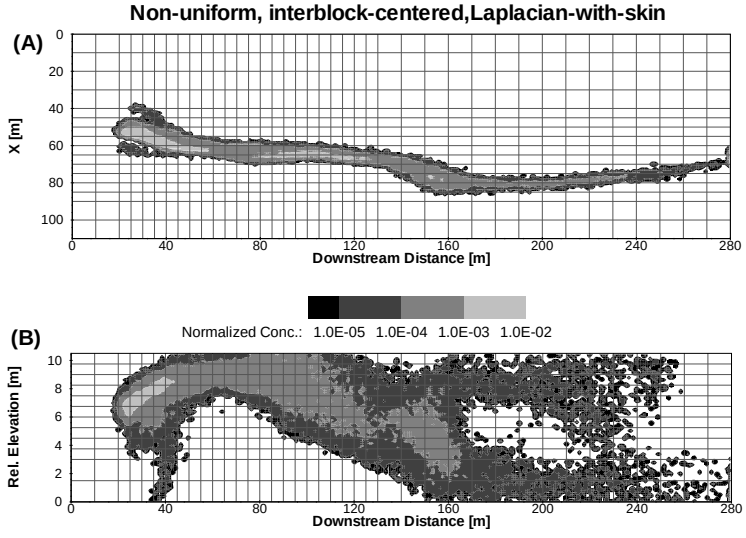

Figure 2.15: Transport at the coarse scale after upscaling the reference realization on a non-uniform grid using an interblock-centered Laplacian-with-skin approach for $t = 328$ days. (A) Depth-integrated normalized concentration distribution. (B) Laterally-integrated normalized concentration distribution.

2.5 Discussion

We have shown that flow and transport can be modeled at the MADE site by the advection dispersion equation on relatively coarse discretization if the spatial variability of hydraulic conductivity at the fine scale is properly characterized and a careful upscaling approach is applied to it. But, why is this so? and why is the non-uniform grid interblock-centered Laplacian-with-skin upscaling the approach to use?

Let's first analyze the progression in the reproduction of the specific discharges with the upscaling approaches. It is well known that the coarse-scale representation of conductivity as a tensor is mostly due to the statistical anisotropy at the fine scale (Lake, 1988). In the limit, with infinite correlation in the horizontal plane, the medium would be perfectly layered and the tensor conductivity will have arithmetic average for the horizontal components and the harmonic average for the vertical ones. At the MADE site, the horizontal continuity is not infinity, but it is quite large compared with the size of the domain, this is the reason why, for the reproduction of the specific discharges across the interfaces which are orthogonal to the direction of maximum continuity, the best average is a power-average with exponent in between those corresponding to the geometric and arithmetic averages, and larger than the theoretical value for statistically isotropic media. Yet, assuming that the conductivity is a scalar (as is done when a simple average is used) implies that it is isotropic to flow. At the MADE site there is still enough anisotropic heterogeneity within the blocks to warrant the need of a tensor to describe hydraulic conductivity at the coarse scale. This is why all the Laplacian-based approaches perform better than the simple averaging ones.

Of the Laplacian-based approaches, it is shown that computing tensor conductivities at block centers and then taking the harmonic average of the components corresponding to the directions orthogonal to adjacent interfaces introduces a noise that can be eliminated by aiming directly at upscaling the interblock conductivity tensor to feed directly into the numerical simulator. This is why all interface-centered approaches outperform the block-centered approach.

Of the interblock-centered approaches, analyzing the local flow within an area extending beyond the limits of the block being upscaled (that is, including a skin) also improves the upscaling. The reason being, that the upscaled conductivities are always nonlocal (Neuman and Orr, 1993; Indelman and Abramovich, 1994), that is, they depend not only on the fine-scale conductivities within the block, but on the ones outside, too. Extracting the block to upscale, plus a skin area surrounding it, and applying the boundary conditions of the local flow problems outside the skin, reduces the impact of the boundary conditions inside the block and allows the immediately surrounding

fine scale conductivities to impose some control on the flow patterns within the block (as it will happen when the block is embedded in the aquifer).

The Laplacian-with-skin approach provides a tensor with arbitrary orientation of its principal directions. For the MADE site, it appears that assuming that the principal directions of the block hydraulic conductivity tensors are parallel to the reference axes for all blocks, does not seem to introduce too large an error (compare Figures 2.9D and 2.9E), something that could be explained on the basis that the statistical anisotropy model used has its principal directions of continuity aligned with the reference axes for the entire domain. In cases such as cross-bedded formations, or aquifers with a heterogeneity description for which anisotropy varies locally with the domain, the assumption that the principal directions are parallel to the reference axes could not be sustained.

Upscaling induces heterogeneity smoothing, by defining a non-uniform coarse grid that tries to reduce the smoothing on those areas with the highest velocities, and also on areas where fluid velocity will have the largest impact in transport predictions, the results after upscaling will be better than if we define a uniform coarse grid. Although this may appear as a trivial result, it often is disregarded.

But a good reproduction of the fluxes at the coarse scale is not guarantee that transport predictions will be equally good. It has been shown (Fernàndez-Garcia and Gómez-Hernández, 2007; Fernàndez-Garcia et al., 2009; Li et al., 2011) that, in some occasions, after coarsening a hydraulic conductivity grid, the removal of the within-block heterogeneity requires some type of transport upscaling, either modifying the transport parameters (such as enhancing dispersivity) or including transport processes besides advection and dispersion (such as mass transfer). Recall that in our work we kept the same transport equation, with the same parameter values for the fine and coarse scale simulations. But, for the MADE site this is not necessary. The reason is related on how much smearing out of the within-block heterogeneity is induced by the conductivity upscaling. When this smearing out is important, then, there is a need to include other processes; but for the MADE site and the chosen upscaling, this is not the case. The ratio between the coarse block size and the correlation ranges of the fine scale conductivities is substantially smaller than one, in the direction of flow, the ratio is 1/8, in the horizontal plane orthogonal to flow, the ratio is 1/3.2 and in the vertical direction is 1/5.5; this means that the variability of logconductivity within the block is much smaller than the overall variance of 4.5, and therefore the heterogeneity wiped out by the upscaling process is not as large as to require a further transport upscaling. In the references cited above, the size of the block was on the order of magnitude of the correlation range of the underlying hydraulic conductivity if not larger, and, therefore, upscaling on those cases implied an important smoothing of

heterogeneity that had to be taken into account in the transport simulation at the coarse scale.

Can the findings from this work be extrapolated to other case studies? We believe that, regarding flow upscaling, yes they can. In fact, the findings from this paper are in agreement with similar works in other case studies. However, regarding transport upscaling, they can be extrapolated only under the same conditions considered here, that is, using coarse blocks smaller than the correlation range, and, using a non-uniform grid with smaller blocks in the areas with highest velocities and in the areas through which the plume will travel.

The final point of discussion is why we have worked trying to reproduce flow and transport on a realization from Salamon et al. (2007) instead of trying to reproduce the available experimental data. This paper did not try to perform a calibration exercise of the MADE site, but rather to help in performing such a calibration in the future. With the work in this paper we show that a coarse scale model, obtained by careful upscaling of a fine scale one, can reproduce the type of transport behavior observed at the MADE site simply using the advection dispersion equation. Trying to calibrate a two-million cell model as obtained by Salamon et al. (2007) is not an easy task, it would require running many times the flow and transport models in many realizations of the site; but those runs would be possible on the coarse models used in our work. The next step in this direction would be to develop a calibration approach that would account for the upscaling step needed to reduce the numerical modeling effort. In its application of such an approach, considering heterogeneity in porosity may also help in obtaining the best calibration; something not needed in our upscaling exercise, since we assume constant porosity attached to the reference conductivity realization.

2.6 Summary and Conclusions

In this paper, we have presented a detailed analysis of the impact of different upscaling techniques on the reproduction of solute transport at the MADE site. We use as a reference a fine scale realization taken from the work by Salamon et al. (2007) that is able to reproduce the contaminant spreading observed in the experiment using an advection-dispersion model. The techniques analyzed span from simple averaging to the estimation of block tensors by local flow models. We have also analyzed the impact that non-uniform coarsening may have in the quality of the results.

This work has three main and important conclusions:

1. In complex environments, such as the MADE site, with hydraulic conductivities which vary over many orders of magnitude, and display an

intricate spatial variability, carefully choosing the upscaling technique is very important. The hydraulic conductivity full tensors obtained using the interblock-centered Laplacian-with-skin upscaling technique with a skin size of half block performs best among the different upscaling methods analyzed, although, at the MADE site, the superiority of the full-tensor upscaling over diagonal tensors upscaling is very limited. This can be explained by the fact that the principal directions of hydraulic conductivity are parallel with the reference axes.

2. A non-uniform coarsening focused in the refinement of the regions through which the solute plume travels can further improve the results.

3. Modeling of flow and transport at the MADE site has been the object of debate for many years, and many complex transport models have been proposed to reproduce the plume spreading observed. We show that the advection-dispersion model can be used on a coarse model to explain the plume migration in the highly heterogeneous MADE site if careful modeling/upscaling of the flow field is performed, as long as the block size remains smaller than the correlation ranges of the underlying fine scale conductivities.

Bibliography

Adams, E. E., Gelhar, L. W., 1992. Field study of dispersion in a heterogeneous aquifer 2. spatial moments analysis. Water Resources Research 28 (12), 3293–3307.

Anderman, E. R., Kipp, K. L., Hill, M. C., Valstar, J., Neupauer, R. M., 2002. MODFLOW-2000, the US geological survey modular Ground-Water Model Documentation of the Model-Layer Variable-Direction horizontal anisotropy (LVDA) capability of the Hydrogeologic-Unit flow (HUF) package. US Geological Survey, Open file Report, 02–409.

Appel, C. A., 1976. A note on computing finite difference interblock transmissivities. Water Resources Research 12 (3), 561–563.

Bachu, S., Cuthiell, D., 1990. Effects of Core-Scale heterogeneity on steady state and transient fluid flow in porous media: Numerical analysis. Water Resources Research 26 (5), 863–874.

Baeumer, B., Benson, D. A., Meerschaert, M. M., Wheatcraft, S. W., 2001. Subordinated advection-dispersion equation for contaminant transport. Water Resources Research 37 (6), 1543–1550.

Barlebo, H. C., Hill, M. C., Rosbjerg, D., 2004. Investigating the macrodispersion experiment (MADE) site in columbus, mississippi, using a three-dimensional inverse flow and transport model. Water Resources Research 40 (4), W04211.

Bear, J., 1972. Dynamics of fluids in porous media. American Elsevier Pub. Co., New York.

Begg, S. H., Carter, R. B. R. C., Dranfield, P. B. A., 1989. Assigning effective values to simulator gridblock parameters for heterogeneous reservoirs. SPE (Society of Petroleum Engineers) Reservoir Engineering.

Benson, D. A., Schumer, R., Meerschaert, M. M., Wheatcraft, S. W., 2001. Fractional dispersion, levy motion, and the MADE tracer tests. Transport in porous media 42 (1), 211–240.

Berkowitz, B., Scher, H., 1998. Theory of anomalous chemical transport in random fracture networks. Physical Review E 57 (5), 5858–5869.

Bierkens, M. F. P., Weerts, H. J. T., 1994. Block hydraulic conductivity of cross-bedded fluvial sediments. Water Resources Research 30 (10), 2665–2678.

Boggs, J., Beard, L., Waldrop, W., Stauffer, T., MacIntyre, W., Antworth, C., 1993. Transport of tritium and four organic compounds during a natural gradient experiment (MADE-2), EPRI Report TR-101998. Electric Power Research Institute, Palo Alto, CA 94304.

Boggs, J. M., Adams, E. E., 1992. Field study of dispersion in a heterogeneous aquifer 4. investigation of adsorption and sampling bias. Water Resources Research 28 (12), 3325–3336.

Boggs, J. M., Young, S. C., Beard, L. M., Gelhar, L. W., Rehfeldt, K. R., Adams, E. E., 1992. Field study of dispersion in a heterogeneous aquifer 1. overview and site description. Water Resources Research 28 (12), 3281–3291.

Bourgeat, A., 1984. Homogenized behavior of two-phase flows in naturally fractured reservoirs with uniform fractures distribution. Computer Methods in Applied Mechanics and Engineering 47 (1-2), 205–216.

Bouwer, H., 1969. Planning and interpreting soil permeability measurements. Journal of the Irrigation and Drainage Division, ASCE 95, 391–402.

Cardwell, W. T., Parsons, R. L., 1945. Averaging permeability of heterogeneous oil sands. Transactions of the American Institute of Mining, Metallurgical and Petroleum Engineers 160, 34–42.

Chen, Y., Durlofsky, L. J., Gerritsen, M., Wen, X. H., 2003. A coupled local-global upscaling approach for simulating flow in highly heterogeneous formations. Advances in Water Resources 26 (10), 1041–1060.

Desbarats, A. J., 1987. Numerical estimation of effective permeability in Sand-Shale formations. Water Resources Research 23 (2), 273–286.

Desbarats, A. J., 1988. Estimation of effective permeabilities in the lower stevens formation of the paloma field, san joaquin valley, california. SPE Reservoir Engineering 3 (4), 1301–1307.

Desbarats, A. J., 1992. Spatial averaging of hydraulic conductivity in three-dimensional heterogeneous porous media. Mathematical Geology 24 (3), 249–267.

Deutsch, C. V., 1989. Calculating effective absolute permeability in Sand-Shale sequences. SPE Formation Evaluation 4 (3), 343–348.

Durlofsky, L. J., 1991. Numerical calculations of equivalent grid block permeability tensors for heterogeneous porous media. Water Resources Research 27 (5), 699–708.

Durlofsky, L. J., Jones, R. C., Milliken, W. J., 1997. A nonuniform coarsening approach for the scale-up of displacement processes in heerogeneous porous media. Advances in Water Resources 20 (5-6), 335–347.

Eggleston, J., Rojstaczer, S., 1998. Identification of Large-Scale hydraulic conductivity trends and the influence of trends on contaminant transport. Water Resources Research 34 (9), 2155–2168.

Feehley, C. E., Zheng, C., Molz, F. J., 2000. A dual-domain mass transfer approach for modeling solute transport in heterogeneous aquifers: Application to the macrodispersion experiment (MADE) site. Water Resources Research 36 (9), 2501–2515.

Fernàndez-Garcia, D., Gómez-Hernández, J. J., 2007. Impact of upscaling on solute transport: Traveltimes, scale dependence of dispersivity, and propagation of uncertainty. Water Resources Research 43 (2).

Fernàndez-Garcia, D., Illangasekare, T. H., Rajaram, H., 2005. Differences in the scale dependence of dispersivity and retardation factors estimated from forced-gradient and uniform flow tracer tests in three-dimensional physically and chemically heterogeneous porous media. Water Resources Research 41 (3), W03012.

Fernàndez-Garcia, D., Llerar-Meza, G., Gómez-Hernández, J. J., 2009. Upscaling transport with mass transfer models: Mean behavior and propagation of uncertainty. Water Resources Research 45, W10411.

Flodin, E. A., Durlofsky, L. J., Aydin, A., 2004. Upscaled models of flow and transport in faulted sandstone: boundary condition effects and explicit fracture modelling. Petroleum Geoscience 10 (2), 173–181.

Freeze, R. A., Cherry, J. A., 1979. Groundwater. Prentice-Hall.

Garcia, M., Journel, A. G., Aziz, K., 1992. Automatic grid generation for modeling reservoir heterogeneities. SPE Reservoir Engineering 1992, 278–284.

Gillham, R. W., Robin, M. J. L., Dytynyshyn, D. J., Johnston, H. M., 1984. Diffusion of nonreactive and reactive solutes through fine-grained barrier materials. Canadian Geotechnical Journal 21 (3), 541–550.

Gómez-Hernández, J. J., 1991. A stochastic approach to the simulation of block conductivity values conditioned upon data measured at a smaller scale. Ph.D. thesis, Stanford University.

Gómez-Hernández, J. J., Journel, A. G., 1993. Joint sequential simulation of multi-Gaussian fields. Geostatistics Troia 92 (1), 85–94.

Gómez-Hernández, J. J., Wen, X. H., 1994. Probabilistic assessment of travel times in groundwater modeling. J. of Stochastic Hydrology and Hydraulics 8 (1), 19–56.

Guan, J., Molz, F. J., Zhou, Q., Liu, H. H., Zheng, C., 2008. Behavior of the mass transfer coefficient during the MADE-2 experiment: New insights. Water Resources Research 44, W02423.

Harbaugh, A. W., Banta, E. R., Hill, M. C., McDonald, M. G., 2000. MODFLOW-2000, the U.S. Geological Survey modular ground-water model. English. U.S. Geological Survey, Branch of Information Services, Reston, VA, Denver, CO.

Harvey, C., Gorelick, S. M., 2000. Rate-Limited mass transfer or macrodispersion: Which dominates plume evolution at the macrodispersion experiment (MADE) site? Water Resources Research 36 (3), 637–650.

Hill, M. C., 1990. Preconditioned conjugate gradient 2 (PCG2). A computer program for solving ground-water flow equations: US Geological Survey Water-Resources Investigations Report, 98–4048.

Hill, M. C., Barlebo, H. C., Rosbjerg, D., 2006. Reply to comment by F. Molz et al. on investigating the macrodispersion experiment (MADE) site in columbus, mississippi, using a three-dimensional inverse flow and transport model. Water Resources Research 42 (6), W06604.

Indelman, P., Abramovich, B., 1994. Nonlocal properties of nonuniform averaged flows in heterogeneous media. Water Resour. Res. 30 (12), 3385–3393.

Jourde, H., Flodin, E. A., Aydin, A., Durlofsky, L. J., Wen, X. H., 2002. Computing permeability of fault zones in eolian sandstone from outcrop measurements. AAPG bulletin 86 (7), 1187–1200.

Journel, A. G., Deutsch, C. V., Desbarats, A. J., 1986. Power averaging for block effective permeability. SPE 15128.

LaBolle, E. M., Fogg, G. E., Tompson, A. F., 1996. Random-walk simulation of transport in heterogeneous porous media: Local mass-conservation problem and implementation methods. Water Resources Research 32 (3), 583–593.

Lake, L. W., 1988. The origins of anisotropy. J. of Petr. Techn. April, 395–396.

Li, L., Zhou, H., Gómez-Hernández, J. J., 2010. Steady-state groundwater flow modeling with full tensor conductivities using finite differences. Computers & Geosciences 36 (10), 1211–1223.

Li, L., Zhou, H., Gómez-Hernández, J. J., 2011. Transport upscaling using multi-rate mass transfer in three-dimensional highly heterogeneous porous media. Advances in Water Resources, in press, doi:10.1016/j.advwatres.2011.01.001.

Liu, G., Chen, Y., Zhang, D., 2008. Investigation of flow and transport processes at the MADE site using ensemble kalman filter. Advances in Water Resources 31 (7), 975–986.

Llopis-Albert, C., Capilla, J. E., 2009. Gradual conditioning of non-Gaussian transmissivity fields to flow and mass transport data: 3. application to the macrodispersion experiment (MADE-2) site, on Columbus Air Force Base in Mississippi (USA). Journal of Hydrology 371 (1-4), 75–84.

Matheron, G., 1967. Elements pour une theorie des milieux poreux. Masson et Cie.

Molz, F. J., Zheng, C., Gorelick, S. M., Harvey, C. F., 2006. Comment on Investigating the macrodispersion experiment (MADE) site in columbus, mississippi, using a three-dimensional inverse flow and transport model by Heidi Christiansen Barlebo, Mary C. Hill, and Dan Rosbjerg. Water Resources Research 42 (6), W06603.

Neuman, S. P., Orr, S., 1993. Prediction of steady state flow in nonuniform geologic media by conditional moments: Exact nonlocal formalism, effective conductivities, and weak approximation. Water Resour. Res. 29 (2), 341–364.

Press, W. H., Flannery, B. P., Teukolsky, S. A., Vetterling, W. T., 1988. Numerical recipes in C. Cambridge University Press, Cambridge.

Rehfeldt, K. R., Boggs, J. M., Gelhar, L. W., 1992. Field study of dispersion in a heterogeneous aquifer 3. geostatistical analysis of hydraulic conductivity. Water Resources Research 28 (12), 3309–3324.

Renard, P., Marsily, G. D., 1997. Calculating equivalent permeability: A review. Advances in Water Resources 20 (5-6), 253–278.

Romeu, R. K., Noetinger, B., 1995. Calculation of internodal transmissivities in finite difference models of flow in heterogeneous porous media. Water Resources Research 31 (4), 943–959.

Salamon, P., Fernàndez-Garcia, D., Gómez-Hernández, J. J., 2006. A review and numerical assessment of the random walk particle tracking method. Journal of Contaminant Hydrology 87 (3-4), 277–305.

Salamon, P., Fernàndez-Garcia, D., Gómez-Hernández, J. J., 2007. Modeling tracer transport at the MADE site: the importance of heterogeneity. Water Resources Research 30 (8).

Sánchez-Vila, X., Carrera, J., Girardi, J. P., 1996. Scale effects in transmissivity. Journal of Hydrology 183 (1-2), 1–22.

Sánchez-Vila, X., Guadagnini, A., Carrera, J., 2006. Representative hydraulic conductivities in saturated groundwater flow. Reviews of Geophysics 44 (3).

Schumer, R., Benson, D. A., Meerschaert, M. M., Baeumer, B., 2003. Fractal mobile/immobile solute transport. Water Resources Research 39 (10), 1296.

Vermeulen, P. T. M., Stroet, C. B. M. T., Heemink, A. W., 2006. Limitations to upscaling of groundwater flow models dominated by surface water interaction. Water Resources Research 42 (10), W10406.

Warren, J. E., Price, H. S., 1961. Flow in heterogeneous porous media. Society of Petroleum Engineering Journal 1, 153–169.

Wen, X. H., Durlofsky, L. J., Edwards, M., 2003. Use of border regions for improved permeability upscaling. Mathematical Geology 35 (5), 521–547.

Wen, X. H., Gómez-Hernández, J. J., 1996a. The constant displacement scheme for tracking particles in heterogeneous aquifers. Groundwater 34 (1), 135–142.

Wen, X. H., Gómez-Hernández, J. J., 1996b. Upscaling hydraulic conductivities: An overview. Journal of Hydrology 183 (1-2), ix–xxxii.

Wen, X. H., Gómez-Hernández, J. J., 1998. Upscaling conductivities in cross-bedded formations. Mathematical Geology 30 (2), 181–212.

Zhou, H., Li, L., Gómez-Hernández, J. J., 2010. Three-dimensional hydraulic conductivity upscaling in groundwater modelling. Computers & Geosciences 36 (10), 1224–1235.

Advances in Water Resources, 34(2011) 478-489.

3

Transport Upscaling Using Multi-Rate Mass Transfer in Three-Dimensional Highly Heterogeneous Media

Abstract

A methodology for transport upscaling of three-dimensional highly heterogeneous formations is developed and demonstrated. The overall approach requires a prior hydraulic conductivity upscaling using an interblock-centered full-tensor Laplacian-with-skin method followed by transport upscaling. The coarse scale transport equation includes a multi-rate mass transfer term to compensate for the loss of heterogeneity inherent to all upscaling processes. The upscaling procedures for flow and transport are described in detail and then applied to a three-dimensional highly heterogeneous synthetic example. The proposed approach not only reproduces flow and transport at the coarse scale, but it also reproduces the uncertainty associated with the predictions as measured by the ensemble variability of the breakthrough curves.

3.1 Introduction

Upscaling flow and transport has been disregarded by some on the basis that it is not needed because our computers are capable of handling larger and larger numerical models. However, we know by experience that there will always be a discrepancy between the scale at which we can characterize the medium, and the scale at which we can run our numerical codes. This discrepancy renders upscaling necessary in order to transfer the information collected at the measurement scale into a coarser scale better suited for numerical modeling.

In the last decades, many reviews have been published dealing with upscaling but mostly focusing on hydraulic conductivity upscaling (e.g., Wen and Gómez-Hernández, 1996b; Renard and Marsily, 1997; Sanchez-Vila et al., 2006). In comparison with the effort devoted to the upscaling of hydraulic conductivity, less attention has been paid to upscaling for solute transport modeling. For example, Dagan (1994) noted that hydraulic conductivity upscaling induces a loss of information and advised to compensate for this loss by splitting the solute plume into subplumes with effective dispersivities derived from stochastic theory. Rubin et al. (1999) developed an upscaling method to derive effective block-scale dispersivities using a perturbation method, which accounts for the loss of subgrid variability in the upscaled numerical model. These two approaches are based on analytical techniques, which have a limited range of application because of their underlying assumptions. Numerical methods, on the contrary, are more general, since they are not restricted by the geometry of the domain, the type of boundary conditions, or the degree of heterogeneity. Scheibe and Yabusaki (1998) examined the impact of hydraulic conductivity upscaling using the power-averaging method with different exponents (Journel et al., 1986). They found that although flows and heads can be preserved after upscaling the hydraulic conductivities, the discrepancy on transport predictions is substantial. Cassiraga et al. (2005) applied the simple-Laplacian technique (Wen and Gómez-Hernández, 1996b) to upscale hydraulic conductivity and evaluated the impact of upscaling on solute transport for various degrees of heterogeneous media in two dimensions. They concluded that the prediction of solute transport at the coarser scale will provide reasonably good estimates of the early particle arrival times but will largely underestimate the late travel times; the explanation for this behavior was the existence and connectedness of extreme-valued hydraulic conductivities at the fine scale, which are lost after upscaling. To overcome this inability, Fernàndez-Garcia and Gómez-Hernández (2007) extended this study and introduced an enhanced block dispersion tensor to compensate for the loss of information. They found that, with this approach the median travel time could be reproduced but that the tails of the breakthrough curves were largely underestimated. They suggested that a mass transfer process should be introduced at the coarse scale

to make up for the information at the small scale that cannot be resolved by the upscaled model in heterogenous media. Fernàndez-Garcia et al. (2009) examined the use of a mass transfer process with different memory functions as part of the constitutive transport equation at the coarse scale, in conjunction with hydraulic conductivity upscaling with the simple-Laplacian technique in 2D. The results showed that considering a double-rate or a truncated power-law mass transfer model at the coarse scale was enough to properly describe the ensemble average behavior of the main features associated with the breakthrough curves. However, the uncertainty associated with the predictions is underestimated after upscaling due to the lack of memory in space during the upscaling process.

It is important to note that the use of a mass transfer process as part of the constitutive equation for transport at the coarse scale model has also been proposed by Guswa and Freyberg (2002), Zinn and Harvey (2003), Willmann et al. (2008) and Frippiat and Holeyman (2008). However, these studies mainly focus on upscaling up to a completely homogeneous aquifer. Guswa and Freyberg (2002) conclude that a mass exchange term is needed only if the equivalent hydraulic conductivity is larger than the geometric mean of the underlying conductivity field, Zinn and Harvey (2003) suggest that a mass exchange is necessary and conclude that the multi-rate model should better compensate for the loss of resolution than the single-rate model, and later Fernàndez-Garcia et al. (2009) demonstrated that, indeed, the double-rate model and the power-law mass transfer model outperform the single-rate model for upscaling purposes.

In the current work, we extend to 3D the study by Fernàndez-Garcia et al. (2009), who proposed a transport upscaling method using a multi-rate mass transfer. We also introduce an elaborated interblock Laplacian-with-skin hydraulic conductivity upscaling approach, for optimal reproduction of the flows at the coarse scale. Although the extension of the methodology to three-dimensions may appear as conceptually straightforward, we have found that it is necessary to make some adjustments to efficiently reproduce the breakthrough curves. Additionally, unlike most studies that focused primarily on a single realization analysis, the present study analyzes the upscaling at the ensemble level in order to analyze also how prediction uncertainty upscales.

The outline of this paper is as follows. We first introduce the flow and transport governing equations at two different support scales. Next, the importance of using an interblock Laplacian-with-skin hydraulic conductivity upscaling is illustrated, with emphasis on the numerical implementation in three-dimensions. We then describe the transport upscaling with mass transfer in two dimensions and discuss the modifications of the method for its application in three-dimensions. Finally, numerical tests demonstrate the accuracy and efficiency of the method. We end with a discussion on the weaknesses

and strengths of the proposed approach, with an indication of avenues for improvement.

3.2 Methodology

3.2.1 Background

Fine scale equations

At the fine scale, denoted herein by the superscript f, under steady-state flow conditions and in the absence of sinks and sources, the flow equation of an incompressible fluid in saturated porous media in a Cartesian coordinate system can be obtained by combining the continuity equation and Darcy's law (Bear, 1972):

$$\nabla\cdot\left[\mathbf{K}^f(\mathbf{x}^f)\nabla h^f(\mathbf{x}^f)\right] = 0 \tag{3.1}$$

where $h^f[L]$ is the piezometric head; $\mathbf{K}^f[LT^{-1}]$ is a symmetric positive-definite rank-two tensor; $\mathbf{x}^f$ represents the fine scale coordinates.

Similarly, using the solute mass conservation equation and assuming that Fick's law is appropriate at the local scale, the three-dimensional advective-dispersive equation (ADE) for solute transport is often written as (Freeze and Cherry, 1979):

$$\phi^f\frac{\partial C^f(\mathbf{x}^f,t)}{\partial t} = -\nabla\cdot\left[\mathbf{q}^f(\mathbf{x}^f)C^f(\mathbf{x}^f,t)\right] + \nabla\cdot\left[\phi^f\mathbf{D}^f\nabla C^f(\mathbf{x}^f,t)\right] \tag{3.2}$$

where $C^f[ML^{-3}]$ is the dissolved concentration of solute in the liquid phase; ϕ^f[dimensionless] is the porosity; $\mathbf{q}^f[LT^{-1}]$ is the Darcy velocity given by $\mathbf{q}^f(\mathbf{x}) = -\mathbf{K}^f(\mathbf{x})\nabla h^f(\mathbf{x})$; $\mathbf{D}^f[L^2T^{-1}]$ is the local hydrodynamic dispersion coefficient tensor with eigenvalues (associated with the principal axes, which are parallel and perpendicular to the direction of flow) given by (Burnett and Frind, 1987):

$$D_i^f = D_m + \alpha_i\frac{|\mathbf{q}^f|}{\phi^f} \tag{3.3}$$

where α_i are the local dispersivity coefficients, more specifically, α_L, α_T^H and α_T^V are, respectively, the longitudinal dispersivity coefficient and the transverse dispersivity coefficient in the directions parallel and orthogonal to flow, and D_m is the effective molecular diffusion coefficient.

The fine scale transport equation (3.2) is only valid if the Fickian assumption is satisfied at the small scale. Here, we assume that the ADE is capable

of reproducing the tracer spreading at the fine scale. Salamon et al. (2007) at the MADE site and Riva et al. (2008) at the Lauswiesen site have shown that for cases in which, apparently, the transport spreading does not look Fickian at the macroscopic scale, the ADE equation is applicable if the small-scale variability of hydraulic conductivity is properly modeled at the smallest scale possible.

Coarse scale equations

There are two main approaches to get the coarse scale equations. On one hand, those who work analytically from the fine scale equations and apply regularization techniques to derive the equations that would express the state of the system on a larger scale. Examples of these works can be found in Cushman (1984); Neuman and Orr (1993); Indelman and Abramovich (1994); Guadagnini and Neuman (1999). On the other hand, those who empirically postulate the coarse scale expression (after the fine scale one) and then try to determine the parameter values of the postulated coarse scale expressions. Examples of these works can be found in Rubin and Gómez-Hernández (1990); Gómez-Hernández and Wen (1994); Gómez-Hernández and Rubin (1990); Guswa and Freyberg (2002). In the first approach, the authors generally obtain equations which are nonlocal, that is, the parameters associated to a given block at the coarse scale depend not only on the fine scale parameters values within the block, but also on the values outside the block. This fact is recognized by some authors using the second approach when the coarse block parameters are computed on local flow and/or transport models which extend beyond size of the block being upscaled, so that the influence of the nearby cells is captured Wen and Gómez-Hernández (1996b). We have opted, in this paper, for the second approach.

At the coarse scale, denoted herein by the superscript c, the flow equation is taken to have the same expression as the fine scale equation, but with $\mathbf{K}^f$ replaced by an upscaled hydraulic conductivity tensor $\mathbf{K}^c$:

$$\nabla\cdot\left[\mathbf{K}^c(\mathbf{x^c})\nabla h^c(\mathbf{x^c})\right] = 0 \tag{3.4}$$

where $h^c[L]$ designates the coarse scale piezometric head, and $\mathbf{x}^c$ refers to the coarse scale coordinates.

In earlier studies of transport at the coarse scale, only upscaling of the flow controlling parameters was performed (e.g., Scheibe and Yabusaki, 1998; Cassiraga et al., 2005; Li et al., 2010a). That is, upscaled $\mathbf{K}^c$ values were derived, and the same advection dispersion equation was used both at the fine and coarse scales. However, recent findings have demonstrated that the transport equation to be used at the coarse scale should include an enhanced dispersion tensor and a fictitious mass exchange process as a proxy to represent the mass

transfer processes taking place within the coarse block and largely associated with the within-block heterogeneity (e.g., Zinn and Harvey, 2003; Fernàndez-Garcia and Gómez-Hernández, 2007; Willmann et al., 2008; Fernàndez-Garcia et al., 2009).

We have chosen the multi-rate mass transfer model (MRMT) (Haggerty and Gorelick, 1995; Carrera et al., 1998) as the mass exchange expression to be used at the coarse scale. Alternative models such as the continuous time random walk (Berkowitz and Scher, 1998) or fractional derivatives (Benson et al., 2000) could be used as well. Fernàndez-Garcia et al. (2009) discussed the use of the MRMT for upscaling purposes in 2D, and its versatility to treat complex heterogeneities; furthermore, it was successfully applied at the MADE aquifer by Feehley et al. (2000) and at the Lauswiesen site by Riva et al. (2008). Many transport codes based on the MRMT model (e.g., Zheng and Wang, 1999; Carrera et al., 1998; Salamon et al., 2006a; Silva et al., 2009) indicate the great potential of this approach.

The upscaled transport equation, including the MRMT model, can be described by the following governing equation (Haggerty and Gorelick, 1995; Carrera et al., 1998):

$$\phi_m^c \frac{\partial C_m^c(\mathbf{x}^c,t)}{\partial t} = -\nabla\cdot\left[\mathbf{q}^c(\mathbf{x}^c)C_m^c(\mathbf{x}^c,t)\right] + \nabla\cdot\left[\phi_m^c\mathbf{D}^c\nabla C_m^c(\mathbf{x}^c,t)\right] - \phi_m^c\Gamma(\mathbf{x}^c,t) \tag{3.5}$$

where ϕ_m^c [dimensionless] defines the pore volume fraction of the mobile domain; $C_m^c[ML^{-3}]$ is the solute concentration in the mobile region of the coarse block; $\mathbf{q}^c[LT^{-1}]$ is the Darcy velocity derived from the upscaled hydraulic conductivity; $\mathbf{D}^c[L^2T^{-1}]$ is an enhanced block dispersion tensor, which includes the fine scale local hydrodynamic dispersion (α_i) and a macrodispersivity term (A_i) (Fernàndez-Garcia and Gómez-Hernández, 2007; Fernàndez-Garcia et al., 2009):

$$D_i^c = D_m + (\alpha_i + A_i)\frac{|\mathbf{q}^c|}{\phi_m^c} \tag{3.6}$$

where D_i^c are the eigenvalues of $\mathbf{D}^c$ associated with the principal axes, which are parallel and perpendicular to the flow direction. The additional mass exchange term $\Gamma(\mathbf{x}^c,t)$ $[ML^{-3}T^{-1}]$ can be expressed in terms of mobile concentrations by using a convolution product with a memory function $g(\mathbf{x}^c,t)$ $[T^{-1}]$ (Carrera et al., 1998; Haggerty et al., 2000):

$$\begin{aligned}\Gamma(\mathbf{x}^c,t) &= \beta(\mathbf{x}^c)\int_0^t g(\mathbf{x}^c,\tau)\frac{\partial C_m^c(\mathbf{x}^c,t-\tau)}{\partial\tau}d\tau \\ g(\mathbf{x}^c,t) &= \int_0^\infty \alpha f(\mathbf{x}^c,\alpha)e^{-\alpha t}d\alpha\end{aligned} \tag{3.7}$$

where $\beta(\mathbf{x}^c)$ [dimensionless] is the so-called capacity ratio; α $[T^{-1}]$ is a continuous positive variable representing the multiple mass transfer rate coefficients, and $f(\mathbf{x}^c, \alpha)$ $[T]$ denotes the probability density function of the mass transfer rate coefficients. Therefore, once $f(\mathbf{x}^c, \alpha)$ is given, the MRMT model equation (3.5) can be numerically solved. It is worth emphasizing that, the macrodispersivity term A_i and the mass transfer model are introduced as fictitious processes to make up for the presence of low and high conductivity zones which are smeared out after upscaling, and for the diffusive-like process occurring within the coarse block due to the heterogeneity. In this respect, it is consistent with Zinn and Harvey (2003), Willmann et al. (2008), and Riva et al. (2008) who used the MRMT model to account for the subgrid heterogeneity in the upscaled transport model.

3.2.2 Hydraulic conductivity upscaling using the Laplacian-with-skin method

In contrast with the previous studies by Fernàndez-Garcia and Gómez-Hernández (2007) and Fernàndez-Garcia et al. (2009) that used the simple-Laplacian scheme to compute the block equivalent conductivities in two dimensions, here, we use a more sophisticated interblock Laplacian-with-skin three-dimensional full-tensor hydraulic conductivity upscaling technique, which is an extension of an earlier two-dimensional approach (Gómez-Hernández, 1991). In essence, the Laplacian-with-skin upscaling scheme is an improved version of the simple-Laplacian approach. With regard to the simple-Laplacian method, Li et al. (2010a) have already demonstrated that it fails to reproduce interblock flow at the coarse scale and further underestimates contaminant spread at the MADE site. The major disadvantage of the simple-Laplacian approach is the assumption that the upscaled conductivity tensor is diagonal. For the details on the different upscaling processes, the reader is referred to the work by Wen and Gómez-Hernández (1996b), or more recently by Li et al. (2010a).

Gómez-Hernández (1991) presented the Laplacian-with-skin approach recognizing the nonlocal nature of the upscaled conductivity tensor. The skin (a ring of cells surrounding the block) is used to approximate the actual boundary conditions around the block being upscaled without having to solve the flow problem for the entire aquifer (as previous authors had done, i.e., White and Horne (1987)). For each block being upscaled, the algorithm consists of three steps: (a) isolate the block, plus a surrounding ring of cells (referred to as the skin), and solve a local flow problem numerically for a set of boundary conditions inducing fluxes in different directions across the block; (b) for each boundary condition the spatially-averaged flow and gradient within the block are calculated; (c) and then, the components of the upscaled hydraulic conductivity tensor are determined by solving the following overdetermined

system of linear equations by a standard least squares procedure:

$$\begin{bmatrix} \langle \partial h/\partial x \rangle_1 & \langle \partial h/\partial y \rangle_1 & \langle \partial h/\partial z \rangle_1 & 0 & 0 & 0 \\ 0 & \langle \partial h/\partial x \rangle_1 & 0 & \langle \partial h/\partial y \rangle_1 & \langle \partial h/\partial z \rangle_1 & 0 \\ 0 & 0 & \langle \partial h/\partial x \rangle_1 & 0 & \langle \partial h/\partial y \rangle_1 & \langle \partial h/\partial z \rangle_1 \\ \langle \partial h/\partial x \rangle_2 & \langle \partial h/\partial y \rangle_2 & \langle \partial h/\partial z \rangle_2 & 0 & 0 & 0 \\ 0 & \langle \partial h/\partial x \rangle_2 & 0 & \langle \partial h/\partial y \rangle_2 & \langle \partial h/\partial z \rangle_2 & 0 \\ 0 & 0 & \langle \partial h/\partial x \rangle_2 & 0 & \langle \partial h/\partial y \rangle_2 & \langle \partial h/\partial z \rangle_2 \\ \cdots & \cdots & \cdots & \cdots & \cdots & \cdots \\ \langle \partial h/\partial x \rangle_n & \langle \partial h/\partial y \rangle_n & \langle \partial h/\partial z \rangle_n & 0 & 0 & 0 \\ 0 & \langle \partial h/\partial x \rangle_n & 0 & \langle \partial h/\partial y \rangle_n & \langle \partial h/\partial z \rangle_n & 0 \\ 0 & 0 & \langle \partial h/\partial x \rangle_n & 0 & \langle \partial h/\partial y \rangle_n & \langle \partial h/\partial z \rangle_n \end{bmatrix} \cdot \begin{bmatrix} K^c_{xx} \\ K^c_{xy} \\ K^c_{xz} \\ K^c_{yy} \\ K^c_{yz} \\ K^c_{zz} \end{bmatrix}$$

$$= - \begin{bmatrix} \langle q_x \rangle_1 \\ \langle q_y \rangle_1 \\ \langle q_z \rangle_1 \\ \langle q_x \rangle_2 \\ \langle q_y \rangle_2 \\ \langle q_z \rangle_2 \\ \cdots \\ \langle q_x \rangle_n \\ \langle q_y \rangle_n \\ \langle q_z \rangle_n \end{bmatrix} \tag{3.8}$$

where q_x q_y q_z are the components of the Darcy flux $\mathbf{q}$ obtained from the local solution of the flow equation; angle brackets indicate spatial averaging within the block; subscript n denotes an index referring to the different boundary conditions; $K^c_{xx} \cdots K^c_{zz}$ are the components of the upscaled equivalent conductivity $\mathbf{K}^c$. Note that the requirement of symmetry is enforced implicitly (Zhou et al., 2010) in this system of equations.

Although we are aware of the works by Zijl and Stam (1992) and Bierkens and Gaast (1998) in which they argue that the upscaled conductivity tensor may be non-symmetric, we prefer to maintain symmetry at the block level to preserve its physical meaning: that opposite gradient vectors should induce opposite specific discharge vectors. Likewise, we enforce positive definiteness, since it is non-physical that the scalar product of the gradient vector and the specific discharge be positive (flow never goes upgradient). However, the approach would be equally applicable without imposing symmetry on the upscaled conductivity tensor.

Since we plan to solve the flow equation by finite differences, a further improvement in the hydraulic conductivity upscaling consists in computing the upscaled hydraulic conductivity tensors at the block interfaces rather than at block centers. This is done by isolating an aquifer volume centered at the in-

terface, plus a skin, prior to solving the local flow problem (Zhou et al., 2010). In fact, this suggestion of an upscaled hydraulic conductivity based on the interface agrees with the works of Chen et al. (2003), Wen et al. (2005), and He and Durlofsky (2006), who already pointed out that the upscaling of transmissibility (the equivalent to interblock conductivity in petroleum engineering) provided a more accurate coarse scale result than permeability upscaling.

3.2.3 Transport upscaling using mass transfer

Both in petroleum engineering and in subsurface hydrogeology, many studies have demonstrated that hydraulic conductivity upscaling is not enough to reproduce transport at the coarse scale (e.g., Scheibe and Yabusaki, 1998; Chen et al., 2003; Fernàndez-Garcia and Gómez-Hernández, 2007). We have adopted the method proposed by Fernàndez-Garcia et al. (2009) to address this problem, whereby the coarse scale transport equation includes a mass transfer term to compensate for the loss of information at the coarse scale. The problem we face is replacing a heterogeneous block within which the heterogeneity induces solute dispersion by a homogeneous block with enhanced dispersion and an associated multi-rate mass transfer process, the parameters of which have to be determined to induce the same solute dispersion induced by the within block heterogeneity. To this extent mass transport is solved at the fine scale using a particle tracking random walk approach and the residence times of the particles within the block are computed resulting in a cumulative distribution of residence times $F_\tau(\tau)$. The objective of transport upscaling is to determine the multi-rate mass transfer parameter resulting in the same residence time distribution. This is accomplished by a curve fitting process making use of an approximate solution for the residence time distribution of the multi-rate mass transfer transport equation in 1D, $F^*_\tau(\tau)$. The Laplacian transform of $F^*_\tau(\tau)$ is given by (Haggerty and Reeves, 2002; Fernàndez-Garcia et al., 2009):

$$\widetilde{F}^*_\tau(p) \approx \frac{1}{p}\exp\left[L_b\left(\frac{v_m}{2D^c_\ell} - \sqrt{\frac{v_m^2}{4D^{c2}_\ell} + \frac{\widetilde{\psi}(p)}{D^c_\ell}}\right)\right] \tag{3.9}$$

where $L_b[L]$ is the mean travel displacement of solute mass particles; the mobile velocity $v_m[LT^{-1}]$ is defined by:

$$v_m = \frac{\|\mathbf{q}^c\|}{\phi^c_m} \qquad \phi^c_m = \frac{\phi^c_e}{1+\beta} \tag{3.10}$$

and $\widetilde{\psi}(p)$ is defined by:

$$\widetilde{\psi}(p) = p + \beta\int_0^\infty f(\alpha)\frac{p\alpha}{p+\alpha}d\alpha \tag{3.11}$$

p is the Laplace transform variable; $f(\alpha)$ is the density function given in terms of the mass transfer coefficients, the expression of which depends on the multi-rate process considered. For instance, for the case of the double-rate mass transfer process it is:

$$f(\alpha) = \frac{\beta_1}{\beta}\delta(\alpha - \alpha_1) + \frac{\beta_2}{\beta}\delta(\alpha - \alpha_2) \tag{3.12}$$

with

$$\beta_1 + \beta_2 = \beta \tag{3.13}$$

where β_1 and β_2 [dimensionless] are the capacities of each immobile phase; α_1 and α_2 $[T^{-1}]$ are the transfer rates in each immobile phase and $\delta(\cdot)$ is the Dirac delta.

We also found that, in order to preserve the mean travel time of the plume to each control plane, it was not enough to match the particle residence time distributions for each block but that it was necessary to make a local upscaling of the effective porosity. For our purpose it was sufficient to define a coarse scale effective porosity ϕ_e^c [dimensionless] piecewise in between each pair of control planes as follows:

$$\phi_{e,i}^c = \frac{\bar{\tau}_{cp,i}^f - \bar{\tau}_{cp,i-1}^f}{\bar{\tau}_{cp,i}^c - \bar{\tau}_{cp,i-1}^c} \qquad i = 1, 2 \cdots n_{cp} \tag{3.14}$$

where $\bar{\tau}_{cp,i}^f$ is the mean travel time at the i control plane computed at the fine scale with porosity ϕ_f; $\bar{\tau}_{cp,i}^c$ is the average travel time computed with unit porosity at the coarse scale at the i^{th} control plane, and n_{cp} is the number of control planes. This estimated effective porosity is an artificial numerical value which also compensates for the loss of information in the upscaling process. This need of upscaling the porosity to preserve the mean travel times is also reported by Zhang (2004) and Fernàndez-Garcia et al. (2009).

For each block, once the particle residence time distribution has been obtained numerically, the model-independent nonlinear parameter estimation program, PEST (Doherty, 2004), is used to determine the best set of mass transfer parameters in equation (3.9) that matches the distribution $F_\tau(\tau)$. For this purpose, a penalty function is established as follows:

$$P(\mathbf{\Theta}) = \xi_1[\bar{\tau} - \bar{\tau}^*(\mathbf{\Theta})]^2 + \xi_2[\sigma_\tau^2 - \sigma_\tau^*(\mathbf{\Theta})^2]^2 + \sum_{i=1}^{n_q} \omega_i \left[F_\tau(\tau_i) - F_\tau^*(\tau_i, \mathbf{\Theta})\right]^2 \tag{3.15}$$

where $\mathbf{\Theta}$ represents a vector with the transport parameters being estimated (we have noted explicitly the dependence of the distribution function on $\mathbf{\Theta}$), $\bar{\tau}$ is the average residence time computed from the particle distribution, $\bar{\tau}^*(\mathbf{\Theta})$

is the average residence time of $F^*_\tau(\tau)$, which can be derived from equation (3.9) as (Lawrence et al., 2002; Fernàndez-Garcia et al., 2009):

$$\bar{\tau}^*(\mathbf{\Theta}) = \frac{L_b}{v_m}(1+\beta) \tag{3.16}$$

${\sigma_\tau}^2$ is the variance of residence time computed from the particle distribution, $\sigma^*_\tau(\mathbf{\Theta})^2$ is the variance of the distribution, which can be derived from equation (3.9) as:

$$\sigma^*_\tau(\mathbf{\Theta})^2 = \frac{2D^c_\ell}{v^3_m}(1+\beta)^2 L_b + \frac{2L_b}{v_m}\beta\int_0^\infty \frac{f(\alpha)}{\alpha}d\alpha \tag{3.17}$$

n_q is the number of particles that travel through the block, and ξ_1, ξ_2 and ω_i are weight coefficients, which in this case are all set to 1.

The PEST code has to evaluate multiple times expression (3.9) for different sets of the mass transfer coefficients being determined; for this purpose we have used the code STAMMT-L (Haggerty and Reeves, 2002).

3.3 Numerical Evaluation

3.3.1 Model Configuration

Consider a synthetic three-dimensional confined aquifer under a uniform, natural-gradient flow condition, as shown in Figure 3.1, it will be the reference. A set of 30 hydraulic conductivity fields was generated using the code GCOSIM3D (Gómez-Hernández and Journel, 1993). The field is parallelepipedic with dimensions of $x = 200$ m, $y = 140$ m, and $z = 70$ m and a discretization of $\Delta x = \Delta y = \Delta z = 1$ m. Only the inner domain consisting of $180 \times 120 \times 60$ cells will be uniformly upscaled to $18 \times 12 \times 12$ blocks, resulting in an overall scale-up factor of 500. The following standardized exponential semivariogram was used for the simulation of the isotropic hydraulic conductivity field:

$$\frac{\gamma_x(r)}{\sigma^2_x} = 1 - \exp\left[-\frac{r}{\lambda_x}\right] \tag{3.18}$$

where λ_x $[L]$ is the range with a value of 12 m in all the directions and r $[L]$ is the directional lag distance. The variance σ^2_x of the natural logarithm of hydraulic conductivity is 4.0 (similar to the one found, for instance, at the MADE site (Rehfeldt et al., 1992)), to represent highly heterogeneous media. The aquifer was modeled with constant head boundaries at $x = 0$ m and $x = 180$ m and with no-flow boundaries at the remaining model faces. The average hydraulic gradient induced by the constant head boundaries is 0.01. The porosity is assumed constant and equal to 0.3.

At the fine scale, the five-point block-centered finite-difference groundwater flow model MODFLOW 2000 (Harbaugh et al., 2000) was employed to solve the flow equation (3.1). The interface velocities were calculated, and then utilized in the random walk particle tracking code RW3D (Fernàndez-Garcia et al., 2005; Salamon et al., 2006b), which was used to solve the fine scale transport equation (3.2). In this approach, the evolution in time of each particle is comprised of a deterministic component, which depends only on the local velocity field, and a superposed Brownian motion responsible for dispersion. A hybrid scheme is used for the velocity interpolation which provides local as well as global divergence-free velocity fields within the solution domain. Meanwhile, a continuous dispersion tensor field provides good mass balance at grid interfaces of adjacent cells with contrasting hydraulic conductivities (LaBolle et al., 1996; Salamon et al., 2006b). Furthermore, in contrast to the common constant-time scheme used in random walk modeling, a constant-displacement scheme (Wen and Gómez-Hernández, 1996a), which modifies automatically the time step size for each particle according to the local velocity, is employed in order to decrease computational effort.

At the coarse scale, the nineteen-point block-centered finite-difference groundwater model FLOWXYZ (Li et al., 2010b) was employed to solve the flow equation (3.4). The most remarkable characteristic of this forward flow simulator is the capacity to deal with full conductivity tensors defined at block interfaces. Hydraulic conductivity tensors are defined at the block interfaces eliminating the need to average conductivity tensors at adjacent blocks to approximate their values at the interfaces. This scheme has been shown to perform better than the MODFLOW LVDA package (Li et al., 2010b), and has been successfully applied in other studies (e.g., Zhou et al., 2010; Li et al., 2010a). Again, the RW3D was used to solve the coarse scale multi-rate transport equation (3.5) based on the methodology presented by Salamon et al. (2006a). Mass transfer processes are efficiently incorporated into the particle tracking algorithm by switching the state of the particle between mobile/immobile states according to appropriate transition probabilities.

For the sake of simplicity, we neglect dispersion, and only consider advection, at the fine scale, i.e., $D_m = 0$ and $\alpha_i = 0$. A total of 20000 particles (a number that we have tested yields stable transport predictions for this specific case) randomly distributed in a rectangular-shaped area of 60 m width and 30 m height located orthogonal to the principal flow direction in the plane at $x = 20$ m were released at time $t = 0$. The variable time step was computed on the basis of a grid Courant number of 0.01. A unit mass was assigned to each particle. Control planes are located within the aquifer to measure the mass arrival at 10 m intervals (see Figure 3.2).

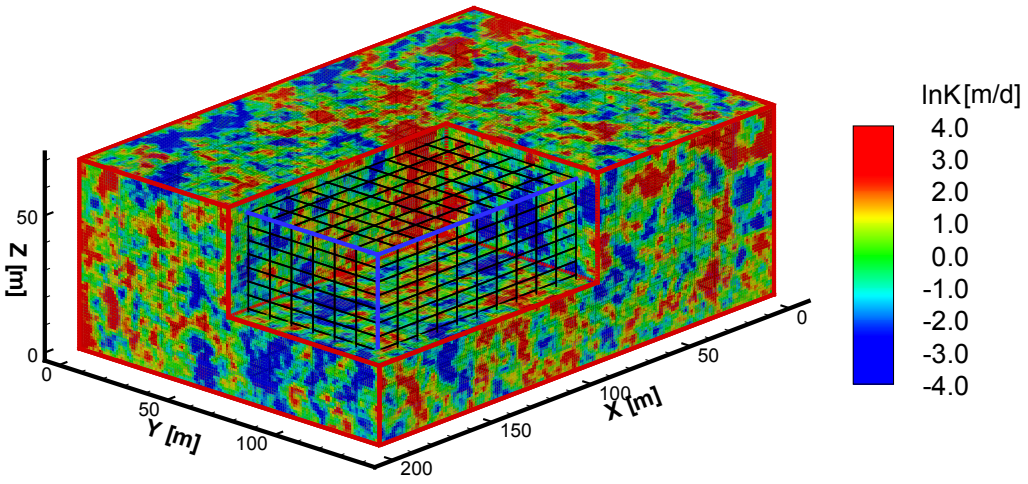

Figure 3.1: A realization of reference lnK field (σ^2_{lnK}=4.0) overlaid with the discretization of the numerical model at the coarse scale.

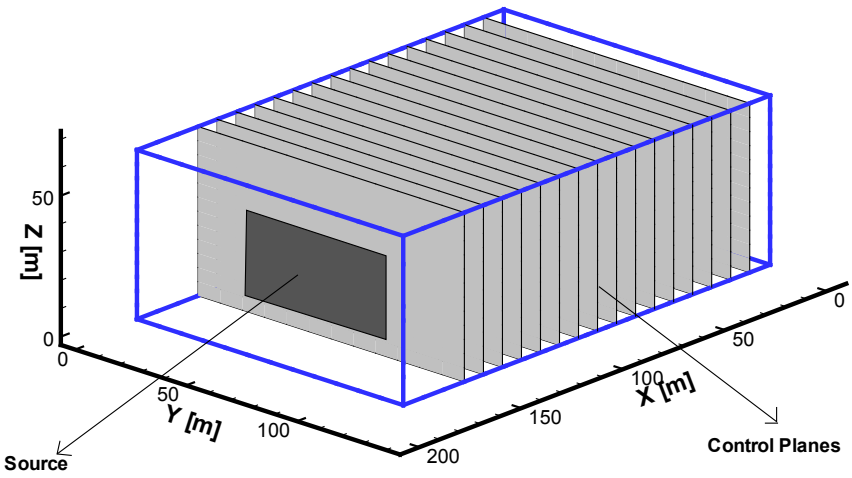

Figure 3.2: Sketch of transport simulations. The shaded rectangle located in the upstream zone delineates the initial particle injection zone. Control planes are also shown for measuring the mass fluxes.

3.3.2 Flow upscaling results

Prior to transport upscaling we wish to demonstrate the effectiveness and robustness of the interblock Laplacian-with-skin approach to flow upscaling as compared with other methods, such as the block-centered simple-Laplacian approach, the interblock-centered simple-Laplacian approach, and the Landau-Lifshitz-Matheron conjecture for 3D isotropic media (Renard and Marsily, 1997). For this purpose a single realization is analyzed. Our goal, as that of any upscaling exercise, is to generate a heterogeneous coarse model which predicts the interblock flows as close as possible to those derived from a fine scale simulation. We will focus on interblock flow reproduction and disregard the analysis of piezometric heads, since the errors in piezometric head reproduction are always much smaller.

We compare the coarse scale flows obtained after solving the flow equation with the upscaled conductivities, with the reference flows obtained from the solution of the flow equation at the fine scale. The mismatch between these two values is measured by a Relative Bias defined as:

$$RB = \left(\frac{1}{N} \sum_{N} \frac{\left| q_x^f - q_x^c \right|}{q_x^f} \right) \cdot 100, \tag{3.19}$$

where N is the number of interblocks used to compute the relative bias; q_x^f is the specific discharge computed on the fine scale solution, and q_x^c represents the specific discharge from the coarse scale simulation. Because the x flow direction plays an important role in this case, the flow comparisons mainly focus on this direction. Similar results (not displayed) are obtained for the orthogonal directions. Also, as noted by Vermeulen et al. (2006), the boundary conditions have an impact on the performance of upscaling for the nearby blocks, for this reason, and in order to filter out this impact in the comparison of the different methods, only the inner $14 \times 8 \times 10$ blocks are used to calculate the relative bias.

Figure 3.3 shows the cross-plots between the flows computed on the fine scale (reference values) and the ones computed on the coarse scale for several upscaling approaches. Results indicate: (1) interblock upscaling is better than block-centered upscaling, since it avoids the additional averaging process within the coarse flow simulator needed to approximate the interblock values (31% relative bias using block-centered simple-Laplacian to 23% relative bias using interblock-centered simple-Laplacian, see Figures 3.3A and 3.3B). This result agrees with previous finding (Li et al., 2010b). (2) Compared with the simple-Laplacian method, the Laplacian-with-skin significantly improves the coarse scale results (23% relative bias using interblock simple-Laplacian to 9% relative bias using interblock Laplacian-with-skin, see Figure 3.3B and 3.3D);

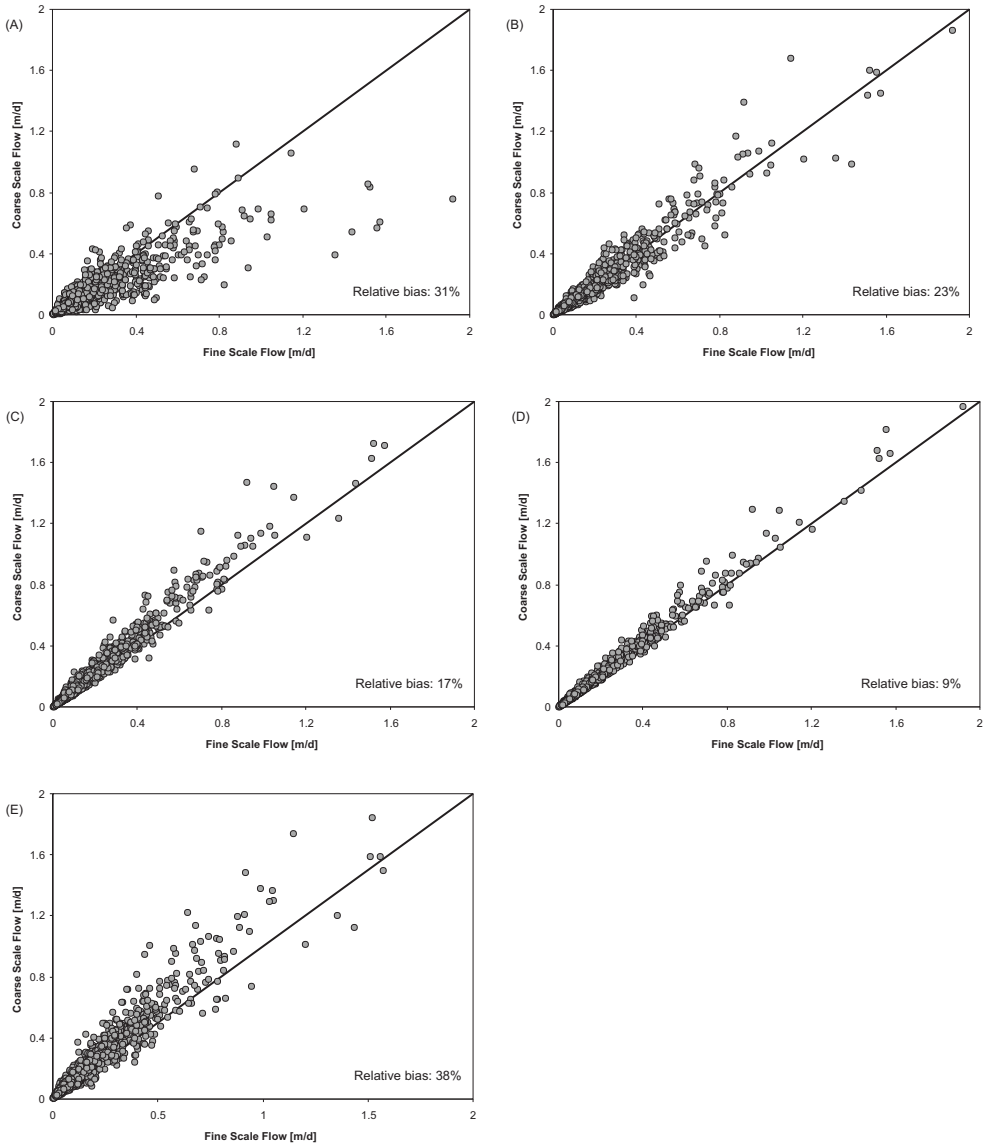

Figure 3.3: Flow comparisons at the fine and coarse scales on a single realization. (A) the block-centered simple-Laplacian method; (B) the interblock-centered simple-Laplacian method; (C) the interblock-centered full-tensor Laplacian-with-skin (skin size 3 m); (D) the interblock Laplacian-with-skin (skin size: 10 m along rows, 10 m along columns and 5 m along layers); (E) Landau-Lifshitz-Matheron conjecture for 3D isotropic media.

the main reasons for these results are the use of a full hydraulic conductivity tensor to represent the interblock property and the use of a skin to approximate the "real" boundary conditions around the interblock, in contrast with the simple-Laplacian approach which seeks a diagonal hydraulic conductivity tensor with boundary conditions directly at the block sides. (3) The significance of the skin size is evident as it was already pointed out by Zhou et al. (2010) (17% relative bias using interblock Laplacian with a skin size of 3 m, down to 9% relative bias using interblock Laplacian with a skin of 10 m in the x and y directions and 5 m in the z direction, see Figures 3.3C and 3.3D). The high variance of hydraulic conductivity, as is the case in this example with σ^2_{lnk}=4.0, can result in local flows departing significantly from the average flow direction (along the x axis in this case), in which case the use of a full tensor and the skin size is more important. (4) For a mild isotropic heterogeneous field, the Landau-Lifshitz-Matheron conjecture (a close expression that gives the upscaled conductivity as a p-norm of the fine scale conductivities within the block, in which p only depends on the dimensionality of the problem) performs well (Desbarats, 1992). However, when the global variance increases, the conjecture loses its accuracy and it is better to resort to the numerical flow experiments as is the case here, i.e., the Laplacian-with-skin method (38% relative bias using conjecture to 9% relative bias using interblock Laplacian-with-skin of 10 m along rows, 10 m along columns and 5 m along layers), see Figure 3.3D and 3.3E).

In short, the best reproduction of the fine scale flows is given by the interblock-centered Laplacian-with-skin approach. This scheme is retained for the subsequent transport upscaling.

3.3.3 Transport upscaling results

We examined two transport upscaling approaches using the same set of upscaled hydraulic conductivities obtained in section 3.3.2; in the first one, we only model advection using the velocities from the coarse scale flow simulation, and in the second one, we include the multi-rate term in the transport equation at the coarse scale and perform transport upscaling to determine enhanced macrodispersion coefficients, upscaled effective porosities and the parameters of the multi-rate transfer model. The multi-rate model estimates the mass transfer parameters as described in section 3.2.3. It should be noted that we do not make the comparison with an intermediate model including only enhanced macrodispersion coefficients, since it has already been shown (e.g., Zinn and Harvey, 2003; Fernàndez-Garcia and Gómez-Hernández, 2007; Frippiat and Holeyman, 2008; Willmann et al., 2008; Fernàndez-Garcia et al., 2009) that upscaled macrodispersion coefficients are not sufficient to reproduce the transport behavior for highly heterogeneous media.

As mentioned previously, the synthetic studies of Fernàndez-Garcia et al. (2009) have shown that the double-rate mass transfer model is better than the singe-rate model in 2D mass transport upscaling. Herein, we only consider the double-rate mass transfer model to represent the mass transfer process, i.e., in each coarse block, the solute transport is assumed to happen in three zones: transport in the mobile zone is mainly by advection, while transport in the other two immobile zones is by diffusion-like processes.

With regard to the double-rate mass transfer model, the mass transfer rate density function $f(\alpha)$ and the memory function $g(t)$ are:

$$\begin{aligned} f(\alpha) &= \frac{\beta_1}{\beta}\delta(\alpha-\alpha_1) + \frac{\beta_2}{\beta}\delta(\alpha-\alpha_2) \\ g(t) &= \alpha_1\frac{\beta_1}{\beta}e^{-\alpha_1 t} + \alpha_2\frac{\beta_2}{\beta}e^{-\alpha_2 t} \end{aligned} \tag{3.20}$$

Accordingly, the parameters being estimated, are collected as a vector in $\mathbf{\Theta} = [\alpha_1, \alpha_2, \beta_1, \beta_2, A_l]$. Notice that the parameters are spatially variable since they are estimated for each upscaled block independently.

We compare the effectiveness of the transport upscaling by analyzing the breakthrough curves at different control planes in one specific realization and by looking at the ensemble results. For the ensemble results we will look at the early (5^{th} percentile of the BTC), median (50^{th} percentile) and late (95^{th} percentile) travel times.

Results using the advective-only model and the double-rate transport model are shown (see Figure 3.4 for the reproduction of BTCs in one realization and Figure 3.5 for the ensemble behavior of early, median and late travel times). From these results, we see that: (1) In contrast to the advective-only model, the double-rate mass transfer upscale model displays a higher accuracy to reproduce the fine scale breakthrough curves, in particular, the late travel times. Therefore, it is important to include the fictitious mass transfer process for solute transport predictions after upscaling. (2) In agreement with the study of Fernàndez-Garcia and Gómez-Hernández (2007), it is shown that the advective-only model even when using a sophisticated hydraulic conductivity upscaling (interblock Laplacian-with-skin here) can result in overestimating the early travel times and underestimating the late travel times in very heterogeneous media. (3) The small deviations in the reproduction of the BTCs by the mass transfer model may be due to fact that the upscaled mass transfer parameters are derived from a one-dimensional analytical solution of the double-rate transport model (see Equation (3.9)).

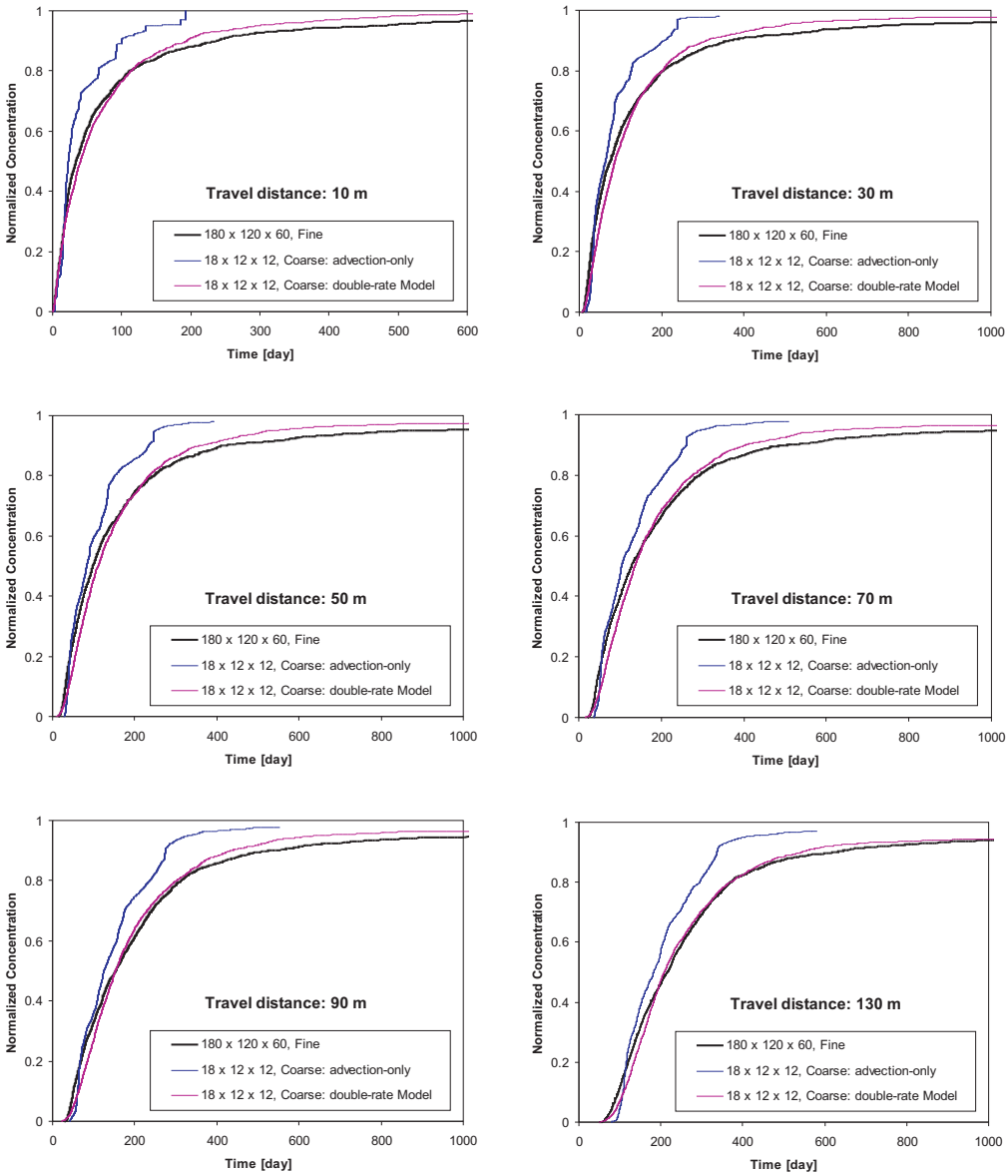

Figure 3.4: Comparison of fine scale cumulative breakthrough curves with those obtained by the upscaled transport models at six different control planes.

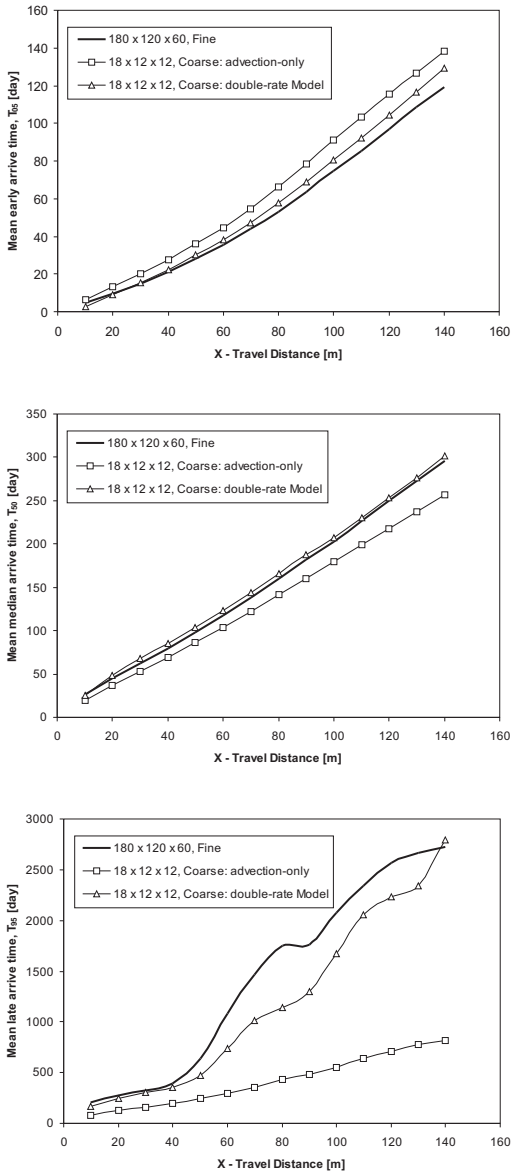

Figure 3.5: Ensemble travel times (early, median, and late travel times) as a function of travel distance, and comparison of the fine scale simulations to the upscaled simulations.

3.3.4 Propagation of Uncertainty

Due to the inherent lack of information in groundwater modeling, an uncertainty assessment is commonly requested in solute transport simulations (e.g., Salamon et al., 2007; Riva et al., 2008). Quantifying the uncertainty associated with flow and transport modeling should be important for the decision maker to assess the degree of confidence of his decisions. Here, we have analyzed how the uncertainty is estimated from the ensemble of realizations at the fine scale and after flow and transport upscaling. We will analyze the propagation of uncertainty through the upscaling process, along the same line as Fernàndez-Garcia and Gómez-Hernández (2007).

The use of 30 realizations may seem a small number to perform an uncertainty evaluation in such a heterogeneous aquifer. However, our purpose is not so much to analyze the number of realizations needed to obtain a good estimation of model uncertainty, but rather to compare the uncertainty derived from 30 realizations, before and after upscaling. If uncertainty upscales well for 30 realizations, it should do so for a larger number of realizations.

We evaluate uncertainty by calculating the spread in the ensemble of cumulative breakthrough curves at all the control planes. More precisely, we quantified uncertainty by the 95% confidence interval related with the early, median, and late arrival time of particles to each control plane. The early arrival time reflects the fastest pathways between source and control plane, which is for example of importance for the safety assessment of nuclear waste repositories. The late arrival time constitutes important information for the calculation, for example, of clean-up times in contaminated aquifer remediation.

The evolution of uncertainty with the travel distance is shown in Figure 3.6. We can see that: (1) For the early arrival time, the advection-only model and double-rate mass transfer model show a slight overestimation of the uncertainty. (2) For the median arrival time, the double-rate mass transfer model is better in reproducing the uncertainty estimated at the fine scale than the advective-only model. (3) For the late time, it is evident that the use of double-rate mass transfer model clearly outperforms the advective-only for distances larger than 60 m, and less clearly (because of the scale the results are plotted) for the shorter distances.

In highly heterogeneous formulations, hydraulic conductivity upscaling is not sufficient to preserve the uncertainty. Transport upscaling, through the use of a mass transfer process at the coarse scale is needed for proper upscaling of the uncertainty associated with solute transport predictions.

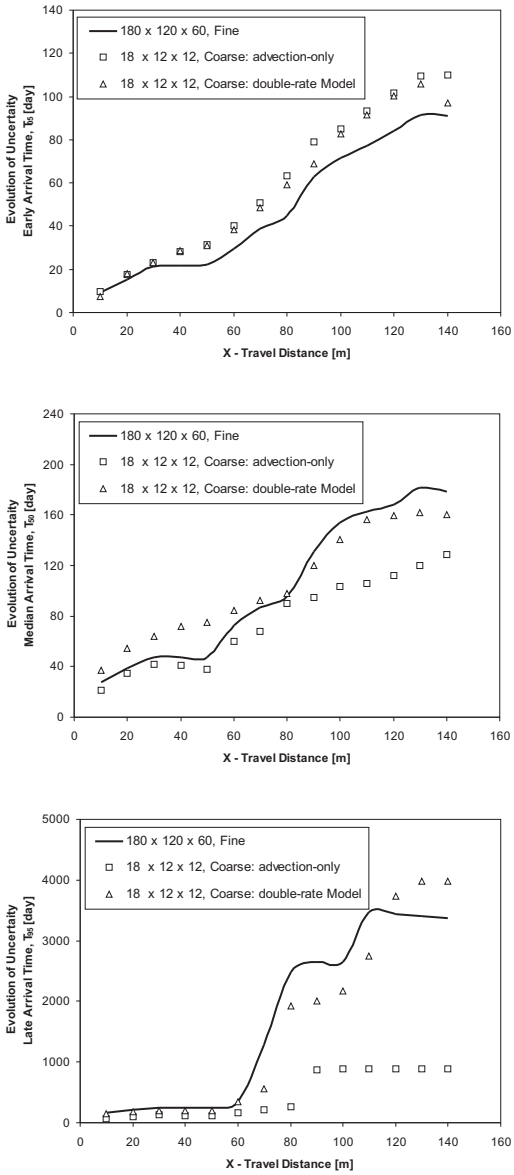

Figure 3.6: Evolution of uncertainty as a function of travel distance for the early, median, and late travel times, as measured by the width of the 95% confidence interval derived from an ensemble of 30 realizations. Calculations were performed at the fine scale, and at the coarse scale for two different upscaling approaches.

3.4 Discussion

We have presented and demonstrated an algorithm for transport upscaling to reduce the computational burden of transport predictions in three-dimensional highly heterogeneous media. But, how general is the algorithm? Will it work for different case studies? Will it work for different transport experiments? Although we recognize that the results obtained are specific to the case study under consideration, we believe that the upscaling procedure is general and it should work for other settings, as discussed below.

We present the results for statistically isotropic fine scale conductivities. What if the fine scale conductivities had been statistically anisotropic, with a much larger correlation length in the horizontal plane than in the vertical direction? What if the fine scale conductivities display curvilinear features, such as those associated with channels? In the case of statistical anisotropy, it would be necessary to adjust the size of the coarse blocks proportionally to the correlation lengths in each direction, in order to reduce the amount of smoothing in the directions of shortest continuity. In the case of curvilinear features, the proposed approach will yield upscaled conductivity tensors, the principal directions of which will change from block to block, inducing fluid velocities in the coarse model following those curvilinear features. The proposed approach has no problem in dealing with hydraulic conductivity tensors with arbitrary orientations of their principal directions. The block-by-block upscaling procedure is local, each block is isolated and a local flow exercise is performed in each block; at this local scale, the anisotropic correlation or the curvilinear features should not be clearly distinguishable from the intrinsic heterogeneity of the fine scale conductivities within the block; therefore, the upscaling algorithm should perform similarly. The question, remained to be answered, is whether when the blocks are assembled they will capture the global behavior of the statistically anisotropic formation or of the curvilinear features, or some specific corrections have to applied in these cases.

We present an analysis for a confined aquifer under steady-state flow conditions. We have not investigated how the upscaled coarse model would behave under transient conditions. We conjecture that the upscaled model should reproduce the the transient flow response of the the fine scale model with a degree of accuracy similar to the one obtained here for steady-state conditions, since the upscaled block conductivities are determined using different flow configurations applied to the block being upscaled. However, the upscaled transport parameters are based on the particle residence times for a specific velocity field; since, for transient flow conditions, the velocity field changes with time, it should be further investigated how much the upscaled transport parameters change as the velocity field changes, and decide whether these transport parameters should be made time dependent or there is a set of

optimal parameters that would work well for the entire transient period. Also, in the case of transient flow, the need to upscale the storage coefficient needs to be addressed. Regarding the application of this approach for an unconfined aquifer, the general upscaling procedure should remain the same, all blocks should be upscaled as if they were fully saturated, and then, special caution should be taken in the numerical simulation model to account for those cells intersected by the phreatic surface at the time of computing the mass balances involving those cells. We have not analyzed this case because we do not have a numerical flow simulator capable of using full conductivity tensors and accounting for a phreatic surface.

The issue of how the upscaled transport parameters will perform under transient conditions (i.e., different velocity fields in time), brings the question of what will happen if the flow geometry changes substantially with respect to that for which the parameters were computed. A priori, we anticipate that the transport parameters would have to be recomputed, since the flow velocity field will change, and so will the residence times in the blocks.

We present a sequential upscaling procedure in which first, we compute the upscaled flow parameters, and then we use these parameters to compute the upscaled transport parameters. However, if the final aim of our analysis were to get the best transport predictions at the coarse scale, even compromising the accuracy of flow reproduction, we could think of performing the flow and transport upscaling jointly, therefore using the particle residence times within the block being upscaled in the computation of the coarse conductivity tensors. This is an interesting avenue of research that has not been investigated in this paper.

We have used a homogeneous porosity throughout the exercise. If porosity had been heterogeneous it would have had to be upscaled, too

There are two main drawbacks in the proposed method: the need to use the particle residence times obtained after a simulation of the flow and transport equations at the fine scale, and the need to correct the porosity at the coarse scale, even though the porosity is homogenous at the fine scale.

The first drawback beats, in principle, the whole purpose of upscaling, which is to avoid having to simulate flow and/or transport at the fine scale. For this reason, this paper loses some of its practicality, and could be justified (from a practical point of view) only if the upscaled model is to be used for a more complex type of modeling (i.e. reactive transport) avoiding the need to run the complex model at the fine scale. In order not to have to obtain the fine scale solution for the transport upscaling, we have tried to follow the same local approach as for the flow upscaling, that is, to isolate the block plus a sufficiently large skin and to solve local transport problems for several boundary conditions, and then derive the upscaled transport parameters; however, we have not succeeded with this approach, which has always resulted in

biased transport predictions. There is, therefore, additional research needed in the transport upscaling procedure in order to yield it more practical. Our contribution with this paper is to demonstrate than, in 3D modeling of flow and transport, it is possible to systematically derive flow and transport upscaled parameters as long as we acknowledge that removing the heterogeneity within the block implies turning conductivities into tensors and including an enhanced macrodispersion and a mass transfer process for the solute transport.

The second drawback requires further investigation. We are not the first ones to face the need to make this adjustment for the coarse scale porosity (e.g., Zinn and Harvey, 2003; Zhang, 2004; Fernàndez-Garcia et al., 2009). The need for this correction is due to the accumulation of small biases in the transport modeling for each coarse block. When the transport parameters of each coarse block are computed, they are determined trying to reproduce the particle residence time distribution within the block with emphasis in matching the mean residence time; however, there seems to be a small systematic bias in this determination, which, at the end, forces us to correct the coarse porosities so that the breakthrough curves from the upscaled model are not shifted with respect to those from the fine scale model.

There is a need to know the fine scale parameters over the entire aquifer. Obviously, these parameter values will never be available, they have to be generated on the basis of available data. The issue of scales has been discussed for many years in the literature; it is a very old issue (known as the change of support problem) in mining (Journel and Huijbregts, 1978), and a little bit more recent in hydrogeology and petroleum engineering; a good paper on the subject from the hydrogeology literature is the one by (Dagan, 1986), in which Dagan talks about measurement and model scales, among other scales. For many years, data were measured, and without further consideration they were used to inform the parameter values of the groundwater flow model elements, until a concern about the so called "missing scale" was risen, mostly in the petroleum literature (Tran, 1995, 1996), and the need to account for the disparity of scales between measurements and model cells was recognized (Gómez-Hernández, 1991). Data are collected at a scale, generally, much smaller than the scale at which models are going to be discretized. Data spatial variability can be characterized at such scale by standard geostatistical methods (Deutsch and Journel, 1992) or by the more powerful and sophisticated multipoint geostatistical approaches (Strebelle, 2002), and this characterization can be used to generate conditional realizations, at the sampling scale, over discretized grids of multi-million cells. It is not proper to characterize the sampled data and use them directly for the generation of realizations at a larger scale suitable for numerical modeling, since the spatial variability patterns of the "equivalent" properties that should inform the larger blocks are completely different from that of the sampled data. Besides, as we

have shown, for the purpose of transport modeling, removing the within-block heterogeneity requires the introduction of additional processes to make up for this loss of variability, which makes virtually impossible to generate the additional parameters directly from a few sampled data. As proposed in this, and many other papers on upscaling, the proper way to account for the disparity of scales is to build fine scale models based on the data, then to upscale them so that the model size is amenable to numerical modeling. It remains open the problem of how to integrate sampled data taken at different scales.

We recognize that the results have been demonstrated in a single case study, but we conjecture that the good performance of the method proposed is not case specific, and we base this conjecture in that the upscaling exercise is performed on a block by block basis at a scale in which the specific features of the different case studies will be less noticeable. We had to upscale several thousands of blocks using a systematic approach, with each block having a different distribution of fine scale conductivities. The upscaled parameters would have been computed similarly had the flow geometry or the conductivity heterogeneity changed. We acknowledge that the final results we present are based on the assembly of these blocks for a specific flow and transport problem, and the performance of this final assembly for a different case study may not work so well as it did in our example.

Further research is needed (i) to avoid the solution of the flow and transport at the fine scale in order to determine the coarse scale transport parameters, (ii) to explain the need for correcting the porosity when moving from the fine to the coarse scale, (iii) to determine how to upscale heterogeneous porosities, (iv) to evaluate the approach for different conditions/scenarios, such as statistical anisotropic conductivities, transient flow conditions or radial flow and (v) to account for data measured at different scales.

3.5 Summary and Conclusions

We have presented and demonstrated an algorithm for transport upscaling in three-dimensional highly heterogeneous media. This work is an extension of the work by Fernàndez-Garcia et al. (2009) in two dimensions. Some of the critical features of this method is that it uses an elaborated Laplacian-with-skin approach to reproduce the flows instead of the simple-Laplacian scheme, the use of a multi-rate mass transfer process at the coarse scale to compensate for the loss of information during upscaling, and the need to perform a piecewise upscaling of effective porosity.

We have used a synthetic example to demonstrate the advantages of the interblock Laplacian-with-skin approach to upscale hydraulic conductivities as compared with other approaches. We found that using interblock centered

conductivities and that using a skin to compute them results in a good reproduction of flows at the fine scale.

Moreover, we found that proper transport upscaling is particularly important for the reproduction of the late time behavior of the solute breakthrough curves. We also found that proper transport upscaling is important to not underestimate the breakthrough curve prediction uncertainty.

Bibliography

Bear, J., 1972. Dynamics of fluids in porous media. American Elsevier Pub. Co., New York.

Benson, D. A., Wheatcraft, S. W., Meerschaert, M. M., 2000. Application of a fractional advection-dispersion equation. Water Resour Res 36 (6), 1403–1412.

Berkowitz, B., Scher, H., 1998. Theory of anomalous chemical transport in random fracture networks. Phys Rev E 57 (5), 5858–5869.

Bierkens, M., Gaast, J., 1998. Upscaling hydraulic conductivity: theory and examples from geohydrological studies. Nutrient Cycling in Agroecosystems 50, 193–207.

Burnett, R. D., Frind, E. O., 1987. Simulation of contaminant transport in three dimensions: 2. dimensionality effects. Water Resour Res 23 (4).

Carrera, J., Sánchez-Vila, X., Benet, I., Medina, A., Galarza, G., Guimerà, J., 1998. On matrix diffusion: formulations, solution methods and qualitative effects. Hydrogeology Journal 6 (1), 178–190.

Cassiraga, E. F., Fernàndez-Garcia, D., Gómez-Hernández, J. J., 2005. Performance assessment of solute transport upscaling methods in the context of nuclear waste disposal. Int J of Rock Mec Min 42 (5-6), 756–764.

Chen, Y., Durlofsky, L. J., Gerritsen, M., Wen, X. H., 2003. A coupled local-global upscaling approach for simulating flow in highly heterogeneous formations. Adv. Water Resour. 26 (10), 1041–1060.

Cushman, J. H., 1984. On unifying the concepts of scale, instrumentation, and stochastics in the development of multiphase transport theory. Water Resour. Res. 20 (11), 1668–1676.

Dagan, G., 1986. Statistical theory of groundwater flow and transport: Pore to laboratory, laboratory to formation, and formation to regional scale. Water Resour. Res. 22 (9), 120S–134S.

Dagan, G., 1994. Upscaling of dispersion coefficients in transport through heterogeneous formations. Computational Methods in Water Resources X 1, 431–439.

Desbarats, A. J., 1992. Spatial averaging of hydraulic conductivity in three-dimensional heterogeneous porous media. Math. Geol. 24 (3), 249–267.

Deutsch, C. V., Journel, A. G., 1992. GSLIB, Geostatistical Software Library and User's Guide. Oxford University Press, New York.

Doherty, J., 2004. PEST model-independent parameter estimation, user manual. Watermark Numerical Computing, Brisbane, Australia, 3349.

Feehley, C. E., Zheng, C., Molz, F. J., 2000. A dual-domain mass transfer approach for modeling solute transport in heterogeneous aquifers: Application to the macrodispersion experiment (MADE) site. Water Resour Res 36 (9), 2501–2515.

Fernàndez-Garcia, D., Gómez-Hernández, J. J., 2007. Impact of upscaling on solute transport: Traveltimes, scale dependence of dispersivity, and propagation of uncertainty. Water Resour Res 43 (2).

Fernàndez-Garcia, D., Illangasekare, T. H., Rajaram, H., 2005. Differences in the scale dependence of dispersivity and retardation factors estimated from forced-gradient and uniform flow tracer tests in three-dimensional physically and chemically heterogeneous porous media. Water Resour Res 41 (3), W03012.

Fernàndez-Garcia, D., Llerar-Meza, G., Gómez-Hernández, J. J., 2009. Upscaling transport with mass transfer models: Mean behavior and propagation of uncertainty. Water Resour Res 45, W10411.

Freeze, R. A., Cherry, J. A., 1979. Groundwater. Prentice-Hall.

Frippiat, C. C., Holeyman, A. E., 2008. A comparative review of upscaling methods for solute transport in heterogeneous porous media. J. of Hydrology 362 (1-2), 150–176.

Gómez-Hernández, J. J., 1991. A stochastic approach to the simulation of block conductivity values conditioned upon data measured at a smaller scale. Ph.D. thesis, Stanford University.

Gómez-Hernández, J. J., Journel, A. G., 1993. Joint sequential simulation of multi-Gaussian fields. Geostatistics Troia 92 (1), 85–94.

Gómez-Hernández, J. J., Rubin, Y., 1990. Spatial averaging of statistically anisotropic point conductivities. In: Optimizing the Resources of Water Management. Asce, pp. 566–571.

Gómez-Hernández, J. J., Wen, X. H., 1994. Probabilistic assessment of travel times in groundwater modeling. J. of Stochastic Hydrology and Hydraulics 8 (1), 19–56.

Guadagnini, A., Neuman, S. P., 1999. Nonlocal and localized analyses of conditional mean steady state flow in bounded, randomly nonuniform domains: 1. theory and computational approach. Water Resour. Res. 35 (10), 2999–3018.

Guswa, A. J., Freyberg, D. L., 2002. On using the equivalent conductivity to characterize solute spreading in environments with low-permeability lenses. Water Resour. Res. 38 (8), 1132.

Haggerty, R., Gorelick, S. M., 1995. Multiple-rate mass transfer for modeling diffusion and surface reactions in media with pore-scale heterogeneity. Water Resour Res 31 (10).

Haggerty, R., McKenna, S. A., Meigs, L. C., 2000. On the late-time behavior of tracer test breakthrough curves. Water Resour Res 36 (12).

Haggerty, R., Reeves, P. C., 2002. STAMMT-L 1.0, formulation and user's guide. Tech. rep., Tech. Rep. 520308, Sandia National Laboratories.

Harbaugh, A. W., Banta, E. R., Hill, M. C., McDonald, M. G., 2000. MODFLOW-2000, the U.S. Geological Survey modular ground-water model. U.S. Geological Survey, Branch of Information Services, Reston, VA, Denver, CO.

He, C., Durlofsky, L. J., 2006. Structured flow-based gridding and upscaling for modeling subsurface flow. Adv. Water Resour. 29 (12), 1876–1892.

Indelman, P., Abramovich, B., 1994. Nonlocal properties of nonuniform averaged flows in heterogeneous media. Water Resour. Res. 30 (12), 3385–3393.

Journel, A. G., Deutsch, C. V., Desbarats, A. J., 1986. Power averaging for block effective permeability. SPE 15128.

Journel, A. G., Huijbregts, C. J., 1978. Mining Geostatistics. Academic Press, London.

LaBolle, E. M., Fogg, G. E., Tompson, A. F., 1996. Random-walk simulation of transport in heterogeneous porous media: Local mass-conservation problem and implementation methods. Water Resour Res 32 (3), 583–593.

Lawrence, A. E., Sanchez-Vila, X., Rubin, Y., 2002. Conditional moments of the breakthrough curves of kinetically sorbing solute in heterogeneous porous media using multirate mass transfer models for sorption and desorption. Water Resour Res 38 (11), 1248.

Li, L., Zhou, H., Gómez-Hernández, J. J., 2010a. A comparative study of three-dimensional hydrualic conductivity upscaling at the macrodispersion experiment (MADE) site, on columbus air force base in mississippi (USA). J. of Hydrology submitted.

Li, L., Zhou, H., Gómez-Hernández, J. J., 2010b. Steady-state groundwater flow modeling with full tensor conductivities using finite differences. Comput Geosci, doi:10.1016/j.cageo.2010.04.002.

Neuman, S. P., Orr, S., 1993. Prediction of steady state flow in nonuniform geologic media by conditional moments: Exact nonlocal formalism, effective conductivities, and weak approximation. Water Resour. Res. 29 (2), 341–364.

Rehfeldt, K. R., Boggs, J. M., Gelhar, L. W., 1992. Field study of dispersion in a heterogeneous aquifer 3. geostatistical analysis of hydraulic conductivity. Water Resour Res 28 (12), 3309–3324.

Renard, P., Marsily, G. D., 1997. Calculating equivalent permeability: A review. Adv. Water Resour. 20 (5-6), 253–278.

Riva, M., Guadagnini, A., Fernàndez-Garcia, D., Sanchez-Vila, X., Ptak, T., 2008. Relative importance of geostatistical and transport models in describing heavily tailed breakthrough curves at the lauswiesen site. J Contam Hydrol 101 (1-4), 1–13.

Rubin, Y., Gómez-Hernández, J. J., 1990. A stochastic approach to the problem of upscaling of conductivity in disordered media, Theory and unconditional numerical simulations. Water Resour. Res. 26 (4), 691–701.

Rubin, Y., Sun, A., Maxwell, R., Bellin, A., 1999. The concept of block-effective macrodispersivity and a unified approach for grid-scale-and plume-scale-dependent transport. J Fluid Mech 395, 161–180.

Salamon, P., Fernàndez-Garcia, D., Gómez-Hernández, J. J., 2006a. Modeling mass transfer processes using random walk particle tracking. Water Resour Res 42, W11417.

Salamon, P., Fernàndez-Garcia, D., Gómez-Hernández, J. J., 2006b. A review and numerical assessment of the random walk particle tracking method. J Contam Hydrol 87 (3-4), 277–305.

Salamon, P., Fernàndez-Garcia, D., Gómez-Hernández, J. J., 2007. Modeling tracer transport at the MADE site: The importance of heterogeneity. Water Resour Res 30 (8).

Sanchez-Vila, X., Guadagnini, A., Carrera, J., 2006. Representative hydraulic conductivities in saturated groundwater flow. Rev Geophys 44 (3).

Scheibe, T., Yabusaki, S., 1998. Scaling of flow and transport behavior in heterogeneous groundwater systems. Adv. Water Resour. 22 (3), 223–238.

Silva, O., Carrera, J., Kumar, S., Dentz, M., Alcolea, A., Willmann, M., 2009. A general real-time formulation for multi-rate mass transfer problems. Hydrol Earth Syst Sc 6 (2), 2415–2449.

Strebelle, S., 2002. Conditional simulation of complex geological structures using multiple-point statistics. Math. Geol. 34 (1), 1–22.

Tran, T., 1995. Stochastic simulation of permeability fields and their scale-up for flow modeling. Ph.D. thesis, Stanford University, Branner Earth Sciences Library.

Tran, T., 1996. The [']missing scale' and direct simulation of block effective properties. Journal of Hydrology 183 (1-2), 37 – 56.

Vermeulen, P. T. M., Stroet, C. B. M. T., Heemink, A. W., 2006. Limitations to upscaling of groundwater flow models dominated by surface water interaction. Water Resour Res 42 (10), W10406.

Wen, X. H., Durlofsky, L. J., Chen, Y., 2005. Efficient three-dimensional implementation of local-global upscaling for reservoir simulation. In: SPE Reservoir Simulation Symposium.

Wen, X. H., Gómez-Hernández, J. J., 1996a. The constant displacement scheme for tracking particles in heterogeneous aquifers. Groundwater 34 (1), 135–142.

Wen, X. H., Gómez-Hernández, J. J., 1996b. Upscaling hydraulic conductivities: An overview. J. of Hydrology 183 (1-2), ix–xxxii.

White, C. D., Horne, R. N., 1987. Computing absolute transmissibility in the presence of Fine-Scale heterogeneity. SPE 16011.

Willmann, M., Carrera, J., Sánchez-Vila, X., 2008. Transport upscaling in heterogeneous aquifers: What physical parameters control memory functions? Water Resour Res 44 (12), W12437.

Zhang, Y., 2004. Upscaling conductivity and porosity in three-dimensional heterogeneous porous media. Chinese Sci Bull 49 (22), 2415–2423.

Zheng, C., Wang, P. P., 1999. MT3DMS: A Modular Three-Dimensional Multispecies Transport Model for Simulation of Advection, Dispersion, and Chemical Reactions of Contaminants in Groundwater Systems; Documentation and User's. ALABAMA UNIV TUSCALOOSA.

Zhou, H., Li, L., Gómez-Hernández, J. J., 2010. Three-dimensional hydraulic conductivity upscaling in groundwater modelling. Comput Geosci, doi:10.1016/j.cageo.2010.03.008.

Zijl, W., Stam, J., 1992. Modeling permeability in imperfectly layered porous media. i. derivation of block-scale permeability tensor for thin grid-blocks. Mathematical Geology 24, 865–883, 10.1007/BF00894656.

Zinn, B., Harvey, C. F., 2003. When good statistical models of aquifer heterogeneity go bad: A comparison of flow, dispersion, and mass transfer in connected and multivariate gaussian hydraulic conductivity fields. Water Resour. Res 39 (3), doi:10.1029/2001WR001146.

Submitted to Water Resources Research.

4

Modeling Transient Groundwater Flow by Coupling Ensemble Kalman Filtering and Upscaling

Abstract

The ensemble Kalman filter (EnKF) is coupled with upscaling to build an aquifer model at a coarser scale than the scale at which the conditioning data (conductivity and piezometric head) had been taken for the purpose of inverse modeling. Building an aquifer model at such scale is most often impractical, since this would imply numerical models with millions of cells. If, in addition, an uncertainty analysis is required involving some kind of Monte-Carlo approach, the task becomes impossible. For this reason, a methodology has been developed that will use the conductivity data, at the scale at which they were collected, to build a model at a (much) coarser scale suitable for the inverse modeling of groundwater flow and mass transport. It proceeds as follows: (i) generate an ensemble of realizations of conductivities conditioned to the conductivity data at the same scale at which conductivities were collected, (ii) upscale each realization onto a coarse discretization; on these coarse realizations, conductivities will become tensorial in nature with arbitrary orientations of their principal directions, (iii) apply the EnKF to the ensemble of

coarse conductivity upscaled realizations in order to condition the realizations to the measured piezometric head data. The proposed approach addresses the problem of how to deal with tensorial parameters, at a coarse scale, in ensemble Kalman filtering, while maintaining the conditioning to the fine scale hydraulic conductivity measurements. It is demonstrated in the framework of a synthetic worth-of-data exercise, in which the relevance of conditioning to conductivities, piezometric heads or both is analyzed.

4.1 Introduction

In this paper we address two problems, each of which has been the subject of many works, but which have not received as much attention when considered together: upscaling and inverse modeling. There are many reviews on the importance and the methods of upscaling (e.g., Wen and Gómez-Hernández, 1996; Renard and de Marsily, 1997; Sánchez-Vila et al., 2006), and there are also many reviews on inverse modeling and its relevance for aquifer characterization (e.g., Yeh, 1986; McLaughlin and Townley, 1996; Zimmerman et al., 1998; Carrera et al., 2005; Hendricks Franssen et al., 2009; Oliver and Chen, 2011). Our interest lies in coupling upscaling and inverse modeling to perform an uncertainty analysis of flow and transport in an aquifer for which measurements have been collected at a scale so small that it is prohibitive, if not impossible, to perform directly the inverse modeling.

The issue of how to reconcile the scale at which conductivity data are collected and the scale at which numerical models are calibrated was termed "the missing scale" by Tran (1996), referring to the fact that the discrepancy between scales was simply disregarded; data were collected at a fine scale, the numerical model was built at a much larger scale, each datum was assigned to a given block, and the whole block was assigned the datum value, even though the block may be several orders of magnitude larger than the volume support of the sample. This procedure induced a variability, at the numerical block scale, much larger than it should be, while at the same time some unresolved issues have prevailed like what to do when several samples fell in the same block.

To the best of our knowledge, the first work to attempt the coupling of upscaling and inverse modeling is the upscaling-calibration-downscaling-upscaling approach by Tran et al. (1999). In their approach, a simple averaging over a uniformly coarsened model is used to upscale the hydraulic conductivities, then, the state information (e.g., dynamic piezometric head data) is incorporated in the upscaled model by the self-calibration technique (Gómez-Hernández et al., 1997). The calibrated parameters are downscaled back to the fine scale by block kriging (Behrens et al., 1998) resulting in a

fine scale realization conditional to the measured parameters (e.g., hydraulic conductivities). Finally, the downscaled conductivities are upscaled using a more precise scheme (Durlofsky et al., 1997; Li et al., 2011a) for prediction purposes. The main shortcoming of this approach is that the inverse modeling is performed on a crude upscaled model, resulting in a downscaled model that will not honor the state data. Tureyen and Caers (2005) proposed the calibration of the fine scale conductivity field by gradual deformation (Hu, 2000; Capilla and Llopis-Albert, 2009), but instead of solving the flow equation at the fine scale they used an approximate solution after upscaling the hydraulic conductivity field to a coarse scale. This process requires an upscaling for each iteration of the gradual deformation algorithm, which is also time-consuming, although they avoid the fine scale flow solution. More recently, an alternative multiscale inverse method (Fu et al., 2010) was proposed. It uses a multiscale adjoint method to compute sensitivity coefficients and reduce the computational cost. However, like traditional inverse methods, the proposed approach requires a large amount of CPU time in order to get an ensemble of conditional realizations. In our understanding, nobody has attempted to couple upscaling and the ensemble Kalman filtering (EnKF) for the generation of hydraulic conductivity fields conditioned to both hydraulic conductivity and piezometric head measurements. Only the work by Peters et al. (2010) gets close to our work as, for the Brugge Benchmark Study, they generated a fine scale permeability field, which was upscaled using a diagonal tensor upscaling; the resulting coarse scale model was provided to the different teams participating in the benchmark exercise, some of which used the EnKF for history matching. We have chosen the EnKF algorithm for the inverse modeling because it has been shown that it is faster than other alternative Monte Carlo-based inverse modeling methods (see for instance the work by Hendricks Franssen and Kinzelbach (2009) who show that the EnKF was 80 tomes fastar than the sequential self-calibration in a benchmark exercise and nearly as good).

Our aim is to propose an approach for the stochastic inverse modeling of an aquifer that has been characterized at a scale at which it is impossible to solve the inverse problem, due to the large number of cells needed to discretize the domain. We start with a collection of hydraulic conductivity and piezometric head measurements, taken at a very small scale, to end with an ensemble of hydraulic conductivity realizations, at a scale much larger than the one at which data were originally sampled, all of which are conditioned to the measurements. This ensemble of realizations will serve to perform uncertainty analyses of both the parameters (hydraulic conductivities) and the system state variables (piezometric heads, fluxes, concentrations, or others).

The rest of the paper is organized as follows. Section 4.2 outlines the coupling of upscaling and the EnKF, with emphasis in the use of arbitrary hydraulic conductivity tensors in the numerical model. Next, in section 4.3, a

synthetic example serves to validate the proposed method. Then, in section 4.4, the results are discussed. The paper ends with a summary and conclusions.

4.2 Methodology

Hereafter, we will refer to a fine scale for the scale at which data are collected, and a coarse scale, for the scale at which the numerical models are built. The methodology proposed can be outlined as follows:

1. At the fine scale, generate an ensemble of realizations of hydraulic conductivity conditioned to the hydraulic conductivity measurements.
2. Upscale each one of the fine scale realizations generated in the previous step. In the most general case, the upscaled conductivities will be full tensors in the reference axes.
3. Use the ensemble of coarse realizations with the EnKF to condition (assimilate) on the measured piezometric heads.

4.2.1 Generation of the Ensemble of Fine Scale Conductivities

The first step of the proposed methodology makes use of geostatistical tools already available in the literature (e.g., Gómez-Hernández and Srivastava, 1990; Deutsch and Journel, 1998; Strebelle, 2002; Mariethoz et al., 2010). The technique to choose will depend on the underlying random function model selected for the hydraulic conductivity: multi-Gaussian, indicator-based, pattern-based, or others. In all cases, the scale at which these fields can be generated is not an obstacle, and the resulting fields will be conditioned to the measured hydraulic conductivity measurements (but only to hydraulic conductivity measurements). These fields could have millions of cells and are not suitable for inverse modeling of groundwater flow and solute transport.

4.2.2 Upscaling

Each one of the realizations generated in the previous step is upscaled onto a coarse grid with a number of blocks sufficiently small for numerical modeling. We use the flow upscaling approach by Rubin and Gómez-Hernández (1990) who, after spatially integrating Darcy's law over a block V,

$$\frac{1}{V}\int_V \mathbf{q}\,dV = -\mathbf{K}^b\Big(\frac{1}{V}\int_V \nabla\mathbf{h}\,dV\Big), \tag{4.1}$$

define the block conductivity tensor ($\mathbf{K}^b$) as the tensor that best relates the block average head gradient ($\nabla\mathbf{h}$) to the block average specific discharge vector

($\mathbf{q}$) within the block. Notice that to perform the two integrals in the previous expressions we need to know the specific discharge vectors and the piezometric head gradients at the fine scale within the block. These values could be obtained after a solution of the flow problem at the fine scale (i.e., White and Horne, 1987), but this approach beats the whole purpose of upscaling, which is to avoid such fine scale numerical simulations. The alternative is to model a smaller domain of the entire aquifer enclosing the block being upscaled. In such a case, the boundary conditions used in this reduced model will be different from the boundary conditions that the block has in the global model, and this will have some impact on the fine scale values of $\nabla\mathbf{h}$ and $\mathbf{q}$. The dependency of the heads and flows within the block on the boundary conditions is the reason why it is said that the block upscaled tensor is non-local.

For the flow upscaling we adopt the so-called Laplacian-with-skin method on block interfaces as described by Gómez-Hernández (1991) and recently extended to three dimensions by Zhou et al. (2010). The two main advantages of this approach are that it can handle arbitrary full conductivity tensors, without any restriction on their principal directions; and that it upscales directly the volume straddling between adjacent block centers, which, at the end, is the parameter used in the standard finite-difference approximation of the groundwater flow equation (avoiding the derivation of this value by some kind of averaging of the adjacent block values). Once the interblock conductivities have been computed, a specialized code capable of handling interblock tensors is necessary. For this purpose, the public domain code FLOWXYZ3D (Li et al., 2010), has been developed. The details of the upscaling approach, the numerical modeling using interblock conductivity tensors, and several demonstration cases can be found in Zhou et al. (2010); Li et al. (2010, 2011a,b). The resulting upscaled interblock tensors produced by this approach are always of rank two, symmetric and positive definite.

The Laplacian-with-skin method on block interfaces for a given realization can be briefly summarized as follows:

- Overlay a coarse grid on the fine scale hydraulic conductivity realization.
- Define the interblock volumes that straddle any two adjacent blocks.
- For each interblock:
  - Isolate the fine scale conductivities within a volume made up by the interblock plus an additional "border ring" or "skin" and simulate flow, at the fine scale, within this volume.
  - As explained by Zhou et al. (2010), there is a need to solve more than one flow problem in order to being able of identifying all components of the interblock conductivity tensor.

  - From the solution of the flow problems, use Equation (4.1) to derive the interblock conductivity tensor.

- Assemble all interblock tensors to build a realization of upscaled hydraulic conductivity tensors at the coarse scale.

The above procedure has to be repeated for all realizations, ending up with an ensemble of realizations of interblock conductivity tensors.

4.2.3 The EnKF with Hydraulic Conductivity Tensors

Extensive descriptions of the EnKF and how to implement it have been given, for instance, by Burgers et al. (1998); Evensen (2003); Naevdal et al. (2005); Chen and Zhang (2006); Aanonsen et al. (2009). Our contribution, regarding the EnKF, is how to deal with an ensemble of parameters that rather than being scalars are tensors. After testing different alternatives, we finally decided not to use the tensor components corresponding to the Cartesian reference system, but to use some of the tensor invariants, more precisely, the magnitude of the principal components and the angles that define their orientation.

For the example discussed later we will assume a two-dimensional domain, with hydraulic conductivity tensors varying in space $\mathbf{K} = \mathbf{K}(\mathbf{x})$ of the form

$$\mathbf{K} = \begin{bmatrix} K_{xx} & K_{xy} \\ K_{xy} & K_{yy} \end{bmatrix}. \tag{4.2}$$

Each conductivity tensor is converted onto a triplet $\{K_{max}, K_{min}, \theta\}$, with K_{max} being the largest principal component, K_{min}, the smallest one, and θ, the orientation, with respect to the x-axis, of the maximum principal component according to the following expressions (Bear, 1972):

$$\begin{aligned} K_{max} &= \frac{K_{xx}+K_{yy}}{2} + \left[\left(\frac{K_{xx}-K_{yy}}{2} \right)^2 + \left(K_{xy} \right)^2 \right]^{1/2}, \\ K_{min} &= \frac{K_{xx}+K_{yy}}{2} - \left[\left(\frac{K_{xx}-K_{yy}}{2} \right)^2 + \left(K_{xy} \right)^2 \right]^{1/2}, \\ \theta &= \frac{1}{2} \arctan\left(\frac{2K_{xy}}{K_{xx}-K_{yy}} \right). \end{aligned} \tag{4.3}$$

After transforming all conductivity tensors obtained in the upscaling step onto their corresponding triplets we are ready to apply the EnKF. We will use the EnKF implementation with an augmented state vector as discussed below; this is the standard implementation used in petroleum engineering and hydrogeology, although alternative implementations and refinements of the algorithm could have been used (see Aanonsen et al., 2009, for a review).

Using the EnKF nomenclature, the state of the system is given by the spatial distribution of the hydraulic heads, the state transition equation is the standard flow equation describing the movement of an incompressible fluid in a fully saturated porous medium (Bear, 1972; Freeze and Cherry, 1979) (in two dimensions for the example considered later), and the parameters of the system are the spatially varying hydraulic conductivities (the storage coefficient is assumed to be homogeneous and known, and therefore, it is a parameter not subject to filtering), i.e.,

$$\mathbf{Y}_k = f(\mathbf{X}_{k-1}, \mathbf{Y}_{k-1}), \tag{4.4}$$

where $\mathbf{Y}_k$ is the state of the system at time step t_k, f represents the groundwater flow model (including boundary conditions, external stresses, and known parameters), and $\mathbf{X}_{k-1}$ represents the model parameters after the latest update at time t_{k-1}.

The EnKF algorithm will proceed as follows:

1. Forecast. Equation (4.4) is used to forecast the system states for the next time step given the latest state and the latest parameter update. This forecast has to be performed in all realizations of the ensemble

2. Analysis. At the forecasted time step, new state observations are available at measurement locations. The discrepancy between these state observations and the forecasted values will serve to update both the parameter values and the system state at all locations in the aquifer model as follows:

   (a) Build the joint vector $\mathbf{\Psi}_k$, including parameters and state values. This vector can be split into as many members as there are realizations in the ensemble, with

   $$\mathbf{\Psi}_{k,j} = \begin{bmatrix} \mathbf{X} \\ \mathbf{Y} \end{bmatrix}_{k,j} \tag{4.5}$$

   being the j^{th} ensemble member at time t_k. Specifically, $\mathbf{X}$ (for a realization) is expressed as:

   $$\mathbf{X} = [(\ln K_{max}, \ln K_{min}, \theta)_1, \ldots, (\ln K_{max}, \ln K_{min}, \theta)_{N_b}]^T \tag{4.6}$$

   where N_b is the number of interfaces in the coarse numerical model. Notice that the logarithm of the conductivity principal components is used, since their distribution is, generally, closer to Gaussian than that of the conductivities themselves.

(b) The joint vector $\mathbf{\Psi}_k$ is updated, realization by realization, by assimilating the observations ($\mathbf{Y}_k^{obs}$):

$$\mathbf{\Psi}_{k,j}^a = \mathbf{\Psi}_{k,j}^f + \mathbf{G}_k\Big(\mathbf{Y}_k^{obs} + \boldsymbol{\epsilon} - \mathbf{H}\mathbf{\Psi}_{k,j}^f\Big), \tag{4.7}$$

where the superscripts a and f denote analysis and forecast, respectively; $\boldsymbol{\epsilon}$ is a random observation error vector; $\mathbf{H}$ is a linear operator that interpolates the forecasted heads to the measurement locations, and, in our case, is composed of $0's$ and $1's$ since we assume that measurements are taken at block centers. Therefore, equation (4.7) can be rewritten as:

$$\mathbf{\Psi}_{k,j}^a = \mathbf{\Psi}_{k,j}^f + \mathbf{G}_k\Big(\mathbf{Y}_k^{obs} + \boldsymbol{\epsilon} - \mathbf{Y}_{k,j}^f\Big), \tag{4.8}$$

where the Kalman gain $\mathbf{G}_k$ is given by:

$$\mathbf{G}_k = \mathbf{P}_k^f\mathbf{H}^T\Big(\mathbf{H}\mathbf{P}_k^f\mathbf{H}^T + \mathbf{R}_k\Big)^{-1}, \tag{4.9}$$

where $\mathbf{R}_k$ is the measurement error covariance matrix, and $\mathbf{P}_k^f$ contains the covariances between the different components of the state vector. $\mathbf{P}_k^f$ is estimated from the ensemble of forecasted states as:

$$\begin{aligned}\mathbf{P}_k^f &\approx E\left[\left(\mathbf{\Psi}_{k,j}^f - \overline{\mathbf{\Psi}}_{k,j}^f\right)\left(\mathbf{\Psi}_{k,j}^f - \overline{\mathbf{\Psi}}_{k,j}^f\right)^T\right] \\ &\approx \sum_{j=1}^{N_e}\frac{\left(\mathbf{\Psi}_{k,j}^f - \overline{\mathbf{\Psi}}_{k,j}^f\right)\left(\mathbf{\Psi}_{k,j}^f - \overline{\mathbf{\Psi}}_{k,j}^f\right)^T}{N_e},\end{aligned} \tag{4.10}$$

where N_e is the number of realizations in the ensemble, and the overbar denotes average through the ensemble.

In the implementation of the algorithm, it is not necessary to calculate explicitly the full covariance matrix $\mathbf{P}_k^f$, since the matrix $\mathbf{H}$ is very sparse, and, consequently, the matrices $\mathbf{P}_k^f\mathbf{H}^T$ and $\mathbf{H}\mathbf{P}_k^f\mathbf{H}^T$ can be computed directly at a strongly reduced CPU cost.

3. The updated state becomes the current state, and the forecast-analysis loop is started again.

The question remains whether the updated conductivity-tensor realizations preserve the conditioning to the fine scale conductivity measurements. In standard EnKF, when no upscaling is involved and conductivity values are the same in all realizations at conditioning locations, the forecasted covariances

and cross-covariances involving conditioning points are zero, and so is the Kalman gain at those locations; therefore, conductivities remain unchanged through the entire Kalman filtering. In our case, after upscaling the fine-scale conditional realizations, the resulting ensemble of hydraulic conductivity tensor realizations will display smaller variances (through the ensemble) for the tensors associated with interfaces close to the fine scale measurements than for those far from the measurements. These smaller variances will result in a smaller Kalman gain in the updating process at these locations, and therefore will induce a soft conditioning of the interblock tensors on the fine scale measurements.

The proposed method is implemented in the C software Upscaling-EnKF3D, which is used in conjunction with the finite-difference program FLOWXYZ3D (Li et al., 2010) in the forecasting step. From an operational point of view, the proposed approach is suitable for parallel computation both in terms of upscaling and EnKF, since each ensemble member is treated independently, except for the computation of the Kalman gain.

4.3 Application Example

In this section, a synthetic experiment illustrates the effectiveness of the proposed coupling of EnKF and upscaling.

4.3.1 Reference Field

We generate a realization of hydraulic conductivity over a domain discretized into 350 by 350 cells of 1 m by 1 m using the code GCOSIM3D (Gómez-Hernández and Journel, 1993).

We assume that, at this scale, conductivity is scalar and its natural logarithm, $\ln K$, can be characterized by a multiGaussian distribution of mean -5 (ln cm/s) and unit variance, with a strong anisotropic spatial correlation at the 45° orientation. The correlation range in the largest continuity direction (x') is $\lambda_{x'} = 90$ m and in the smallest continuity direction (y') is $\lambda_{y'} = 18$ m. The variogram is given by:

$$\gamma(\mathbf{r}) = 1.0 \cdot \left\{ 1 - \exp\left[- \sqrt{\left(\frac{3r_{x'}}{90}\right)^2 + \left(\frac{3r_{y'}}{18}\right)^2} \right] \right\}, \tag{4.11}$$

with

$$\begin{bmatrix} r_{x'} \\ r_{y'} \end{bmatrix} = \begin{bmatrix} 1/\sqrt{2} & 1/\sqrt{2} \\ -1/\sqrt{2} & 1/\sqrt{2} \end{bmatrix} \begin{bmatrix} r_x \\ r_y \end{bmatrix}, \tag{4.12}$$

and $r = (r_x, r_y)$ being the separation vector in Cartesian coordinates. The reference realization is shown in Figure 4.1A. From this reference realization

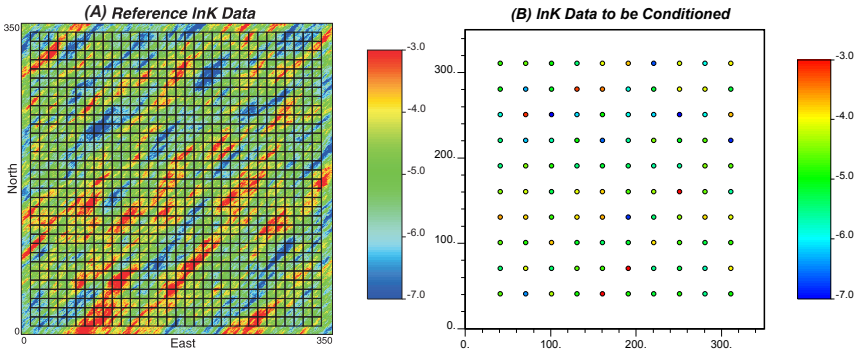

Figure 4.1: (A) Reference ln$K$ field overlaid with the discretization of the numerical model at the coarse scale. (B) Conditioning ln$K$ data.

100 conductivity data are sampled at the locations shown in Figure 4.1B. These data will be used for conditioning.

The forward transient groundwater flow model is run in the reference realization with the boundary conditions shown in Figure 4.2 and initial heads equal to zero everywhere. The total simulation time is 500 days, discretized into 100 time steps following a geometric sequence of ratio 1.05. The aquifer is confined. Specific storage is assumed constant and equal to 0.003 m^{-1}. The simulated piezometric heads at the end of time step 60 (67.7 days) are displayed in Figure 4.4. Piezometric heads at locations W1 to W9 in Figure 4.2 are sampled for the first 60 time steps to be used as conditioning data. The simulated heads at locations W10 to W13 will be used as validation data.

4.3.2 Hydraulic Conductivity Upscaling

For the reasons explained by Zhou et al. (2010); Li et al. (2010), the fine scale realizations must be slightly larger than the aquifer domain in order to apply the Laplacian-with-skin upscaling approach. We assume that the aquifer of interest is comprised by the inner 320 by 320 cell domain for all realizations. Each one of these realizations is upscaled onto a 32 by 32 square-block model implying an order-of-two magnitude reduction in the discretization of the aquifer after upscaling. After several tests, the skin selected for the upscaling procedure has a width of 10 m, since it is the one that gives best results in the reproduction of the interblock specific discharges when compared to those computed on the fine scale underlying realizations. Since the upscaling is applied to the interblock volume straddling between adjacent block centers, there are 32 by 31 column-to-column interblock tensors ($\mathbf{K}^{b,c}$) plus 31 by 32 row-

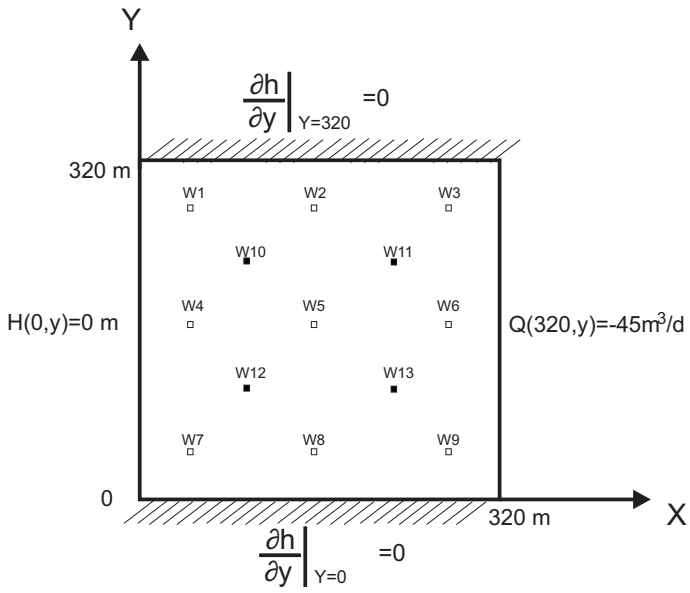

Figure 4.2: Sketch of the flow problem with boundary conditions, observation and prediction wells. Empty squares correspond to the piezometric head observation wells (W1-W9); filled squares correspond to the control wells (W10-W13).

Table 4.1: Definition of Cases depending on the the different sets of conditioning data.

Conditioning Data	Case A	Case B	Case C	Case D
Hydraulic conductivities(K)	No	Yes	No	Yes
Dynamic piezometric heads(h)	No	No	Yes	Yes

to-row interblock tensors ($\mathbf{K}^{b,r}$). All interblock tensors are transformed into their corresponding triplet of invariants prior to starting the EnKF algorithm.

For illustration purposes, Figure 4.3 shows the resulting triplets for the reference field. This figure will be used later as the reference upscaled field to analyze the performance of the proposed method. On the right side of Figure 4.4, the simulated piezometric heads at the end of the 60th time step are displayed side by side with the simulated piezometric heads at the fine scale. The reproduction of the fine scale spatial distribution by the coarse scale simulation is, as can be seen, very good; the average absolute discrepancy between the heads at the coarse scale and heads at the fine scale (on the block centers) is only 0.087 m.

4.3.3 Case Studies

Four cases, considering different types of conditioning information, are analyzed to study the performance of the proposed approach (see Table 4.1). They will show that the coupling of the EnKF with upscaling can be used to construct aquifer models that are conditional to conductivity and piezometric head data, when there is an important discrepancy between the scale at which the data are collected and the scale at which the flow model is built. The cases will serve also to carry out a standard worth-of-data exercise in which we analyze the trade-off between conductivity data and piezometric head data regarding aquifer characterization.

Case A is unconditional, 200 realizations are generated according to the spatial correlation model given by Equation (4.11) at the fine scale. Upscaling is performed in each realization and the flow model is run. No Kalman filtering is performed.

Case B is conditional to logconductivity measurements, 200 realizations of logconductivity conditional to the 100 logconductivity measurements of Figure 4.4B are generated at the fine scale. Upscaling is performed in each realization and the flow model is run. No Kalman filtering is performed.

Cases A and B act as base cases to be used for comparison when the piezometric head data are assimilated through the EnKF.

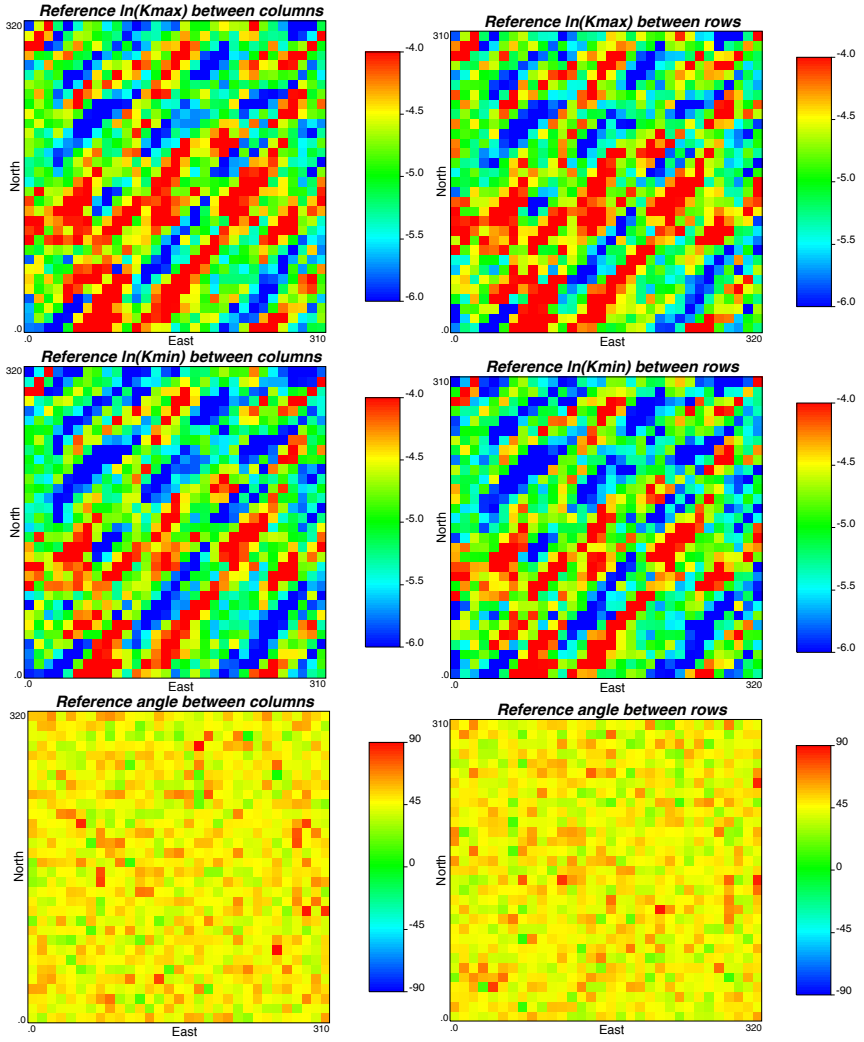

Figure 4.3: Upscaled values for the interblock tensor components: $\ln(Kmax)$, $\ln(Kmin)$ and rotation angle for the maximum component measured from the x-axis θ (in degrees), for both the interblocks between columns and the interblocks between rows. Upscaling method used: Laplacian with a skin of 10 m

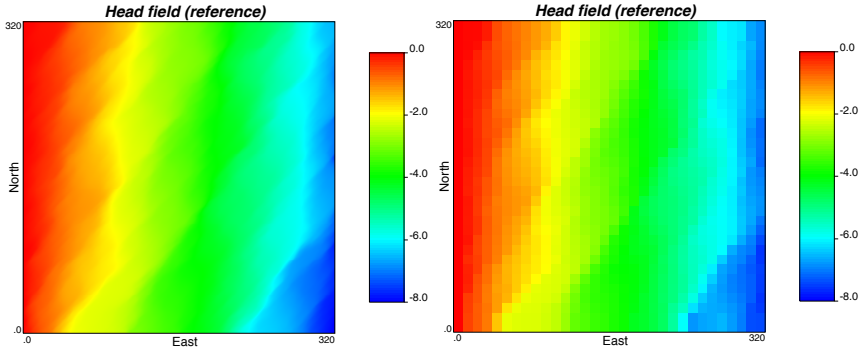

Figure 4.4: Reference piezometric head at the 60th time step. Left, as obtained at the fine scale; right, as obtained at the coarse scale

Case C is conditional to piezometric heads. The same 200 coarse realizations from Case A serve as the initial ensemble of realizations to be used by the EnKF to assimilate the piezometric head measurements from locations W1 to W9 for the first 60 time steps (66.7 days).

Case D is conditional to both logconductivity and piezometric heads. The same 200 coarse realizations from Case B serve as the initial ensemble of realizations to be used by the EnKF to assimilate the piezometric head measurements from locations W1 to W9 for the first 60 time steps (66.7 days).

In Cases C and D we use the measured heads obtained at the fine scale in the reference realization as if they were measurements obtained at the coarse scale. There is an error in this assimilation that we incorporate into the measurement error covariance matrix. Specifically we here assumed a diagonal error covariance matrix, with all the diagonal terms equal to 0.0025 m^2; this value is approximately equal to the average dispersion variance of the fine scale piezometric heads within the coarse scale blocks.

4.3.4 Performance Measurements

Since this is a synthetic experiment, the "true" aquifer response, evaluated at the fine scale, is known. We also know the upscaled conductivity tensors for the reference aquifer, which we will use to evaluate the performance of the updated conductivity tensors produced by the EnKF.

The following criteria will be used to analyze the performance of the proposed method and the worth of data:

1. Ensemble mean map. (It should capture the main patterns of variability of the reference map.)

2. Ensemble variance map. (It gives an estimate of the precision of the maps.)

3. Ensemble average absolute bias map, ϵ_X, made up by:

$$\epsilon_{X_i} = \frac{1}{N_e} \sum_{r=1}^{N_e} |X_{i,r} - X_{i,ref}|, \tag{4.13}$$

where X_i is the parameter being analyzed, at location i, $X_{i,r}$ represents its value for realization r, $X_{i,ref}$ is the reference value at location i, and N_e is the number of realizations of the ensemble (200, in this case). (It gives an estimate of the accuracy of the maps.)

4. Average absolute bias

$$AAB(X) = \frac{1}{N_b} \sum_{i=1}^{N_b} \epsilon_{X_i}, \tag{4.14}$$

where N_b is the number of interblocks when X is coarse logconductivity tensor component, or the number of blocks when X is piezometric head. (It gives a global measure of accuracy.)

5. Square root of the average ensemble spread

$$AESP(X) = \left[\frac{1}{N_b} \sum_{i=1}^{N_b} \sigma^2_{X_i} \right]^{1/2}, \tag{4.15}$$

where $\sigma^2_{X_i}$ is the ensemble variance at location i. (It gives a global measure of precision.)

6. Comparison of the time evolution of the piezometric heads at the conditioning piezometers W1 to W9, and at the control piezometers W10 to W13. (It evaluates the capability of the EnKF to update the forecasted piezometric heads using the measured values.)

4.4 Discussion

Ensembles of coarse realizations for the four cases have been generated according to the conditions described earlier. Figure 4.5 shows the evolution of the piezometric heads in piezometers W1 and W9 for the 500 days of simulation; the first 60 steps (66.7 days) were used for conditioning in cases C and D. Similarly, Figure 4.6 shows piezometers W10 and W13; these piezometers

were not used for conditioning. Figure 4.7 shows the ensemble mean and variance of the piezometric heads at the 60th time step, while Figure 4.8 shows the ensemble average absolute bias. Figure 4.9 shows the ensemble mean and variance of $\ln(K_{max})$ for interblocks between rows, and Figure 4.10 shows the ensemble average absolute bias. Finally, Table 4.2 shows the metric performance measurements for $\ln(K_{max})$ between rows and for piezometric heads at the 30th, 60th and 90th time steps.

4.4.1 The EnKF Coupled with Upscaling

The EnKF has the objective of updating conductivity realizations so that the solution of the flow equation on the updated fields will match the measured piezometric heads. Analyzing cases C and D in Figure 4.5, we can observe how the updated fields, when piezometric head is assimilated by the EnKF, produce piezometric head predictions that reproduce the measured values very well, particularly when compared with case A, which corresponds to the case in which no conditioning data are considered. Notice also that piezometric head data are assimilated only for the first 66.7 days (the period in which the heads are almost perfectly reproduced in the EnKF updated fields) while the rest of the simulation period serves as validation. Additional validation of the EnKF generated realizations, is given in Figure 4.6 that shows two of the piezometers not used for conditioning; we can also observe the improvement in piezometric head reproduction for cases C and D as compared to case A. Furthermore, the analysis of Figure 4.7 shows how, for cases C and D, the average spatial distribution, at the end of time step 60, follows closely the reference piezometric head distribution, while the ensemble variance is reduced to very small values everywhere. The ensemble average head bias is also noticeably reduced when conditioning to heads, not just at the conditioning locations (as expected) but also elsewhere. A final analysis to show how conditioning to the heads improves the overall reproduction of the head spatial distribution is by looking at the metrics displayed in Table 4.2. Comparing cases B and C, it is interesting to notice the increasing impact of the conditioning to piezometric heads as time passes; at time step 30, the initial effect of just conditioning to hydraulic conductivity measurements (which occurs from time step 0) is still larger than just conditioning to the heads measured during the first 30 time steps, but at time step 60, this effect is clearly reversed, and it is maintained to time step 90 even though the heads between steps 60 and 90 are not used for conditioning. As expected, conditioning to both piezometric heads and hydraulic conductivities gives the best results in terms of smallest bias and smallest spread.

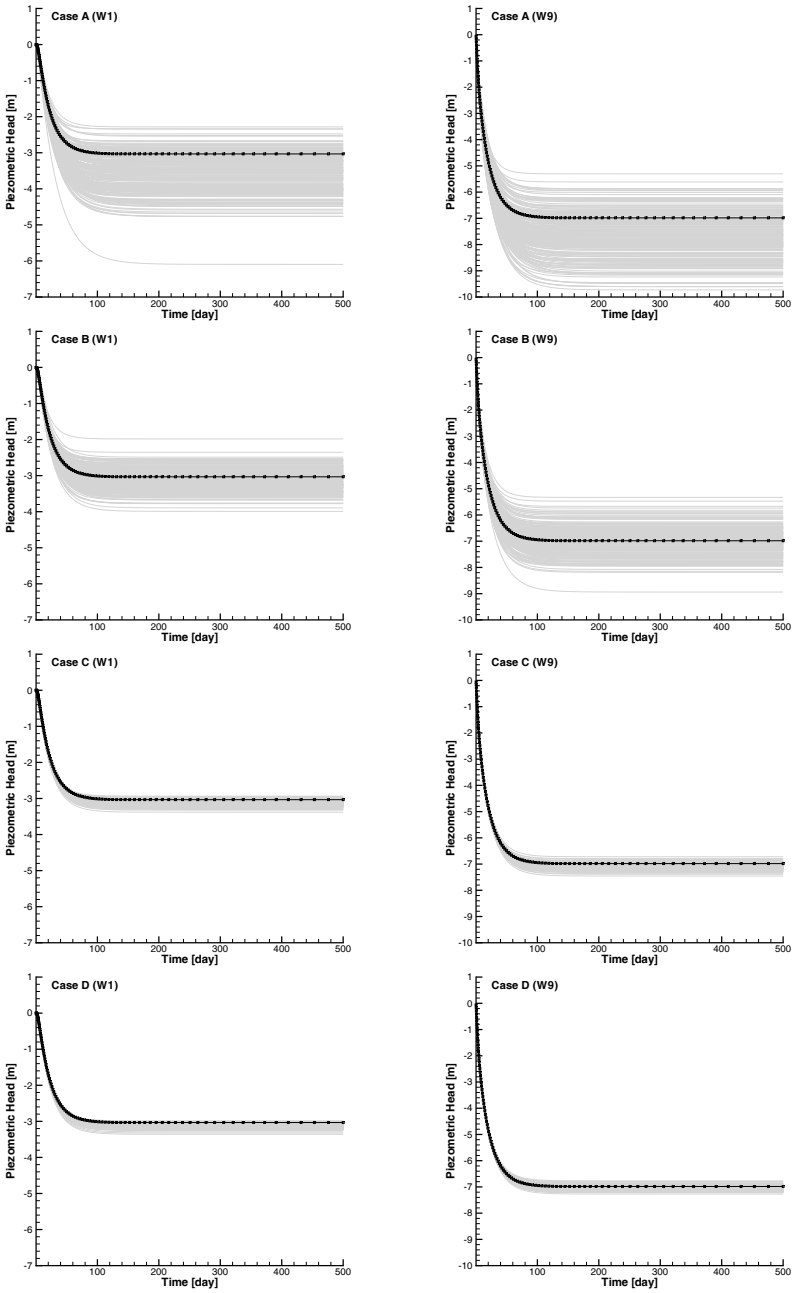

Figure 4.5: Piezometric head time series in the reference field and simulated ones for all cases at wells W1 (left column) and W9 (right column). The piezometric heads measured at these wells during the first 67.7 days were used as conditioning data for cases B and D.

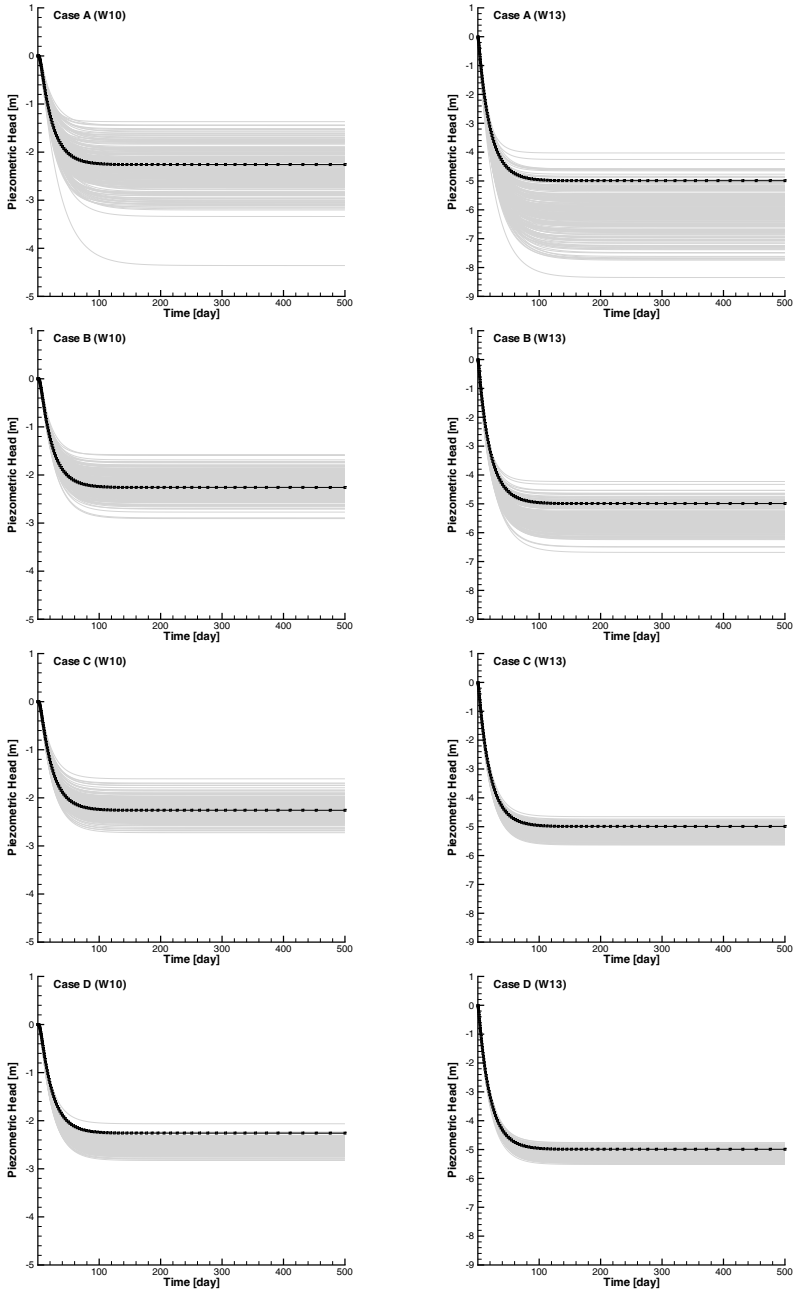

Figure 4.6: Piezometric head time series in the reference field and simulated ones for all cases at control wells W10 (left column) and W13 (right column). These wells were not used as conditioning data for any case.

From this analysis we conclude that the EnKF coupled with upscaling is able to generate an aquifer model at a scale two orders of magnitude coarser than the reference aquifer scale that is conditional to the piezometric heads.

Besides achieving the original goal of the EnKF algorithm, it is also important to contrast the final conductivity model given by the EnKF, with the reference aquifer model. For this purpose we will compare the final ensemble of realizations obtained for cases C and D with the upscaled realization obtained from the reference, fine scale aquifer model. Conditioning to piezometric head data should improve the characterization of the logconductivities. Indeed, this is what happens as it can be seen when analyzing Figures 4.9 and 4.10 and Table 4.2. In these figures only the maximum component of the logconductivity tensors for the interblocks between rows is displayed, but the members of the triplet for the tensor between rows, as well as the members of the triplet for the tensors between columns, show a similar behavior. The ensemble mean maps are closer to the reference map in case that conditioning data are used; the variance maps display smaller values as compared to case A; and the bias map shows values closer to zero than in case A. All in all, we can conclude that the EnKF updates the block conductivity tensors to produce realizations which get closer to the aquifer model obtained after upscaling the reference aquifer.

There remains the issue of conditioning to the fine scale conductivity measurements. Since the fine scale conductivity measurements were used to condition the fine scale realizations, the conditioning should be noticed in the upscaled model only if the correlation scale of the conductivity measurements is larger than the upscaled block size. In such a case (as is the case for the example), the ensemble variance of the upscaled block conductivity values should be smaller for blocks close to conditioning datum locations than for those away from the conditioning points. Case B is conditioned only on the fine scale logconductivity measurements. Comparing cases A and B in Figure 4.9 and in Table 4.2 we notice that for the unconditional case, the ensemble mean of $\ln(K_{max})$ between rows is spatially homogeneous and so is the variance; however, as soon as the fine scale conductivity data are used for the generation of the fine scale realizations, the ensemble of upscaled realizations displays the effects of such conditioning, the ensemble mean starts to show patterns closer to the patterns in the upscaled reference field (Figure 4.3), and the ensemble variance becomes smaller for the interblocks closer to the conditioning measurements. Analyzing case D in Figure 4.9, which takes the ensemble of realizations from case B and updates it by assimilating the piezometric head measurements at piezometers W1 to W9, we conclude that the initial conditioning effect (to hydraulic conductivity data) is reinforced by the new conditioning data, the patterns observed in the ensemble mean maps are even closer to the patterns in the reference realization, and the ensemble vari-

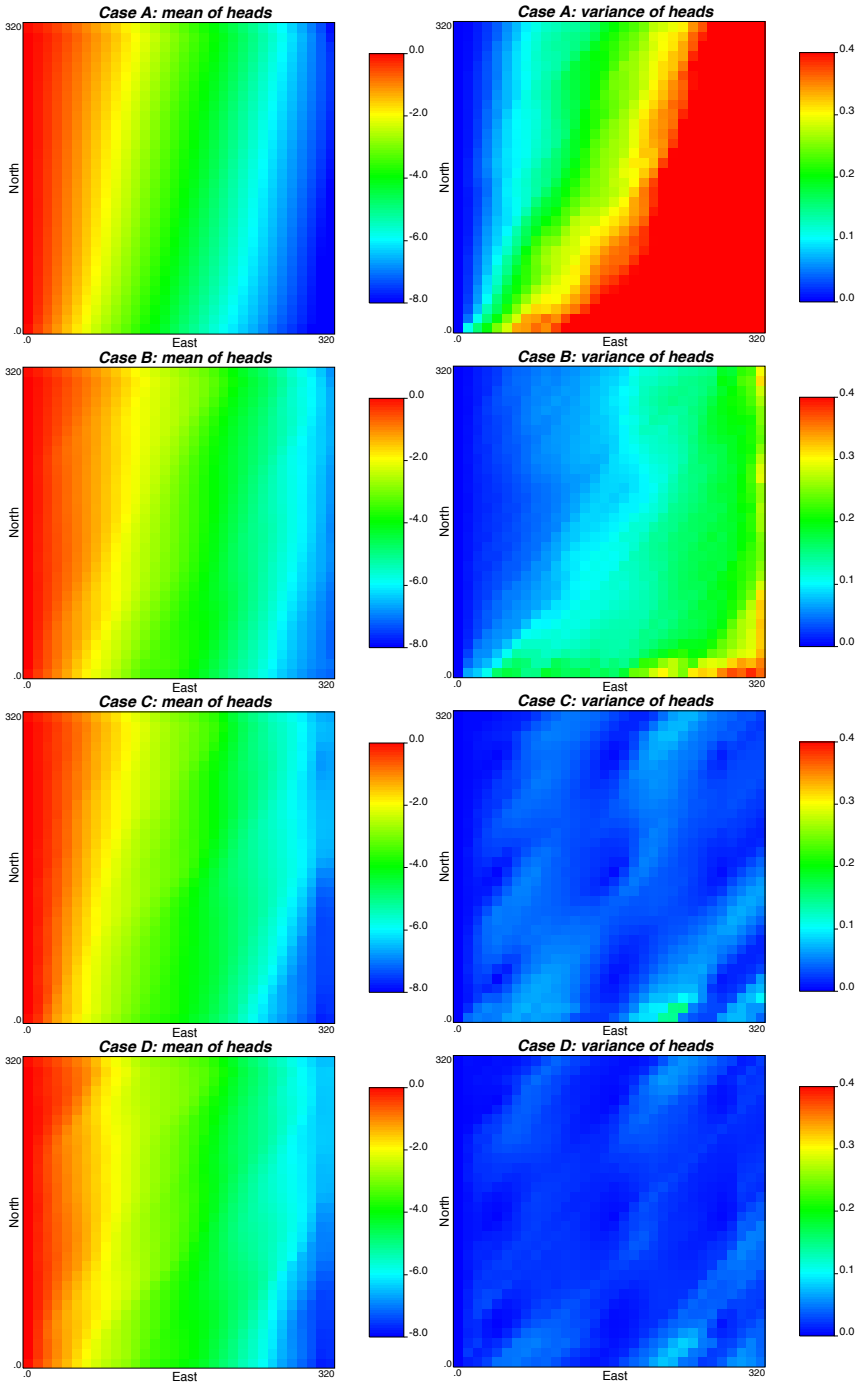

Figure 4.7: Ensemble average and variance of piezometric heads for the different cases.

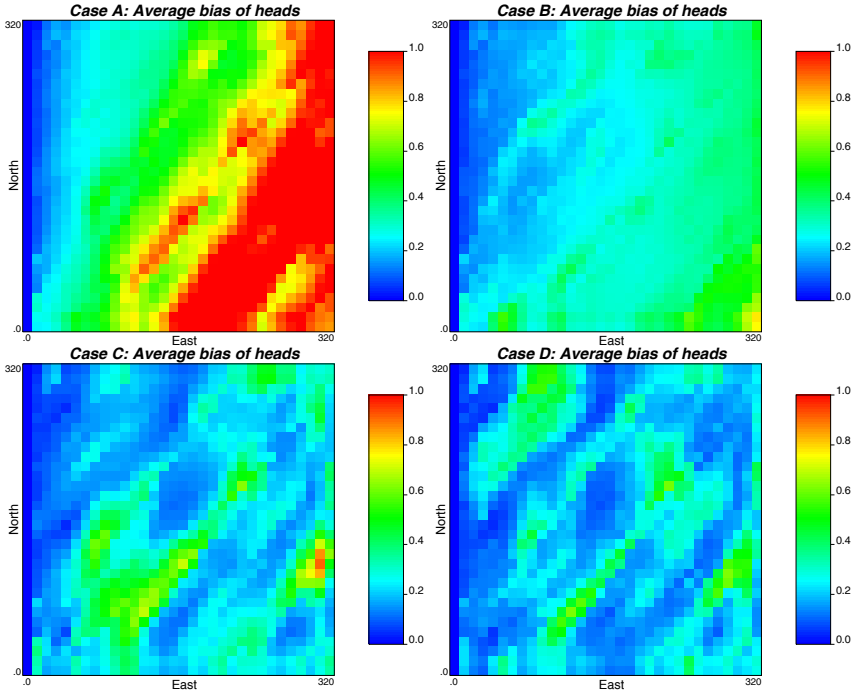

Figure 4.8: Ensemble average absolute bias of piezometric heads for the different cases.

ance remains small close to logconductivity conditioning locations and, overall, is smaller than for case B.

Finally, when no conductivity data are used to condition the initial ensemble of realizations, conditioning to piezometric heads through EnKF also serves to improve the characterization of the logconductivities as can be seen analyzing case C in Figure 4.9 and Table 4.2. Some patterns of the spatial variability of $\ln(K_{max})$ are captured by the ensemble mean and the ensemble variance is reduced with respect to the unconditional case, although in a smaller magnitude than when logconductivity data are used for conditioning.

From this analysis we conclude that conditioning to piezometric head data by the EnKF coupled with upscaling improves the characterization of aquifer logconductivities whether conductivity data are used for conditioning or not.

It should be emphasized that, since the EnKF algorithm starts after the upscaling of the ensemble of fine scale realizations ends, the EnKF-coupled-with-upscaling performance will be much restricted by the quality of the upscaling algorithm. It is important to use as accurate an upscaling procedure as possible in the first step of the process, otherwise the EnKF algorithm may fail. An interesting discussion on the importance of the choice of upscaling can be read in the study of the MADE site by Li et al. (2011a).

4.4.2 Worth of Data

We can use the results obtained to make a quick analysis of the worth of data in aquifer characterization, which confirms earlier findings (e.g., Capilla et al., 1999; Wen et al., 2002; Hendricks Franssen, 2001; Hendricks Franssen et al., 2003) and serves to show that the proposed approach works as expected. By analyzing Figures 4.5, 4.6, 4.7, 4.8, 4.9, and 4.10, and Table 4.2, we can conclude that conditioning to any type of data improves the characterization of the aquifer conductivities, and improves the characterization of the state of the aquifer (i.e., the piezometric heads). The largest improvement occurs when both, hydraulic conductivity and piezometric head measurements are used. These improvements can be seen qualitatively on the ensemble mean maps, which are able to display patterns closer to those in the reference maps; on the ensemble variance maps, which display smaller values than for the unconditional case; and on the ensemble average bias maps, which also show reduced bias when compared with the unconditional case. Quantitatively, the same conclusions can be made by looking at the metrics in the Table. The reproduction of the piezometric heads also improves when conditioning to any type of data.

It is also interesting to analyze the trade-off between conductivity data and piezometric head data by comparing cases B and C. As expected, the characterization of the spatial variability of hydraulic conductivity is better

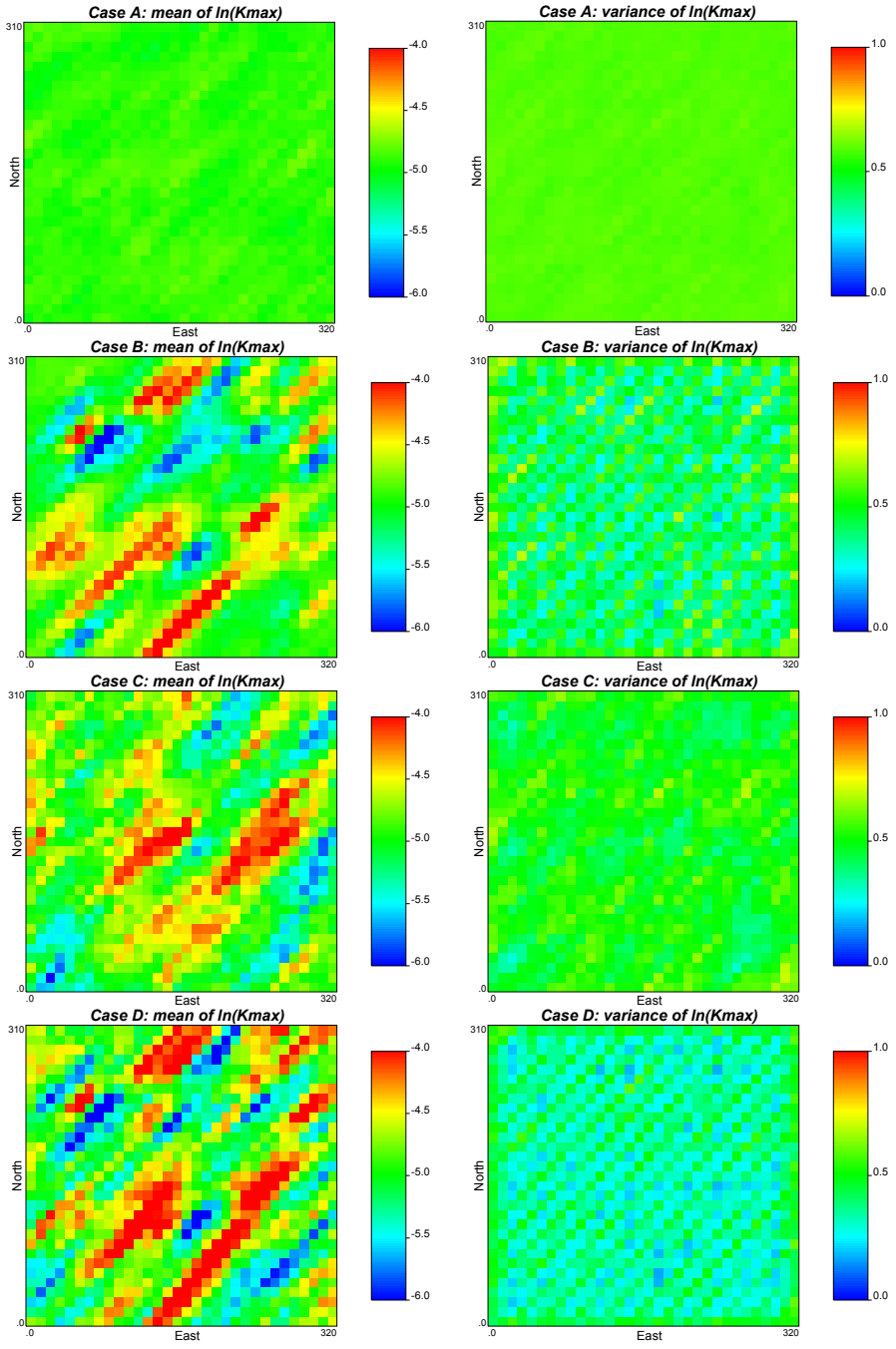

Figure 4.9: Ensemble average and variance of $\ln(Kmax)$ for the different cases.

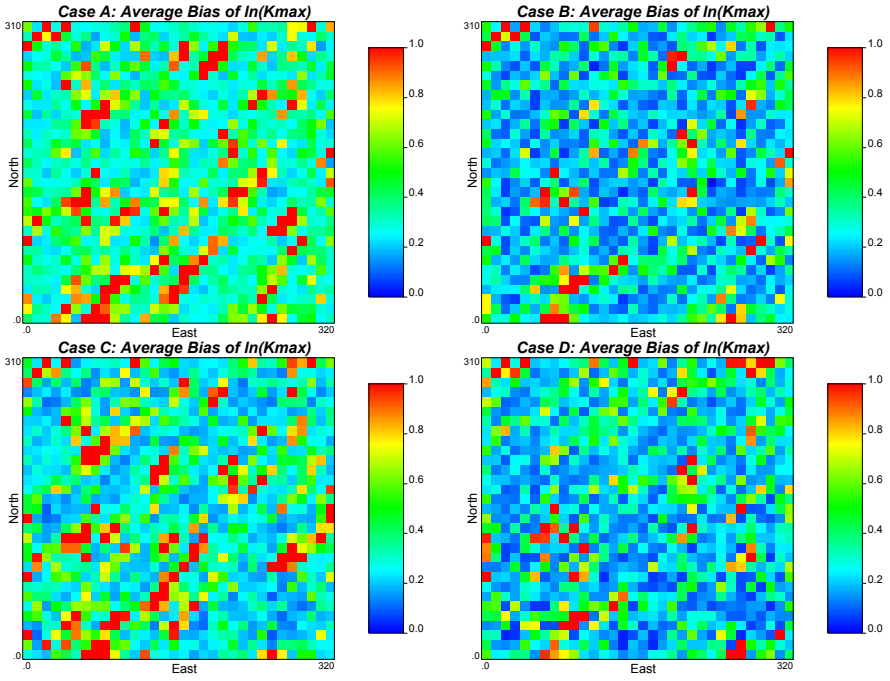

Figure 4.10: Ensemble average absolute bias of $\ln(Kmax)$ for the different cases.

Table 4.2: Bias and spread of predicted heads at time steps 30, 60 and 90 and of updated loghydraulic conductivity $\ln K_{max}^{b,r}$ at time step 60.

	Case A	Case B	Case C	Case D
$AAB(h_{nt=30})$	0.189	0.119	0.124	0.118
$AESP(h_{nt=30})$	0.201	0.132	0.111	0.086
$AAB(h_{nt=60})$	0.580	0.256	0.224	0.195
$AESP(h_{nt=60})$	0.533	0.323	0.186	0.146
$AAB(h_{nt=90})$	0.672	0.281	0.236	0.204
$AESP(h_{nt=90})$	0.627	0.355	0.195	0.153
$AAB(\ln K_{max})$	0.452	0.306	0.417	0.296
$AESP(\ln K_{max})$	0.805	0.660	0.702	0.594

when conductivity data are used for conditioning than when piezometric head are; however, the opposite occurs for the characterization of the piezometric heads.

4.4.3 Other Issues

We have chosen a relatively small-sized fine scale model to demonstrate the methodology, since we needed the solution at the fine scale to create the sets of conditioning data and to verify that the coarse scale models generated by the proposed approach give good approximations of the "true" response of the fine scale aquifer. We envision that the proposed approach should be used only when the implementation of the numerical model and the EnKF are impractical at the fine scale.

To our understanding, it is the first time that the EnKF is applied on an aquifer with conductivities characterized by full tensors. The approach of representing the tensors by their invariants seems to work in this context. More sophisticated EnKF implementations could have been used, which would have worked equally well or better than the standard EnKF.

The example has been demonstrated using a reference conductivity field that was generated following a multiGaussian stationary random function. Could the method be applied to other types of random functions, i.e., non-multiGaussian or non-stationary? It could, as long as each step of the approach (see Section 4.2) could. More precisely, for the first step, the generation of the fine scale hydraulic conductivity measurements, there are already many algorithms that can generate realizations from a wide variety of random functions, including non-multiGaussian and non-stationary; the second step is basically deterministic, we replace an assembly of heterogeneous values by an equivalent

block tensor, the underlying random function used to generate the fine scale realizations has no interference on the upscaling; however, for the third step, the application of EnKF to non-multiGaussian parameter fields is more difficult, some researchers propose moving on to particle filtering (Arulampalam et al., 2002), some others have worked on variants of the EnKF to handle the non-multiGaussianity (Zhou et al., 2011); the non-stationarity is not an issue, since the EnKF deals, by construction, with non-stationary states.

4.5 Conclusion

The "missing scale" issue brought out by Tran (1996) is still, today, much overlooked. Data, particularly conductivity data, are collected at smaller support volumes and in larger quantities than years ago, yet, when constructing a numerical model based on these data, the discrepancy between the scale at which data are collected and the scale of the numerical model is most often disregarded.

We have presented an approach to rigorously account for fine-scale conductivity measurements on coarse-scale conditional inverse modeling. The resulting model is composed of an ensemble of realizations of conductivity tensors at a scale (much) coarser than the scale at which conductivities were measured. The ensemble of final realizations is conditioned to both conductivity and piezometric head measurements. The latter conditioning is achieved by using the ensemble Kalman filter on realizations of conductivity tensors. To handle the tensor parameters, we propose to work with the invariants of the tensors, instead of their representations on a specific reference system, this approach allows the ensemble Kalman filter to perform a tensor updating which produces realizations that are conditioned to the transient piezometric head measurements.

Bibliography

Aanonsen, S. L., Naevdal, G., Oliver, D. S., Reynolds, A. C., Valles, B., 2009. Ensemble kalman filter in reservoir engineering - a review. SPE Journal 14 (3), 393–412.

Arulampalam, M. S., Maskell, S., Gordon, N., Clapp, T., 2002. A tutorial on particle filters for online nonlinear/non-Gaussian Bayesian tracking. IEEE Transactions on signal processing 50 (2), 174–188.

Bear, J., 1972. Dynamics of fluids in porous media. American Elsevier Pub. Co., New York.

Behrens, R., MacLeod, M., Tran, T., Alimi, A., 1998. Incorporating seismic attribute maps in 3D reservoir models. SPE Reservoir Evaluation & Engineering 1 (2), 122–126.

Burgers, G., van Leeuwen, P., Evensen, G., 1998. Analysis scheme in the ensemble Kalman filter. Monthly Weather Review 126, 1719–1724.

Capilla, J., Llopis-Albert, C., 2009. Gradual conditioning of non-Gaussian transmissivity fields to flow and mass transport data: 1. Theory. Journal of Hydrology 371 (1-4), 66–74.

Capilla, J. E., Rodrigo, J., Gómez-Hernández, J. J., 1999. Simulation of non-gaussian transmissivity fields honoring piezometric data and integrating soft and secondary information. Math. Geology 31 (7), 907–927.

Carrera, J., Alcolea, A., Medina, A., Hidalgo, J., Slooten, L., 2005. Inverse problem in hydrogeology. Hydrogeology Journal 13 (1), 206–222.

Chen, Y., Zhang, D., 2006. Data assimilation for transient flow in geologic formations via ensemble Kalman filter. Advances in Water Resources 29 (8), 1107–1122.

Deutsch, C. V., Journel, A. G., 1998. GSLIB, Geostatistical Software Library and User's Guide, 2nd Edition. Oxford University Press, New York.

Durlofsky, L. J., Jones, R. C., Milliken, W. J., 1997. A nonuniform coarsening approach for the scale-up of displacement processes in heterogeneous porous media. Adv. in Water Resour. 20 (5-6), 335–347.

Evensen, G., 2003. The ensemble Kalman filter: Theoretical formulation and practical implementation. Ocean dynamics 53 (4), 343–367.

Freeze, R. A., Cherry, J. A., 1979. Groundwater. Prentice-Hall.

Fu, J., Tchelepi, H. A., Caers, J., 2010. A multiscale adjoint method to compute sensitivity coefficients for flow in heterogeneous porous media. Advances in Water Resources 33 (6), 698–709.

Gómez-Hernández, J. J., 1991. A stochastic approach to the simulation of block conductivity values conditioned upon data measured at a smaller scale. Ph.D. thesis, Stanford University.

Gómez-Hernández, J. J., Journel, A. G., 1993. Joint sequential simulation of multi-Gaussian fields. Geostatistics Troia 92 (1), 85–94.

Gómez-Hernández, J. J., Sahuquillo, A., Capilla, J. E., 1997. Stochastic simulation of transmissivity fields conditional to both transmissivity and piezometric data, 1, Theory. Journal of Hydrology 203 (1–4), 162–174.

Gómez-Hernández, J. J., Srivastava, R. M., 1990. ISIM3D: an ANSI-C three dimensional multiple indicator conditional simulation program. Computers & Geosciences 16 (4), 395–440.

Hendricks Franssen, H., 2001. Inverse stochastic modelling of groundwater flow and mass transport. Ph.D. thesis, Technical University of Valencia.

Hendricks Franssen, H., Alcolea, A., Riva, M., Bakr, M., van der Wiel, N., Stauffer, F., Guadagnini, A., 2009. A comparison of seven methods for the inverse modelling of groundwater flow. application to the characterisation of well catchments. Advances in Water Resources 32 (6), 851–872.

Hendricks Franssen, H., Kinzelbach, W., 2009. Ensemble Kalman filtering versus sequential self-calibration for inverse modelling of dynamic groundwater flow systems. Journal of Hydrology 365 (3-4), 261–274.

Hendricks Franssen, H. J., Gómez-Hernández, J. J., Sahuquillo, A., 2003. Coupled inverse modelling of groundwater flow and mass transport and the worth of concentration data. Journal of Hydrology 281 (4), 281–295.

Hu, L. Y., 2000. Gradual deformation and iterative calibration of gaussian-related stochastic models. Math. Geology 32 (1), 87–108.

Li, L., Zhou, H., Gómez-Hernández, J. J., 2010. Steady-state groundwater flow modeling with full tensor conductivities using finite differences. Computers & Geosciences 36 (10), 1211–1223.

Li, L., Zhou, H., Gómez-Hernández, J. J., 2011a. A comparative study of three-dimensional hydrualic conductivity upscaling at the macrodispersion experiment (MADE) site, on columbus air force base in mississippi (USA). Journal of Hydrology, in press, doi: 10.1016/j.jhydrol.2011.05.001.

Li, L., Zhou, H., Gómez-Hernández, J. J., 2011b. Transport upscaling using multi-rate mass transfer in three-dimensional highly heterogeneous porous media. Advances in Water Resources 34 (4), 478–489.

Mariethoz, G., Renard, P., Straubhaar, J., 2010. The direct sampling method to perform multiple-point geostatistical simulaitons. Water Resources Research 46, W11536.

McLaughlin, D., Townley, L., 1996. A reassessment of the groundwater inverse problem. Water Resources Research 32 (5), 1131–1161.

Naevdal, G., Johnsen, L., Aanonsen, S., Vefring, E., Mar. 2005. Reservoir monitoring and continuous model updating using ensemble kalman filter. SPE Journal 10 (1).

Oliver, D., Chen, Y., 2011. Recent progress on reservoir history matching: a review. Computational Geosciences 15 (1), 185–221.

Peters, L., Arts, R. J., Brower, G. K., Geel, C. R., Cullick, S., Lorentzen, R. J., Chen, Y., Dunlop, N., Vossepoel, F., Xu, R., Sarman, P., H., A. A. H., Reynolds, A., 2010. Results of the brugge benchmark study for flooding optimization and history matching. SPE Reservoir Evaluation & Engineering 13 (3), 391–405.

Renard, P., de Marsily, G., 1997. Calculating equivalent permeability: A review. Advances in Water Resources 20 (5-6), 253–278.

Rubin, Y., Gómez-Hernández, J. J., 1990. A stochastic approach to the problem of upscaling of conductivity in disordered media, theory and unconditional numerical simulations. Water Resour. Res. 26 (4), 691–701.

Sánchez-Vila, X., Guadagnini, A., Carrera, J., 2006. Representative hydraulic conductivities in saturated groundwater flow. Reviews of Geophysics 44 (3).

Strebelle, S., 2002. Conditional simulation of complex geological structures using multiple-point statistics. Mathematical Geology 34 (1), 1–21.

Tran, T., 1996. The 'missing scale' and direct simulation of block effective properties. Journal of Hydrology 183 (1-2), 37–56.

Tran, T., Wen, X., Behrens, R., 1999. Efficient conditioning of 3D fine-scale reservoir model to multiphase production data using streamline-based coarse-scale inversion and geostatistical downscaling. In: SPE Annual Technical Conference and Exhibition.

Tureyen, O., Caers, J., 2005. A parallel, multiscale approach to reservoir modeling. Computational Geosciences 9 (2), 75–98.

Wen, X. H., Deutsch, C., Cullick, A., 2002. Construction of geostatistical aquifer models integrating dynamic flow and tracer data using inverse technique. Journal of Hydrology 255 (1-4), 151–168.

Wen, X. H., Gómez-Hernández, J. J., 1996. Upscaling hydraulic conductivities: An overview. J. of Hydrology 183 (1-2), ix–xxxii.

White, C. D., Horne, R. N., 1987. Computing absolute transmissibility in the presence of Fine-Scale heterogeneity. SPE 16011.

Yeh, W., 1986. Review of parameter identification procedures in groundwater hydrology: The inverse problem. Water Resources Research 22 (2), 95–108.

Zhou, H., Gómez-Hernández, J. J., Hendricks Franssen, H.-J., Li, L., 2011. An approach to handling Non-Gaussianity of parameters and state variables in ensemble Kalman filter. Advances in Water Resources, in press, doi:10.1016/j.advwatres.2011.04.014.

Zhou, H., Li, L., Gómez-Hernández, J. J., 2010. Three-dimensional hydraulic conductivity upscaling in groundwater modelling. Computers & Geosciences 36 (10), 1224–1235.

Zimmerman, D., De Marsily, G., Gotway, C., Marietta, M., Axness, C., Beauheim, R., Bras, R., Carrera, J., Dagan, G., Davies, P., et al., 1998. A comparison of seven geostatistically based inverse approaches to estimate transmissivities for modeling advective transport by groundwater flow. Water Resources Research 34 (6), 1373–1413.

Submitted to Journal of Hydrology.

5

Jointly Mapping Hydraulic Conductivity and Porosity by Assimilating Concentration Data via Ensemble Kalman Filter

Abstract

Real-time data from on-line sensors offer the possibility to update environmental simulation models in real-time. Information from on-line sensors concerning contaminant concentrations in groundwater allow for the real-time characterization and control of a contaminant plume. In this paper it is proposed to use the CPU-efficient Ensemble Kalman Filter (EnKF) method, a data assimilation algorithm, for jointly updating the flow and transport parameters (hydraulic conductivity and porosity) and state variables (piezometric head and concentration) of a groundwater flow and contaminant transport problem. A synthetic experiment is used to demonstrate the capability of the EnKF to estimate hydraulic conductivity and porosity by assimilating dynamic head and multiple concentration data in a transient flow and transport model. In this work the worth of hydraulic conductivity, porosity, piezometric head, and

concentration data is analyzed in the context of aquifer characterization and prediction uncertainty reduction. The results indicate that the characterization of the hydraulic conductivity and porosity fields is continuously improved as more data are assimilated. Also, groundwater flow and mass transport predictions are improved as more and different types of data are assimilated. The beneficial impact of accounting for multiple concentration data is patent.

5.1 Introduction

During the last several decades numerical simulation is routinely utilized to evaluate the groundwater resources and predict the fate of contaminant plumes. The adequate characterization of spatially distributed hydrogeological parameters like hydraulic conductivity and porosity plays an important role in groundwater flow and transport simulations. However, due to the scarcity of measurements in combination with the large spatial heterogeneity it is not trivial how to characterize the spatial distribution of the mentioned parameters, and, consequently, groundwater flow and transport predictions call for an uncertainty assessment. Inverse modeling is often used to reduce model uncertainty by jointly conditioning on hard data (e.g., hydraulic conductivity and porosity) and indirect data (e.g., the observed state information, such as piezometric heads, concentrations and temperatures) to characterize the spatial variation of hydrogeological parameters. The issue of how to condition on the direct measurements has been extensively investigated in the geostatistical literature (e.g., Journel, 1974; Gómez-Hernández and Srivastava, 1990; Strebelle, 2002). Likewise, inverse modeling, i.e., conditioning to indirect data, has been reviewed in the literature (e.g., Yeh, 1986; McLaughlin and Townley, 1996; Zimmerman et al., 1998; Carrera et al., 2005; Hendricks Franssen et al., 2009). Commonly, inverse methods define an objective function that includes the mismatch between calculated and observed state values, as well as the perturbation of the initial parameter estimates. This objective function is minimized by an optimization approach. Examples are the self-calibration method (Sahuquillo et al., 1992; Gómez-Hernández et al., 1997; Capilla et al., 1999; Wen et al., 2002; Hendricks Franssen et al., 2003), the pilot point method (Ramarao et al., 1995; LaVenue et al., 1995; Alcolea et al., 2006), the Markov chain Monte Carlo method (Oliver et al., 1997), and the gradual deformation method (Hu, 2000; Capilla and Llopis-Albert, 2009).

Albeit the abundant literature on inverse conditioning of conductivities to piezometric head, only a few works have paid attention on jointly conditioning on head and concentration data to improve the characterization of multiple hydrogeological parameters. Medina and Carrera (1996) extended the maximum likelihood approach (Carrera and Neuman, 1986) to condition on concentra-

tion data for a better characterization of zoned hydraulic conductivity maps. The main shortcoming of this approach is that the small-scale heterogeneity is ignored due to the estimation of hydraulic conductivity for larger zones. Hendricks Franssen et al. (1999) calibrated both hydraulic conductivity and storativity by conditioning to transient head data using the self-calibration method (Gómez-Hernández et al., 1997). More recently, Hendricks Franssen et al. (2003) further extended the self-calibration method to calibrate hydraulic conductivity by conditioning on piezometric head and concentration data. Huang et al. (2004) also employed the self-calibration method to jointly identify hydraulic conductivity and sorption partitioning coefficient by conditioning on tracer breakthrough data. Fu and Gómez-Hernández (2009) employed the block Markov chain Monte Carlo method to calibrate conductivity by jointly conditioning to head and travel time data. Llopis-Albert and Capilla (2009) utilized the gradual deformation method to estimate the conductivity by incorporating head, concentration and travel time data. Schwede and Cirpka (2009) used the quasi-linear geostatistical approach of Kitanidis (1995) to estimate conductivity by conditioning on steady-state concentration measurements. Barnhart et al. (2010) employed PEST (Doherty, 2004), a model-independent nonlinear parameter estimation program, to calibrate hydraulic conductivity by conditioning to concentration data collected from wireless sensor networks. These approaches are able to generate multiple equally-likely parameter fields conditional to static and dynamic measurements, thus capable of depicting small-scale variability of hydraulic conductivity. However, the main shortcoming of those methods is that they are CPU-intensive; these methods require running the forward model multiple times during the iterative optimization process of each realization.

The Ensemble Kalman Filter (EnKF) (Burgers et al., 1998; Evensen, 2003), based on the sequential Bayesian updating rule, can be used to obtain results similar to those obtained by Monte-Carlo (MC) type inverse methods but with reduced CPU time (see section 5.2.2), and it is also flexible to incorporate multiple sources of uncertainty. Hendricks Franssen and Kinzelbach (2009) carried out a synthetic exercise and demonstrated that EnKF needs around a factor of 80 less CPU time than the self-calibration method to attain similar results. The EnKF can also handle data from on-line sensors that become available in real-time and assimilate them into an on-line model. The traditional inverse methods are not well suited to assimilate information that becomes available in real-time. EnKF provides an ensemble of updated stochastic realizations which can be used for uncertainty analysis.

The EnKF is increasingly applied, in atmospheric sciences, land-atmosphere interaction, petroleum engineering and hydrogeology (e.g. Anderson, 2001; Reichle et al., 2002; Wen and Chen, 2005; Chen and Zhang, 2006; Nowak, 2009; Hendricks Franssen et al., 2011; Zhou et al., 2011b). In atmospheric sciences

or land surface models in general only the model states are updated, whereas in petroleum engineering and hydrogeology both system parameters and state variables are commonly addressed (Naevdal et al., 2005).

The EnKF has been successfully applied to assimilate dynamic piezometric head data to improve model predictions (e.g., Chen and Zhang, 2006; Hendricks Franssen and Kinzelbach, 2008; Sun et al., 2009; Li et al., 2011c; Zhou et al., 2011a). With regard to assimilating concentration data, Huang et al. (2008) conducted a synthetic experiment and calibrated hydraulic conductivity fields by assimilating piezometric head and concentration data. In their experiment, flow was at steady-state. Liu et al. (2008) estimated multiple parameters (i.e., hydraulic conductivity, dispersivities, mobile/immobile porosities) by assimilating piezometric head and concentration data in the steady-state flow model for the MADE site. It is worth to note that they used constant values as the prior estimates for the mentioned parameters, and perturbed the parameters, by assimilating observation data via EnKF, to yield heterogeneous fields. Our aim is to quantify the uncertainty of parameters and states starting with heterogeneous fields by conditioning on the direct measurements. Schöniger et al. (2011) assimilated normal-score transformed concentration data to calibrate hydraulic conductivities. They concluded that the improvement by the normal-score transformation (as compared with the classical EnKF, which uses untransformed data) is limited because after univariate normal transformation of the state variable, the concentration distribution is far from multi-Gaussian.

In comparison with the effort devoted to characterize the spatial variability of hydraulic conductivity by conditioning state information, less attention has been paid to identifying the spatial variability of porosity, probably due to its relatively small spatial variability ranging from 0.1 to 0.55 in unconsolidated granular aquifers (Freeze and Cherry, 1979). Additionally, various authors (e.g., Hassan, 2001; Riva et al., 2008; Hu et al., 2009; Jiang et al., 2010) have demonstrated (both in synthetic examples and real aquifers) the significance of accounting for the heterogeneity of porosity on predictions of solute movement.

We will demonstrate the capability of the EnKF to jointly map the hydraulic conductivity and porosity fields by assimilating dynamic piezometric head and multiple concentration data. Few studies have considered the conditioning with help of both multiple concentration data and dynamic piezometric head data to characterize unknown parameters. Also, to the best of our knowledge, this is the first work proposing the joint estimation of spatially distributed hydraulic conductivity and porosity fields in hydrogeology.

The remaining of this paper is organized as follows. We first summarize in section 5.2 the mathematical framework of the EnKF and discuss the jointly mapping of hydraulic conductivity and porosity by assimilating multiple concentration data. In section 5.3, a synthetic example is used to demonstrate

the effectiveness of the EnKF. The paper ends with summary and conclusions in section 5.4.

5.2 Data Assimilation with the EnKF

First, the flow and transport equations (i.e, the transfer functions) will be presented, and then the algorithm of EnKF is introduced with emphasis on the assimilation of concentration data.

5.2.1 Flow and Transport Equations

The well known flow equation of an incompressible or slightly compressible fluid in saturated porous media can be expressed by combining Darcy's Law and the continuity equation (Bear, 1972; Freeze and Cherry, 1979):

$$\nabla\cdot\big(K\nabla h\big) = S\frac{\partial h}{\partial t} + W \tag{5.1}$$

where K is the hydraulic conductivity $[LT^{-1}]$ (which, without loss of generality, will be considered as a scalar at the characterization scale), h is the piezometric head $[L\,]$; W represents sources or sinks $[L^3\,T^{-1}]$; S is the specific storage coefficient $[L^{-1}]$; t is the time $[\,T\,]$; $\nabla\cdot = (\partial/\partial x + \partial/\partial y + \partial/\partial z)$ is the divergence operator of a vector field, and $\nabla = (\partial/\partial x, \partial/\partial y, \partial/\partial z)^T$ is the gradient operator of a scalar field.

Solute transport with linear equilibrium adsorption is governed by the following differential equation (Bear, 1972; Freeze and Cherry, 1979):

$$\phi R\frac{\partial c}{\partial t} = \nabla(\phi\mathbf{D}\cdot\nabla c) - \nabla\mathbf{q}c \tag{5.2}$$

where c is solute concentration of solute in the water phase $[ML^{-3}]$; ϕ is the porosity [dimensionless]; $\mathbf{D}$ is the local hydrodynamic dispersion coefficient tensor $[L^2T^{-1}]$, with eigenvalues associated with principal axes parallel and perpendicular to the direction of flow, defined as $D_I = \alpha_L|\mathbf{q}| + D_m$, $D_{II} = \alpha_T|\mathbf{q}| + D_m$, $D_{III} = \alpha_T|\mathbf{q}| + D_m$ (α_L and α_T are respectively the longitudinal and transverse pore-scale dispersivity; D_m is the molecular diffusion coefficient set to zero in this study, and $\mathbf{q}$ is the Darcy velocity given by $\mathbf{q} = -K\nabla h$ $[LT^{-1}]$); R is retardation factor expressed by $R = 1 + \rho_b K_d/\phi$ (ρ_b is the bulk density of soil; K_d is the distribution coefficient).

5.2.2 Ensemble Kalman Filter

Extensive descriptions of EnKF and its algorithm can be found in Burgers et al. (1998) and Evensen (2003). Here, we mainly focus on the use of EnKF

with updating both parameters (i.e., hydraulic conductivity and porosity) and states (i.e., piezometric head and concentration). It involves a forecast step and an analysis step, after the generation of the initial ensemble of hydraulic conductivity and porosity realizations.

- Step 1: Forecast model. The flow equation (5.1) or transport equation (5.2) is solved, i.e.,

$$\mathbf{Y}_k = f(\mathbf{X}_{k-1}, \mathbf{Y}_{k-1}), \tag{5.3}$$

where $\mathbf{Y}_k$ is the state of the system (piezometric heads and/or concentration data) at time step t_k, f represents the groundwater flow and transport model (including boundary conditions, external stresses, and known parameters), and $\mathbf{X}_{k-1}$ denotes the model parameters (hydraulic conductivity and/or porosity) after the latests update at time t_{k-1}. Specifically, $\mathbf{X}$ and $\mathbf{Y}$ are expressed as:

$$\begin{cases} \text{Case A}: \mathbf{X} = \big[\ln K\big]^T & \mathbf{Y} = \big[h\big]^T, & \text{if only } h \text{ data are available.} \\ \text{Case B}: \mathbf{X} = \big[\ln K, \boldsymbol{\phi}\big]^T & \mathbf{Y} = \big[c\big]^T, & \text{if only } c \text{ data are available.} \\ \text{Case C}: \mathbf{X} = \big[\ln K, \boldsymbol{\phi}\big]^T & \mathbf{Y} = \big[h, c\big]^T, & \text{if } h \text{ and } c \text{ data are available.} \end{cases} \tag{5.4}$$

- Step 2: Analysis step. Using the observed dynamic piezometric head and concentration data, the model parameters are updated as follows:

  1. Build the joint vector $\boldsymbol{\Psi}_k$, which includes the parameters ($\mathbf{X}$) and the forecasted state values ($\mathbf{Y}$). This vector can be split into as many members as there are realizations in the ensemble, with

$$\boldsymbol{\Psi}_{k,j} = \begin{bmatrix} \mathbf{X} \\ \mathbf{Y} \end{bmatrix}_{k,j}, \tag{5.5}$$

  being the j^{th} ensemble member of the augmented state vector at time t_k.

  As an example, if the number of discretization blocks in the domain is N_k and we are in case C, i.e., updating both $\ln K$ and ϕ using both h and c data, the dimension of vector $\boldsymbol{\Psi}_k$ will be $4 \times N_k$.

  2. The joint vector is updated, realization by realization, by assimilating the observations ($\mathbf{Y}_k^{obs}$):

$$\boldsymbol{\Psi}_{k,j}^a = \boldsymbol{\Psi}_{k,j}^f + \mathbf{G}_k\Big(\mathbf{Y}_{k,j}^{obs} + \boldsymbol{\epsilon} - \mathbf{H}\boldsymbol{\Psi}_{k,j}^f\Big), \tag{5.6}$$

  where the superscripts a and f denote analysis and forecast, respectively; $\boldsymbol{\epsilon}$ is a random observation error vector; $\mathbf{H}$ is a linear operator that interpolates the forecasted heads to the measurement

locations, and, in our case, is composed of $0's$ and $1's$ since we assume that measurements are taken at block centers. Therefore, equation (5.6) can be expressed as:

$$\mathbf{\Psi}^a_{k,j} = \mathbf{\Psi}^f_{k,j} + \mathbf{G}_k\Big(\mathbf{Y}^{obs}_{k,j} + \boldsymbol{\epsilon} - \mathbf{Y}^f_{k,j}\Big), \tag{5.7}$$

where the Kalman gain $\mathbf{G}_k$ is given by:

$$\mathbf{G}_k = \mathbf{P}^f_k\mathbf{H}^T\Big(\mathbf{H}\mathbf{P}^f_k\mathbf{H}^T + \mathbf{R}_k\Big)^{-1}, \tag{5.8}$$

where $\mathbf{R}_k$ is the measurement error covariance matrix, and $\mathbf{P}^f_k$ contains the covariances between the different components of the state vector. $\mathbf{P}^f_k$ can be estimated from the ensemble of forecasted results as:

$$\begin{aligned}\mathbf{P}^f_k &\approx E\left[\left(\mathbf{\Psi}^f_{k,j} - \overline{\mathbf{\Psi}}^f_{k,j}\right)\left(\mathbf{\Psi}^f_{k,j} - \overline{\mathbf{\Psi}}^f_{k,j}\right)^T\right] \\ &\approx \sum_{j=1}^{N_e}\frac{\left(\mathbf{\Psi}^f_{k,j} - \overline{\mathbf{\Psi}}^f_{k,j}\right)\left(\mathbf{\Psi}^f_{k,j} - \overline{\mathbf{\Psi}}^f_{k,j}\right)^T}{N_e},\end{aligned} \tag{5.9}$$

where N_e is the number of realizations in the ensemble, and the overbar denotes average over the ensemble.

In the implementation of the algorithm, it is not necessary to calculate explicitly the full covariance matrix $\mathbf{P}^f_k$ (of dimensions $(4 \times N_k) \times (4 \times N_k)$ for case C). The matrix $\mathbf{H}$ is very sparse, and, consquently, the matrices $\mathbf{P}^f_k\mathbf{H}^T$ and $\mathbf{H}\mathbf{P}^f_k\mathbf{H}^T$ can be computed directly at a strongly reduced CPU cost.

- Step 3: Loop back. The updated states become the current states and the forecast-analysis loop is started again.

When the number of observation locations used in the assimilation step is not very large, the computational cost of calculating the covariances is limited. The main cost is related with the forward simulations for each of the stochastic realizations.

During the updating step, the forecasted state variables may have no physical meaning, e.g., negative concentrations. In our case, we remove negative values resetting them to zero. We have checked that when this may happen at locations far from the concentration plume and always with small values. This approach follows the one by Gu and Oliver (2006), who had a similar problem when dealing with water saturation in a reservoir characterization exercise.

Table 5.1: Parameters of the random functions for modeling the spatial distributions of $\ln K$ and porosity

	Mean	Variance	Variogram type	λ_x [m]	λ_y [m]	rotation angle β
$\ln K$	-5	1	exponential	180	60	45°
ϕ	0.3	0.0036	exponential	240	60	45°

β denotes the rotation angle of one clockwise rotation of positive y axis.

The algorithm is implemented in the C software EnKF3D which is used in conjunction with finite-difference program MODFLOW (Harbaugh et al., 2000), to solve the confined transient flow equation (5.1), and the solute transport code MT3DMS (Zheng et al., 1999). MT3DMS uses a third-order total-variation-diminishing (TVD) solution scheme, to solve the transport equation (5.2).

5.3 Synthetic Example

In this section, a synthetic example will be presented to demonstrate the capability of the EnKF to calibrate the hydraulic conductivities and porosities by assimilating piezometric head and concentration data. The resulting ensemble of realizations will be used also for uncertainty characterization; in a real-world case study, uncertainty may stem both from the conceptual model (e.g., the boundary conditions, aquifer geometry) and from the parameters. Here, we only consider the uncertainty due to the heterogeneity of hydraulic conductivity and porosity, no conceptual uncertainty is considered.

5.3.1 Experiment Setup

Reference Field

The reference conductivity and porosity fields are generated using the code GCOSIM3D (Gómez-Hernández and Journel, 1993) over a domain of 250 m $\times$ 250 m $\times$ 1 m, which is discretized into grid cells of size 5 m by 5 m by 1 m (see Figure 5.1A and 5.1C). Here, we assume that the two variables are independent of each other. The parameters of each random function are listed in Table 5.1. From these reference realizations nine conductivity and nine porosity data are sampled for conditioning purposes. The locations are shown in Figure 5.1B and 5.1D.

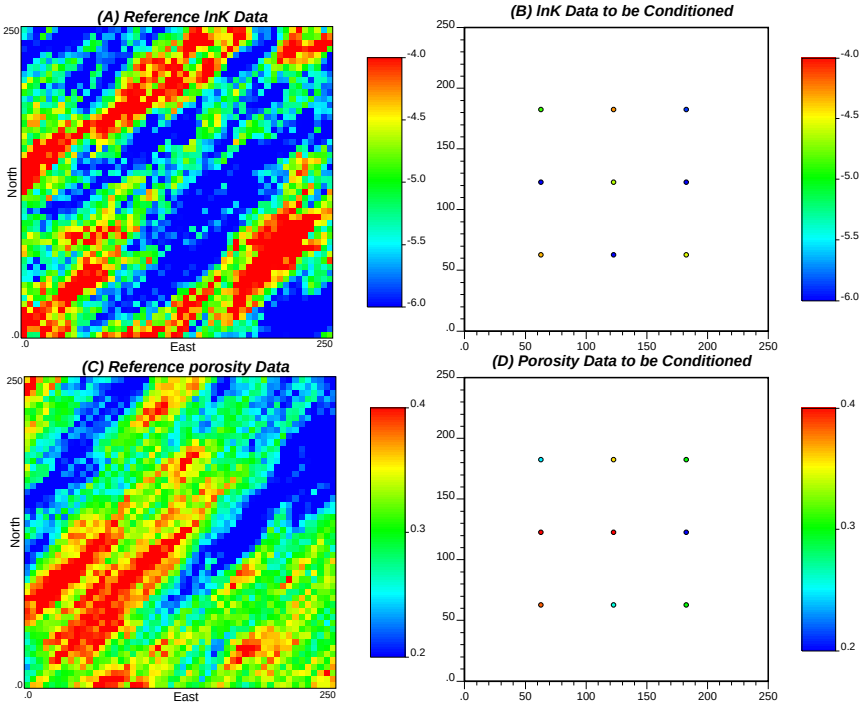

Figure 5.1: (A) Reference $\ln K$ field, (B) Conditioning $\ln K$ data, (C) Reference porosity(ϕ) field, (D) Conditioning porosity(ϕ) data.

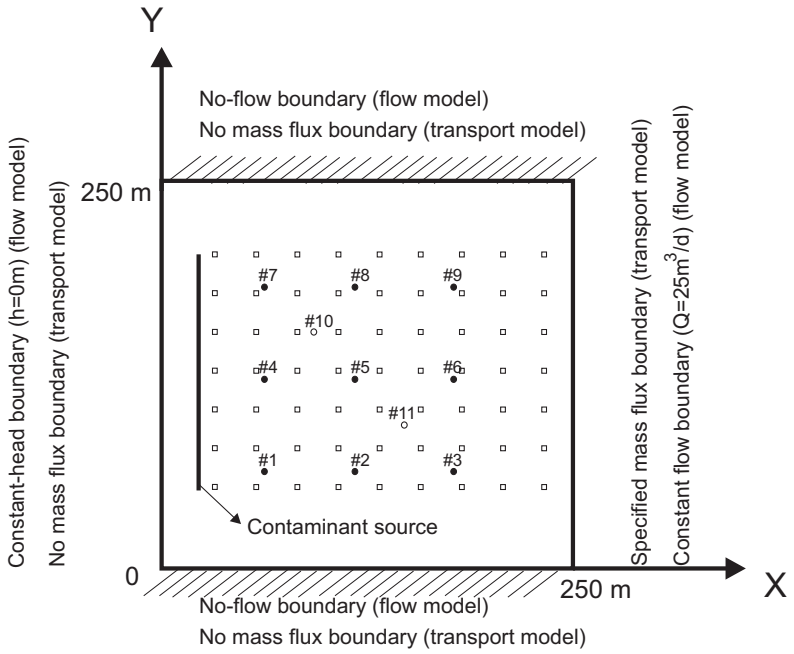

Figure 5.2: Sketch of the flow and transport simulation with boundary conditions and observation and prediction wells. Filled circles correspond to the pressure head observation wells (#1-#9); Open circles denote the control wells (#10-#11). Empty squares indicate the wells where concentration is sampled.

It is assumed that the sampled data have the same support as the grid cell. If the data support would be much smaller than the grid cell size, the additional problem of upscaling must be considered for generating the parameter realizations conditional to the direct measured data (e.g., Li et al., 2011a; Zhou et al., 2010; Li et al., 2011b).

The aquifer is assumed to be confined with impermeable boundaries on south and north, prescribed head values on the western boundary and constant flow rate on the eastern boundary (see Figure 5.2). The prescribed head value is 0 m along the western boundary. The total flow rate through the eastern boundary is -25 m^3/d, distributed uniformly along the boundary. The initial head value is 0 m over the entire domain. The total simulation time is 500 days, and this period is discretized into 100 time steps following a geometric sequence of ration 1.05. Specific storage is assumed constant with a value of 0.003 m^{-1}. The simulated dynamic piezometric heads at the observation wells #1 to #9 in Figure 5.2 are sampled and will be used as assimilating data. The simulated heads at the wells #10 and #11 will be used as validation data.

The boundary conditions for the transport model are no-mass flux boundaries on the western, northern, and southern borders of the model. The eastern border is a specified advective mass flux boundary, acting as a line of sinks taking mass out of the aquifer (see Figure 5.2).

The code MODFLOW (Harbaugh et al., 2000) is used to solve the transient groundwater flow equation for the reference field and the pore velocities across the grid cell interfaces are calculated using the porosities in Figure 5.1C. This velocity field is used as input for solving the solute transport problem with help of the MT3DMS code (Zheng et al., 1999). We only consider advection and dispersion as transport mechanisms with $\alpha_L = 1.0$ m and $\alpha_T = 0.1$ m. Conservative solute is uniformly placed over a line transverse to the groundwater flow at time $t = 0$ (see Figure 5.2). The source concentration is 900 ppm. To avoid the boundary effect as described by Naff et al. (1998), the contaminant source is separated 20 m from the western boundary and 50 m from the northern and southern boundaries. The plume snapshots at 300, 400 and 500 days will be used here to compare the EnKF solutions with the reference plume maps (see Figures 5.3A, 5.3C and 5.3E). The concentration is measured at 63 wells, uniformly distributed over the domain (see Figure 5.2). These measured multiple concentration data (see Figures 5.3B, 5.3D, 5.3F) will serve as assimilating data.

Scenario Studies

Six simulation scenarios are considered for which different types of measurement data are assimilated (see Table 5.2). Scenario 1 (S1) is an unconditional case. In Scenario 2 (S2) geostatistical simulation (Gómez-Hernández and Journel, 1993) is used in order to condition on the nine measured hydraulic conductivities and the nine porosities shown in Figures 5.1B and 5.1D, repsectively. For S1 and S2, 500 realizations of hydraulic conductivity and porosity are generated using the same random functions as for the reference fields. Flow and transport are calculated for each of the 500 $\ln K$-ϕ realization couples, without conditioning to head or concentration data.

For scenario 3 (S3) dynamic piezometric head data are used to update the geostatistical realizations conditioned on hydraulic conductivity and porosity data of scenario S2. Piezometric head data from wells #1 to #9 are sequentially assimilated for the first 60 time steps (approximately 67.7 days).

In scenarios 4, 5 and 6 (S4, S5, S6) concentration data are assimilated by EnKF, in addition to hydraulic conductivity data and piezometric head data. S4 uses concentration data at 400 days, S5 uses concentration data at 300 and 400 days, and S6 uses concentration data at 300, 400 and 500 days.

The piezometric head and concentration data are sampled from the reference simulations without error. However, during the assimilation process it

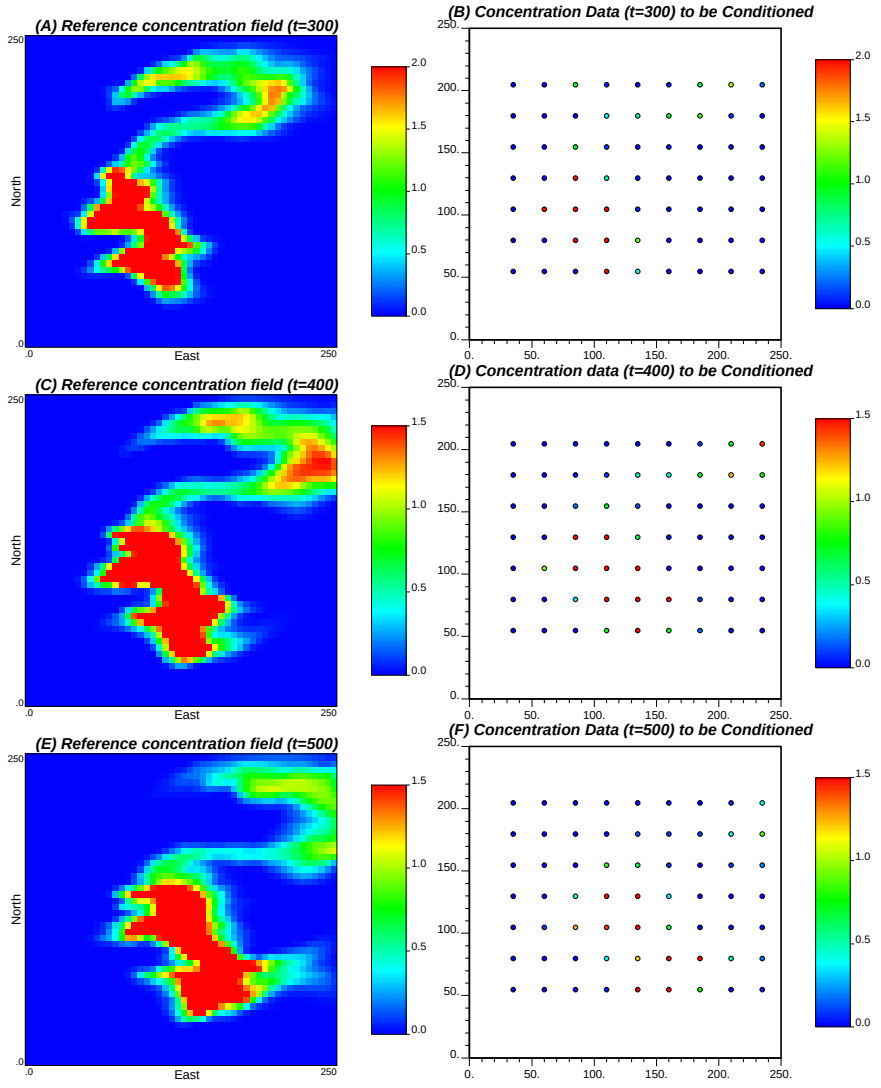

Figure 5.3: Reference concentration fields at time 300(A), 400(C) and 500(E) days. Conditioning concentration data at time 300 (B), 400 (D), and 500 (F) days.

Table 5.2: Definition of scenarios based on the different sets of conditioning data.

Scenario	S1	S2	S3	S4	S5	S6
Hydraulic conductivities (K)	No	Yes	Yes	Yes	Yes	Yes
Porosity (ϕ)	No	Yes	Yes	Yes	Yes	Yes
Dynamic piezometric heads (h)	No	No	Yes	Yes	Yes	Yes
Concentrations ($t = 300$ day)	No	No	No	Yes	Yes	Yes
Concentrations ($t = 400$ day)	No	No	No	No	Yes	Yes
Concentrations ($t = 500$ day)	No	No	No	No	No	Yes

is considered that the data might contain measurement errors and therefore a diagonal error covariance matrix was used, with all non-zero terms equal to 0.0025 m^2 for head data and 0.0025 ppm^2 for concentration data. We note, in practice, the errors for the heads and concentration data would be not the same, and the observation errors would change with the time. From an operational point of view, it is straightforward to integrate them into the assimilation procedure.

5.3.2 Assessment Measures

The results for the six scenarios will be analyzed with the help of two metrics:

1. The average absolute bias (AAB) is a measure of accuracy and defined as follows:
$$AAB(X) = \frac{1}{N_b}\sum_{i=1}^{N_b}\frac{1}{N_e}\sum_{r=1}^{N_e}|X_{i,r} - X_{ref,i}| \tag{5.10}$$
where X_i is, either the logconductivity $\ln K$, porosity ϕ, hydraulic head h or concentration c, at location i, $X_{i,r}$ represents its value for realization r, $X_{ref,i}$ is the reference value at location i, N_b is number of nodes, and N_e is the number of realizations in the ensemble (500, in this case).

2. The ensemble spread ($AESP$) represents the estimated uncertainty and defined as follows:
$$AESP(X) = \left(\frac{1}{N_b}\sum_{i=1}^{N_b}\sigma^2_{X_i}\right)^{1/2}, \tag{5.11}$$
where $\sigma^2_{X_i}$ is the ensemble variance at location i.

The smaller the values for AAB and $AESP$, the better the prediction of variable X.

5.3.3 Data Assimilation Results

Hydraulic Conductivities and Porosities

Figures 5.4 and 5.5 show the ensemble mean and variance of the 500 log-conductivity realizations for all six scenarios. Figures 5.6 and 5.7 show the ensemble mean and variance of the 500 porosity realizations and scenarios. The ensemble mean is used to check whether the main patterns of variability of the parameter are captured. In contrast to the individual realization showing distinctive patterns of high and low values, the ensemble means are smoothed representations of the spatial variability of the parameters. The ensemble variance illustrates how conditioning reduces the differences between the realizations.

In scenario 1, with no conditional data, the ensemble mean and variance of $\ln K$ and ϕ are very close to the prior mean and variance. In scenario 2, using 9 conditioning hydraulic conductivities and porosities, the overall spatial patterns are captured, resulting in typical kriging maps. The ensemble variance maps show the typical bull-eye look of kriging maps, with zero variance at the sample locations and increasing variance away from them. The dynamic piezometric head data included in S3 help to capture better the main patterns of hydraulic conductivity with a further reduction of the variance. S4, S5 and S6 also include concentration data for conditioning. The ensemble mean maps better delineate the main patterns of variability, and at the same time, unlike previous scenarios with strongly smoothed representations of $\ln K$, also show some degree of the small-scale variability. The characterization of the main patterns of $\ln K$ improves quite remarkable with the conditioning of concentration data. For the scenario that uses the largest amount of conditioning data (S6), the patterns in the left upper corner of the area are identified very well, whereas this is not the case if only hydraulic conductivity, porosity and piezometric heads are used for conditioning. The role of concentration data on the characterization of porosity is also observable. The main patterns of porosity are clearer than without conditioning, and closer to the reference distribution. As expected, the ensemble variance, both for $\ln K$ and ϕ, reduces further in S6 as compared with the other scenarios.

From a more quantitative point of view, the calculated two metrics (see Table 5.3) lead to similar conclusions. When the measured hydraulic conductivity, porosity, piezometric head and multiple concentration data are all used for conditioning (S6), the average absolute bias and the ensemble spread have the smallest values. More precisely, when conditioning to $\ln K$, the $AAB(\ln K)$ decreases 14% (S2 vs. S1), if we further condition to piezometric head, $AAB(\ln K)$ further decreases a 10% (S3 vs. S2), and there is an additional reduction of a 7% when conditioning to concentrations (S6 vs. S3).

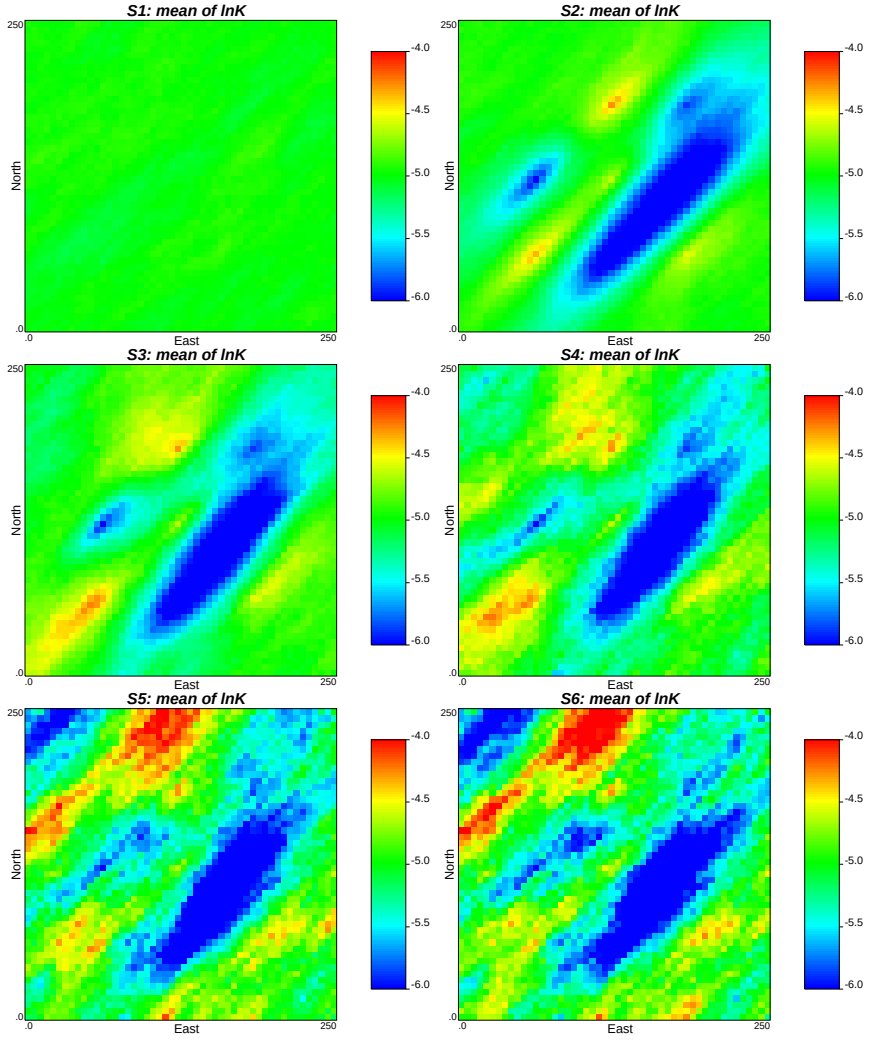

Figure 5.4: Ensemble average logconductivity fields for the different scenarios.

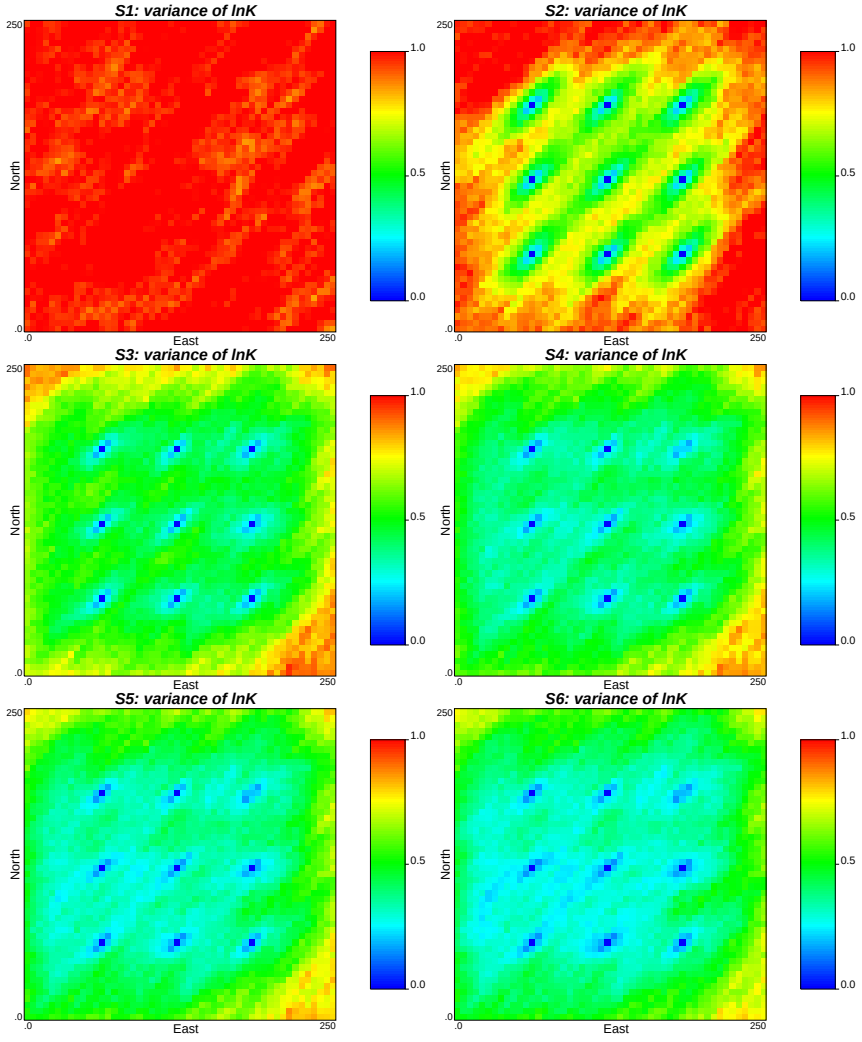

Figure 5.5: Ensemble logconductivity variance fields for the different scenarios

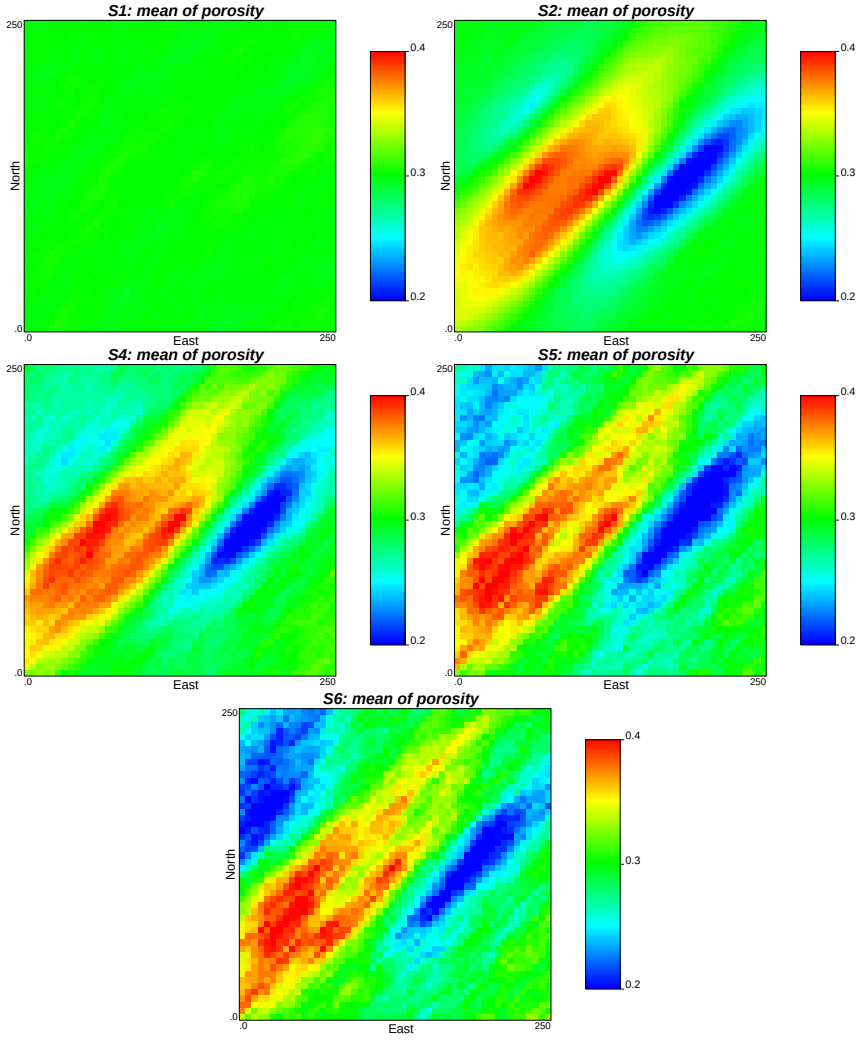

Figure 5.6: Ensemble average porosity fields for the different scenarios.

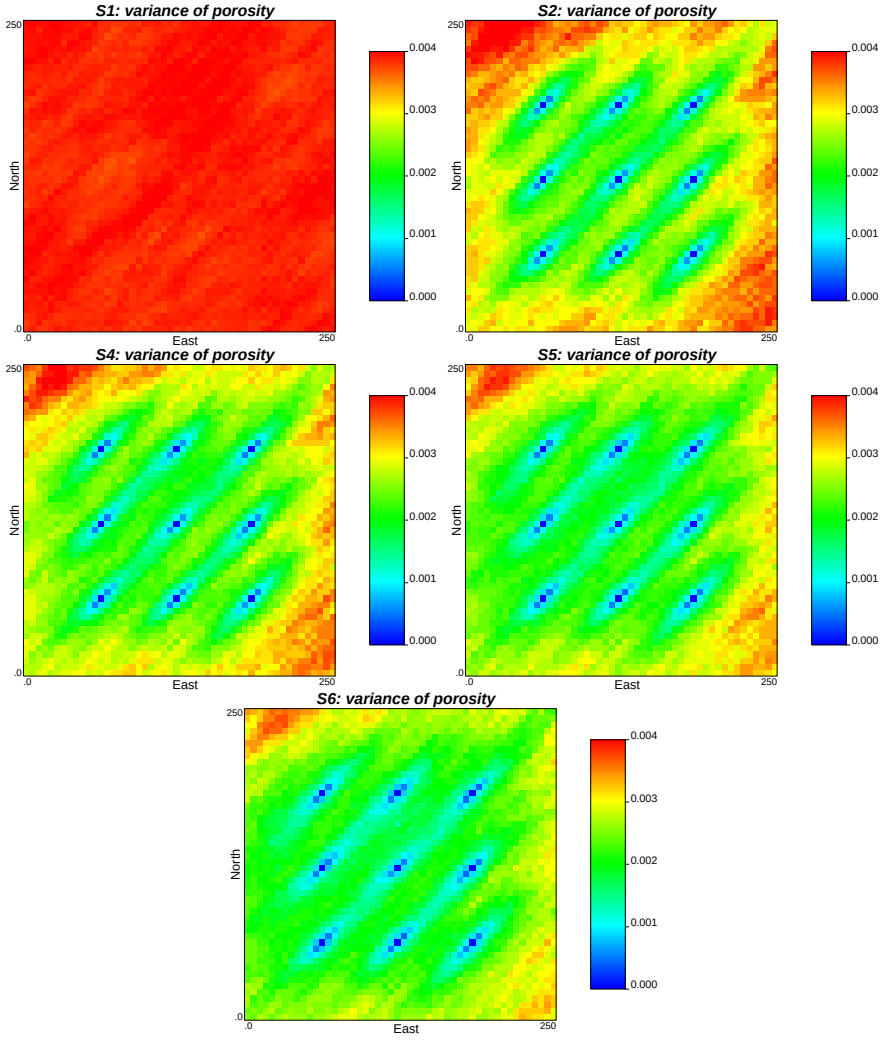

Figure 5.7: Ensemble porosity variance fields for the different scenarios.

Table 5.3: Bias and spread of lnK and porosity for the different scenarios.

Scenario	S1	S2	S3	S4	S5	S6
$AAB(\ln K)$	1.112	0.949	0.852	0.816	0.796	0.790
$AESP(\ln K)$	1.001	0.874	0.728	0.680	0.650	0.624
$AAB(\phi)$	0.072	0.059	-	0.057	0.056	0.055
$AESP(\phi)$	0.060	0.051	-	0.049	0.047	0.046

Likewise $AESP(\ln K)$ goes down 12% from S1 to S2, an additional 16% from S2 to S3 and 14% more from S3 to S6. Similar results can be observed when analyzing the evolution of $AAB(\phi)$ and $AESP(\phi)$. The $AAB(\phi)$ shows an 18% reduction as a consequence of conditioning to measured ϕ (S2 vs. S1), and 7% additional reduction related with conditioning to concentration data (S6 vs. S2) and $AESP(\phi)$ shows a 15% reduction as a consequence of conditioning to measured ϕ (S2 vs. S1), and 9% additional reduction related with conditioning to concentration data (S6 vs. S2).

From the results, we can conclude that: (1) The direct measured hard data play the most important role to reduce the absolute bias of parameters; (2) The indirect measured head and concentration data reduce both the absolute bias and ensemble spread; (3) The best characterization of the aquifer in terms of $\ln K$ and ϕ is achieved by combining all the data.

Piezometric Heads Reproduction

Figure 5.8 shows the piezometric head evolution at well #2 and #10 for scenarios S1, S2, S3 and S6. Recall that the piezometric head data continuously collected from well #1 to #9 are used for conditioning, while wells #10 and #11 are for validation. Figure 5.8 shows that for S1 uncertainty is largest and that the uncertainty is reduced for increasing amounts of conditioning data. For S2 the uncertainty is still considerable, but if piezometric head data are used for conditioning (S3) the conditional well #2 has a good head reproduction and the control well #10, also shows a large reduction of spread. The measured head data play a critical role to reduce the uncertainty of predicted heads. The concentration data do not result in a further improvement of the characterization of hydraulic head since the dynamic heads are already reproduced very well in S3.

Table 5.4 shows the metrics regarding the piezometric head characterization at time $t = 67.7$ days (i.e., the 60th time step). The introduction of measured hydraulic conductivities attains around 27% reductions both for the $AAB(h)$ and $AESP(h)$. An additional 66% reduction of $AAB(h)$ and 73% re-

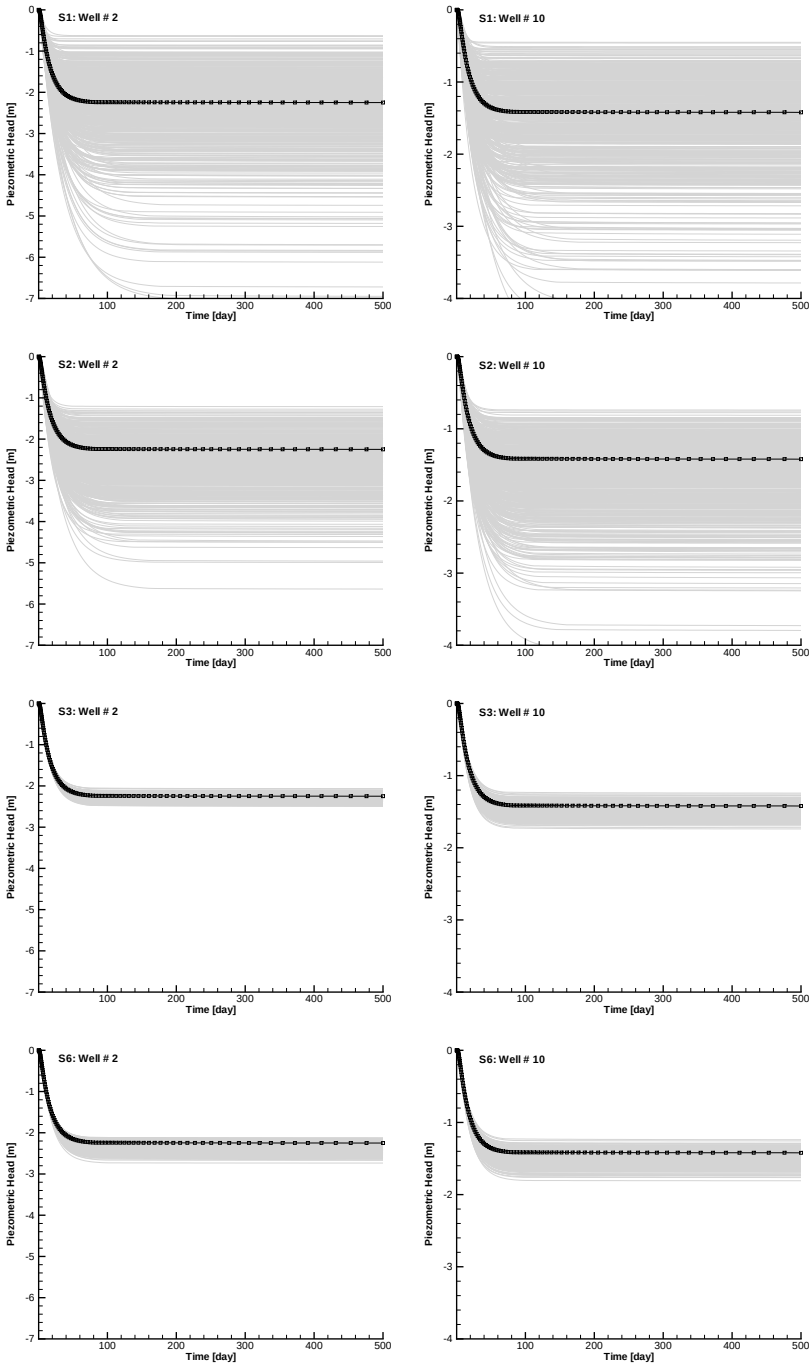

Figure 5.8: Piezometric head time series for the reference field (black) and simulated ones (gray lines) for the S1,S2,S3 and S6 scenarios at the conditioning well W2 (left column) and verification well W10 (right column).

Table 5.4: Bias and spread of predicted piezometric heads at time $t = 67.7$ days for the different scenarios.

Scenario	S1	S2	S3	S4	S5	S6
$AAB(h_{t=67.7})$	0.690	0.503	0.169	0.170	0.179	0.179
$AESP(h_{t=67.7})$	0.901	0.649	0.175	0.172	0.169	0.162

duction of $AESP(h)$ is achieved by conditioning to head data. The reductions of $AAB(h)$ and $AESP(h)$ almost can be ignored when concentration data are used for conditioning in S4, S5 and S6.

The main conclusions are: (1) of all the data, the measured piezometric head data are most informative for improving head predictions and reducing the prediction uncertainty; (2) the impact of concentration data for characterizing piezometric head is very small.

Concentrations Reproduction

Figure 5.9 to 5.12 show the ensemble mean and variance of 500 concentration realizations at time 300 and 500 days resulting from the transport simulation for all the six scenarios.

These ensemble mean maps of concentration for scenario 1 show that even though each realization will have a non-Gaussian plume similar to those in the reference, the random location of high and low concentrations makes that the ensemble mean maps of plume show a Gaussian shape. Introducing the hydraulic conductivity data (S2) rectifies the plume but still does not reproduce the reference. The ensemble mean of the plume is further rectified when the conductivity, porosity and head data are jointly used for conditioning (S3). The reproduction of piezometric heads is very good in S3, but the limited improvement of the plume characterization indicates the importance of further conditioning on concentration data. The results for scenarios S4 and S6 show that conditioning remarkably improves the characterization of the plume. Conditioning to concentration data at $t = 300$ days (S4) also improves strongly the prediction for 500 days (although the concentration data sampled at $t = 500$ days are not used for conditioning in scenario S4). For scenarios S5 and S6 the additional concentration data from $t = 400$ and 500 days improve further the characterization of the plume so that they are very close to the reference plumes.

The ensemble variance maps of the concentration fields show that the ensemble variance decreases away from the barycenter of the plume and is

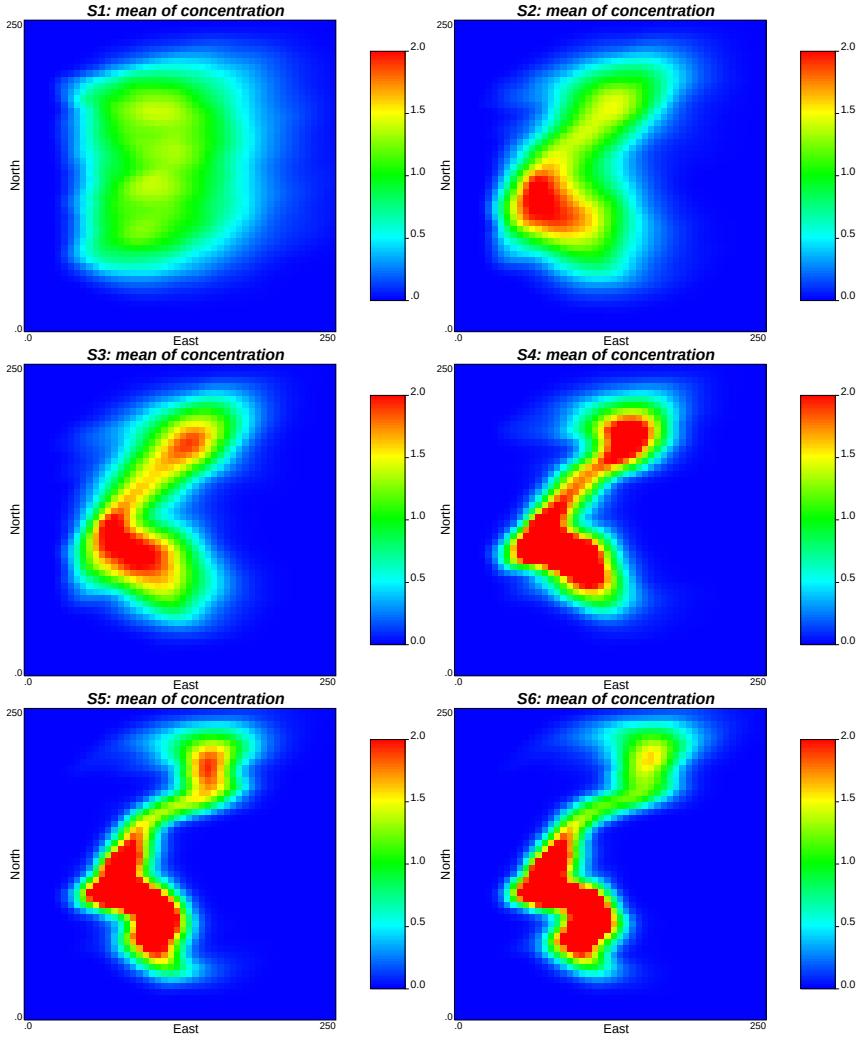

Figure 5.9: Ensemble average concentration fields at $t = 300$ day for the different scenarios.

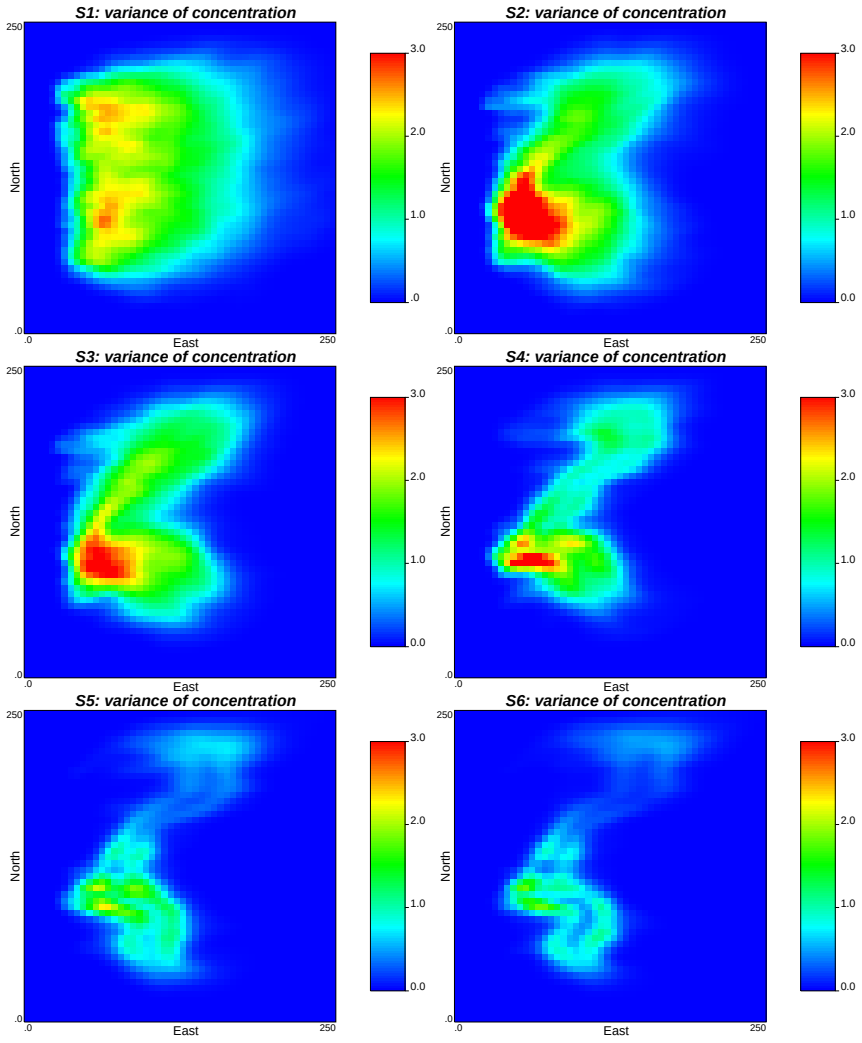

Figure 5.10: Ensemble variance of concentration fields at $t = 300$ day for the different scenarios.

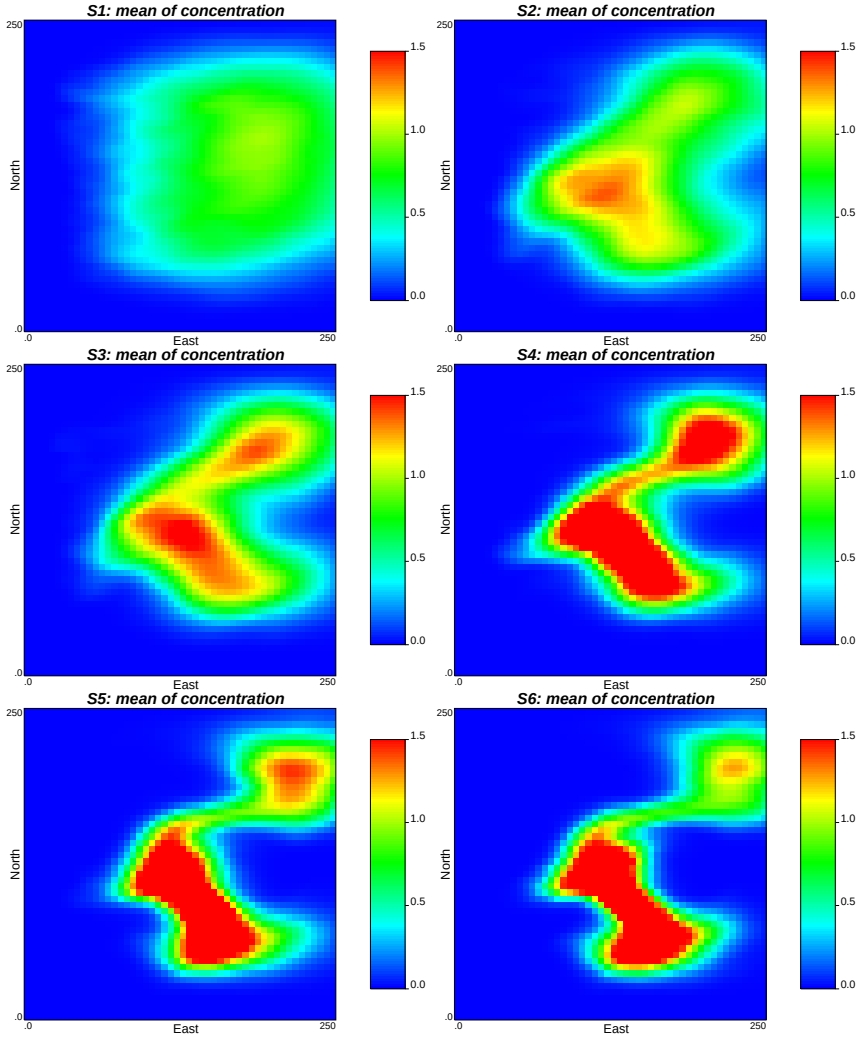

Figure 5.11: Ensemble average concentration fields at $t = 500$ day for the different scenarios.

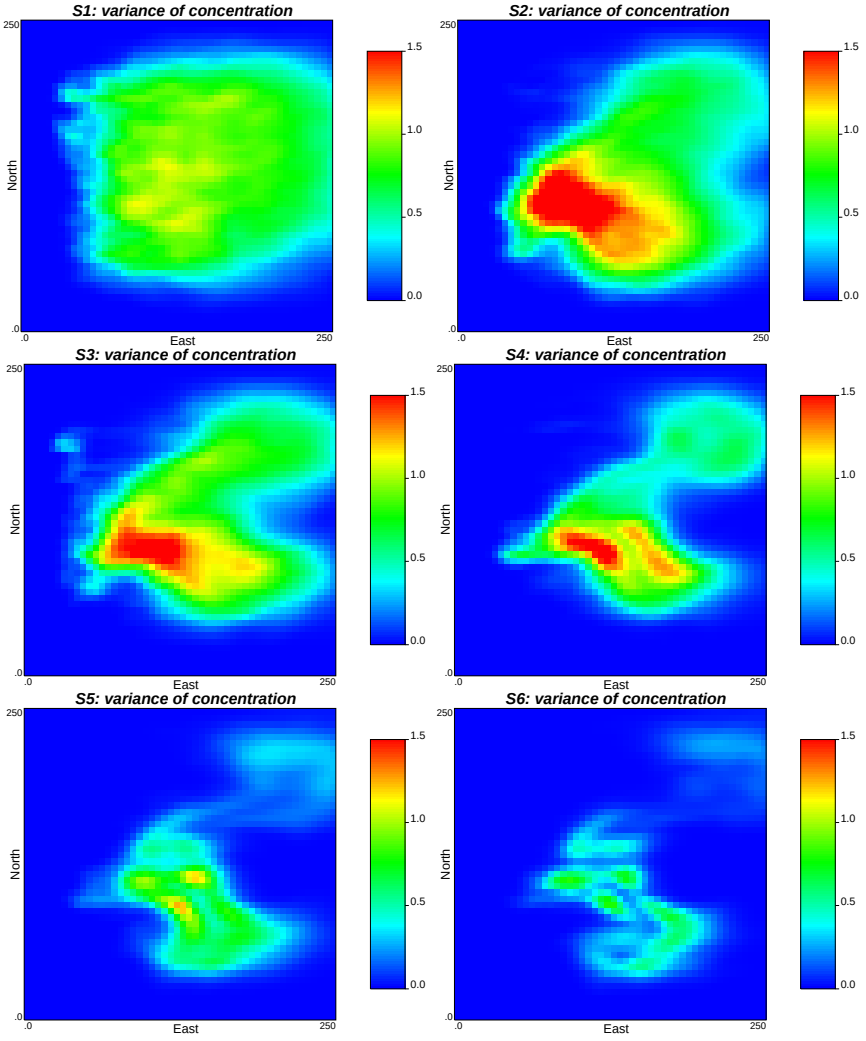

Figure 5.12: Ensemble variance of concentration fields at $t = 500$ day for the different scenarios.

Table 5.5: Bias and spread of predicted concentrations at time $t = 300$, $t = 400$, $t = 500$ days for the different scenarios.

Scenario	S1	S2	S3	S4	S5	S6
$AAB(c_{t=300})$	0.493	0.402	0.384	0.318	0.252	0.225
$AESP(c_{t=300})$	0.781	0.703	0.652	0.496	0.400	0.337
$AAB(c_{t=400})$	0.506	0.422	0.403	0.331	0.249	0.209
$AESP(c_{t=400})$	0.710	0.662	0.613	0.470	0.371	0.300
$AAB(c_{t=500})$	0.452	0.393	0.374	0.303	0.226	0.176
$AESP(c_{t=500})$	0.634	0.624	0.577	0.457	0.358	0.274

close to zero outside of the plume. The ensemble variance of concentration decreases continuously if more data are used for conditioning.

Table 5.5 shows the AAB and $AESP$ values for the concentrations at three times. Conditioning to hydraulic conductivity and porosity data (S2) results in an average AAB reduction of 15% (compared with S1) and $AESP$ reduces around 5%. Additional conditioning to piezometric head data (S3), results on average in an additional 5% reduction of AAB and an $AESP$ reduction of around 7%. Further conditioning to concentration data (S4, S5 and S6), yields prominent reduction of AAB and $AESP$ (on average 19% and 20%, respectively).

We can see from the results: (1) concentration data is the type of data to most reduce the absolute bias and uncertainty of predicted concentration; (2) the direct measured data and indirect head data also have an important impact on the predicted concentrations; (3) when all the data are considered, the concentration fields are best characterized.

5.3.4 Reactive Transport Prediction Analysis

In this subsection, a reactive transport prediction experiment is conducted with modified flow boundary conditions using the conductivity and porosity obtained in the data assimilation exercise to further demonstrate the robustness of EnKF.

The flow and transport configurations are the same as before but the flow is at steady-state. The eastern constant flow rate boundary condition is replaced with the constant head boundary condition ($h = -15$ m) and the solute mass is subject to sorption. Besides advection and dispersion also sorption according to a reversible linear equilibrium isotherm is considered with $\rho_b = 1.81$ g/cm^3 and $K_d = 0.52$ cm^3/g (similar to the values reported in the Borden aquifer (Mackay et al., 1986; Burr et al., 1994)). The reactive tracer is also

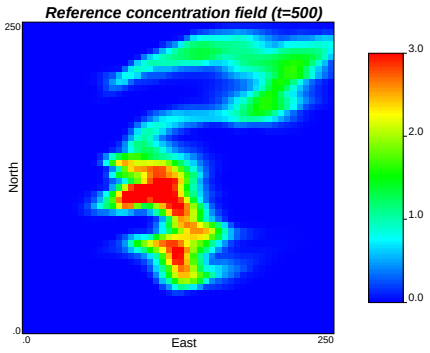

Figure 5.13: The reference concentration field at $t = 500$ days for the reactive transport prediction experiment.

released near the western boundary (see Figure 5.2) with the same total initial concentration. The plume snapshot at time $t = 500$ days (see Figure 5.13) is used to evaluate the worth of the different data.

MODFLOW and MT3DMS are employed to solve the flow equation (5.1) and reactive transport equation (5.2), respectively.

Figure 5.14 shows the ensemble mean and variance of predicted concentration fields at $t = 500$ days for the fields estimated from the scenarios S2, S3 and S6. It clearly shows that the predicted plume is close to the reference when multiple types of information are used for conditioning. Besides, the ensemble variance is the smallest for S6.

5.4 Conclusion

We have presented and demonstrated the Ensemble Kalman Filter, a data assimilation algorithm, to jointly estimate hydraulic conductivity and porosity by assimilating dynamic piezometric head and multiple concentration data in a hydrogeological stochastic model. Some of the attractive features of EnKF are the capability of assimilating data in real-time, CPU efficiency, ease of implementation without need of an adjoint model and the flexibility with regard to accounting for multiple sources of uncertainty jointly.

We have used a synthetic example (1) to demonstrate the potential EnKF has to condition in a CPU efficient way to concentration data and (2) to analyze the worth of data for the characterization of aquifer parameters and states (with a special focus on solute concentrations). We have found that the head data have a distinctive impact to reduce the uncertainty of predicted piezometric head, but only a limited influence for improving the characterization of concentration distributions. Additional conditioning to multiple concentra-

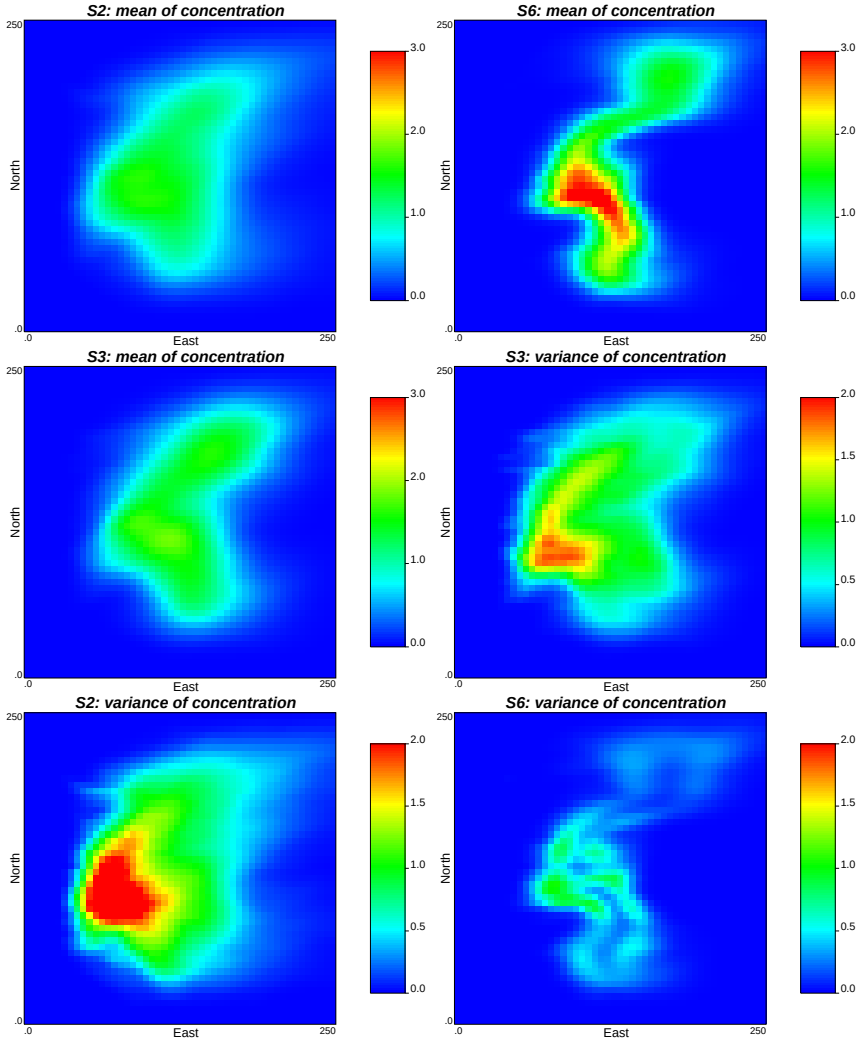

Figure 5.14: Ensemble mean and variance of concentration fields at $t = 500$ day for the S2,S3 and S6.

tion data was shown to improve strongly the predicted solute plume and also the characterization of hydraulic conductivity and porosity.

Bibliography

Alcolea, A., Carrera, J., Medina, A., 2006. Pilot points method incorporating prior information for solving the groundwater flow inverse problem. Advances in Water Resources 29 (11), 1678–1689.

Anderson, J., 2001. An ensemble adjustment Kalman filter for data assimilation. Monthly weather review 129, 2884–2903.

Barnhart, K., Urteaga, I., Han, Q., Jayasumana, A., Illangasekare, T., 2010. On Integrating Groundwater Transport Models with Wireless Sensor Networks. Ground Water 48 (5), 771–780.

Bear, J., 1972. Dynamics of fluids in porous media. American Elsevier Pub. Co., New York.

Burgers, G., van Leeuwen, P., Evensen, G., 1998. Analysis scheme in the ensemble Kalman filter. Monthly Weather Review 126, 1719–1724.

Burr, D., Sudicky, E., Naff, R., 1994. Nonreactive and reactive solute transport in three-dimensional heterogeneous porous media: Mean displacement, plume spreading, and uncertainty. Water Resources Research 30 (3), 791–815.

Capilla, J., Llopis-Albert, C., 2009. Gradual conditioning of non-Gaussian transmissivity fields to flow and mass transport data: 1. Theory. Journal of Hydrology 371 (1-4), 66–74.

Capilla, J. E., Rodrigo, J., Gómez-Hernández, J. J., 1999. Simulation of non-gaussian transmissivity fields honoring piezometric data and integrating soft and secondary information. Math. Geology 31 (7), 907–927.

Carrera, J., Alcolea, A., Medina, A., Hidalgo, J., Slooten, L., 2005. Inverse problem in hydrogeology. Hydrogeology Journal 13 (1), 206–222.

Carrera, J., Neuman, S., 1986. Estimation of aquifer parameters under transient and steady state conditions: 1. Maximum likelihood method incorporating prior information. Water Resources Research 22 (2), 199–210.

Chen, Y., Zhang, D., 2006. Data assimilation for transient flow in geologic formations via ensemble Kalman filter. Advances in Water Resources 29 (8), 1107–1122.

Doherty, J., 2004. PEST model-independent parameter estimation, user manual. Watermark Numerical Computing, Brisbane, Australia, 3349.

Evensen, G., 2003. The ensemble Kalman filter: Theoretical formulation and practical implementation. Ocean dynamics 53 (4), 343–367.

Freeze, R. A., Cherry, J. A., 1979. Groundwater. Prentice-Hall.

Fu, J., Gómez-Hernández, J., 2009. Uncertainty assessment and data worth in groundwater flow and mass transport modeling using a blocking Markov chain Monte Carlo method. Journal of Hydrology 364 (3-4), 328–341.

Gómez-Hernández, J. J., Journel, A. G., 1993. Joint sequential simulation of multi-Gaussian fields. Geostatistics Troia 92 (1), 85–94.

Gómez-Hernández, J. J., Sahuquillo, A., Capilla, J. E., 1997. Stochastic simulation of transmissivity fields conditional to both transmissivity and piezometric data, 1, Theory. Journal of Hydrology 203 (1–4), 162–174.

Gómez-Hernández, J. J., Srivastava, R. M., 1990. ISIM3D: an ANSI-C three dimensional multiple indicator conditional simulation program. Computers & Geosciences 16 (4), 395–440.

Gu, Y., Oliver, D., 2006. The ensemble Kalman filter for continuous updating of reservoir simulation models. Journal of Energy Resources Technology 128, 79.

Harbaugh, A. W., Banta, E. R., Hill, M. C., McDonald, M. G., 2000. MODFLOW-2000, the U.S. Geological Survey modular ground-water model. U.S. Geological Survey, Branch of Information Services, Reston, VA, Denver, CO.

Hassan, A., 2001. Water flow and solute mass flux in heterogeneous porous formations with spatially random porosity. Journal of Hydrology 242 (1-2), 1–25.

Hendricks Franssen, H., Alcolea, A., Riva, M., Bakr, M., van der Wiel, N., Stauffer, F., Guadagnini, A., 2009. A comparison of seven methods for the inverse modelling of groundwater flow. application to the characterisation of well catchments. Advances in Water Resources 32 (6), 851–872.

Hendricks Franssen, H., Gómez-Hernández, J., Capilla, J., Sahuquillo, A., 1999. Joint simulation of transmissivity and storativity fields conditional to steady-state and transient hydraulic head data. Advances in Water Resources 23 (1), 1–13.

Hendricks Franssen, H., Gómez-Hernández, J., Sahuquillo, A., 2003. Coupled inverse modelling of groundwater flow and mass transport and the worth of concentration data. Journal of Hydrology 281 (4), 281–295.

Hendricks Franssen, H., H. P. Kaiser, U. Kuhlmann, G. B. F. S. R. M., Kinzelbach, W., 2011. Operational real-time modeling with EnKF of variably saturated subsurface flow including stream-aquifer interaction and parameter updating. Water Resources Research, in press,doi:10.1029/2010WR009480.

Hendricks Franssen, H., Kinzelbach, W., 2008. Real-time groundwater flow modeling with the Ensemble Kalman Filter: Joint estimation of states and parameters and the filter inbreeding problem. Water Resources Research 44 (9), W09408.

Hendricks Franssen, H., Kinzelbach, W., 2009. Ensemble Kalman filtering versus sequential self-calibration for inverse modelling of dynamic groundwater flow systems. Journal of Hydrology 365 (3-4), 261–274.

Hu, B., Meerschaert, M., Barrash, W., Hyndman, D., He, C., Li, X., Guo, L., 2009. Examining the influence of heterogeneous porosity fields on conservative solute transport. Journal of contaminant hydrology 108 (3-4), 77–88.

Hu, L. Y., 2000. Gradual deformation and iterative calibration of gaussian-related stochastic models. Math. Geology 32 (1), 87–108.

Huang, C., Hu, B. X., Li, X., Ye, M., 2008. Using data assimilation method to calibrate a heterogeneous conductivity field and improve solute transport prediction with an unknown contamination source. Stochastic Environmental Research and Risk Assessment 23 (8), 1155–1167.

Huang, H., Hu, B., Wen, X., Shirley, C., 2004. Stochastic inverse mapping of hydraulic conductivity and sorption partitioning coefficient fields conditioning on nonreactive and reactive tracer test data. Water Resources Research 40 (1), W01506.

Jiang, X., Wan, L., Cardenas, M., Ge, S., Wang, X., 2010. Simultaneous rejuvenation and aging of groundwater in basins due to depth-decaying hydraulic conductivity and porosity. Geophysical Research Letters 37 (5), L05403.

Journel, A., 1974. Geostatistics for conditional simulation of ore bodies. Economic Geology 69 (5), 673.

Kitanidis, P., 1995. Quasi-linear geostatistical theory for inversing. Water Resources Research 31 (10), 2411–2419.

LaVenue, A. M., Ramarao, B. S., de Marsily, G., Marietta, M. G., 1995. Pilot point methodology for automated calibration of an ensemble of conditionally simulated transmissivity fields, 2, Application. Water Resour. Res. 31 (3), 495–516.

Li, L., Zhou, H., Gómez-Hernández, J. J., 2011a. A comparative study of three-dimensional hydrualic conductivity upscaling at the macrodispersion experiment (MADE) site, on columbus air force base in mississippi (USA). Journal of Hydrology, doi:10.1016/j.jhydrol.2011.05.001.

Li, L., Zhou, H., Gómez-Hernández, J. J., 2011b. Transport upscaling using multi-rate mass transfer in three-dimensional highly heterogeneous porous media. Advances in Water Resources 34 (4), 478–489.

Li, L., Zhou, H., Hendricks Franssen, H., Gómez-Hernández, J. J., 2011c. Modeling transient flow by coupling ensemble kalman filtering and upscaling. Water Resources Research, submitted.

Liu, G., Chen, Y., Zhang, D., 2008. Investigation of flow and transport processes at the MADE site using ensemble kalman filter. Advances in Water Resources 31 (7), 975–986.

Llopis-Albert, C., Capilla, J., 2009. Gradual conditioning of non-Gaussian transmissivity fields to flow and mass transport data: 2. Demonstration on a synthetic aquifer. Journal of Hydrology 371 (1-4), 53–65.

Mackay, D., Freyberg, D., Roberts, P., Cherry, J., 1986. A natural gradient experiment on solute transport in a sand aquifer: 1. Approach and overview of plume movement. Water Resources Research 22 (13), 2017–2029.

McLaughlin, D., Townley, L., 1996. A reassessment of the groundwater inverse problem. Water Resources Research 32 (5), 1131–1161.

Medina, A., Carrera, J., 1996. Coupled estimation of flow and solute transport parameters. Water Resources Research 32 (10), 3063–3076.

Naevdal, G., Johnsen, L., Aanonsen, S., Vefring, E., 2005. Reservoir monitoring and continuous model updating using ensemble kalman filter. SPE Journal 10 (1).

Naff, R., Haley, D., Sudicky, E., 1998. High-resolution Monte Carlo simulation of flow and conservative transport in heterogeneous porous media 1. Methodology and flow results. Water Resources Research 34 (4), 663–677.

Nowak, W., 2009. Best unbiased ensemble linearization and the quasi-linear kalman ensemble generator. Water Resources Research 45 (4), W04431.

Oliver, D., Cunha, L., Reynolds, A., 1997. Markov chain Monte Carlo methods for conditioning a permeability field to pressure data. Mathematical Geology 29 (1), 61–91.

Ramarao, B. S., LaVenue, A. M., de Marsily, G., Marietta, M. G., 1995. Pilot point methodology for automated calibration of an ensemble of conditionally simulated transmissivity fields, 1, Theory and computational experiments. Water Resour. Res. 31 (3), 475–493.

Reichle, R., Walker, J., Koster, R., Houser, P., 2002. Extended versus ensemble Kalman filtering for land data assimilation. Journal of hydrometeorology 3, 728–740.

Riva, M., Guadagnini, A., Fernandez-Garcia, D., Sanchez-Vila, X., Ptak, T., 2008. Relative importance of geostatistical and transport models in describing heavily tailed breakthrough curves at the lauswiesen site. Journal of Contaminant Hydrology 101 (1-4), 1–13.

Sahuquillo, A., Capilla, J. E., Gómez-Hernández, J. J., Andreu, J., 1992. Conditional simulation of transmissivity fields honouring piezometric head data. In: Blair, W. R., Cabrera, E. (Eds.), Hydraulic Engineering Software IV, Fluid Flow Modeling. Vol. II. Elsevier Applied Science, London, UK, pp. 201–214.

Schöniger, A., Nowak, W., Hendricks Franssen, H. J., 2011. Parameter estimation by ensemble Kalman filters with transformed data: approach and application to hydraulic tomography, in preparation for Water Resources Research.

Schwede, R., Cirpka, O., 2009. Use of steady-state concentration measurements in geostatistical inversion. Advances in Water Resources 32 (4), 607–619.

Strebelle, S., 2002. Conditional simulation of complex geological structures using multiple-point statistics. Mathematical Geology 34 (1), 1–21.

Sun, A. Y., Morris, A. P., Mohanty, S., Jul. 2009. Sequential updating of multimodal hydrogeologic parameter fields using localization and clustering techniques. Water Resources Research 45, 15 PP.

Wen, X., Deutsch, C., Cullick, A., 2002. Construction of geostatistical aquifer models integrating dynamic flow and tracer data using inverse technique. Journal of Hydrology 255 (1-4), 151–168.

Wen, X. H., Chen, W., 2005. Real-time reservoir model updating using ensemble Kalman filter. In: SPE reservoir simulation symposium.

Yeh, W., 1986. Review of parameter identification procedures in groundwater hydrology: The inverse problem. Water Resources Research 22 (2), 95–108.

Zheng, C., Wang, P., TUSCALOOSA., A. U., 1999. MT3DMS: A modular three-dimensional multispecies transport model for simulation of advection, dispersion, and chemical reactions of contaminants in groundwater systems; Documentation and user's guide.

Zhou, H., Gómez-Hernández, J. J., Hendricks Franssen, H., Li, L., 2011a. Handling non-gaussian distributions with Ensemble Kalman Filter. Advances in Water Resources, in press, doi:10.1016/j.advwatres.2011.04.014.

Zhou, H., Li, L., Gómez-Hernández, J. J., 2010. Three-dimensional hydraulic conductivity upscaling in groundwater modelling. Computers & Geosciences 36 (10), 1224–1235.

Zhou, H., Li, L., Hendricks Franssen, H., Gómez-Hernández, J. J., 2011b. Pattern recongition in a bimodal aquifer with normal-score Ensemble Kalman Filter. Mathematical Geosciences, under review.

Zimmerman, D., De Marsily, G., Gotway, C., Marietta, M., Axness, C., Beauheim, R., Bras, R., Carrera, J., Dagan, G., Davies, P., et al., 1998. A comparison of seven geostatistically based inverse approaches to estimate transmissivities for modeling advective transport by groundwater flow. Water Resources Research 34 (6), 1373–1413.

Submitted to Hydrol. Earth Syst. Sci..

6

Groundwater Flow Inverse Modeling in non-multiGaussian Media: Performance Assessment of the Normal-Score Ensemble Kalman Filter

Abstract

The normal-score ensemble Kalman filter (NS-EnKF) is tested on a synthetic aquifer characterized by the presence of channels with a bimodal distribution of its hydraulic conductivities. Fourteen scenarios are analyzed which differ among them in one or various of the following aspects: the prior random function model, the boundary conditions of the flow problem, the number of piezometers used in the assimilation process, or the use of covariance localization in the implementation of the Kalman filter. The performance of the NS-EnKF is evaluated through the ensemble mean and variance maps, the connectivity patterns of the individual conductivity realizations and the degree of reproduction of the piezometric heads. The results show that (i) the

localized NS-EnKF can identify correctly the channels when a large number of conditioning piezometers are used even when an erroneous prior random function model is used, (ii) localization plays an important role to prevent filter inbreeding and results in a better logconductivity characterization, and (iii) the NS-EnKF works equally well under very different flow configurations.

6.1 Introduction

Accurate characterization of the spatial variability of hydrogeologic properties and its corresponding uncertainty is a key issue for environmental risk assessment, site remediation and restoration engineering, and the design of underground repositories for radioactive material.

In a Monte Carlo framework, heterogeneity of hydrogeologic properties is commonly characterized by the following two steps: (i) on the basis of a limited amount of direct measurements (i.e., hard data), multiple representations of aquifer properties are generated by means of the geostatistical techniques such as sequential Gaussian simulation (Deutsch and Journel, 1998), sequential indicator simulation (Gómez-Hernández and Srivastava, 1990), multiple-point geostatistical approach (Strebelle, 2002; Mariethoz et al., 2010b) or other related methods; and then (ii) on the basis of indirect measurements such as piezometric head and concentration data, inverse modeling is utilized to reduce the uncertainty by integrating these data to better characterize the spatial variability of hydrogeologic properties (e.g., for an overview see Yeh, 1986; McLaughlin and Townley, 1996; Zimmerman et al., 1998; Carrera et al., 2005; Hendricks Franssen et al., 2009).

Commonly used Monte Carlo type inverse algorithms (i.e., which generate many equally likely solutions to the inverse problems) include the self-calibration method (Sahuquillo et al., 1992; Gómez-Hernández et al., 1997; Capilla et al., 1999; Wen et al., 2002; Hendricks Franssen et al., 2003), the pilot point method (Ramarao et al., 1995; LaVenue et al., 1995; Alcolea et al., 2006), the Markov chain Monte Carlo method (Oliver et al., 1997; Fu and Gómez-Hernández, 2009; Alcolea and Renard, 2010), and the gradual deformation method (Hu, 2000; Capilla and Llopis-Albert, 2009), among others. These methods have in common that a multi-part objective function is minimized. The objective function is generally composed of the sum of squared differences (SSD) between simulated and observed state values plus the SSD of prior and calibrated parameters values. In order to minimize this objective function the hydrogeologic parameters are modified using derivative-based methods or by sampling the posterior distribution. The main difference between the various methods is how to solve the optimization problem.

The Ensemble Kalman Filter (EnKF) (Burgers et al., 1998; Anderson, 2001; Reichle et al., 2002; Evensen, 2003), a continuous implementation of the Bayesian update rule, is a further alternative to generate multiple equally likely solutions to the inverse problem. The EnKF is increasingly studied in hydrogeology as well as in petroleum engineering (e.g. Wen and Chen, 2005; Chen and Zhang, 2006; Hendricks Franssen and Kinzelbach, 2008; Sun et al., 2009; Nowak, 2009; Nan and Wu, 2010; Li et al., 2010b). The attractive characteristics of the EnKF are: (i) the efficiency in computation (e.g., Hendricks Franssen and Kinzelbach (2009) conducted a synthetic example to demonstrate that the needed CPU-time was reduced by a factor of 80 compared with the self-calibration method, to achieve comparable results); (ii) the flexibility of handling multiple sources of uncertainty, for instance, Hendricks Franssen and Kinzelbach (2008) successfully used EnKF to account for the uncertainty of both recharge and hydraulic conductivity together; Li et al. (2011c) used the EnKF to jointly calibrate porosity and hydraulic conductivity by assimilating dynamic head and multiple concentration data; (iii) real-time data assimilation without the need to store all previous states, for instance, Hendricks Franssen et al. (2011) operationally implemented the EnKF to calibrate the conductivity and leakage coefficient together in real-time in a real-world case study. On the contrary, the traditional inverse approaches mentioned above (self-calibration, pilot point, etc) are CPU-intensive, need recalibration when new data are available and handling multiple sources of uncertainty is less straightforward with these methods.

The EnKF provides an optimal solution when the state vector follows a multiGaussian distribution and the state function is linear (Arulampalam et al., 2002). In the literature of hydrogeology, most of studies applying the EnKF technique assume that the hydraulic conductivities follow a multi-Gaussian distribution (e.g., Chen and Zhang, 2006; Hendricks Franssen and Kinzelbach, 2008; Huang et al., 2008; Li et al., 2011c). The significance of accounting for non-multiGaussian distributions of hydraulic conductivity for flow and transport predictions has been stressed in many studies (e.g., Gómez-Hernández and Wen, 1998; Zinn and Harvey, 2003; Knudby and Carrera, 2005). Hence, extending the EnKF to deal with non-Gaussian state vectors would facilitate more extensive applications. Sun et al. (2009) and Zhou et al. (2011a,b), developed variants of the EnKF which are better accommodated to handle non-Gaussianity of parameter distributions. Sun et al. (2009) resort to couple the EnKF with a Gaussian mixture model to update the parameters of a multi-modal distribution by assimilating head data. Zhou et al. (2011a,b) transformed the augmented state vector (containing both the hydraulic conductivities and piezometric heads) with marginal multi-modal distributions into a new vector with marginal Gaussian distributions, perform the EnKF on the transformed state vector and backtransform the updated vector to the

original space. Both studies show that these variants of EnKF result in significant improvements in the characterization of the aquifer properties and in the predictions of flow and transport for non-multiGaussian hydraulic conductivity fields. It is worth noting that, in both studies, it was assumed that the prior random function is known, i.e., the reference field and the initial set of non-multiGaussian conductivity fields are both generated with the same geostatistical approach and the same random function model, which, in this particular case, amounted to using the same training image in the multiple-point geostatistical generator. However, in practice, it is not trivial to decide about a reasonable training image given the limited amount of information available. Partly for this reason, traditional two-point variogram-based geostatistical methods are still employed in practice. One of the motivations of this work is to explore the capacity of the normal score EnKF proposed by Zhou et al. (2011a,b) to identify a highly channelized aquifer when there are no (hard) conductivity data available and the prior random function model is not the one used to generate the reference field.

Several studies (e.g., Gómez-Hernández and Wen, 1998; Western et al., 2001; Zinn and Harvey, 2003; Knudby and Carrera, 2005; Lee et al., 2007) showed that flow and transport predictions strongly differ between multiGaussian and non-multiGaussian logconductivity fields, even when both types of fields share the same histogram and the same covariance function. These results demonstrated that the reproduction of the connectivity is of significance in practice. For the inverse conditioning, Kerrou et al. (2008) applied the self-calibration (Gómez-Hernández et al., 1997) method on a fluvial-sediment aquifer with a wrong prior model (i.e., multiGasussian instead of non-multiGaussian) and concluded that the channel structures cannot be retrieved, even when a large number of direct and indirect data are used for conditioning.

In this paper, we apply the normal-score EnKF (NS-EnKF) to a channelized aquifer characterized by a bimodal conductivity distribution, and analyze the performance of the method for fourteen scenarios which differ among them in one or several of the following aspects: the prior random function model, the boundary conditions of the flow problem, the number of piezometers used in the assimilation process, or the use of covariance localization in the implementation of the Kalman filter. None of the scenarios uses any conductivity conditioning data. The analysis focus on the ensemble mean and variance maps, the connectivity patterns of the individual conductivity realizations and the degree of reproduction of the piezometric heads.

This paper revisits the mathematical framework of the NS-EnKF as applied in the synthetic experiment and briefly presents its numerical implementation (section 6.2 and 6.3); the impact of the choice of the prior random function model is discussed in section 6.4.1, the effect of using localization

functions for the covariance while computing the Kalman gain is discussed in section 6.4.2, the performance under different boundary conditions inducing very different flow patterns in the aquifer is discussed in section 6.4.3, and, finally the impact of reducing the number of conditioning piezometers is discussed in 6.4.4. The paper ends with some conclusions (section 6.5).

6.2 Mathematic Framework

6.2.1 Flow equation

The flow equation of an incompressible fluid in saturated porous media in a Cartesian coordinate system can be obtained by combining the continuity equation and Darcy's law (Bear, 1972):

$$\nabla\cdot\big[\mathbf{K}(\mathbf{x})\nabla h(\mathbf{x})\big] = S_s\frac{\partial h}{\partial t} + Q \tag{6.1}$$

where $h[L]$ is the piezometric head; $\mathbf{K}[LT^{-1}]$ is a symmetric positive-definite rank-two tensor; $Q[T^{-1}]$ is the volumetric source flow per unit volume; $S_s[L^{-1}]$ is the specific storage coefficient ; $t\,[T\,]$ is the time; $\nabla\cdot = (\partial/\partial x + \partial/\partial y + \partial/\partial z)$ is the divergence operator of a vector field, and $\nabla = (\partial/\partial x, \partial/\partial y, \partial/\partial z)^T$ is the gradient operator of a scalar field.

6.2.2 The Normal-Score Ensemble Kalman Filter with Localization

The NS-EnKF method aims at generating equally-likely realizations of parameters and state variables, conditioned to real-time measurements such as piezometric head data following non-Gaussian marginal distributions. The basic algorithm is described in Zhou et al. (2011a) and is summarized next for the case of assimilating observed piezometric head data at time t in a bimodal aquifer.

1. Initialization step. Generate the initial ensemble of logconductivity fields (in case that there are logconductivity measurements, these fields must be conditional to them); this is achieved by any of many geostatistical simulation algorithms, such as sequential indicator simulation (e.g., Deutsch and Journel, 1992) or the multiple-point method (e.g., Strebelle, 2002). The choice of the algorithm will depend on the random function model adopted to describe the spatial variability of logconductivity. Here, it is assumed that the scale of hydraulic conductivity measurements have a support coinciding with that of the numerical model discretization gridblocks. If there were a discrepancy between the measurement scale and the gridblock scale, an upscaling technique would

have been needed to reconcile these two scales (e.g., Zhou et al., 2010; Li et al., 2011a,b).

2. Normal-score function step. Build the logconductivity local conditional distribution functions at each grid cell from the ensemble of logconductivity realizations, and the corresponding local normal-score transfer functions (ϕ) (for the details see: Goovaerts, 1997).

3. Forecast step. For each realization, the transient groundwater flow equation (6.1) is solved from time $t-1$ to t using standard block-centered finite differences (e.g., Harbaugh et al., 2000; Li et al., 2010a). The solution can be schematically represented by:

$$\mathbf{Y}_k = f(\mathbf{X}_{k-1}, \mathbf{Y}_{k-1}) \tag{6.2}$$

where $\mathbf{X}_{k-1}$ and $\mathbf{Y}_{k-1}$ denote the hydraulic conductivity and piezometric head estimates at time t_{k-1} respectively, and $\mathbf{Y}_k$ are the forecasted piezometric heads at time step t_k; f represents the groundwater flow model including the boundary conditions, stresses and other known parameters.

4. Normal-score function step. Build the piezometric head local conditional distribution functions from the ensemble of forecasted realizations, and the corresponding local normal-score transfer functions (φ).

5. Filter step. Update the state variables by the NS-EnKF based on the observed head data at time t.

   (a) Normal-score transform each conductivity, each forecasted head, and also the observed heads

$$\begin{aligned} \hat{\mathbf{X}} &= \phi(\mathbf{X}) \\ \hat{\mathbf{Y}} &= \varphi(\mathbf{Y}) \\ \hat{\mathbf{Y}}^{obs} &= \varphi(\mathbf{Y}^{obs}) \end{aligned} \tag{6.3}$$

   (b) Build the augmented normal-score transformed vector $\hat{\mathbf{\Psi}}$, which includes both the transformed conductivities ($\hat{\mathbf{X}}$) and the transformed forecasted heads ($\hat{\mathbf{Y}}$).

$$\hat{\mathbf{\Psi}}_{k,j} = \begin{bmatrix} \hat{\mathbf{X}} \\ \hat{\mathbf{Y}} \end{bmatrix}_{k,j}, \tag{6.4}$$

   where $\hat{\mathbf{\Psi}}_{k,j}$ is the j^{th} ensemble member of the augmented state vector at time t_k.

(c) Calculate the localized Kalman gain ($\mathbf{G_k}$) (e.g., Gaspari and Cohn, 1999; Hamill et al., 2001; Chen and Oliver, 2010).

$$\mathbf{G_k} = \rho_{\hat{X}\hat{Y}} \circ \mathbf{C}_{\hat{\mathbf{X}}\hat{\mathbf{Y}}} \left(\rho_{\hat{Y}\hat{Y}} \circ \mathbf{C}_{\hat{\mathbf{Y}}\hat{\mathbf{Y}}} + \mathbf{C_D}\right)^{-1} \tag{6.5}$$

where $\mathbf{C}_{\hat{\mathbf{X}}\hat{\mathbf{Y}}}$ is the cross-covariance between transformed logconductivity and head data; $\mathbf{C}_{\hat{\mathbf{Y}}\hat{\mathbf{Y}}}$ is the covariance of transformed head data, $\mathbf{C_D}$ is the diagonal matrix of expected measurement error variances; $\circ$ indicates the Schur product; and $\rho_{\hat{X}\hat{Y}}$ and $\rho_{\hat{Y}\hat{Y}}$ are localization functions used for the $\mathbf{C}_{\hat{\mathbf{X}}\hat{\mathbf{Y}}}$ and $\mathbf{C}_{\hat{\mathbf{Y}}\hat{\mathbf{Y}}}$, respectively; the specific localization functions used in this work will be given later.

(d) Update each ensemble member of the state vector (e.g., Burgers et al., 1998; Evensen, 2003).

$$\hat{\mathbf{\Psi}}^{u}_{k,j} = \hat{\mathbf{\Psi}}^{f}_{k,j} + \mathbf{G_k}(\hat{\mathbf{Y}}^{obs} + \epsilon - \hat{\mathbf{Y}}^{f}) \tag{6.6}$$

where superscripts u and f denote updated and forecasted, respectively; ϵ is a random observation error vector, and $\hat{\mathbf{Y}}^{f}$ is a vector containing the transformed forecasted heads at sampling locations (a subset of $\hat{\mathbf{Y}}$).

(e) Back transform the state vector $\hat{\mathbf{\Psi}}$.

$$\begin{aligned} \mathbf{X} &= \phi^{-1}(\hat{\mathbf{X}}) \\ \mathbf{Y} &= \varphi^{-1}(\hat{\mathbf{Y}}) \end{aligned} \tag{6.7}$$

6. Go to step 3 for the next time step.

The NS-EnKF assures that the non-Gaussianity of the marginal distributions of states and parameters is preserved, through the use of the normal-score transform. The distance-dependent localization functions are used to reduce the influence of spurious correlations for large separation distances that may appear in the covariance computed through the ensemble of realizations.

6.3 Synthetic Example

6.3.1 Reference

The domain area is 300 m by 240 m by 1 m, and is discretized into 100 × 80 × 1 blocks of size 3 m × 3 m × 1 m. The reference logconductivity field is generated in two steps: (i) the SNESIM code, a pattern-based multiple-point geostatistical algorithm, is utilized to generate a facies realization (Strebelle, 2002). (In contrast with traditional two-point variogram-based models, the multiple-point method is able to reproduce complex and realistic

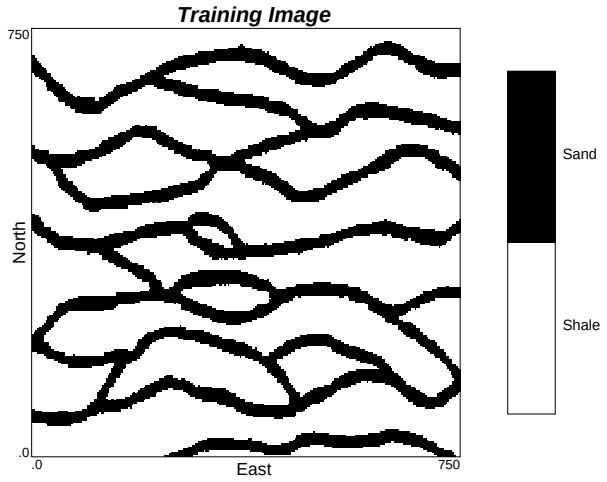

Figure 6.1: Training image used to generate the facies distribution.

Table 6.1: Parameters of the random functions describing the sand and shale

	Mean	Variance	Variogram type	λ_x [m]	λ_y [m]	sill
Sand	2.1	0.49	exponential	144	72	1
Shale	-1.4	0.49	exponential	72	72	0.35

curvilinear structures characteristic of fluvial deposits.) We used the training image in Strebelle (2002), which is commonly used for benchmarking to compare algorithms (e.g., Wu et al., 2008; Mariethoz et al., 2010a). This training image serves as a conceptual model for the channelized bimodal aquifer, where the channels have high conductivities representing preferential paths and are embedded in a floodplain fine-grid deposits with low conductivities (see Figure 6.1); (ii) the generated facies realizations is populated with conductivities using a sequential Gaussian simulation algorithm (Gómez-Hernández and Journel, 1993) with the parameters listed in Table 6.1. This procedure results in the spatial distribution of logconductivity values shown in Figure 6.2A, which serves as the reference $\ln K$ realization. This realization displays well-connected sand channels (approximately 30% of the system) on a low-conductivity matrix. The histogram of $\ln K$, shown in Figure 6.2B, clearly shows a bimodal logconductivity distribution typical of fluvial deposits.

To explore the role of boundary conditions on pattern identification, two sets of boundary conditions are considered: (i) Boundary conditions inducing parallel flow (Figure 6.3A), consisting of a combination of prescribed head

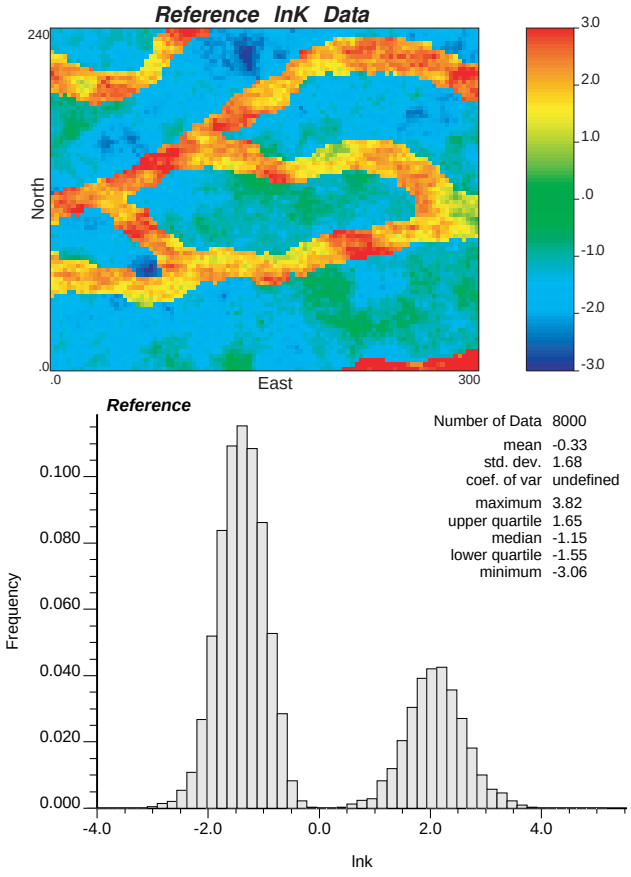

Figure 6.2: Reference lnK data

Table 6.2: Definition of scenarios

Scenario	1	2	3	4	5	6	7	8	9	10	11	12	13	14
Parallel flow	√	√	√	√	√	√							√	√
Radial flow							√	√	√	√	√	√		
Well (111)			√	√	√	√			√	√	√	√		
Well (32)													√	√
Correct Prior	√		√	√			√		√	√			√	
Wrong Prior		√			√	√		√			√	√		√
NS-EnKF			√		√				√		√		√	√
L-NS-EnKF$^{\alpha}$				√		√				√		√		

α indicates the localized NS-EnKF.

boundary (West), prescribed flux boundary (East) and impermeable boundaries (North and South); (ii) boundary conditions inducing radial flow (Figure 6.3B), with impermeable boundaries and a set of injection/extraction wells in a typical configuration for contaminant remediation or for reservoir exploitation. For both boundary conditions, groundwater flow is simulated for a period of 500 days starting with an initial head equal to zero everywhere. The simulation time is discretized into 100 time steps, the sizes of which follow a geometric series with a ratio of 1.05. The specific storage is assumed constant and equal to 0.003 m^{-1}. The MODFLOW 2000 code (Harbaugh et al., 2000) is used to solve the transient flow equation (6.1). The head data are sampled at the first 60 time steps (approximately 67.7 days) and will be used as the conditioning data in the NS-EnKF. The spatial distribution of the sampling wells is shown in Figure 6.3. Although the sampled head data are error-free since they are taken from the "true" field, in the following data assimilation procedures it was assumed that they have a normalized measurement error with a mean of zero and a standard deviation of 0.05 m.

6.3.2 Scenarios

Fourteen scenarios are analyzed with the characteristics indicated in the Table 6.2. The impact of the prior model, the use of a localization function and the different boundary conditions is tested with help of fourteen scenarios (Table 6.2).

The scenarios are organized to show how the characterization of the hydraulic conductivities evolves starting from an unconditional ensemble of realizations as piezometric heads are incorporated, and then when localization

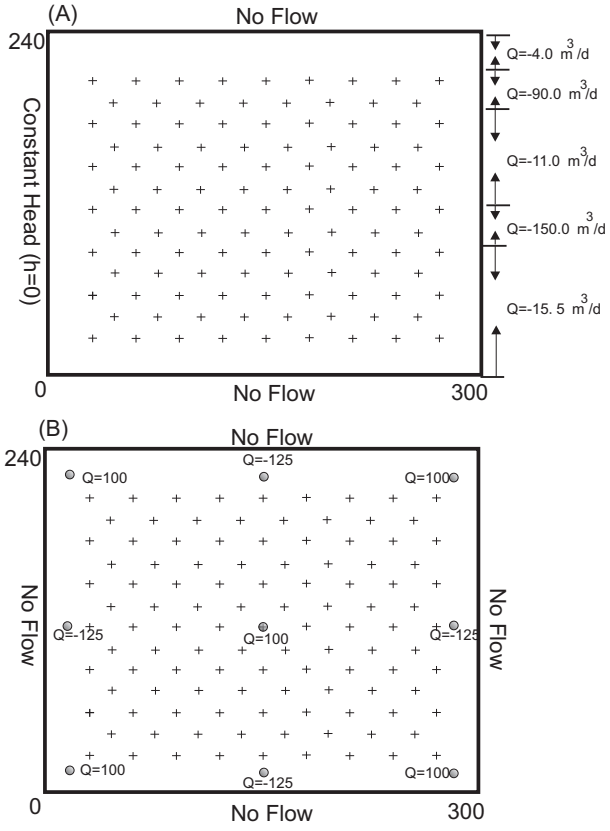

Figure 6.3: Spatial distribution of sampled head data and flow configurations: (A) boundary conditions A (B) boundary conditions B (the unit of flow in wells: m^3/d).

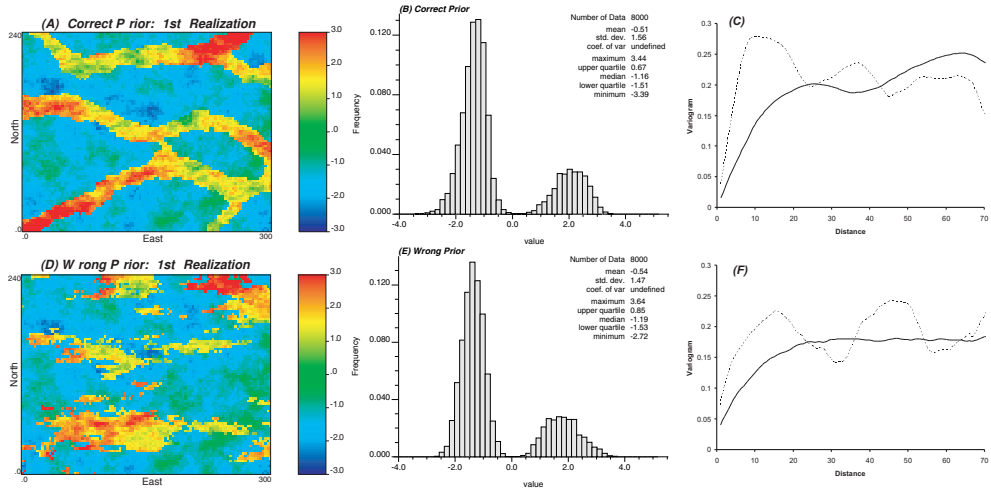

Figure 6.4: A-C show the spatial distribution of lnK, histogram and variogram of the 1st realization from the correct prior model; D-F show the same characteristics of the 1st realization from wrong prior model. In C and F, solid line and dotted line correspond to the experimental facies variogram in X and Y direction, respectively.

is used. This evolution is analyzed for each of the two flow patterns induced by the two sets of boundary conditions, and also for the cases in which the correct and an erroneous prior random functions are used.

Scenarios S1, S2, S7 and S8 are unconditional, they are the base cases containing the initial ensemble realizations to be used by the NS-EnKF in the other scenarios. They will produce the worst results in terms of conductivity characterization and piezometric head predictions and will serve as a starting point to assess the benefits of using the correct prior model, the assimilation of dynamic piezometric head information, and the use of localization.

Scenarios S1 to S6, S13 and S14 use boundary conditions inducing parallel flow through the aquifer, and scenarios S7 to S12 boundary conditions inducing radial flow.

The prior random function models for all realizations share the same histogram and variogram but they differ in their higher order moments. Scenarios S3, S4, S9, S10, and S13, use the same random function model used to generate the reference, i.e., the facies follow the random function model implicit in the training image of Figure 6.1 on which two independent multiGaussian random functions are overlaid to describe the variability of conductivity within each facies. Scenarios S5, S6, S11, S12 and S14, use a random function model for

the facies based on the indicator variogram computed on the training image on which the same independent multiGaussian random functions of the reference field are overlaid. For the first set of scenarios the multiple point code SNESIM Strebelle (2002) is used to generate the facies realizations, whereas the indicator simulation code ISIM3D (Gómez-Hernández and Srivastava, 1990) is used for the second set. The parameters defining the two multiGaussian random functions are given in Table 6.1. Figure 6.4 shows the first realization for the correct and the incorrect model, their histograms and their variograms. While both realizations follow the same histogram and variograms, the variogram-based sequential indicator simulation cannot generate the curvilinear patters for the sand facies observed in the training image, which are well reproduced in the multipoint sequential simulation.

For the scenario S3, S5, S9, S11, S13 and S14 head data are assimilated without using localization whereas for the scenarios S4, S6, S10 and S12 localization is employed.

The EnKF tends to filter inbreeding if the ensemble size is small, and the heterogeneity is large (Hendricks Franssen and Kinzelbach, 2009). It is therefore expected that the NS-EnKF applied to a complex geological environment will suffer this problem, too. To analyze this aspect, a fifth-order distance-dependent localization function (Hamill et al., 2001) is used to reduce the sampling errors in the computation of the ensemble covariances. Considering previous works (Chen and Oliver, 2010), the size of the domain, the separation between piezometers, and the distance between wells for the boundary conditions inducing radial flow, the localization function is set to zero at a distance of 80 m, implying that for distances larger than that, the sampled non-stationary covariances used to compute the Kalman gain are zero. More specifically, the distance function that is used for both $\rho_{\hat{X}\hat{Y}}$ and $\rho_{\hat{Y}\hat{Y}}$ in Equation (6.5) is:

$$\Omega(d) = \begin{cases} -\frac{1}{4}(\frac{d}{40})^5 + \frac{1}{2}(\frac{d}{40})^4 + \frac{5}{8}(\frac{d}{40})^3 - \frac{5}{3}(\frac{d}{40})^2 + 1, & 0 \leq \mathrm{d} \leq 40; \\ \frac{1}{12}(\frac{d}{40})^5 - \frac{1}{2}(\frac{d}{40})^4 + \frac{5}{8}(\frac{d}{40})^3 + \frac{5}{3}(\frac{d}{40})^2 - 5(\frac{d}{40}) + 4 - \frac{2}{3}(\frac{d}{40})^{-1}, & 40 \leq \mathrm{d} \leq 80; \\ 0 & \mathrm{d} > 80. \end{cases} \tag{6.8}$$

where d is the distance between observed head and $\ln K$ data (when applied to $\rho_{\hat{X}\hat{Y}}$) or between observed heads (when applied to $\rho_{\hat{Y}\hat{Y}}$) $[L]$. Here, the distance function is constant in time, isotropic, and used both for the cross-covariances between observed heads and parameters and the covariances of the head data.

Scenarios S13 and S14 stand apart from the rest of the conditional scenarios in that the number of piezometers used for assimilation is reduced to one third. Recall that no conductivity conditioning data are used for any scenario,

therefore, the ability to identify the channels is solely thanks to the dynamic head data that are assimilated at each time step, and it is expected that the quality of the characterization of the conductivities will be affected by the number of conditioning piezometers.

For all the scenarios, 1000 unconditional realizations of logconductivity are generated.

6.3.3 Evaluation Criteria

For every scenario, the following criteria are used to assess the results (Chen and Zhang, 2006; Zhou et al., 2011b):

1. Root mean square error ($RMSE$). $RMSE$ measures the accuracy of the estimation.

$$RMSE(X) = \left[\frac{1}{N_b}\sum_{i=1}^{N_b}(\overline{X}_i - X_{ref,i})^2\right]^{1/2} \tag{6.9}$$

   where X_i is either logconductivity $\ln K$ or hydraulic head h at location i, $\overline{X}_i$ represents its ensemble mean value at node i, $X_{ref,i}$ is the reference value at location i, N_b is the number of nodes.

2. Ensemble spread (ES). ES indicates the uncertainty (precision) of the estimation.

$$ES(X) = \left[\frac{1}{N_b}\sum_{i=1}^{N_b}\sigma^2_{X_i}\right]^{1/2} \tag{6.10}$$

   where $\sigma^2_{X_i}$ is the ensemble variance at location i.

   The smaller the values for $RMSE$ and ES, the better the prediction of variable X. As discussed in Chen and Zhang (2006), when $RMSE$ and ES have a similar magnitude filter inbreeding is avoided.

3. Connectivity. The flow and transport behaviors are strongly impacted by the presence of connected high-conductivities and connected low-conductivities (e.g., Wen and Gómez-Hernández, 1998; Knudby and Carrera, 2005). Here, we adopt the connectivity function defined by Pardo-Igúzquiza and Dowd (2003) to evaluate the connectivity. In this work, two steps are needed to analyze the connectivity for the continuous variable:

   (i) An indicator image is obtained as:

$$I(x) = \begin{cases} 1, & \text{if } \ln K \geq \alpha \\ 0, & \text{otherwise} \end{cases} \tag{6.11}$$

where α is the threshold that classifies the logconductivity into sand and shale. In our case, α is set to zero since this value approximately splits the histogram of logconductivity in two (see Figure 6.2).

(ii) The code CONNEC3D, a computer program for connectivity analysis of 3D random model, is used to calculate the probability that two points with logconductivity larger than α are connected. The result is a function of distance that gives the probability that two points located in the sand facies are connected by a continuous path in that same facies.

6.4 Results and discussion

Ensembles of conductivity realizations are generated for the fourteen scenarios according to the configurations described earlier. As mentioned earlier, scenarios 13 and 14 stand apart in that they are the only ones using a smaller number of conditioning piezometric heads, for this reason most of the figures group the results for scenarios S1 to S12. Scenarios S13 and 14 are analyzed later by themselves. Figure 6.5 and Figure 6.6 show the ensemble average and ensemble variance of logconductivity at time step 60 for the first twelve scenarios. Figure 6.7 shows the evolution of $RMSE$ and ES as function of the updating time step. Figure 6.8 displays the connectivity function for sand as a function of the horizontal distance. Figure 6.9 shows the $RMSE$ and ES of the predicted heads computed on the updated hydraulic conductivities after 60 time steps (67.7 days) by rerunning the flow model from $t = 0$.

6.4.1 Effect of prior random function model

For the scenarios S1, S2, S7 and S8 no conditioning data were used. For those scenarios, the ensemble average of hydraulic logconductivity is approximately spatially uniform and equal to the prior mean (see Figure 6.5) and, similarly, the ensemble variance map is approximately equal to the prior variance (see Figure 6.6). As expected, the unconditional average maps do not capture any spatial pattern, although individual realizations do display the spatial variability according to their prior random function models (see the first realization in Figure 6.4A and 6.4D).

For the scenarios where head data are used for assimilation, the ensemble means of hydraulic conductivity (estimated after 60 time steps of assimilation), depict the facies distribution well in visual comparison with the reference. The ensemble variances of logconductivity are clearly reduced in comparison with the prior variances and display a feature with higher variance at the boundaries of the channels and at places far away from the head measurements such as the boundaries of the domain. Comparing the two columns on Figures 6.5

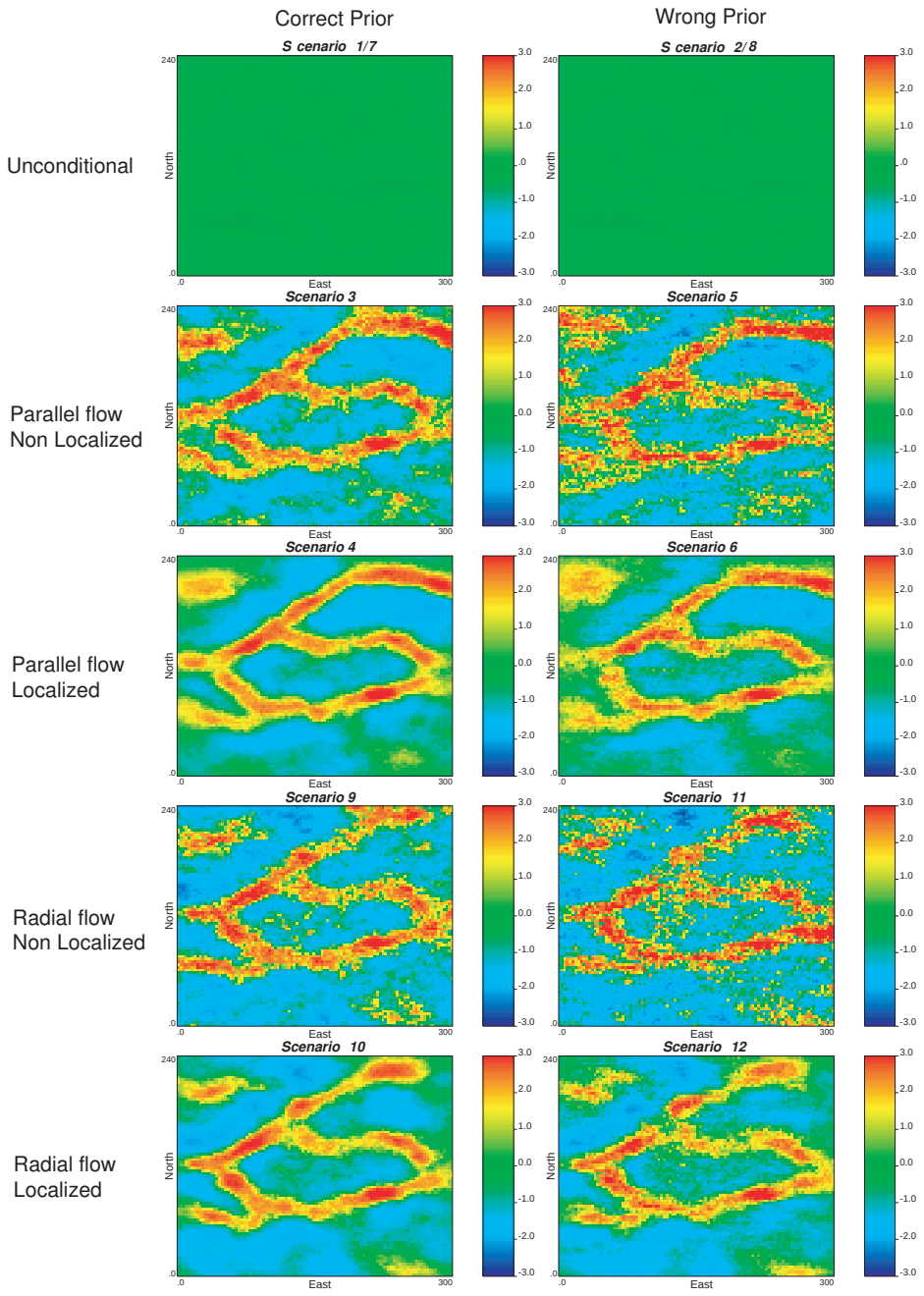

Figure 6.5: Ensemble average logconductivity fields at time step $nT = 60$ for the different scenarios.

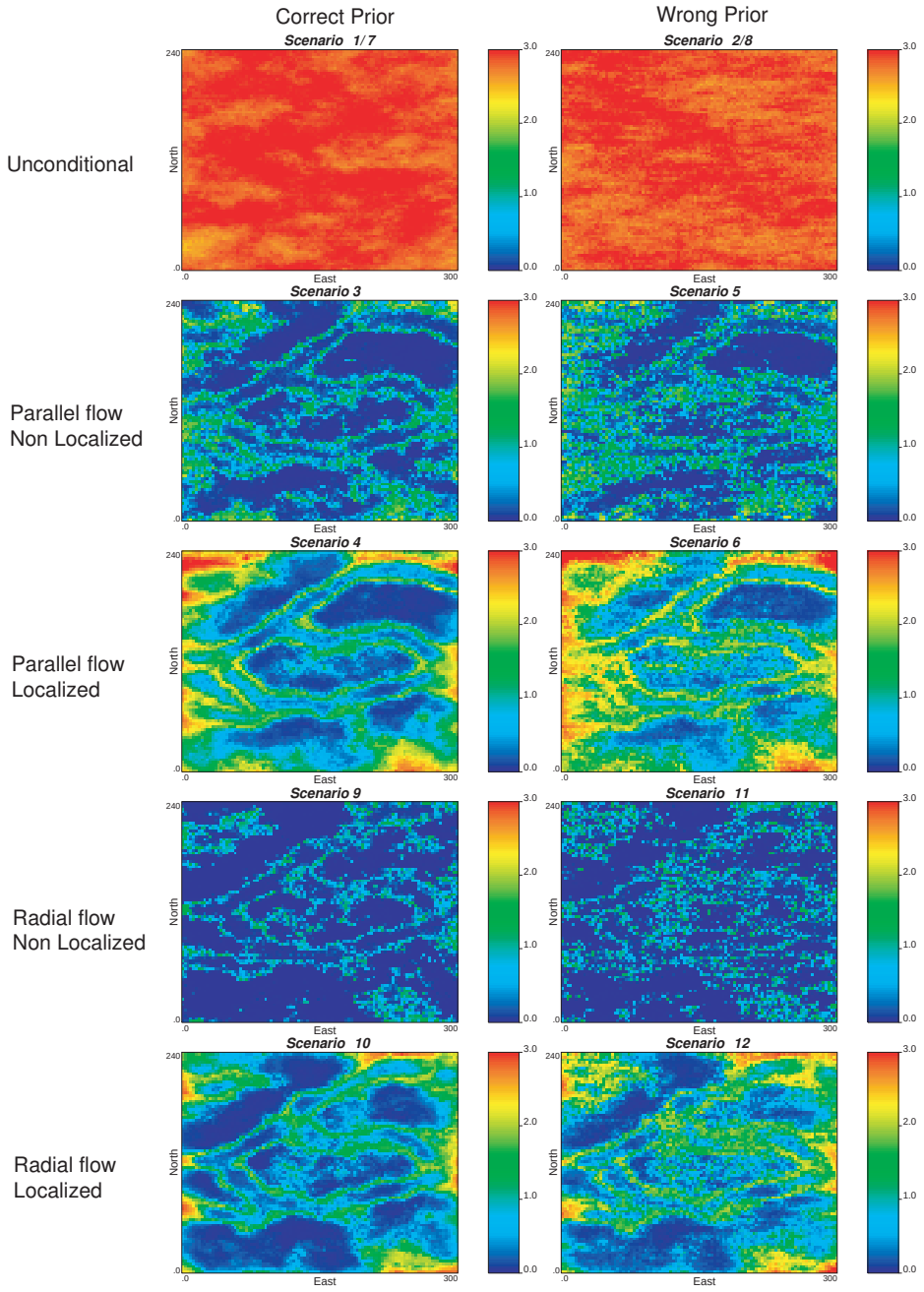

Figure 6.6: Ensemble variance logconductivity fields at time step $nT = 60$ for the different scenarios.

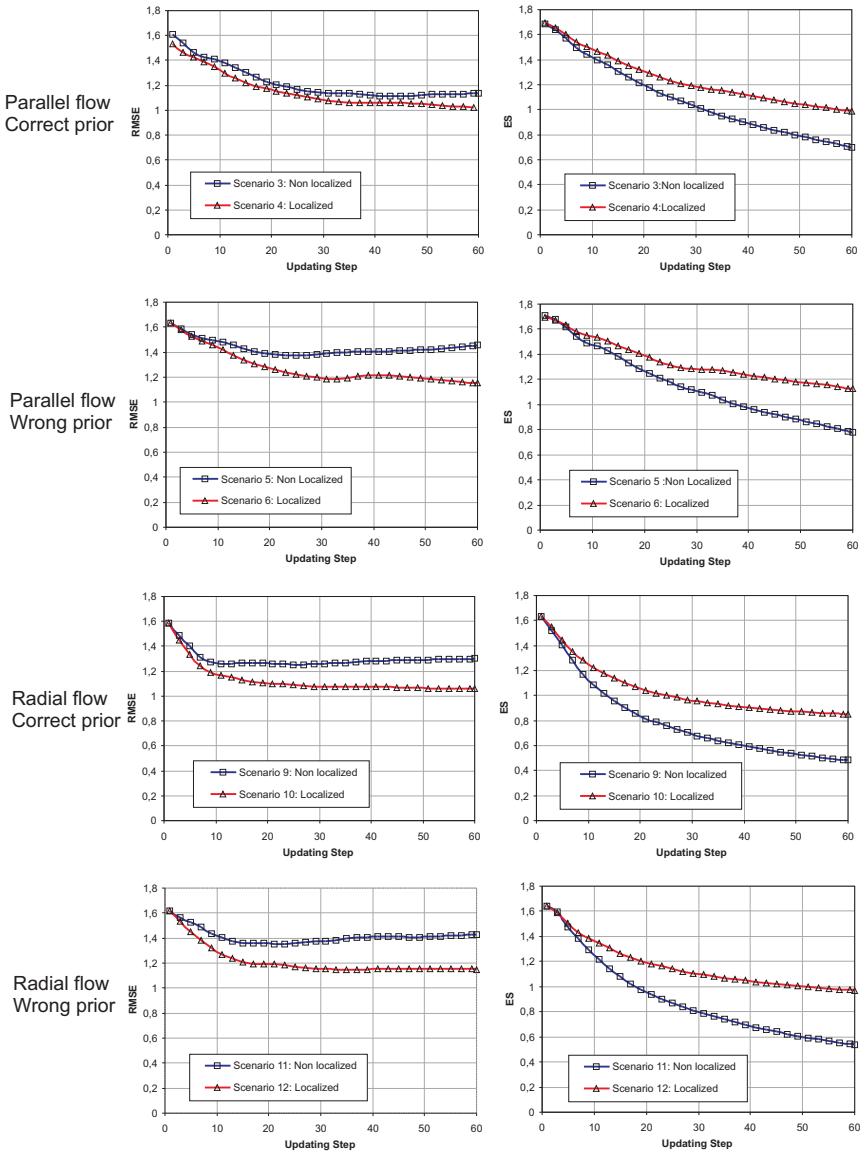

Figure 6.7: $RMSE$ and ES of lnK for the different cases.

and 6.6, it is quite striking to realize that, even for the wrong prior random function model, assimilating the piezometric head data with the NS-EnKF, yields ensembles of realizations which, on average, capture the location of the channels in the reference field and display the highest uncertainty at the boundary channels.

For a more quantitative analysis, Figure 6.7 shows how both the $RMSE$ and the ES evolve for the different conditional scenarios as a function of the updating step. It is not surprising that the wrong prior always gives higher values for the average departure between individual realizations and the reference and also for the average spread, being most noticeable for the case of parallel flow.

Regarding the reproduction of the connectivity function, Figure 6.8 shows the individual connectivity functions for all realizations, their average and the connectivity of the reference field for the first 12 scenarios. The discrepancy between the results obtained with the correct and the wrong prior are more significant in this case, something that is quite understandable since the wrong prior only uses the indicator variogram of the facies distribution as the starting set of ensemble realizations. The average connectivity of the wrong prior is significantly smaller than the reference connectivity for the unconditional case; then, conditioning to piezometric heads helps increasing the average connectivity as well as the spread of the individual connectivity functions, however, the connectivity remains below that of the reference for all cases. The average connectivity of the correct prior starts slightly above the reference one with a very wide spread of the individual functions, and gets closer to the reference when the piezometric heads are assimilated.

Finally, regarding the reproduction of the piezometric heads, Figure 6.9 shows the $RMSE$ and ES as a function of the updating step for the first 12 scenarios. In these figures we have as a reference the metric values for the unconditional cases to show the important reduction in both metrics induced by conditioning to the piezometric heads. Like in Figure 6.7, these metrics are average values computed over the entire aquifer, not just for the conditioning piezometers. The behavior of the wrong prior is very similar to that of the correct prior with the only noticeable difference that the localization tends to worsen the $RMSE$ for the wrong model whereas for the correct prior, localization improves the $RMSE$.

In summary, the NS-EnKF displays a great potential to capture the patterns of variability of logconductivities on the sole basis of piezometric information for clearly non-multiGaussian fields even when the prior random function model is not fully consistent with the reference realization.

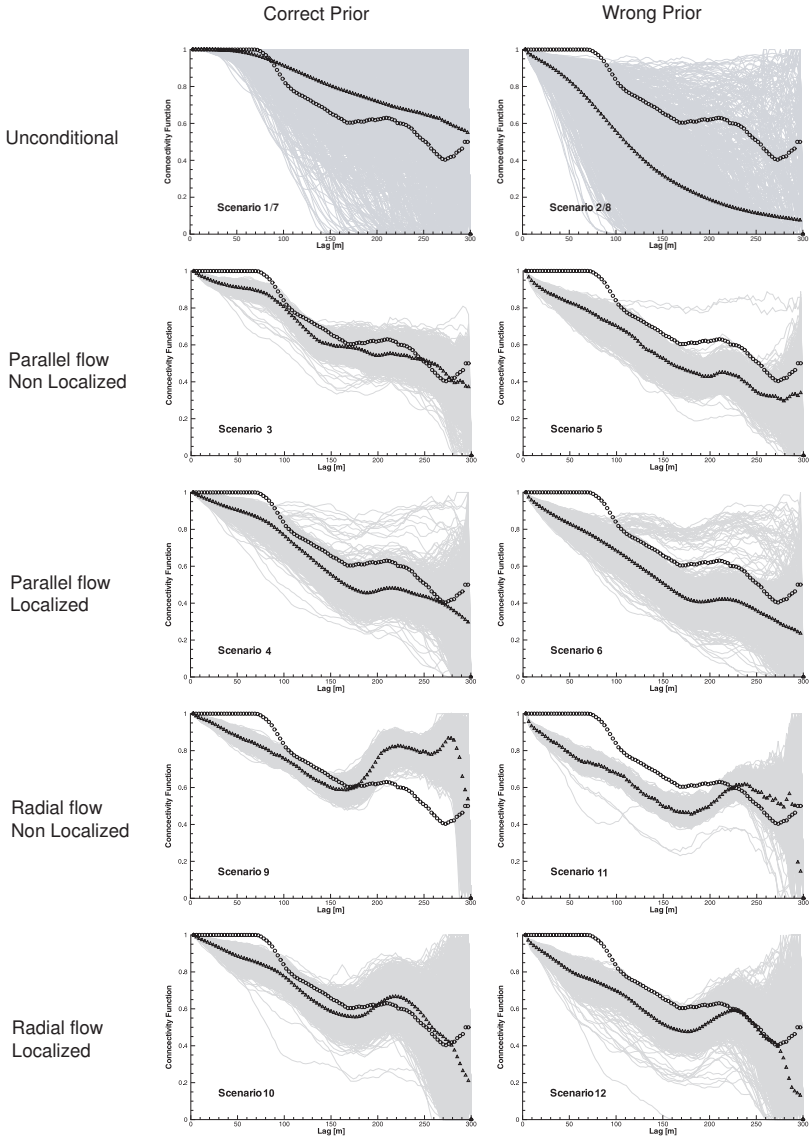

Figure 6.8: Connectivity function of logconductivity fields at time step $nT = 60$ for the different scenarios. Gray curves correspond to individual realizations, their mean is given by the triangles and the circles correspond to the reference.

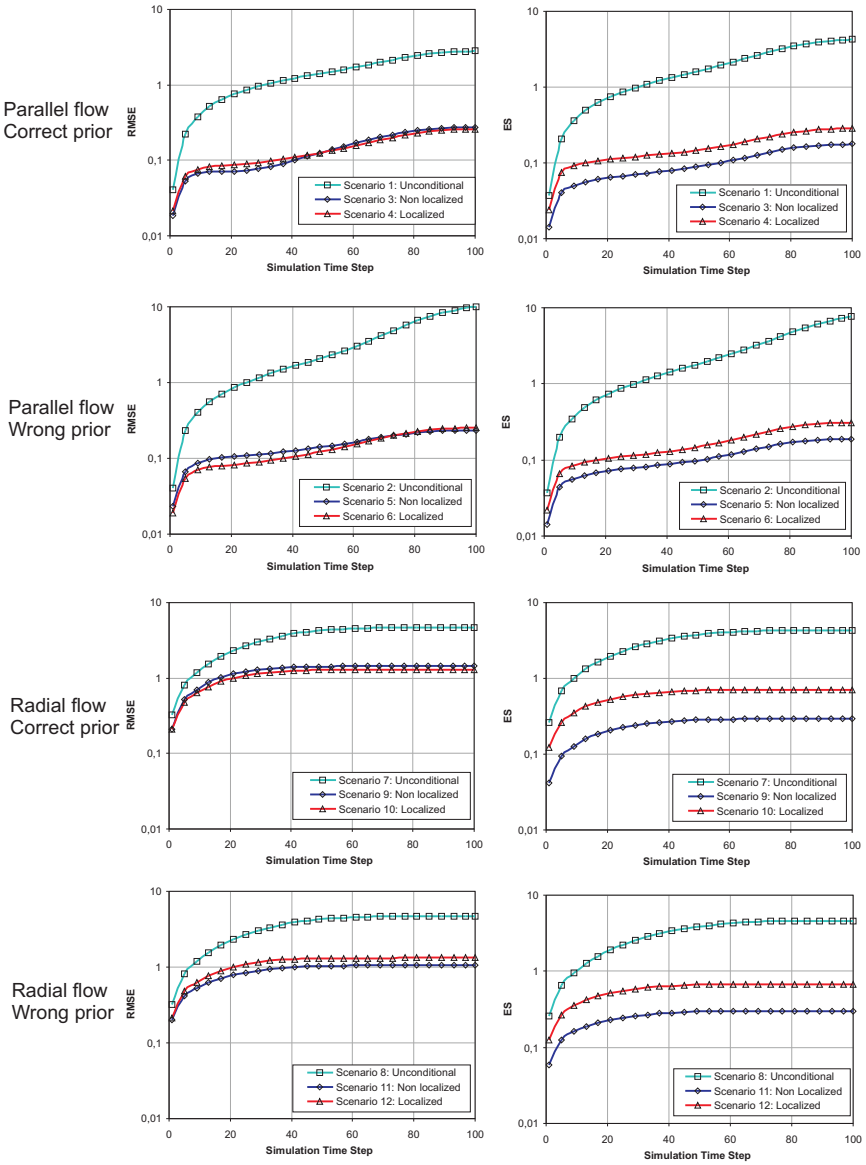

Figure 6.9: $RMSE$ and ES of simulated heads for the different scenarios.

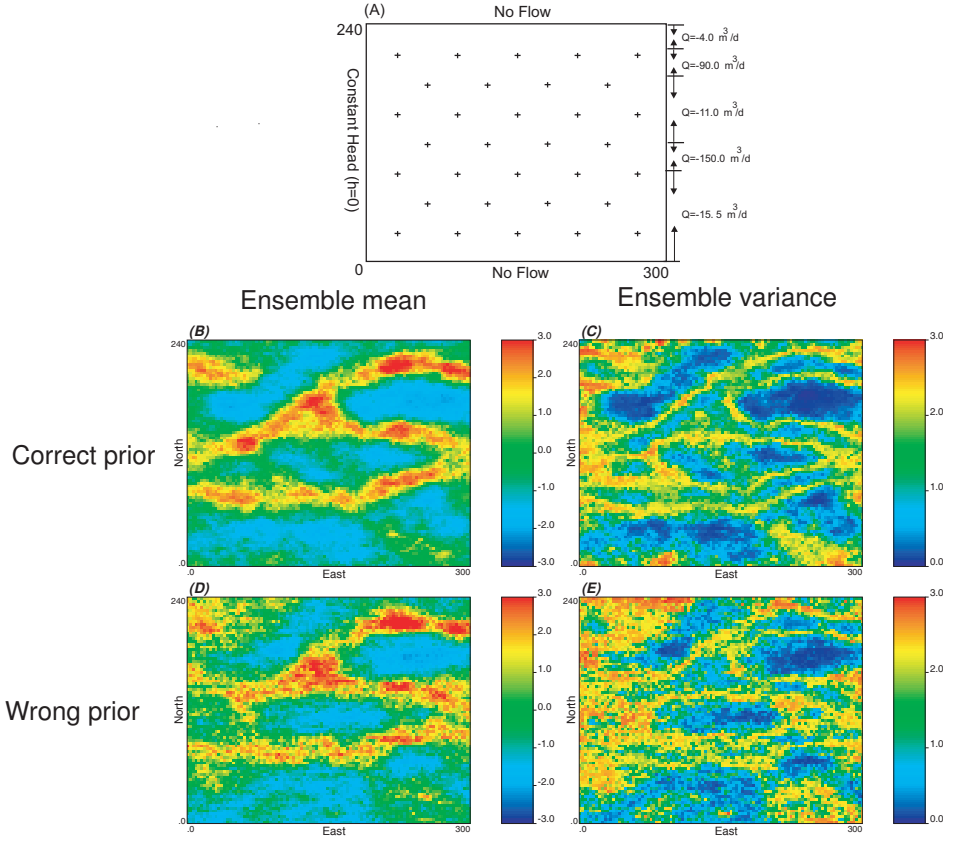

Figure 6.10: (A) flow configuration and spatial distribution of sampled head data. (B) the ensemble mean of logconductivity with correct prior model. (C) the ensemble variance of logconductivity with correct prior model.(D) the ensemble mean of logconductivity with wrong prior model. (E) the ensemble variance of logconductivity with wrong prior model.

6.4.2 Effect of localization

It is well known that the standard EnKF has the problem of filter inbreeding, which leads to a final ensemble of realizations too similar among them resulting in the underestimation of uncertainty of flow and transport predictions (Hendricks Franssen and Kinzelbach, 2009; Devegowda et al., 2010; Zhou et al., 2011a). The ensemble size we have used is large, 1000 realizations, yet, when analyzing the piezometric head covariances, and cross-covariances with logconductivity we observe the same type of spurious correlation values that, eventually, lead to filter inbreeding; therefore, we have decided to apply localization techniques and compare the resulting ensembles with and without localization. In general, localization should increase the ensemble spread and, at the same time, reducing the $RMSE$, that is, there is a gain in accuracy at the cost of precision, which also helps to avoid filter inbreeding.

Analyzing Figures 6.5 and 6.6 we observe that the ensemble mean hydraulic conductivity maps produced with the localized NS-EnKF are smoother than the same mean maps without localization, and capture better the main channels of the reference field. All artifacts in the non-localized realizations are removed after localization; the local ensemble variances in the localized ensembles increase, particularly significant values appear in the northwestern corner of the parallel flow exercise an area without conditioning data and too close to a prescribed head boundary where the sensitivity of the piezometric head to a change in logconductivity is close to zero. These results may indicate that even in this case with a large number of realizations, the ensemble variance estimate obtained from a non-localized NS-EnKF may be too optimistic.

The effect of localization is also quite clear when analyzing the $RMSE$ and ES of the calibrated conductivity fields (see Figure 6.7). On one hand, localization induces a reduction of the $RMSE$ in all cases, and an increase in the ES. In all cases, these changes result in values of $RMSE$ and ES that are very similar in value at the end of the updating steps, which is indicative, according to Chen and Zhang (2006), of reduced filter inbreeding. Taking the ratio $ES/RMSE$ as an index of filter inbreeding, this is worse for the radial flow scenarios without localization. In previous synthetic studies, Chen and Zhang (2006) and Hendricks Franssen and Kinzelbach (2008) have found that 200 realizations are enough to avoid filter inbreeding without localization for multiGaussian fields. Here we observe that filter inbreeding can be serious when EnKF is used without localization in a highly channelized aquifer.

Regarding sand connectivity it is not clear whether localization improves its characterization. The spread of the connectivity functions is much larger for the localized ensemble than for the non localized one, and, at least for parallel flow, the average of the connectivity functions does not get closer to the real one after localization; the small spread exhibited by the non localized

connectivity functions makes the reference connectivity one fall outside the cloud of individual functions for the radial flow case. After localization, the reference connectivity is within the cloud for the correct prior function model, while still falls partly outside for the wrong prior. The falling of the reference connectivity function outside the cloud of individual functions is also an indication of underestimation of the ensemble variability induced by the non localized NS-EnKF.

Finally, localization has a minimal impact in the reproduction of the piezometric heads as seen in Figure 6.9, the $RMSE$ is almost the same with and without, although localization serves to reduce the $RMSE$ for the correct prior scenarios, but increases it for the wrong prior ones. Localization, as expected, increases the ES in all cases.

It is concluded that, for this particular case, in which the underlying aquifer is highly variable with channel features, 1000 realizations is not enough to avoid filter inbreeding in the application of the EnKF. For this reason we recommend the use of localization together with the NS-EnKF to improve the results.

6.4.3 Effect of boundary conditions

The NS-EnKF has been tested for two sets of boundary conditions which basically induce parallel flow and radial flow, the rest of the setup being the same.

The characterization of the hydraulic conductivities is good under both flow conditions. The mean of the final ensemble of realizations gets closer to the reference field for the parallel flow case than for the radial flow one, as can be observed by looking at the channels identified in Figure 6.5, their width is more uniform and their extent go through the entire aquifer for parallel flow. As already mentioned, the local ensemble variance (Figure 6.6) show the highest values for the cells close to the prescribed head boundary and extending through the shale area in the parallel flow case as it would be expected given the lack of sensitivity of head to conductivity changes at those locations.

There is not a significantly different behavior on the evolution of the $RMSE$ and the SE (Figure 6.7) for the two sets of boundary conditions. Just notice that the final values of both metrics tend to converge to the same value after localization for both flow conditions, while prior to localization they are different (larger $RMSE$ and smaller ES for radial flow than for parallel flow).

Regarding the reproduction of the connectivity, it is apparently more difficult to reproduce it for radial flow case than for parallel flow; for radial flow, there seems to be an important filter inbreeding that leaves the reference connectivity function outside the cloud of individual functions; apart from

that, there is no significant difference on the performance of the NS-EnKF in characterizing the connectivity under radial or parallel flow conditions.

Finally, regarding the reproduction of the piezometric heads (Figure 6.9), the main difference between parallel and radial flow is that for radial flow the overall reduction of $RMSE$ with regard to the unconditional realizations is smaller than for parallel flow, but this is easily understandable since the piezometric head fluctuations with respect to the initial state are stronger for radial flow than for parallel due to the several pumping and recharge wells used for the radial flow scenarios.

We conclude that the NS-EnKF performs similarly well for either radial flow or parallel flow conditions. However, from the analysis of the $RMSE(\ln K)$ and $ES(\ln K)$, the radial flow case apparently is more prone to filter inbreeding than the parallel flow case. Inbreeding that disappears after localizing the filter.

6.4.4 Effect of number of conditioning piezometers

Scenarios 1 to 12 have been analyzed considering that there are 111 piezometers (Figure 6.3) providing dynamic hydraulic head measurements during the first 66.7 days (first 60 simulation time steps), which are assimilated through the NS-EnKF to update an ensemble of hydraulic conductivity realizations. For this number of piezometers, the NS-EnKF seems to perform reasonably well for a variety of scenarios, including the case in which an incorrect prior random function model is used. Since there are no logconductivity data, the information provided by the piezometer is crucial for the identification of the hydraulic conductivity spatial patterns. We decided to reduce the number of piezometers to one third of the original ones and keep only 32 of them (Figure 6.10A) to analyze two more scenarios, under parallel flow and without localization; scenario 13 assumes the correct prior random function model and scenario 14 the wrong one.

Maps B and D in Figure 6.10 show the ensemble mean of logconductivity and maps C and E the ensemble variance for the correct and wrong prior, respectively. As expected, the characterization of the channels is worse and the ensemble variance is larger when fewer piezometers are used; however, the characterization is not bad. The overall location of the channels is well captured and the highest local variances occur at channel borders, with a much better performance for the correct prior random function than for the wrong one.

We conclude that the number of piezometers is important for the characterization of the logconductivity, particularly when the prior random function is wrong.

6.4.5 Discussion

This paper presented a performance assessment of the NS-EnKF, a real-time data assimilation algorithm, in a two dimensional bimodal aquifer, and focused on four aspects: (1) the impact of random function choice; (2) the effect of introducing a localization function (3) the flow regimes and (4) the number of piezometers used during assimilation.

The results show that assimilating piezometric head data with the NS-EnKF allows the detection of the channel structures, even if the prior geostatistical model is erroneous and not capable to reproduce the types of channels of the underlying reference aquifer. This result may have important implications for groundwater modeling studies, since it implies that a sufficiently large number of piezometers may offset the negative impact of an erroneous choice of the random function model used to generate the starting ensemble of conductivity realizations. For those who are not keen on using training images to characterize the spatial variability of the hydraulic conductivity, a variogram-based simulation algorithm may serve as the starting point, leaving to the NS-EnKF the task to identify the curvilinear features that the variogram-based algorithm cannot.

Although it might be argued that we had access to the "correct" prior histogram in the wrong prior analysis, if the contrast in conductivities between the channel and non-channel facies is large enough, the really important a priori information that would be needed would be the proportions of each facies and the contrast between their average conductivities.

Our results are more optimistic than the ones from Kerrou et al. (2008), who concluded that an erroneous prior geostatitical model cannot be corrected by inverse modeling, even if many hydraulic head data are available. We attribute this impossibility to the inverse modeling method utilized and claim that the NS-EnKF can help to produce an acceptable characterization of the hydraulic conductivities even when the prior random function model is incorrect.

We also demonstrate the importance of coupling the NS-EnKF with a distance-dependent localization function, even for a case such as this in which the ensemble consisted of 1000 realizations. A future research topic is the improvement of the localization functions, allowing for anisotropy and non-stationarity (i.e., time and/or space dependence), and with the option to have different formulations for piezometric head covariances and piezometric-conductivity cross-covariances.

Apparently, the NS-EnKF works equally well for both parallel and radial flow conditions. And, it is clear that for a case such as this one in which the conductivity identification is based solely on the information conveyed by the

dynamic piezometric head data, the number of piezometers is very important, more so, when the prior random function model is wrong.

6.5 Conclusion

The complexity of subsurface geological structures calls for a characterization technique, which can incorporate the conductivity measurement data as well as the responses of aquifers in an efficient and effective way. The NS-EnKF, a real-time data assimilation technique which couples EnKF with normal score transformation, has been recently developed by Zhou et al. (2011a). The method avoids the classical multiGaussianity inherent to most simulation algorithms.

In this paper, we have analyzed 14 scenarios to present a detailed analysis of the impact of (i) prior model choice, (ii) use of localization functions, (iii) flow regime, and (iv) number of piezometers used, on the performance of the NS-EnKF algorithm in a synthetic 2D bimodal aquifer. The following conclusions can be drawn from the simulation exercises:

- The NS-EnKF performs relatively well when an incorrect prior geostatistical model incapable of producing channeled realizations is used. Results are worse than when the correct prior is used, but acceptable.
- Coupling the NS-EnKF with a distance-dependent localization function improves both the characterization of conductivity and the prediction of groundwater flow.
- The performance of NS-EnKF was similar for two different flow scenarios (parallel flow and radial flow), in both cases, the patterns of conductivity are identified very well.
- The quality of the characterization is directly related to the number of piezometers used, more so when a wrong a priori model is used.

Bibliography

Alcolea, A., Carrera, J., Medina, A., 2006. Pilot points method incorporating prior information for solving the groundwater flow inverse problem. Advances in Water Resources 29 (11), 1678–1689.

Alcolea, A., Renard, P., 2010. Blocking Moving Window algorithm: Conditioning multiple-point simulations to hydrogeological data. Water Resources Research 46 (8), W08511.

Anderson, J., 2001. An ensemble adjustment Kalman filter for data assimilation. Monthly weather review 129, 2884–2903.

Arulampalam, M., Maskell, S., Gordon, N., Clapp, T., 2002. A tutorial on particle filters for online nonlinear/non-Gaussian Bayesian tracking. IEEE Transactions on signal processing 50 (2), 174–188.

Bear, J., 1972. Dynamics of fluids in porous media. American Elsevier Pub. Co., New York.

Burgers, G., van Leeuwen, P., Evensen, G., 1998. Analysis scheme in the ensemble Kalman filter. Monthly Weather Review 126, 1719–1724.

Capilla, J., Llopis-Albert, C., 2009. Gradual conditioning of non-Gaussian transmissivity fields to flow and mass transport data: 1. Theory. Journal of Hydrology 371 (1-4), 66–74.

Capilla, J. E., Rodrigo, J., Gómez-Hernández, J. J., 1999. Simulation of non-gaussian transmissivity fields honoring piezometric data and integrating soft and secondary information. Math. Geology 31 (7), 907–927.

Carrera, J., Alcolea, A., Medina, A., Hidalgo, J., Slooten, L., 2005. Inverse problem in hydrogeology. Hydrogeology Journal 13 (1), 206–222.

Chen, Y., Oliver, D., 2010. Cross-covariances and localization for EnKF in multiphase flow data assimilation. Computational Geosciences, 1–23.

Chen, Y., Zhang, D., 2006. Data assimilation for transient flow in geologic formations via ensemble Kalman filter. Advances in Water Resources 29 (8), 1107–1122.

Deutsch, C. V., Journel, A. G., 1992. GSLIB, Geostatistical Software Library and User's Guide. Oxford University Press, New York.

Deutsch, C. V., Journel, A. G., 1998. GSLIB, Geostatistical Software Library and User's Guide, 2nd Edition. Oxford University Press, New York.

Devegowda, D., Arroyo-Negrete, E., Datta-Gupta, A., 2010. Flow relevant covariance localization during dynamic data assimilation using EnKF. Advances in Water Resources 33 (2), 129–145.

Evensen, G., 2003. The ensemble Kalman filter: Theoretical formulation and practical implementation. Ocean dynamics 53 (4), 343–367.

Fu, J., Gómez-Hernández, J. J., 2009. A Blocking Markov Chain Monte Carlo Method for Inverse Stochastic Hydrogeological Modeling. Mathematical Geosciences 41 (2), 105–128.

Gaspari, G., Cohn, S., 1999. Construction of correlation functions in two and three dimensions. Quarterly Journal of the Royal Meteorological Society 125 (554), 723–757.

Gómez-Hernández, J., Wen, X., 1998. To be or not to be multi-Gaussian? A reflection on stochastic hydrogeology. Advances in Water Resources 21 (1), 47–61.

Gómez-Hernández, J. J., Journel, A. G., 1993. Joint sequential simulation of multi-Gaussian fields. Geostatistics Troia 92 (1), 85–94.

Gómez-Hernández, J. J., Sahuquillo, A., Capilla, J. E., 1997. Stochastic simulation of transmissivity fields conditional to both transmissivity and piezometric data, 1, Theory. Journal of Hydrology 203 (1–4), 162–174.

Gómez-Hernández, J. J., Srivastava, R. M., 1990. ISIM3D: an ANSI-C three dimensional multiple indicator conditional simulation program. Computers & Geosciences 16 (4), 395–440.

Goovaerts, P., 1997. Geostatistics for natural resources evaluation. Oxford University Press, USA.

Hamill, T., Whitaker, J., Snyder, C., 2001. Distance-dependent filtering of background error covariance estimates in an ensemble Kalman filter. Monthly Weather Review 129 (11), 2776–2790.

Harbaugh, A. W., Banta, E. R., Hill, M. C., McDonald, M. G., 2000. MODFLOW-2000, the U.S. Geological Survey modular ground-water model. U.S. Geological Survey, Branch of Information Services, Reston, VA, Denver, CO.

Hendricks Franssen, H., Alcolea, A., Riva, M., Bakr, M., van der Wiel, N., Stauffer, F., Guadagnini, A., 2009. A comparison of seven methods for the inverse modelling of groundwater flow. application to the characterisation of well catchments. Advances in Water Resources 32 (6), 851–872.

Hendricks Franssen, H., Gómez-Hernández, J., Sahuquillo, A., 2003. Coupled inverse modelling of groundwater flow and mass transport and the worth of concentration data. Journal of Hydrology 281 (4), 281–295.

Hendricks Franssen, H., H. P. Kaiser, U. Kuhlmann, G. B. F. S. R. M., Kinzelbach, W., 2011. Operational real-time modeling with EnKF of variably saturated subsurface flow including stream-aquifer interaction and parameter updating. Water Resources Research, in press,doi:10.1029/2010WR009480.

Hendricks Franssen, H., Kinzelbach, W., 2008. Real-time groundwater flow modeling with the Ensemble Kalman Filter: Joint estimation of states and parameters and the filter inbreeding problem. Water Resources Research 44 (9), W09408.

Hendricks Franssen, H., Kinzelbach, W., 2009. Ensemble Kalman filtering versus sequential self-calibration for inverse modelling of dynamic groundwater flow systems. Journal of Hydrology 365 (3-4), 261–274.

Hu, L. Y., 2000. Gradual deformation and iterative calibration of gaussian-related stochastic models. Math. Geology 32 (1), 87–108.

Huang, C., Hu, B. X., Li, X., Ye, M., 2008. Using data assimilation method to calibrate a heterogeneous conductivity field and improve solute transport prediction with an unknown contamination source. Stochastic Environmental Research and Risk Assessment 23 (8), 1155–1167.

Kerrou, J., Renard, P., Hendricks Franssen, H., Lunati, I., 2008. Issues in characterizing heterogeneity and connectivity in non-multiGaussian media. Advances in Water Resources 31 (1), 147–159.

Knudby, C., Carrera, J., 2005. On the relationship between indicators of geostatistical, flow and transport connectivity. Advances in Water Resources 28 (4), 405–421.

LaVenue, A. M., Ramarao, B. S., de Marsily, G., Marietta, M. G., 1995. Pilot point methodology for automated calibration of an ensemble of conditionally simulated transmissivity fields, 2, Application. Water Resour. Res. 31 (3), 495–516.

Lee, S., Carle, S., Fogg, G., 2007. Geologic heterogeneity and a comparison of two geostatistical models: Sequential Gaussian and transition probability-based geostatistical simulation. Advances in water resources 30 (9), 1914–1932.

Li, L., Zhou, H., Gómez-Hernández, J. J., 2010a. Steady-state groundwater flow modeling with full tensor conductivities using finite differences. Computers & Geosciences 36 (10), 1211–1223.

Li, L., Zhou, H., Gómez-Hernández, J. J., 2011a. A comparative study of three-dimensional hydrualic conductivity upscaling at the macrodispersion experiment (MADE) site, columbus air force base, mississippi (USA). Journal of Hydrology, in press, doi:10.1016/j.jhydrol.2011.05.001.

Li, L., Zhou, H., Gómez-Hernández, J. J., 2011b. Transport upscaling using multi-rate mass transfer in three-dimensional highly heterogeneous porous media. Advances in Water Resources 34 (4), 478–489.

Li, L., Zhou, H., Gómez-Hernández, J. J., Hendricks Franssen, H., 2011c. Jointly mapping hydraulic conductivity and porosity by assimilating concentration data via ensemble kalman filter. Journal of Hydrology, submitted for publication.

Li, L., Zhou, H., Hendricks Franssen, H., Gómez-Hernández, J. J., 2010b. Modeling transient flow by coupling ensemble kalman filtering and upscaling. Water Resources Research, submitted.

Mariethoz, G., Renard, P., Caers, J., 2010a. Bayesian inverse problem and optimization with iterative spatial resampling. Water Resources Research 46 (11), W11530.

Mariethoz, G., Renard, P., Straubhaar, J., 2010b. The Direct Sampling method to perform multiple-point geostatistical simulations. Water Resources Research, W11536.

McLaughlin, D., Townley, L., 1996. A reassessment of the groundwater inverse problem. Water Resources Research 32 (5), 1131–1161.

Nan, T., Wu, J., 2010. Groundwater parameter estimation using the ensemble Kalman filter with localization. Hydrogeology Journal, 1–15.

Nowak, W., 2009. Best unbiased ensemble linearization and the quasi-linear Kalman ensemble generator. Water Resour. Res 45.

Oliver, D., Cunha, L., Reynolds, A., 1997. Markov chain Monte Carlo methods for conditioning a permeability field to pressure data. Mathematical Geology 29 (1), 61–91.

Pardo-Igúzquiza, E., Dowd, P., 2003. CONNEC3D: a computer program for connectivity analysis of 3D random set models* 1. Computers & geosciences 29 (6), 775–785.

Ramarao, B. S., LaVenue, A. M., de Marsily, G., Marietta, M. G., 1995. Pilot point methodology for automated calibration of an ensemble of conditionally simulated transmissivity fields, 1, Theory and computational experiments. Water Resour. Res. 31 (3), 475–493.

Reichle, R., Walker, J., Koster, R., Houser, P., 2002. Extended versus ensemble Kalman filtering for land data assimilation. Journal of hydrometeorology 3, 728–740.

Sahuquillo, A., Capilla, J. E., Gómez-Hernández, J. J., Andreu, J., 1992. Conditional simulation of transmissivity fields honouring piezometric head data. In: Blair, W. R., Cabrera, E. (Eds.), Hydraulic Engineering Software IV, Fluid Flow Modeling. Vol. II. Elsevier Applied Science, London, UK, pp. 201–214.

Strebelle, S., 2002. Conditional simulation of complex geological structures using multiple-point statistics. Mathematical Geology 34 (1), 1–21.

Sun, A. Y., Morris, A. P., Mohanty, S., Jul. 2009. Sequential updating of multimodal hydrogeologic parameter fields using localization and clustering techniques. Water Resources Research 45, 15 PP.

Wen, X., Deutsch, C., Cullick, A., 2002. Construction of geostatistical aquifer models integrating dynamic flow and tracer data using inverse technique. Journal of Hydrology 255 (1-4), 151–168.

Wen, X., Gómez-Hernández, J., 1998. Numerical modeling of macrodispersion in heterogeneous media: a comparison of multi-Gaussian and non-multi-Gaussian models. Journal of contaminant hydrology 30 (1-2), 129–156.

Wen, X. H., Chen, W., 2005. Real-time reservoir model updating using ensemble Kalman filter. In: SPE reservoir simulation symposium.

Western, A., Bloschl, G., Grayson, R., 2001. Toward capturing hydrologically significant connectivity in spatial patterns. Water Resources Research 37 (1), 83–97.

Wu, J., Boucher, A., Zhang, T., 2008. A sgems code for pattern simulation of continuous and categorical variables: Filtersim. Computers & Geosciences 34 (12), 1863–1876.

Yeh, W., 1986. Review of parameter identification procedures in groundwater hydrology: The inverse problem. Water Resources Research 22 (2), 95–108.

Zhou, H., Gómez-Hernández, J. J., Hendricks Franssen, H., Li, L., 2011a. Handling non-gaussian distributions with ensemble kalman filter. Advances in Water Resources, in press, doi:10.1016/j.advwatres.2011.04.014.

Zhou, H., Li, L., Gómez-Hernández, J. J., 2010. Three-dimensional hydraulic conductivity upscaling in groundwater modelling. Computers & Geosciences 36 (10), 1224–1235.

Zhou, H., Li, L., Gómez-Hernández, J. J., Hendricks Franssen, H., 2011b. Pattern identification in bimodal aquifer by normal score ensemble kalman filter. Mathematical Geosciences, submitted.

Zimmerman, D., De Marsily, G., Gotway, C., Marietta, M., Axness, C., Beauheim, R., Bras, R., Carrera, J., Dagan, G., Davies, P., et al., 1998. A comparison of seven geostatistically based inverse approaches to estimate transmissivities for modeling advective transport by groundwater flow. Water Resources Research 34 (6), 1373–1413.

Zinn, B., Harvey, C. F., 2003. When good statistical models of aquifer heterogeneity go bad: A comparison of flow, dispersion, and mass transfer in connected and multivariate gaussian hydraulic conductivity fields. Water Resour. Res 39 (3), 1051.

7 Conclusions

7.1 Summary

Uncertainty assessment and risk analysis of groundwater flow and solute transport predictions call for the use of stochastic models in a Monte-Carlo framework. On a first step, the characterization of an aquifer can be represented by multiple equally-likely realizations conditional on the direct measurements using the geostatistical approach. Since the scale of the conductivity measurements is usually smaller than the scale of the numerical model, there is a need to find a set of conductivities, defined at a coarser scale, which produce similar flow behavior as the finely discretized model. This is achieved by upscaling. Moreover, due to the limited knowledge of the aquifer geological structure, inverse modeling is used to incorporate the state information and hence improve the characterization of the aquifer and reduce the uncertainty on flow and transport predictions.

In Chapter 2, we reviewed several upscaling techniques ranging from simple averaging over a uniform grid to sophisticated Laplacian-with-skin method on non-uniform grids. We choose a high-resolution conductivity realization as a reference for the upscaling. This image was generated using a hole-effect variogram and it was shown that flow and transport modeling on this realization can reproduce the observed plume. The different upscaling methods are then applied on this realization. The results show that (1) the Laplacian-with-skin technique with a skin size of half block performs best; (2) a non-uniform coarsening focused in the refinement of the regions through which the solute plume

travels can further improve the results, and (3) the advection-dispersion equation can be used at the coarser scale to model the plume migration if careful modeling/upscaling is performed, as long as the block size remains smaller than the correlation ranges of the underlying fine scale conductivities.

Chapter 3 presented a three-dimensional transport upscaling methodology in highly heterogeneous media. This approach introduced an advanced Laplacian-with-skin hydraulic conductivity upscaling prior to the transport upscaling. Transport upscaling requires the introduction, at the coarse scale, of a multi-rate mass transfer process on the classical advection-dispersion equation for the modeling. The methodology is demonstrated on a 3D synthetic example. The advantages of the Laplacian-with-skin over other approaches as well as the multi-rate mass transfer model-based upscaling over the advection-only-based upscaling are proved in the exercise.

Chapter 4 introduced a new methodology to model transient groundwater flow in a high-resolution numerical model by coupling upscaling with ensemble Kalman filtering. This approach consists of three steps: (1) conductivity realizations are generated at the scale of the measurements, (2) an advanced upscaling approach such as the Laplacian-with-skin method is used to reduce the dimensions of the numerical model, and (3) the ensemble Kalman filter is used in a set of upscaled conductivity tensors to condition on the observed piezometric head data. The proposed new method is demonstrated in a 2D synthetic data-worth exercise.

Chapter 5 applied the ensemble Kalman filter to jointly map hydraulic conductivities and porosities by assimilating the dynamic piezometric head and multiple concentration data. Compared with other inverse methods, the EnKF is remarkable for its computational efficiency, but more importantly for the easiness to account for multiple types of conditioning data. The capability of the EnKF for the characterization of conductivities and porosities is demonstrated in a 2D synthetic example. The uncertainty on flow and transport predictions is reduced to the minimum when all the data are assimilated.

Finally, in Chapter 6, the normal-score Ensemble Kalman Filter, an algorithm recently developed to deal with the non-Gaussianity of parameter and state vectors in EnKF, is used to assess the impact of prior conceptual model uncertainty on the characterization of conductivity and on the prediction of flow in a synthetic bimodal aquifer. In addition, the effect of distance-dependent localization functions and different set-ups of the boundary conditions in the aquifer are also examined. The results are evaluated in terms of ensemble means, variances and connectivities of the conditional realizations of conductivity and also looking at the uncertainty of predicted heads after solving the flow equation in the conditional conductivity realizations. For the cases analyzed it is found that (i) the patterns of simulated conductivity and flow prediction can be reproduced close to the reference for both the correct

and wrong prior model using either the NS-EnKF or localized NS-EnKF as long as a sufficient number of piezometric head data are used for conditioning, (ii) coupling NS-EnKF with the localization function improves the conductivity identification, (iii) the performance of the NS-EnKF is not affected by the types of boundary conditions used.

7.2 Recommendations for Future Research

- **Further development and improvement of transport upscaling methodology.** The transport upscaling method as outlined in Chapter 3 provides an approach to deal with the loss of heterogeneity inherent to all upscaling processes. We demonstrated that it is possible to include the multi-rate mass transfer process to model the mass transport at the coarse scale. However, the obvious drawback of the method proposed is the need of the transport solution at the fine scale to determined the upscaled parameters, what, in principle, beats the purpose of upscaling (i.e., to avoid the modeling at the fine scale). Hence, it would be very significant to find an avenue to circumvent the need to solve the transport problem at the fine scale, especially regarding on how to obtain the upscaled effective porosity, which controls the mean travel times in each block.

- **Extending the approach of coupling EnKF and upscaling to a real case study.** To handle the inverse modeling at the large model, we proposed a new methodology by coupling the EnKF and upscaling as stated in Chapter 4. We used a 2D synthetic example to prove that the conductivity and piezometric head data at the measurement scale can be used for conditioning at the coarse scale and hence leading to a reduced uncertainty of flow prediction. In Chapter 2, we applied different upscaling method at the MADE site and concluded that the Laplacian-with-skin performs best in terms of flow and transport reproductions. Hence, the coupling approach developed could be applied and tested in the field case at the MADE site.

- **Coupling the localization function with EnKF and evaluating its effect on concentration assimilation.** As stated in Chapter 5, we applied the standard EnKF to assimilate multiple concentration data and dynamic head data. The results shown the characterization of parameters and flow and transport predictions are both improved. It seems that some artifacts are observed when the concentration data is used for conditioning. It would be interesting to couple the localization function with the EnKF to see the precision and spread of estimations and model

predictions. Also, we only considered the heterogeneity of conductivity and porosity in the assimilation procedure. It is also significant to test the capacity of EnKF in identifying multiple parameters such as conductivity, storage, porosity, dispersivity and retardation all together.

- **Extending NS-EnKF to assimilate concentration data in non-multiGaussian media.** The capability of the NS-EnKF was demonstrated in the context of parameter identification when the prior statistical is wrong in Chapter 6. We show that, when the number of conditioning head data is smaller, the identification of channels is difficult. Hence, it is necessary to see if other state information such as concentration as shown in Chapter 5 can be used to complement the piezometric head data.

A

FLOWXYZ3D - A Three-Dimensional Finite-Difference Simulator with Full Conductivity Tensors

A nineteen-point block-centered finite-difference procedure for the solution of saturated groundwater steady flow in 3D with full tensor conductivities is described here. In the absence of sinks and sources, the partial differential equation governing flow in three-dimensions can be expressed as:

$$\frac{\partial}{\partial x}\Big(K_{xx}\frac{\partial h}{\partial x}+K_{xy}\frac{\partial h}{\partial y}+K_{xz}\frac{\partial h}{\partial z}\Big)+\frac{\partial}{\partial y}\Big(K_{xy}\frac{\partial h}{\partial x}+K_{yy}\frac{\partial h}{\partial y}+K_{yz}\frac{\partial h}{\partial z}\Big)+ \frac{\partial}{\partial z}\Big(K_{xz}\frac{\partial h}{\partial x}+K_{yz}\frac{\partial h}{\partial y}+K_{zz}\frac{\partial h}{\partial z}\Big)=0 \tag{A.1}$$

If this equation is discretized with a nineteen-point block-centered finite-difference stencil over a non-uniform grid of parallelpipedal blocks, the following equation results for a generic block (i,j,k) of size $\Delta x|_{i,j,k} \times \Delta y|_{i,j,k} \times \Delta z|_{i,j,k}$ (see Figure A.1):

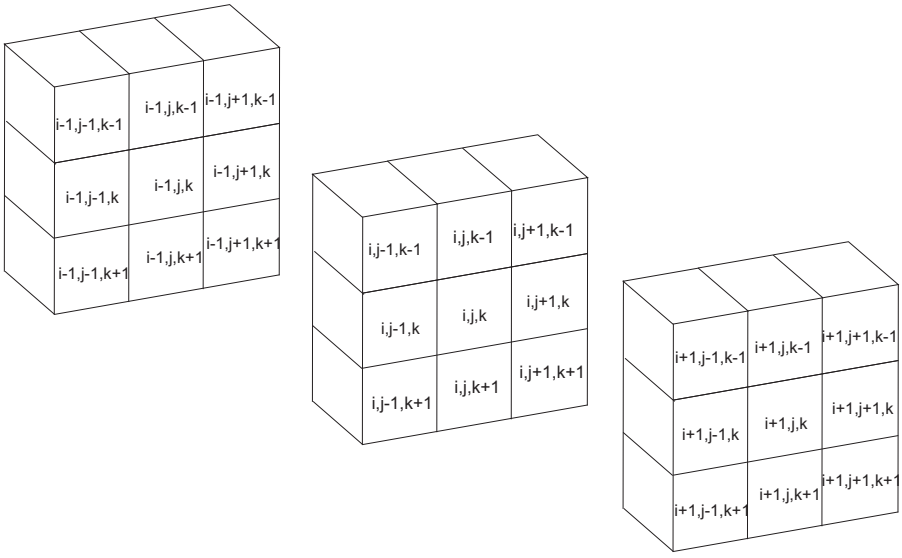

Figure A.1: Schematic illustration of the 3D finite-difference spatial discretization

$$
\begin{aligned}
&\frac{1}{\Delta x|_{i,j,k}}\left[\left(K_{xx}\frac{\partial h}{\partial x}+K_{xy}\frac{\partial h}{\partial y}+K_{xz}\frac{\partial h}{\partial z}\right)\Big|_{i+1/2,j,k}-\right.\\
&\qquad\left.\left(K_{xx}\frac{\partial h}{\partial x}+K_{xy}\frac{\partial h}{\partial y}+K_{xz}\frac{\partial h}{\partial z}\right)\Big|_{i-1/2,j,k}\right]+\\
&\frac{1}{\Delta y|_{i,j,k}}\left[\left(K_{xy}\frac{\partial h}{\partial x}+K_{yy}\frac{\partial h}{\partial y}+K_{yz}\frac{\partial h}{\partial z}\right)\Big|_{i,j+1/2,k}-\right.\\
&\qquad\left.\left(K_{xy}\frac{\partial h}{\partial x}+K_{yy}\frac{\partial h}{\partial y}+K_{yz}\frac{\partial h}{\partial z}\right)\Big|_{i,j-1/2,k}\right]+\\
&\frac{1}{\Delta z|_{i,j,k}}\left[\left(K_{xz}\frac{\partial h}{\partial x}+K_{yz}\frac{\partial h}{\partial y}+K_{zz}\frac{\partial h}{\partial z}\right)\Big|_{i,j,k+1/2}-\right.\\
&\qquad\left.\left(K_{xz}\frac{\partial h}{\partial x}+K_{yz}\frac{\partial h}{\partial y}+K_{zz}\frac{\partial h}{\partial z}\right)\Big|_{i,j,k-1/2}\right]=\quad 0
\end{aligned}
\tag{A.2}
$$

The hydraulic gradients at the interfaces are approximated by central differences from the heads at the nineteen blocks surrounding (i, j, k), That is,

$$\left.\frac{\partial h}{\partial x}\right|_{i+1/2,j,k} = \frac{h_{i,j+1,k} - h_{i,j-1,k}}{\triangle x|_{i,j+1,k} + 2\triangle x|_{i,j,k} + \triangle x|_{i,j-1,k}} + \frac{h_{i+1,j+1,k} - h_{i+1,j-1,k}}{\triangle x|_{i+1,j+1,k} + 2\triangle x|_{i+1,j,k} + \triangle x|_{i+1,j-1,k}}$$

$$\left.\frac{\partial h}{\partial y}\right|_{i+1/2,j,k} = \frac{2(h_{i+1,j,k} - h_{i,j,k})}{\triangle y|_{i+1,j,k} + \triangle y|_{i,j,k}} \tag{A.3}$$

$$\left.\frac{\partial h}{\partial z}\right|_{i+1/2,j,k} = \frac{h_{i,j,k+1} - h_{i,j,k-1}}{\triangle z|_{i,j,k+1} + 2\triangle z|_{i,j,k} + \triangle z|_{i,j,k-1}} + \frac{h_{i+1,j,k+1} - h_{i+1,j,k-1}}{\triangle z|_{i+1,j,k+1} + 2\triangle z|_{i+1,j,k} + \triangle z|_{i+1,j,k-1}}$$

The partial derivatives of the hydraulic head in the other five interfaces can be given by similar expressions. Substituting (A.3) into (A.2), multiplying both sides by $\Delta x|_{i,j,k}\Delta y|_{i,j,k}\Delta z|_{i,j,k}$, and rearranging terms, the nineteen-point results in:

$$\begin{aligned} &Ah_{i,j+1,k} + Bh_{i,j,k} + Ch_{i+1,j+1,k} + Dh_{i-1,j+1,k} + Eh_{i+1,j,k} + Fh_{i-1,j,k} + \\ &Gh_{i,j+1,k+1} + Hh_{i,j+1,k-1} + Ih_{i,j,k+1} + Jh_{i,j,k-1} + Kh_{i,j-1,k} + Lh_{i+1,j-1,k} + \\ &Mh_{i-1,j-1,k} + Nh_{i,j-1,k+1} + Oh_{i,j-1,k-1} + Ph_{i+1,j,k+1} + Qh_{i+1,j,k-1} + \\ &Rh_{i-1,j,k+1} + Sh_{i-1,j,k-1} = 0 \end{aligned} \tag{A.4}$$

where A, B, ..., S are function of the block sizes and interface hydraulic conductivity components. Equation (A.4) is written for all the nodes within the aquifer, except for those for which head is prescribed, resulting in a set of linear equations.